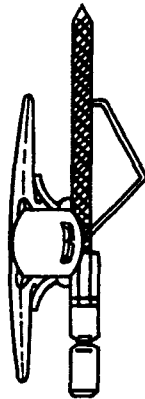
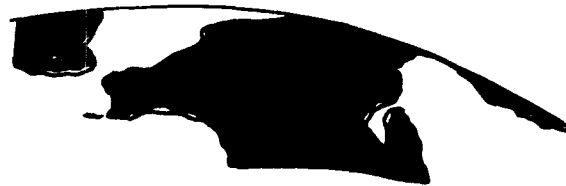


30 JULY 1981

MDC G9390



NASA-CR-161017  
19810018627



# DEVELOPMENT OF A COMPOSITE GEODETIC STRUCTURE FOR SPACE CONSTRUCTION

## Phase 2 Final Report

NASA CONTRACT NO. NAS 9-15678  
DRL NO. T-1522  
DRD NO. MA-201 TB  
LINE ITEM NO. 3

LIBRARY COPY

MCDONNELL DOUGLAS ASTRONAUTICS COMPANY

LANGLEY RESEARCH CENTER  
LIBRARY, NASA  
HAMPTON, VIRGINIA

MCDONNELL DOUGLAS



NF01811



**DEVELOPMENT OF A COMPOSITE GEODETIC  
STRUCTURE FOR SPACE CONSTRUCTION  
PHASE II FINAL REPORT**

**30 JULY 1981**

**MDC G9390**

**PREPARED FOR: NATIONAL AERONAUTICS AND SPACE ADMINISTRATION  
JOHNSON SPACE CENTER  
HOUSTON, TEXAS**

**CONTRACT NO. NAS 9-15678  
DRL NO. T-1522  
DRD NO. MA-201TB  
LINE ITEM NO. 3**

**MCDONNELL DOUGLAS ASTRONAUTICS COMPANY-HUNTINGTON BEACH**  
*5301 Bolsa Avenue Huntington Beach, California 92647 (714) 896-3311*

*N81-27165#*

*Sam*  
*Deane*

**MCDONNELL  
DOUGLAS**

DEVELOPMENT OF A COMPOSITE GEODETIC  
STRUCTURE FOR SPACE CONSTRUCTION

Technical Letter Progress  
Report No. 31

November 1981

NAS9-15678

Prepared by

J. W. Maxted

Approved by

*R. F. Zemer*

R. F. Zemer, Director  
Advanced Programs  
Design & Technology  
Engineering Division

Prepared under Contract NAS9-15678, DRL No. T-1522, Line Item 1,  
DRD No. MA-003 for

NASA-Johnson Space Center, Houston, Texas 77058

**MCDONNELL DOUGLAS ASTRONAUTICS COMPANY-WEST**

5301 Bolsa Avenue, Huntington Beach, CA 92647

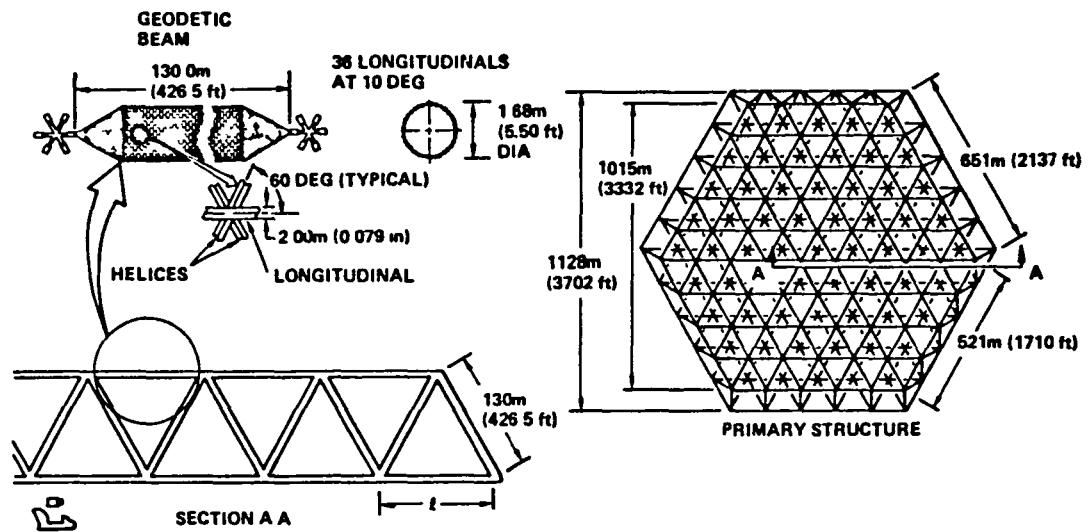
DEC 7 1981

## 1.0 INTRODUCTION

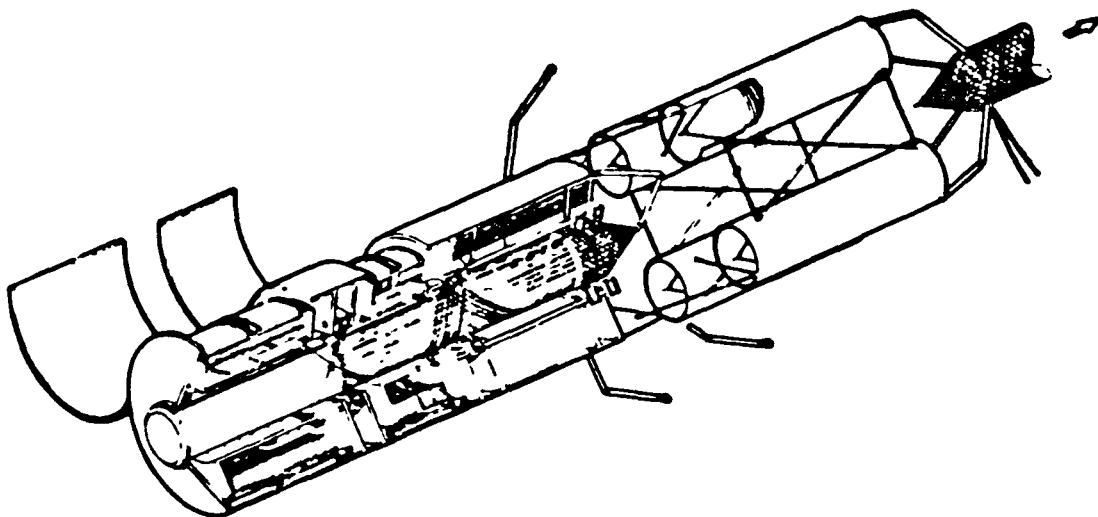
The overall objective of this program is to develop a structurally efficient composite geodetic beam and a beam fabrication machine for on-orbit construction of large space structures (Figure 1). Phase II of the program ended 30 July 1981. Phase IIA was initiated on 1 July 1981 and is proceeding on schedule.

The overall program is divided into three phases to provide an orderly flow of technical accomplishments starting with demonstration of geodetic beam feasibility, continuing with verification of a full size beam, and finally providing a ground demonstration of automatic fabrication of a geodetic beam. Phase I consisted of tasks to (1) develop structural design requirements, (2) develop analytical procedures and select the best configuration for a geodetic beam, (3) develop structural termination concepts for the geodetic beam, (4) accomplish beam preliminary sizing, (5) develop pultruded composite rod stock for use in joining tests and feasibility test articles, (6) select a reliable joining technique, (7) design, fabricate, and test two geodetic test articles to establish concept feasibility, and initiate the preliminary design of a beam fabrication machine. Additional Phase I efforts consisted of preparation of an Orbital Flight Test (OFT) plan and fabrication of a scale model to demonstrate a key subsystem of the geodetic beam machine. Phase II was devoted to detailed material characterization tests of the pultruded composite rods and encapsulated joints (Task 8), parameter tests of a geodetic test cylinder and a cylinder/conical closeout test article (Task 9), and an improved geodetic beam analysis based on the parameter tests (Task 10). Phase IIA, currently being conducted, consists of Tasks 11 and 13. Task 11 involves designing, fabricating, and instrumenting a 25-ft. long verification beam that will be tested at NASA/JSC. Task 13 will establish the feasibility of using metal matrix composite (MMC) materials in fabrication of geodetic beams. Task 12, the detailed design of a geodetic beam machine, was deferred until Phase III. In Phase III, the ground demonstration of automatic fabrication of geodetic beams will be accomplished using pilot-plant equipment capable of automatically fabricating demonstration articles.





a. Geodetic Beam Application to a Microwave Power Transmission Antenna



b. Geodetic Beam Machine Concept

Figure 1. Geodetic Beam and Beam Machine Concept

## 2.0 SUMMARY OF PROGRESS

Design details of the verification test beam were finalized in October. The HMS/Glass/P1700 tape was ordered for Task 11. The preliminary metal matrix composite rod stock was being fabricated for Task 13. Phase IIA progress is proceeding on schedule as shown in Figure 2.

## 3.0 VERIFICATION BEAM (Task 11)

Details of the verification test beam design were finalized in October. Unigraphics has been utilized for the design activity resulting in high quality computer-generated drawings. The overall beam length is 298.3 inches with a nominal beam diameter of 30 inches. A total of thirty longitudinals are planned which will result in a nominal node spacing of 3.63 inches. Since increased axial loads are anticipated for the cone longitudinals, the closeout node spacing is reduced to 3.44 inches. The HMS/Glass/P1700 tape was ordered which will result in a nominal rod stock diameter of 0.103 inches. The latest weight estimate is shown in Table 1. The verification test beam design is shown in Figure 3. The beam will include twelve 1/4-inch diameter holes on both end frames for ease of attachment to test and handling fixtures. The interface is shown in Figure 4. The cylinder/closeout frames were modified in October to facilitate ease of fabrication. The cylinder to frame joint design is shown in Figure 5. The closeout to frame joint design is shown in Figure 6. Preliminary work has begun on fixture design.

Table 1  
VERIFICATION TEST BEAM WEIGHT ASSESSMENT

<u>Description</u>	<u>TOTAL</u> <u>Weight</u>
HMS/Glass/P1700 Rods	12.4 Lbs.
Versimid 1200 Encapsulant	2.1 Lbs.
Cylinder/Closeout Frames (2 required)	6.2 Lbs.
End Fittings (2 required)	1.6 Lbs.
Adhesive	0.6 Lbs.
Verification Beam Total	<u>22.9 Lbs.</u>

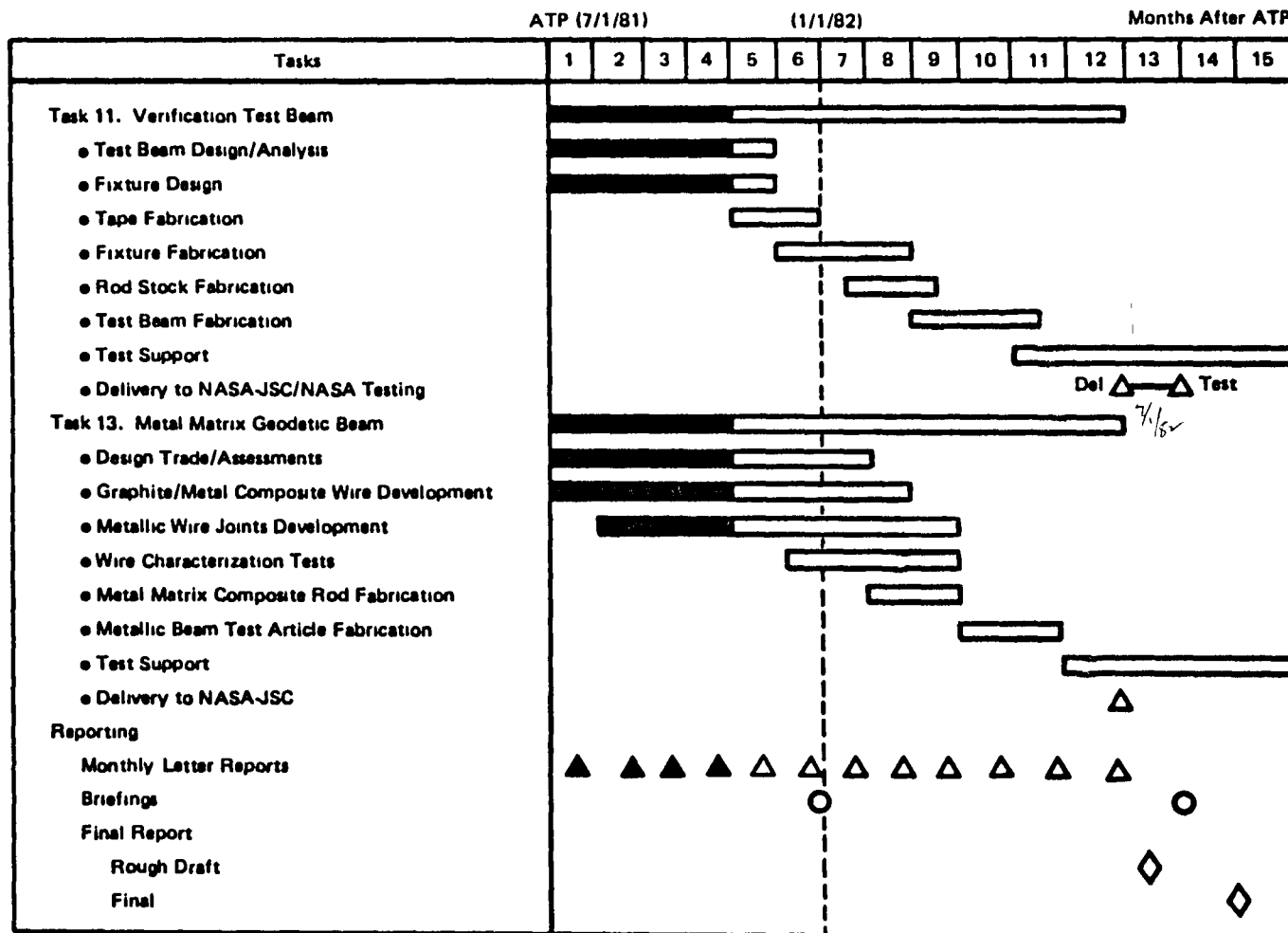
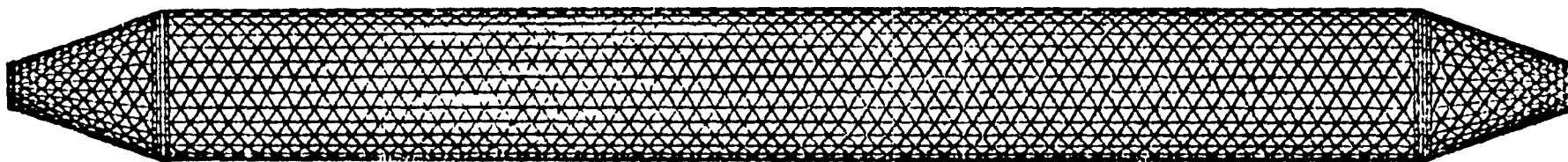


Figure 2. Development of Geodetic Structure for Space Construction – Phase IIA Schedule



- Overall beam length is 298.3 inches.
- Nominal beam diameter is 30 inches.
- 30 Longitudinals planned.
- Nominal cylinder node spacing is 3.63 inches.
- Nominal closeout node spacing is 3.44 inches.
- Closeout half-angle is 20 degrees.
- Minimum closeout diameter is 9 inches.
- Helix angle is 60 degrees.
- Nominal HMS/Glass/P1700 rod diameter is .103 inches.

Figure 3. Detailed Sizing of Verification Test Beam.

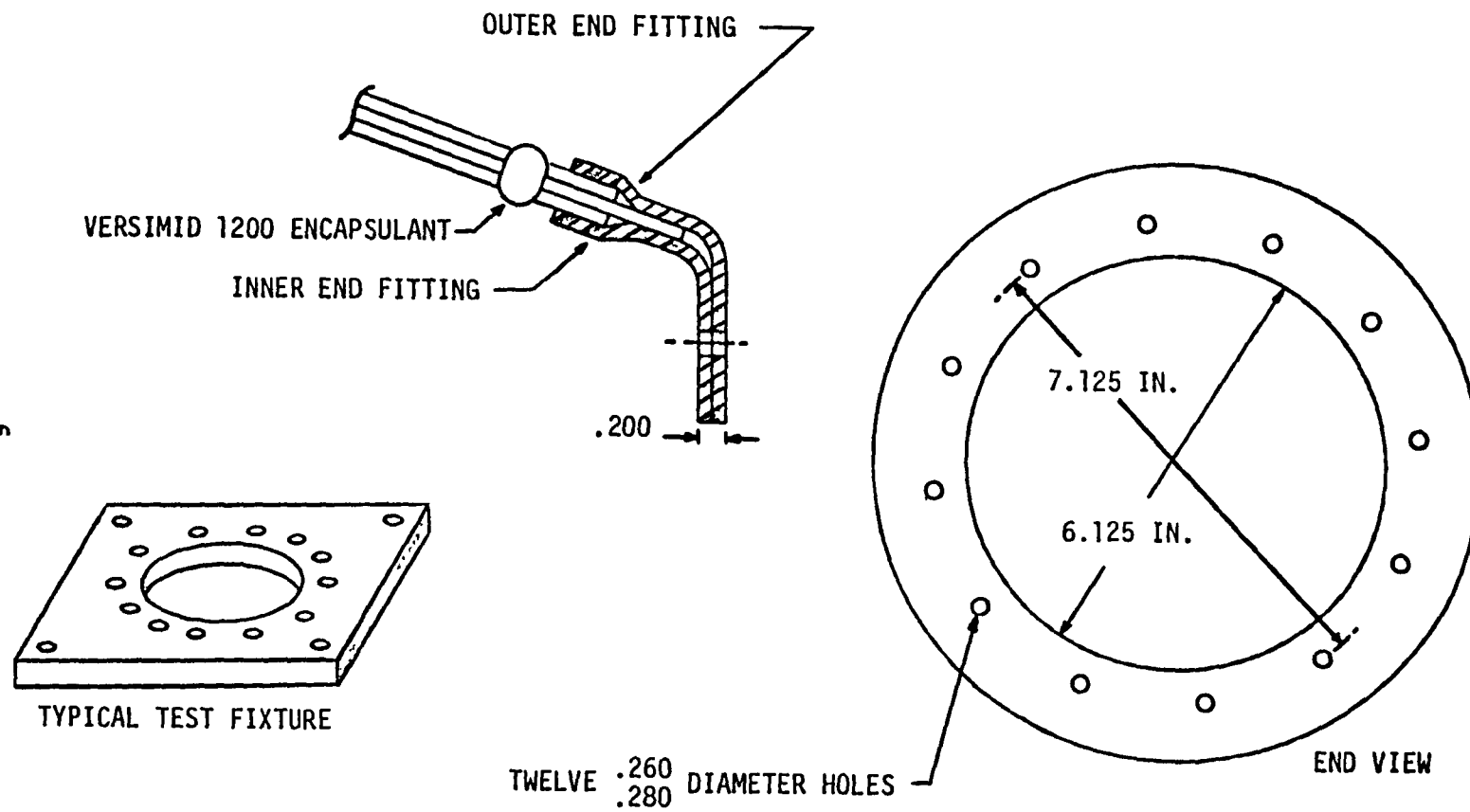


Figure 4. Beam Interface

CLOSEOUT RODS AND ENCAPSULANT  
OMITTED FOR CLARITY

INNER FRAME

OUTER FRAME

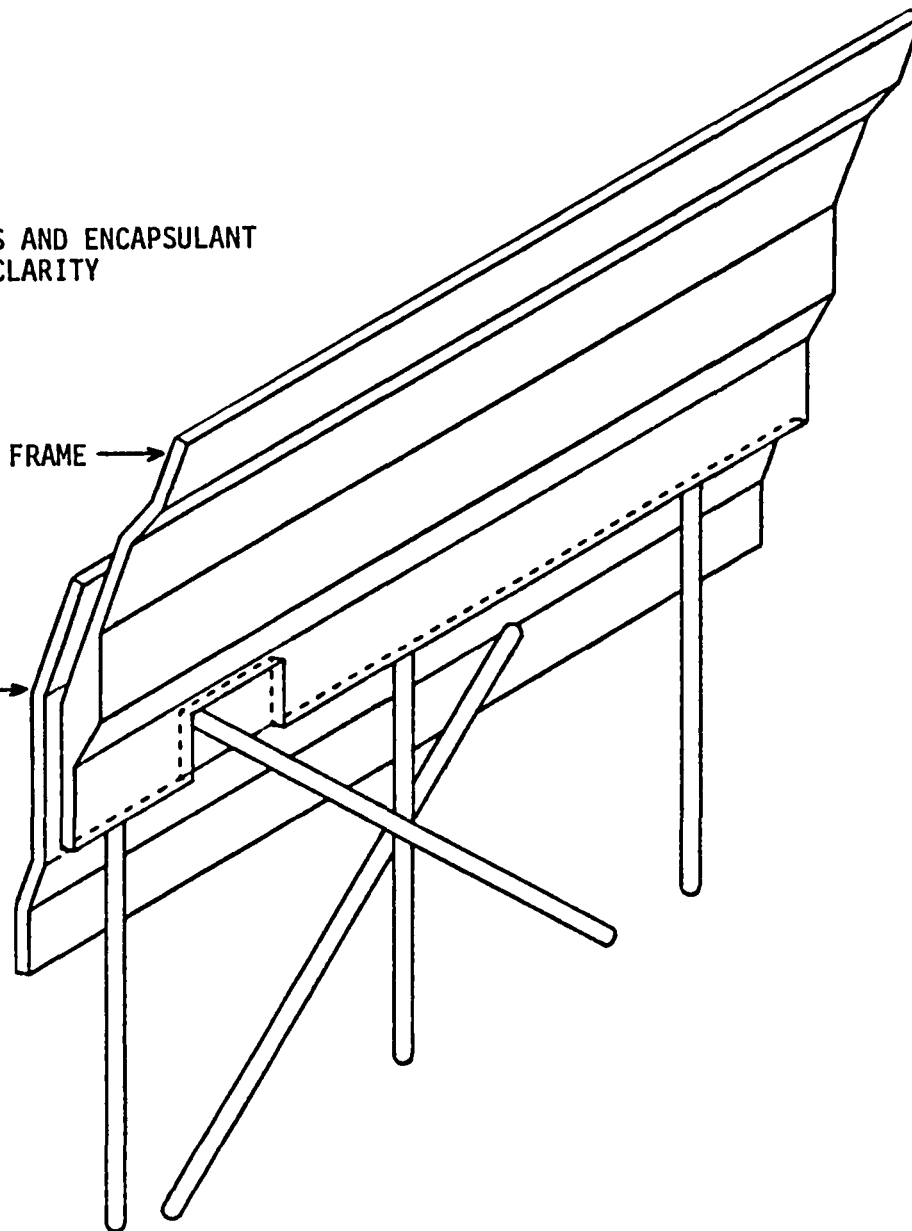


Figure 5. Cylinder to Frame Joint Design.

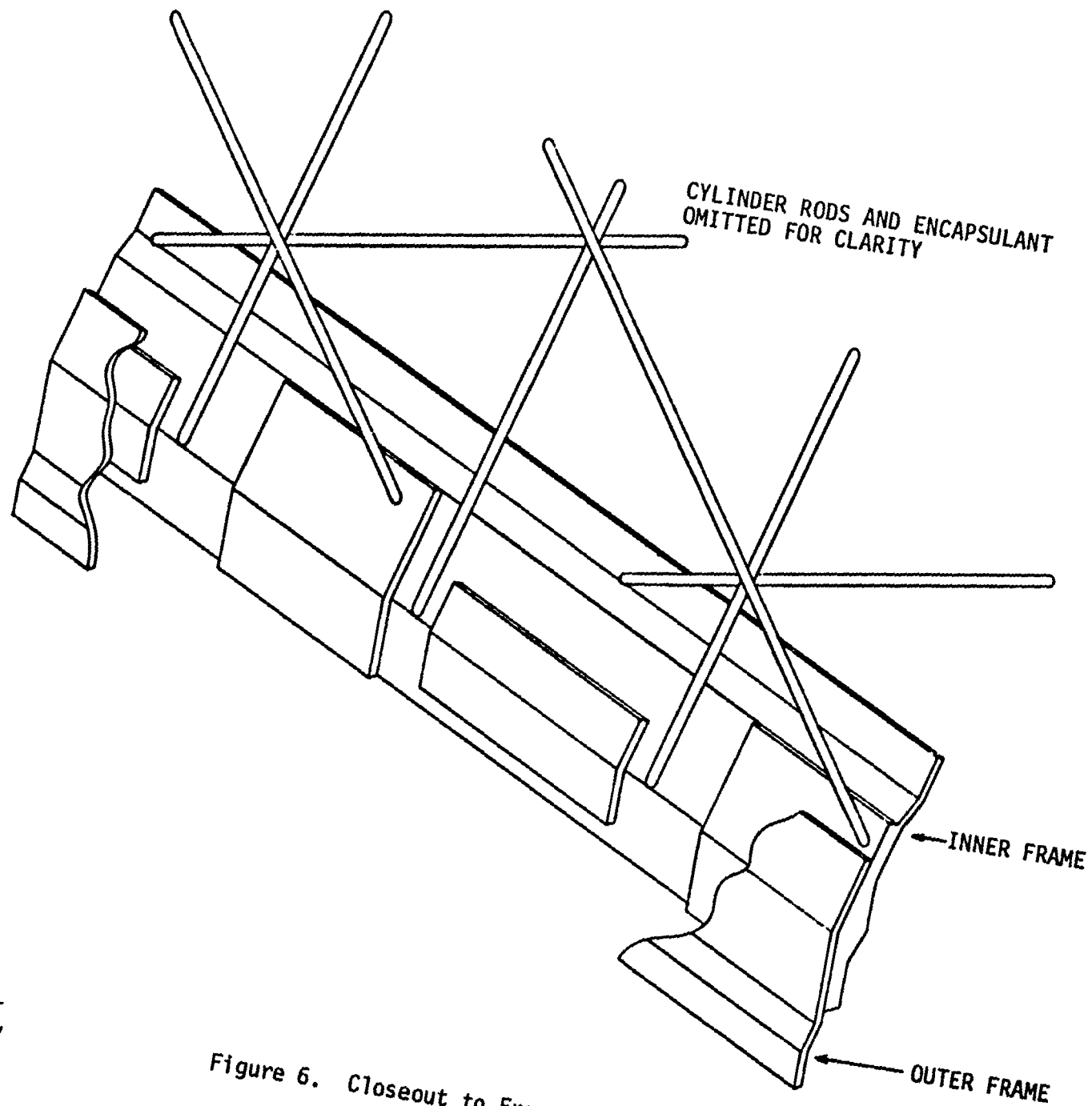


Figure 6. Closeout to Frame Joint Design.

#### 4.0 METAL MATRIX COMPOSITE FEASIBILITY (Task 13)

The preliminary assessment of candidate metal matrix composite (MMC) materials and joining techniques has been completed to support the development of a MMC geodetic beam segment for fabrication and test. The primary material candidate selected is P100/6061 aluminum MMC. The aluminum matrix represents adequate stiffness to weight with a minimum risk of oxidation/joining problems. A secondary material candidate is P100/AZ91C magnesium MMC. The magnesium matrix represents superior stiffness to weight, but is difficult to join and is subject to rapid oxidation.

An order has been placed with Material Concepts, Inc. (MCI) of Columbus, Ohio. This order is for the following items:

1. On a best effort basis, MCI will develop, produce, and deliver the following wire by standard infiltration techniques.
  - a. 100 feet of VS0054/6061 aluminum 7 ended (.066" diameter) composite wire.
  - b. 100 feet of VS0054/AZ91C magnesium 7 ended (.066" diameter) composite wire.
2. On a best effort basis, MCI will develop, produce, and deliver 200 feet of VS0054/6061 (.066" diameter) die sized wire.

The VS0054 represents a graphite fiber with an extensional modulus in excess of 100 million psi. Upon receipt of the material, characterization and joining tests shall be performed to finalize the material and fabrication process according to the schedule shown in Figure 2.

#### 5.0 PROBLEM AREAS

No problems exist at this time.

#### 6.0 FUTURE WORK

Work will continue on Tasks 11 and 13 during the next reporting period. Detailed analysis of the verification beam will continue. Design of the tooling will be finalized.

#### 7.0 PROGRAM COST AND SCHEDULE

The program is currently under cost projections and on schedule.





DEVELOPMENT OF A COMPOSITE GEODETIC  
STRUCTURE FOR SPACE CONSTRUCTION

Technical Letter Progress  
Report No. 21

November 1980

NAS9-15678

Prepared by

A. J. Cwiertny, Jr.  
R. Johnson, Jr.

Approved by:

A handwritten signature in dark ink, appearing to read 'R. F. Zemer'.

R. F. Zemer  
Director - Structures & Materials  
Engineering Division

Prepared under Contract NAS9-15678, DRL No. T-1522, Line  
Item 1, DRD No. MA-003 for  
NASA-Johnson Space Center, Houston, Texas 77058

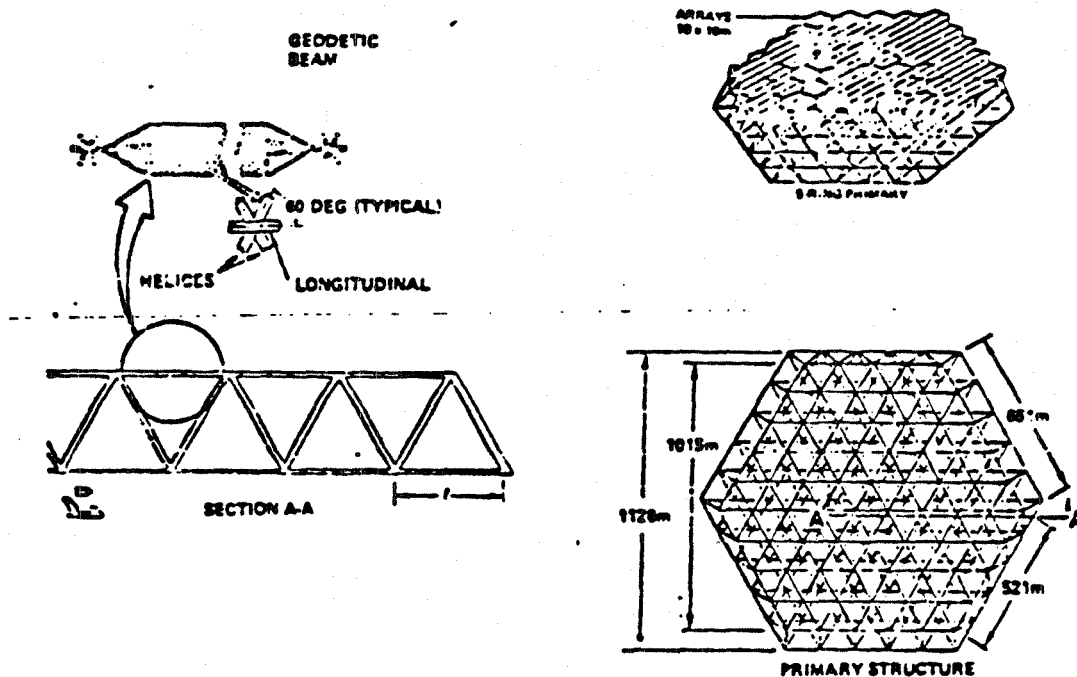
**MCDONNELL DOUGLAS ASTRONAUTICS COMPANY-HUNTINGTON BEACH**

5301 Bolsa Avenue Huntington Beach, California 92647 (714) 896-3311

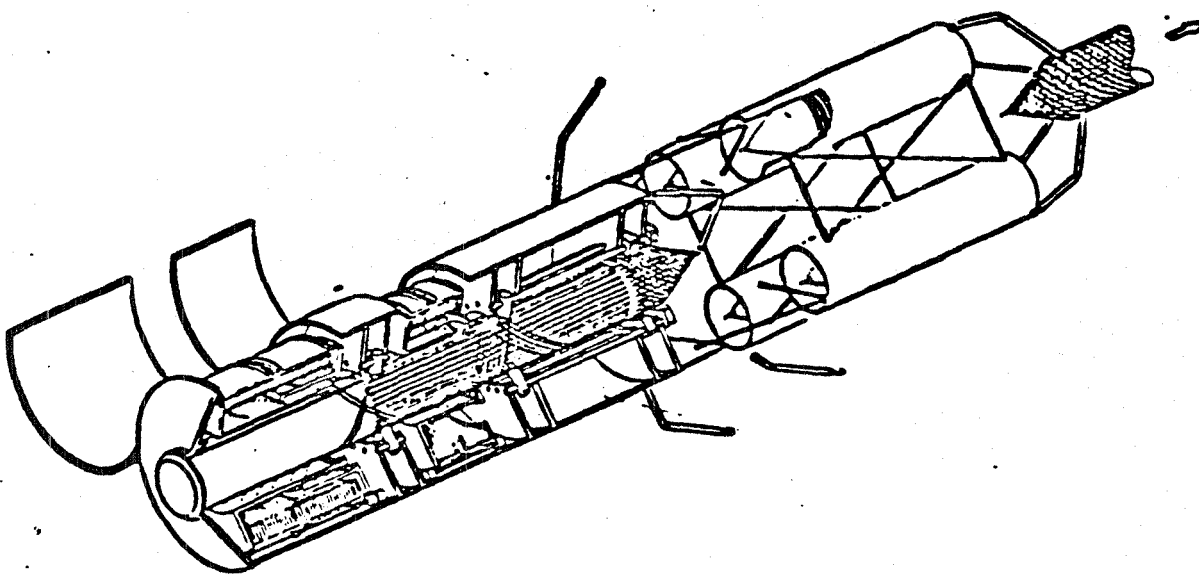
## 1.0 INTRODUCTION

The overall objective of this program is to develop a structurally efficient composite geodetic beam and a beam fabrication machine for on-orbit construction of large space structures (Figure 1). Phase I of the program ended 31 January 1980, and Phase II was initiated on 1 March.

The program efforts are divided into three phases with each phase scheduled for approximately one year in duration. Phase I, initiated on 24 August 1978, consisted of tasks to (1) develop structural design requirements, (2) develop analytical procedures and select the best configuration for a geodetic beam, (3) develop structural termination concepts for the geodetic beam, (4) accomplish beam preliminary sizing, (5) develop pultruded composite rod stock for use in joining tests and feasibility test articles, (6) select a reliable joining technique, (7) design, fabricate, and test two geodetic test articles to establish concept feasibility, and initiate the preliminary design of a beam fabrication machine. Additional Phase I efforts consisted of preparation of an Orbital Flight Test (OFT) plan and fabrication of a scale model to demonstrate a key subsystem of the geodetic beam machine. Phase II will be devoted to detailed material characterization tests of the pultruded composite rods and encapsulated joints (Task 8), parameter tests of a geodetic test cylinder and a cylinder/conical closeout test article (Task 9), and an improved geodetic beam analysis based on the parameter tests (Task 10). Two tasks (Tasks 11 and 12) of Phase II have been deferred. Task 11 is the verification tests of a full scale test article and Task 12 is the completion of the beam machine design. In Phase III, the ground demonstration of automatic fabrication of geodetic beams will be accomplished using pilot-plant equipment capable of automatically fabricating demonstration articles.



a. Geodetic Beam Application to a Microwave Power Transmission Antenna



b. Geodetic Beam Machine Concept

## 2.0 SUMMARY OF PROGRESS

The program schedule is shown in Figure 2. As indicated in Figure 2, work is now in progress on Tasks 9 and 10. In the area of Task 9, tests of the parametric test cylinder were completed, and fabrication of the fixture for building the conical closeout was continued. Further analysis (Task 10) was held in abeyance until reduction of the test results of the parametric cylinder is completed. Data reduction is currently in progress.

### 2.1 MATERIAL CHARACTERIZATION (TASK 8)

The objective of this task was to define all of the primary physical and mechanical properties of the pultruded hybrid HMS/E-glass/P1700 rod material. Key properties developed in Task 8 will be used in analysis of the parameter test articles. Approximately eighty feet of 2.36 mm (0.093 in.) diameter hybrid rod stock was procured from Compositek Engineering for use in characterization tests. Tests performed in Task 8 are listed in Tables 1 and 2, and the current status of testing is indicated for each type of test. As seen in Table 1, all tests in Task 8 have been completed.

### 2.2 PARAMETER TESTS (TASK 9)

Task 9 has the objective of evaluating more fully the structural parameters and characteristics of the type of geodetic beam being developed under this program. As part of the parameter tests, a test cylinder having three ratios of longitudinal-to-helical sizes has been fabricated for test during Phase II. All helicals are the same size while three different sizes of longitudinals are used, each of three circumferential sectors of the cylinder having a different size of longitudinal rod. In this manner, the global stiffness effect of the helical mesh will be different in each trisector and the different effects on the local failure of the longitudinals can be evaluated.

Compression tests of the geodetic cylinder were completed during this reporting period and data for two of the three sectors were reduced. Data for the 120-degree sectors using 2.11 mm (0.083 in.) and 2.62 mm (0.103 in.) diameter longitudinals were reduced and strains were plotted as a function

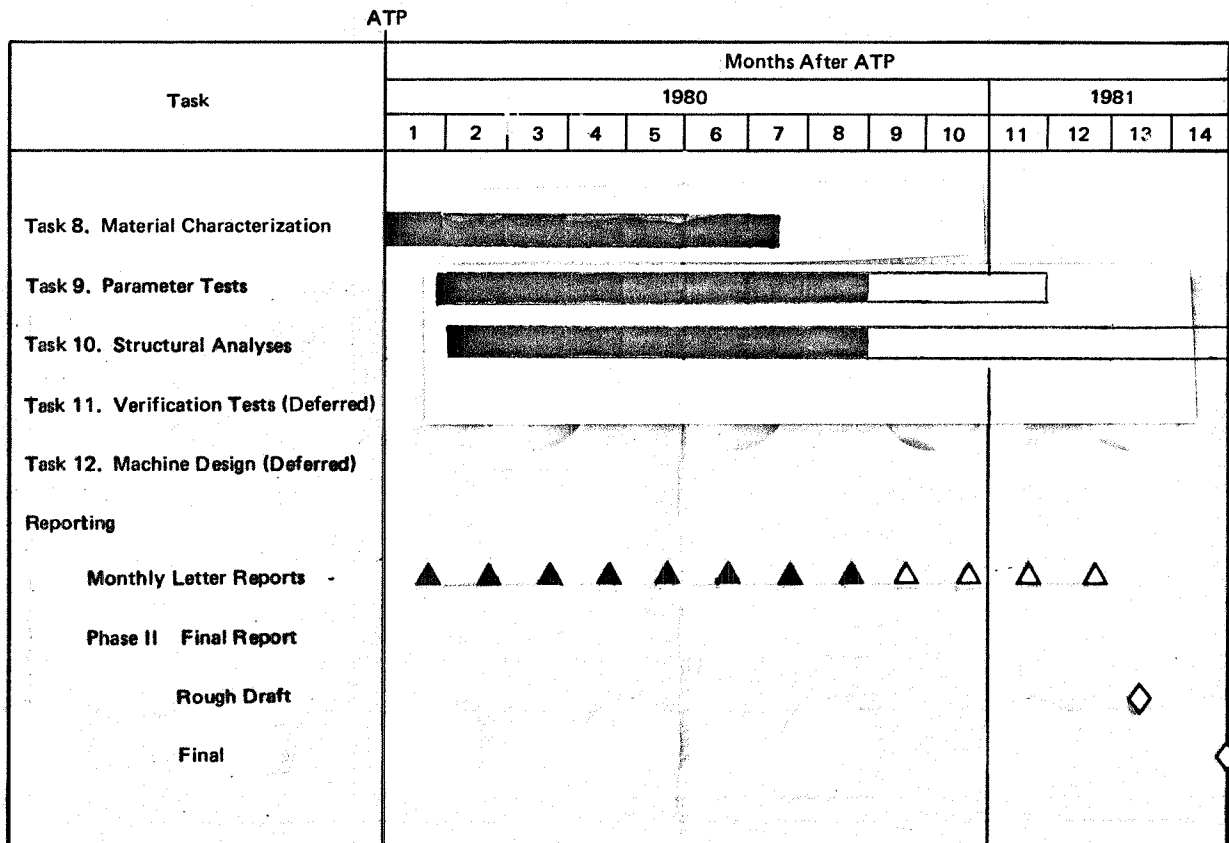


Figure 2. Development of a Geodetic Structure for Space Construction – Phase II Schedule

Table 1

## Physical Property Tests - HMS/E-Glass/P1700 Pultruded Rods

Type of Test	Status of Tests
Density and Fiber/Resin Content	Tests completed for Material Lot No. 1 (see Table 3, Reference 1)
Coefficient of Thermal Expansion	Tests completed
Specific Heat	Tests completed
Solar Absorptivity	Test completed
Thermal Conductivity	Tests completed
Electrical Conductivity	Tests completed
Infrared Emittance	Tests completed

Table 2

## Mechanical Property Tests - HMS/E-Glass/P1700 Pultruded Rods

Type of Test	Status of Tests
Tensile Strength and Modulus	Tests completed
Compressive Strength and Modulus	Tests completed
Torsion Strength and Modulus	Tests completed
Flexural Strength and Modulus	Tests completed
Strength Degradation (from vacuum and elevated temperature exposure)	Tests completed.

of compression load.

The overall test setup of the parameter cylinder is shown in Figure 3 and a closeup of the instrumentation for measuring the helical rotation that occurs during buckling of the longitudinals is shown in Figure 4. The first sector tested was the one containing the 2.11 mm (0.083 in.) diameter longitudinals. The maximum load attained was 3114N (700 lb.), a compressive load that was within approximately three percent of the predicted buckling load of 3034N (682 lb.). Figure 5 shows the measured strains from the back-to-back gages located on a longitudinal rod at the center of the sector. A distinct roundover indicating elastic buckling of the rod is seen in Figure 5 at approximately 2669N (600 lb.). Figure 6 shows the strains measured at the remaining gage positions. A photograph of the buckled 2.11 mm (0.083 in.) diameter longitudinals is presented in Figure 7.

Data from the test of the sector using 2.62 mm (0.103 in.) diameter longitudinals is shown in Figures 8, 9, and 10. Strains from the back-to-back gages in the center of the sector are shown in Figure 8. The buckling characteristics of this sector appeared to differ from that of the smaller diameter 2.11 mm (0.083 in.) longitudinals. The sector containing the 2.62 mm (0.103 in.) diameter longitudinals did not buckle at the center of the area, appearing instead to deform into larger dished areas covering several nodes rather than the previously observed sinusoidal shape in each longitudinal with points of inflection at each node. Figure 9 shows the buckle pattern in the sector with 2.62 mm longitudinals, and the larger buckled area is evident. The center longitudinal in this sector was located at the edge of a large buckle pattern and thus did not show the sharp roundover strain pattern associated with buckling in three smaller 2.11 mm longitudinals. Figure 10 shows strains recorded by the gages located at the ends and sides of this sector. The maximum load for this sector was 5052N (1135 lb.) which was within 1 percent of the predicted buckling load of 5026N (1130 lb.).

Data from the third sector containing longitudinals of 2.36 mm (0.093 in.) diameter have not been completely reduced at this time, completion of data reduction being expected during the next reporting period. Data from the torsional rotation of the helicals also are expected to be reduced during the next reporting period.



Figure 3. Test Setup for Parameter Cylinder Tests



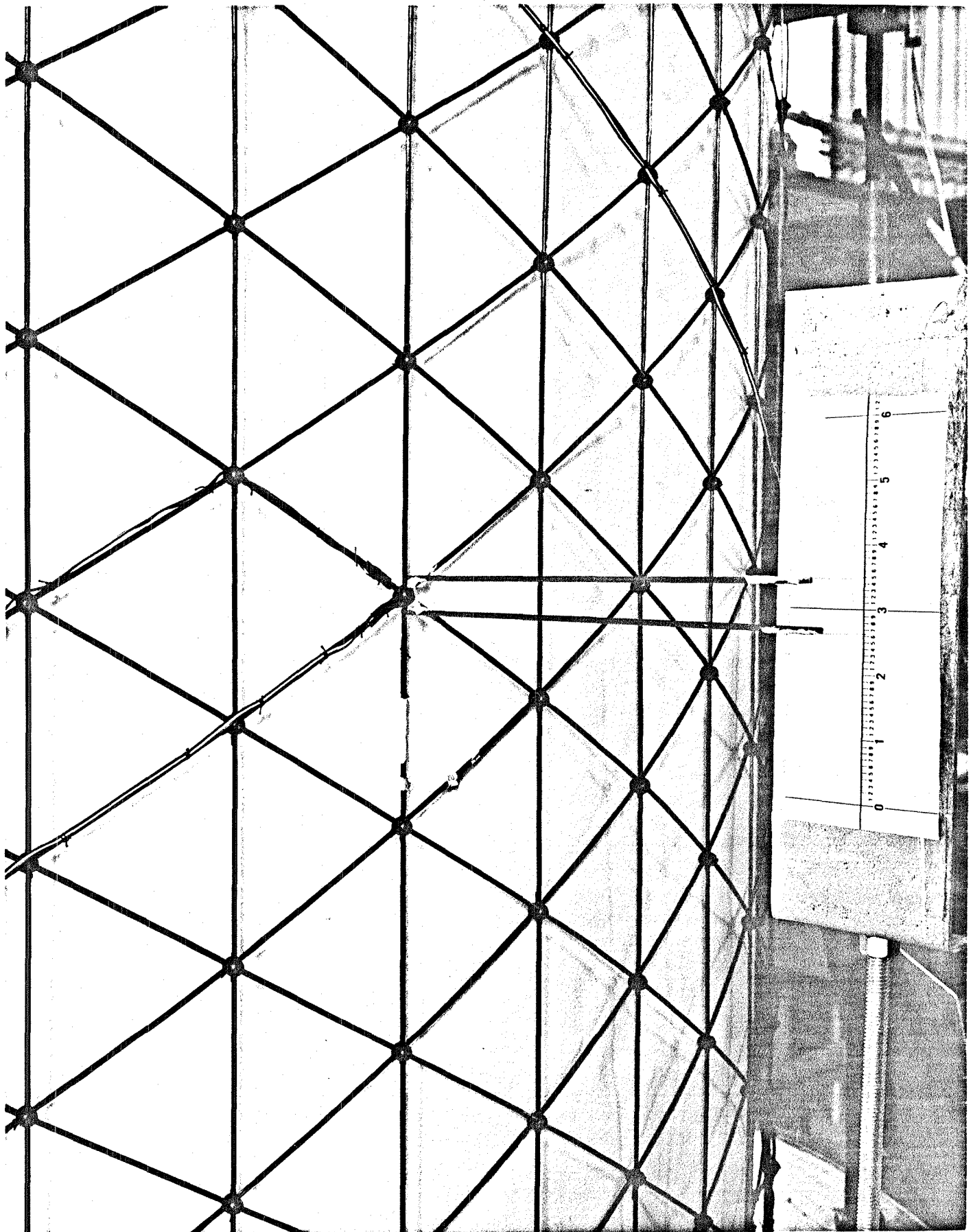


Figure 4. Torsional Rotation Instrumentation for Helical Twist

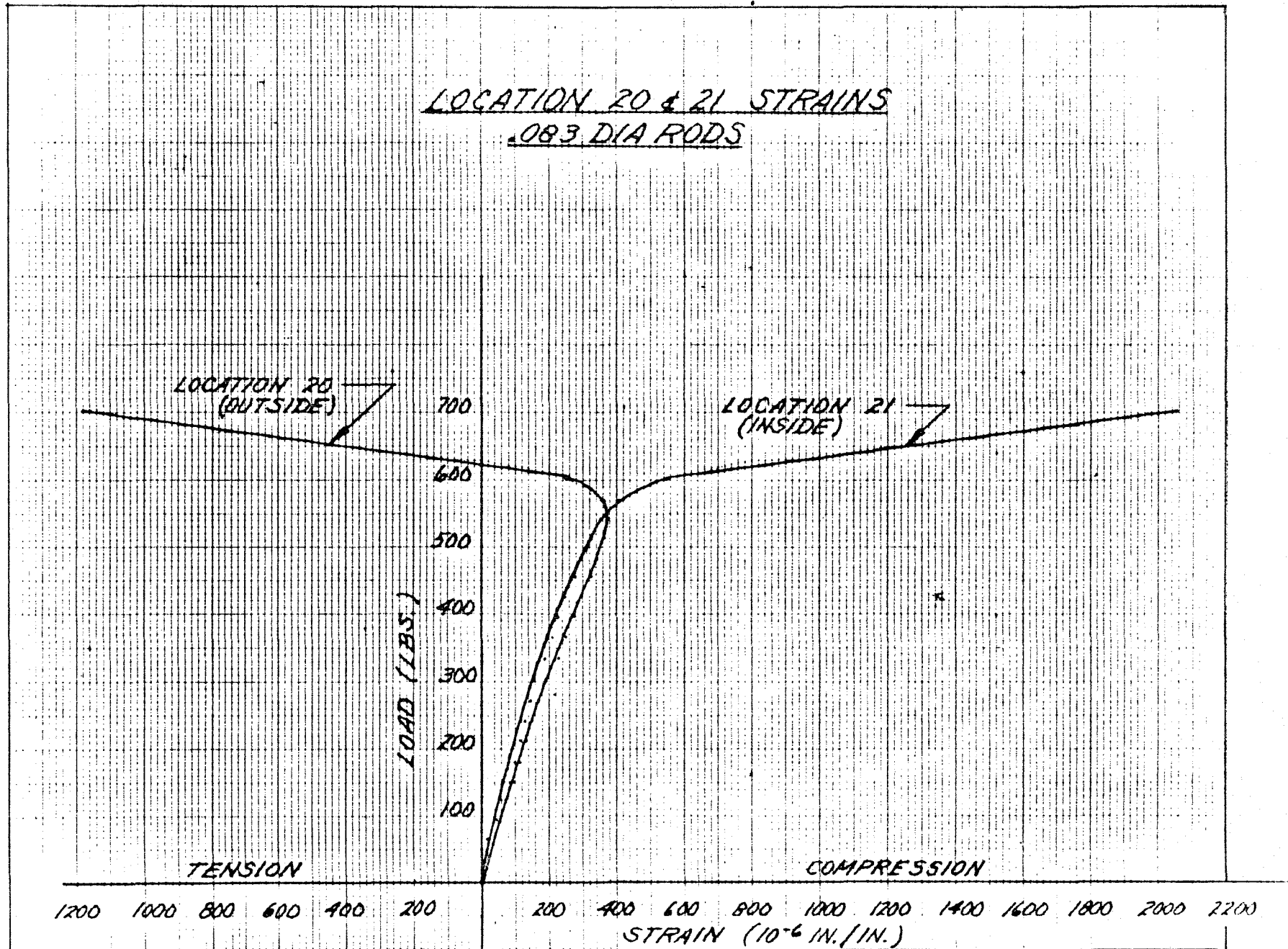
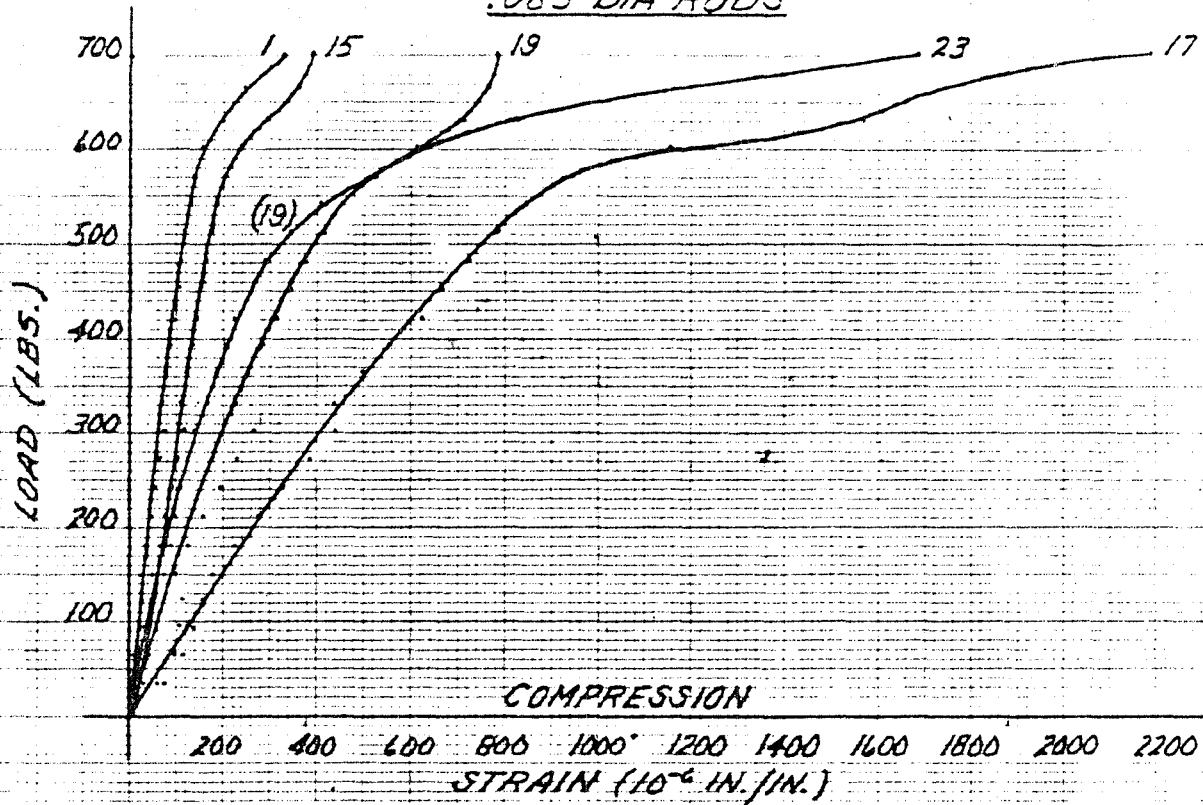


Figure 5. Strains Measured by Back-to-Back Gages at Center of Sector (2.11 mm Diameter Longitudinals)

LOCATION 1, 15, 17, 19 & 23 STRAINS  
.083 DIA RODS



LOCATION 2, 16, 18, 22 & 24 STRAINS

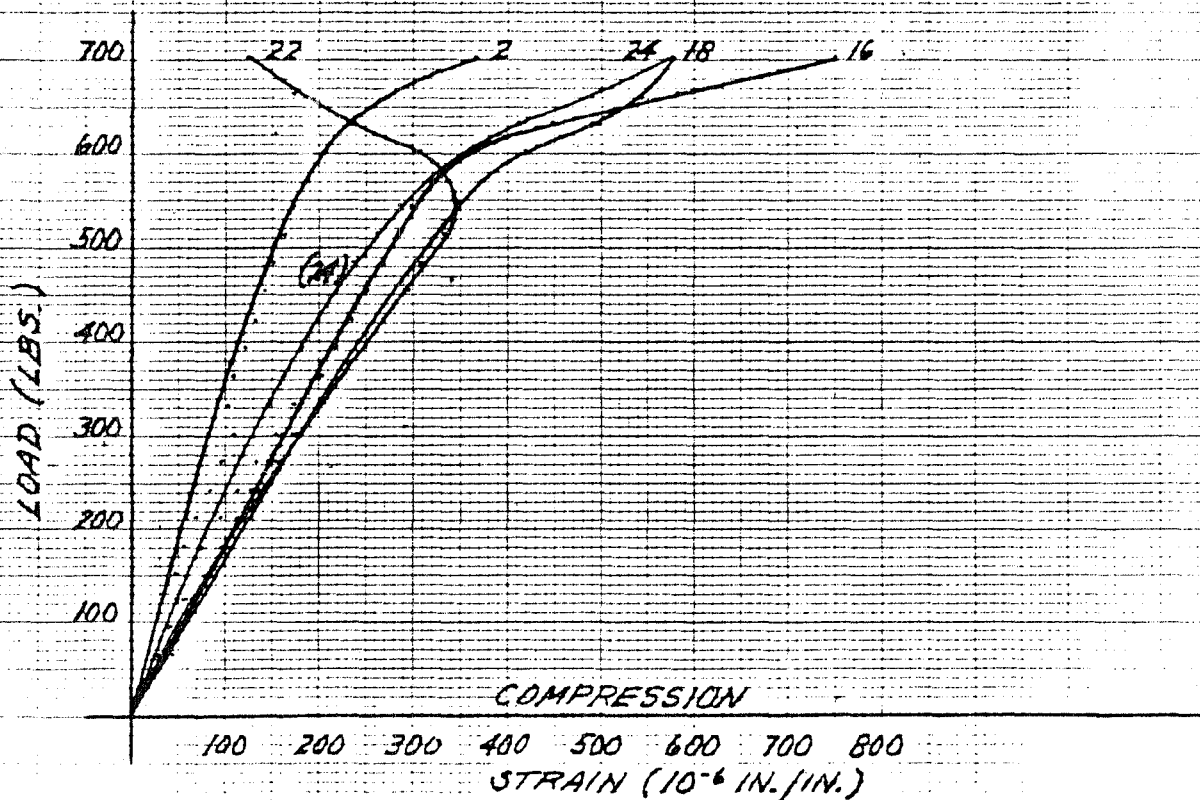


Figure 6. Strains Measured at Ends and Sides of Sector  
 (2.11 mm Diameter Longitudinals)

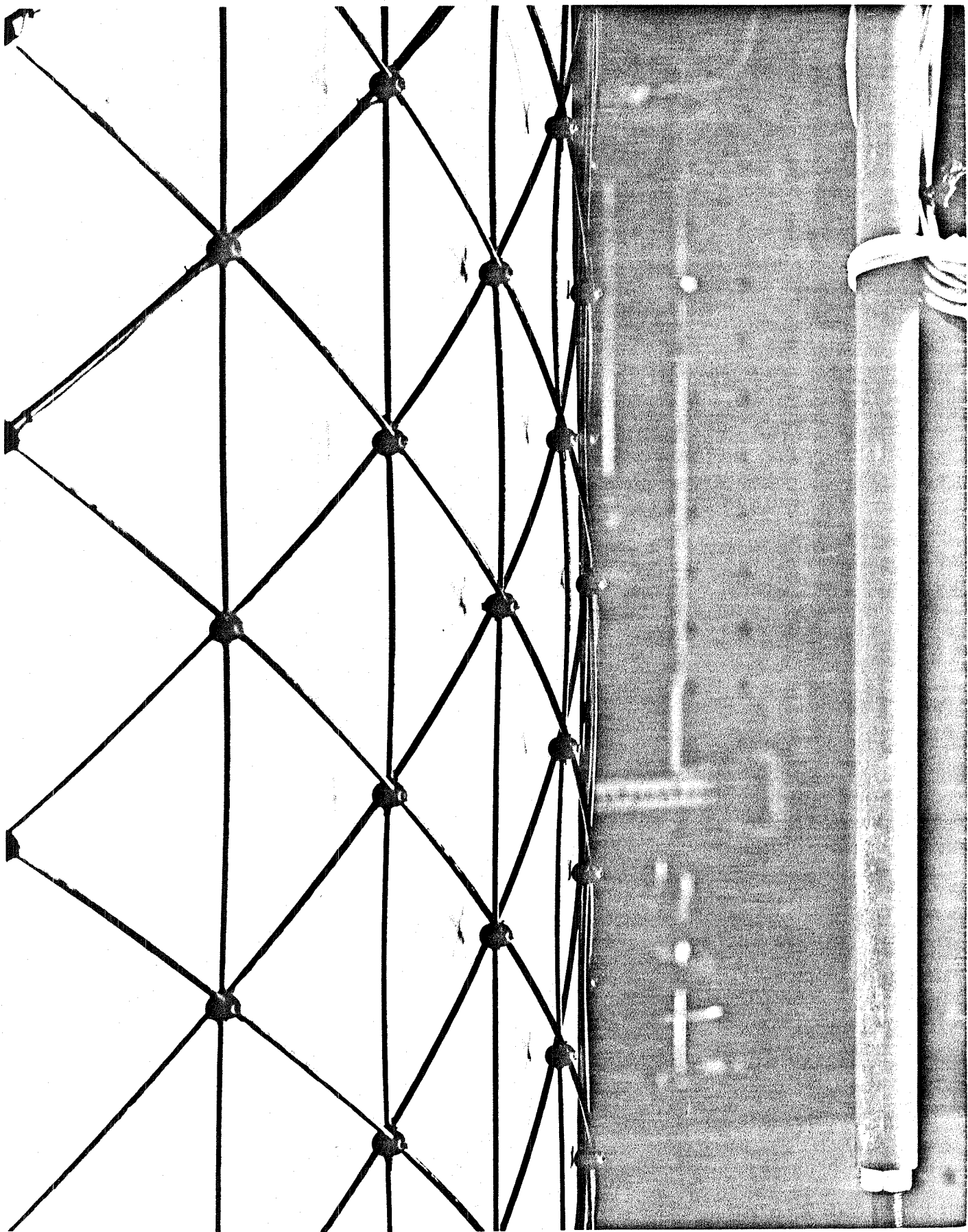


Figure 7. Compressive Buckling of 2.11 mm Diameter Longitudinals

LOCATIONS 4 & 5 STRAINS  
.103 DIA RODS

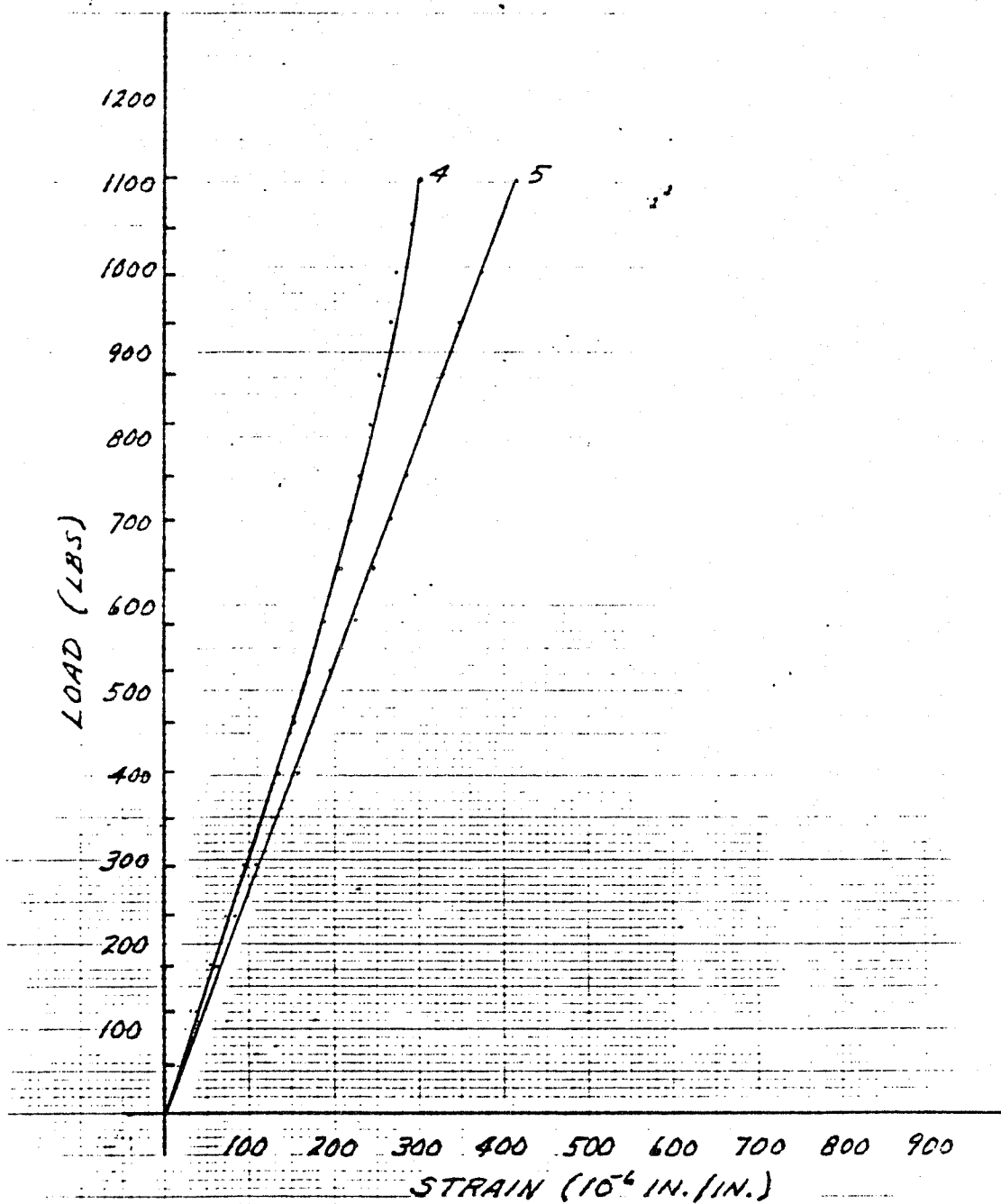


Figure 8. Strains Measured by Back-to-Back Gages at Center of Sector  
(2.62 mm Diameter Longitudinals)



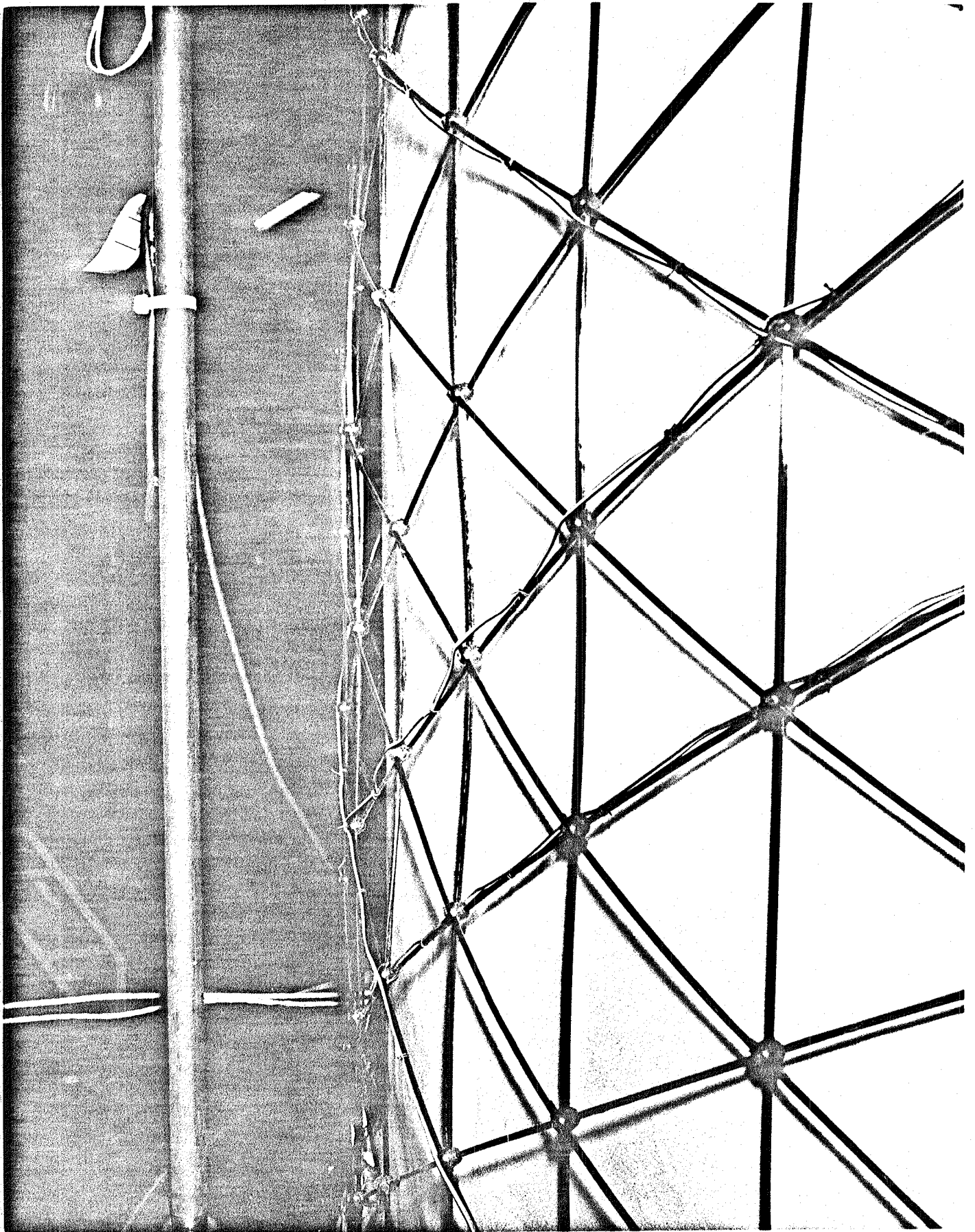


Figure 9. Compressive Buckling of 2.62 mm Diameter Longitudinals

LOCATIONS 1, 3, 7, 9 & 23 STRAINS  
.103 DIA RODS

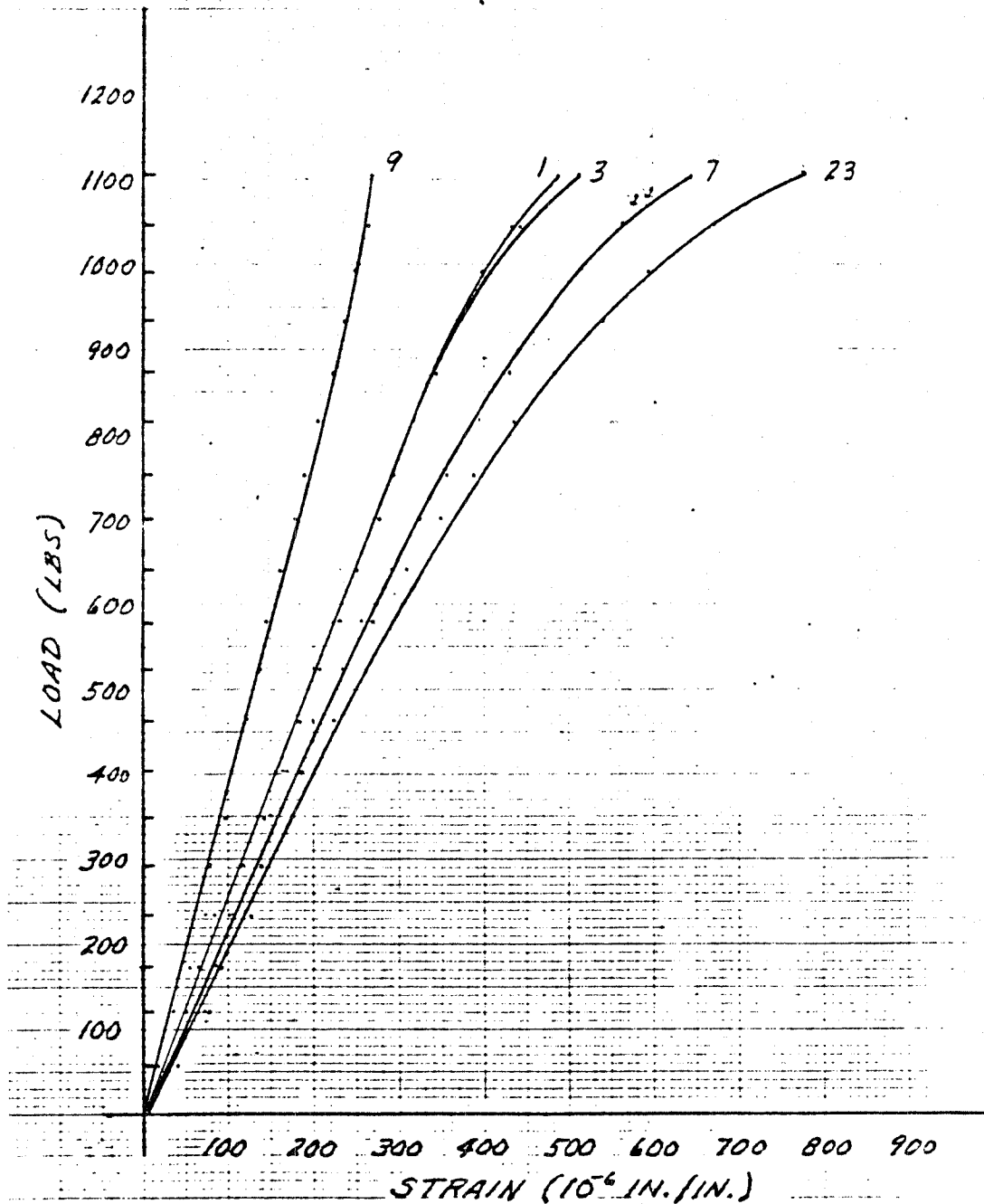


Figure 10. Strains Measured at Ends and Sides of Sector  
(2.62 mm Diameter Longitudinals)

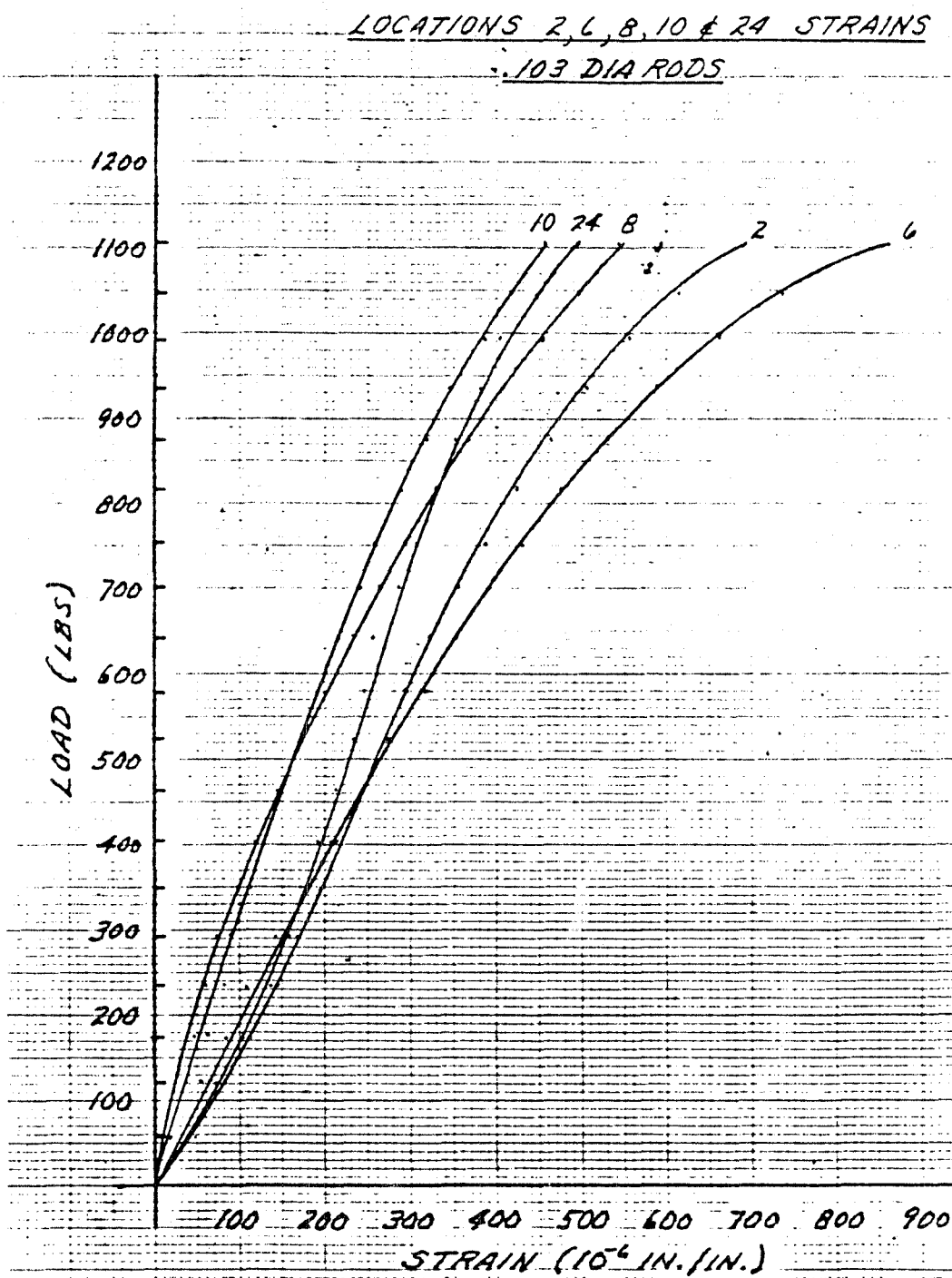


Figure 10. (Concluded)



Fabrication of the conical end closeout fixture was continued during this reporting period. This fixture will be used to fabricate the conical closeout portion of the cylinder/conical closeout test article. The existing fixture for a cylinder will be used for fabricating the cylindrical portion of the second test article. Completion of the conical closeout fixture is expected during the next reporting period.

Pultrusion of the rod stock required to fabricate the cylinder/conical closeout test article is pending completion of trial runs by Glassform, Inc. of San Jose, California. Haveg was a second alternate vendor, but declined to bid for fabrication of the rod stock because their pultrusion equipment contains an inline resin bath process and changing to accommodate prepreg tape would not have been cost-effective for the present quantities required for the cylinder/cone test article. Glassform is expected to complete trial runs by 25 November. The original program schedule is expected to be delayed by a minimum of two months because of delays in pultruding the rod stock for the cylinder/cone test article.

### 3.0 PROBLEM AREAS

As noted in Section 2.0, a minimum delay of two months is expected to result from delays in obtaining pultruded rod stock for the cylinder/cone test article. This delay is reflected in the program schedule shown in Figure 2.

### 4.0 FUTURE WORK

Work will continue on Tasks 9 and 10 during the next reporting period.

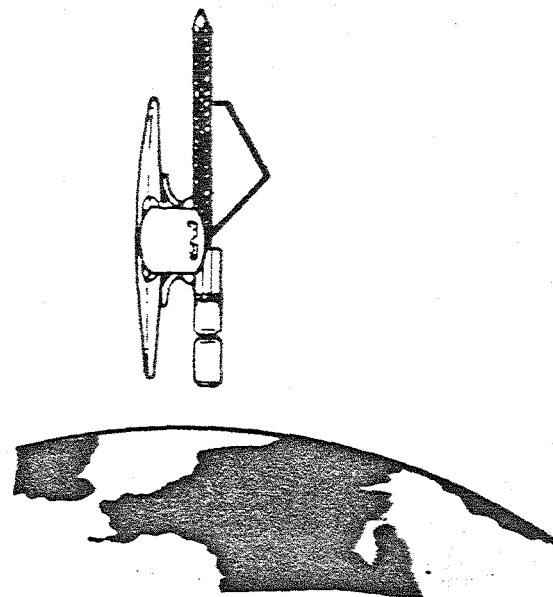
### 5.0 PROGRAM COST AND SCHEDULE

The program is currently within cost projections. However, a delay of two months is expected due to delays in obtaining pultruded rod stock.

45619

**DEVELOPMENT OF A COMPOSITE GEODETIC  
STRUCTURE FOR SPACE CONSTRUCTION  
NAS9-15678**

McDonnell Douglas  
Astronautics Company  
Huntington Beach, California  
USA

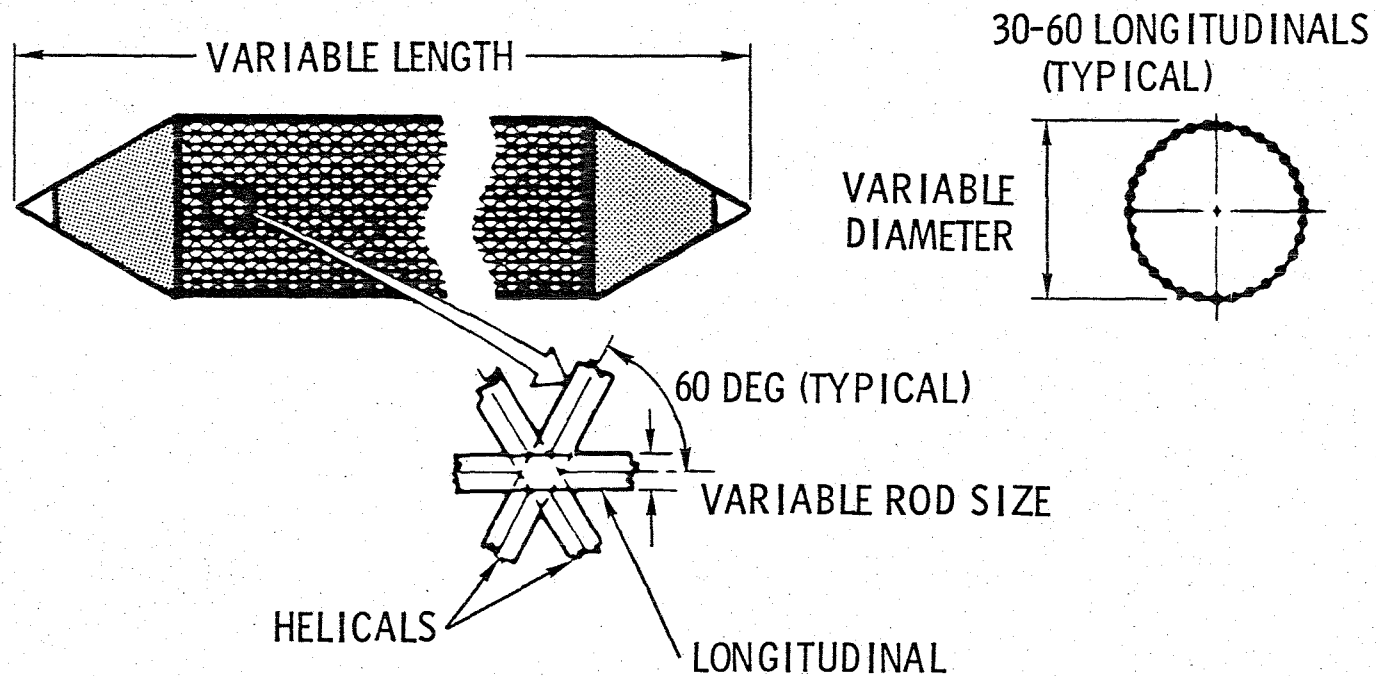




## PROGRAM DESCRIPTION

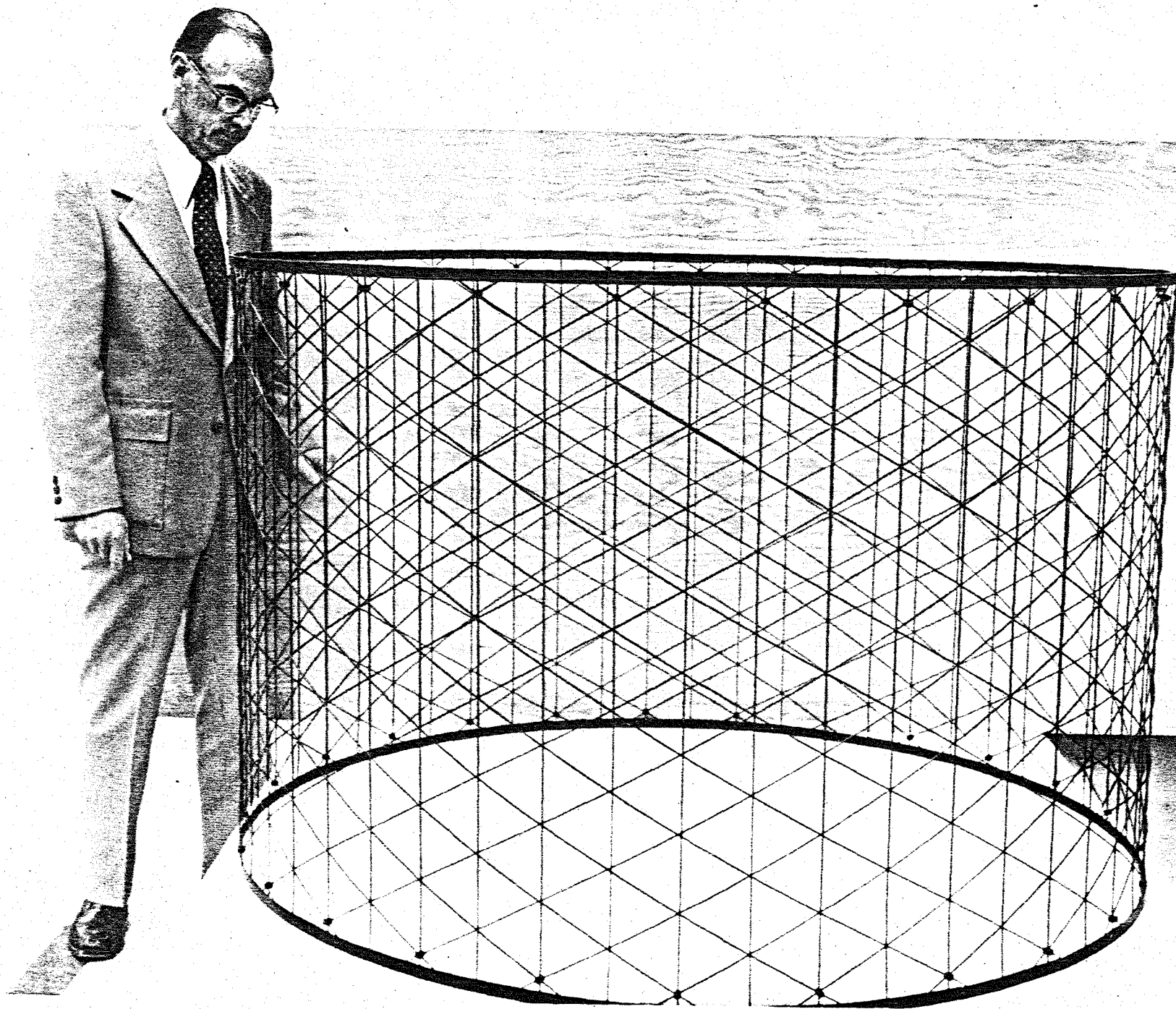
- THREE-PHASE NASA-JSC PROGRAM, 62 MONTHS DURATION,  
TECHNICAL MONITOR: T. J. DUNN
- CURRENTLY FUNDED PORTION, PHASE IIA, 14 MONTHS DURATION  
NAS9-15678
- OVERALL PROGRAM GOAL:  
DEVELOP A STRUCTURALLY EFFICIENT COMPOSITE  
GEODETIC BEAM AND A BEAM FABRICATION MACHINE  
FOR ON-ORBIT CONSTRUCTION OF LARGE SPACE  
STRUCTURES.

## GEODETIC BEAM

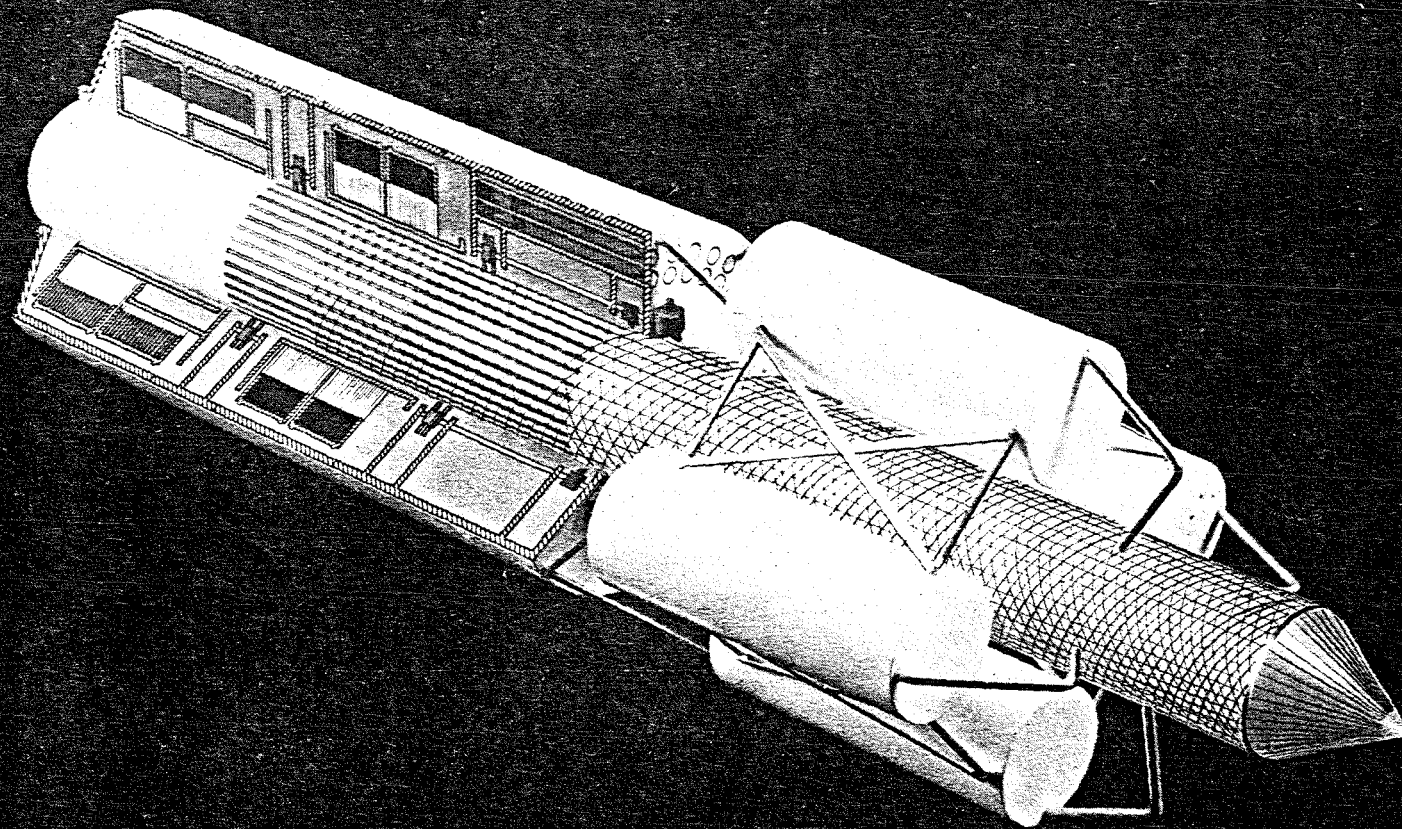


### MATERIALS

- METALS
- RESIN MATRIX COMPOSITES
- METAL MATRIX COMPOSITES

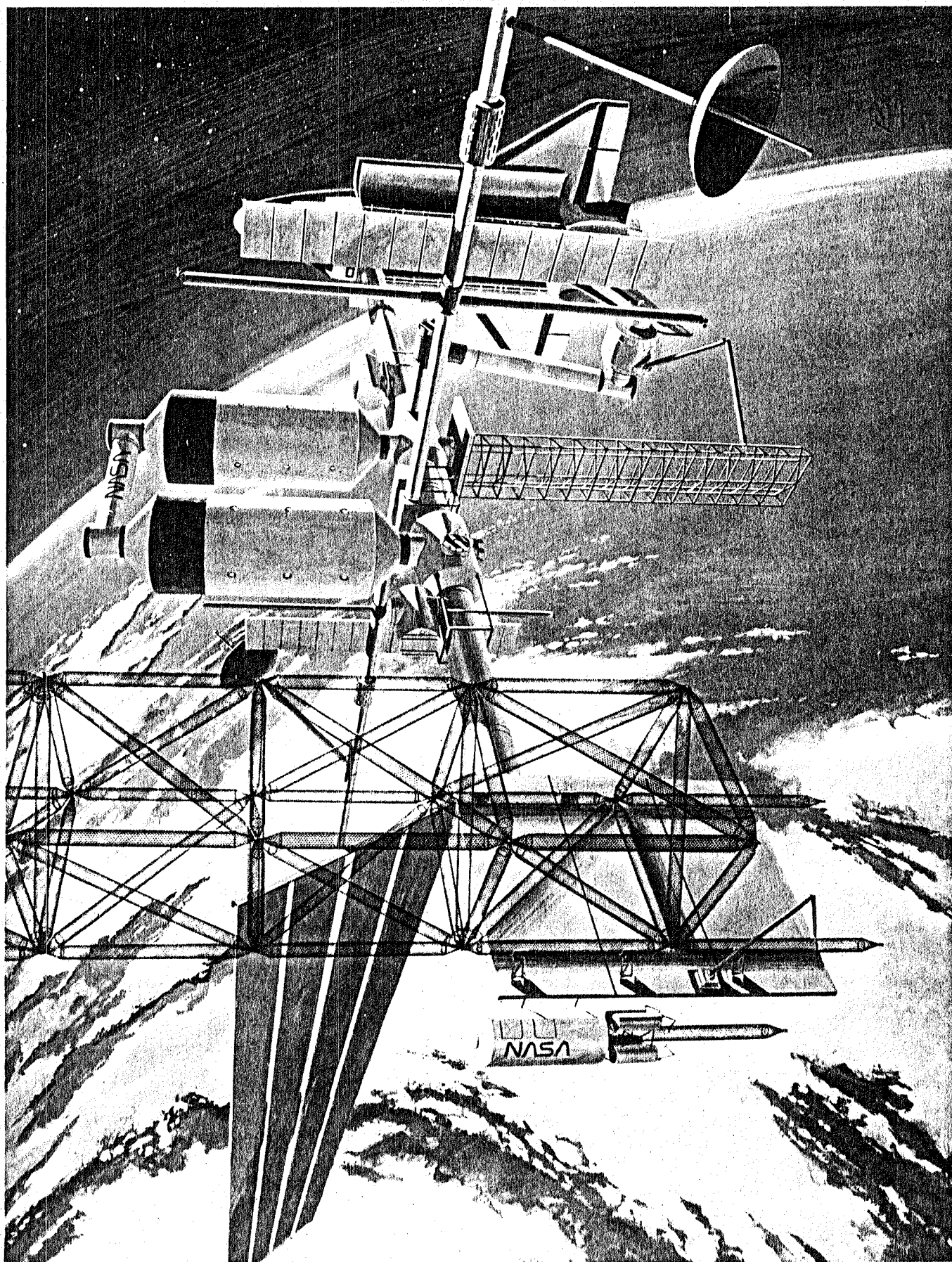


49004



**GEODETIC BEAM BUILDER**



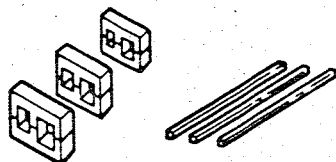


# OVERALL PROGRAM SUMMARY

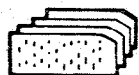
## PHASE I AND IA

### GEODETIC BEAM AND BEAM BUILDER CONCEPT DEFINITION

- FEASIBILITY ASSESSMENT



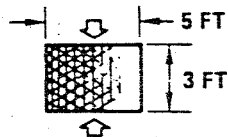
- PULTRUDED ROD STOCK  
- 2500 FT 0.080 IN X 0.080 IN
- HI-TEMP DEVELOPMENT  
MATERIAL (IA)



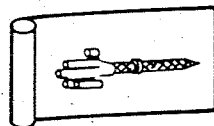
- COMPUTER CODE  
FOR GEODETIC  
STRUCTURE DESIGN



- 2500 COMPOSITE ROD  
STOCK JOINING TESTS
- HIGH-TEMP JOINT  
MATERIAL (IA)



- 2 FEASIBILITY  
TEST CYLINDERS
- 1 DEMONSTRATION  
TEST CYLINDER



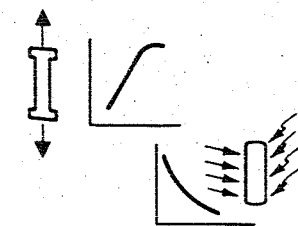
- BEAM AND BEAM  
MACHINE CONCEPT  
DEFINITION
- SHELL LOCAL  
ATTACHMENT  
CONCEPTS (IA)



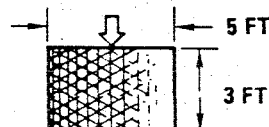
- FINAL REPORT
- PRELIMINARY  
ORBITAL FLIGHT  
TEST PLAN FOR  
FAB DEMO USING  
BEAM BUILDER

## PHASE II AND IIA

### GEODETIC BEAM AND BEAM BUILDER DESIGN DEVELOPMENT



- MATERIAL  
CHARACTERIZATION  
TESTS

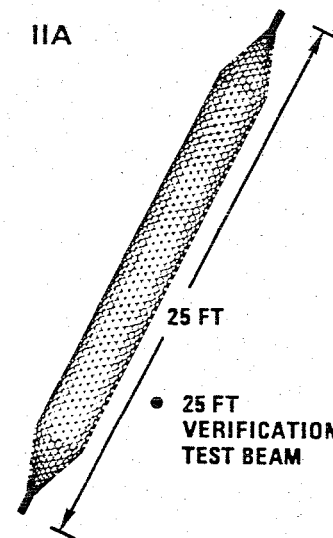


- TEST STRUCTURES  
- PARAMETER CYLINDER  
- CONE/CYLINDER

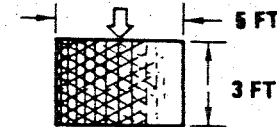


- FINAL REPORT

## IIA



- METAL MATRIX  
COMPOSITE FEASIBILITY  
TESTS  
- GR/AL, GR/MG  
- JOINING TESTS  
- FEASIBILITY TEST  
CYLINDER

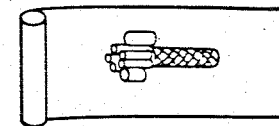


- IMPROVED ANALYSIS  
CORRELATED WITH  
PARAMETRIC TESTS

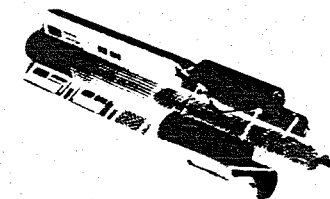
## PHASE III

### PROTOTYPE GEODETIC BEAM FABRICATION DEMONSTRATION

- SYSTEM APPLICATION STUDIES



- COMPLETED PRELIMINARY  
DESIGN OF BEAM MACHINE



- GROUND DEMONSTRATION OF  
GEODETIC BEAM AUTOMATIC  
FABRICATION

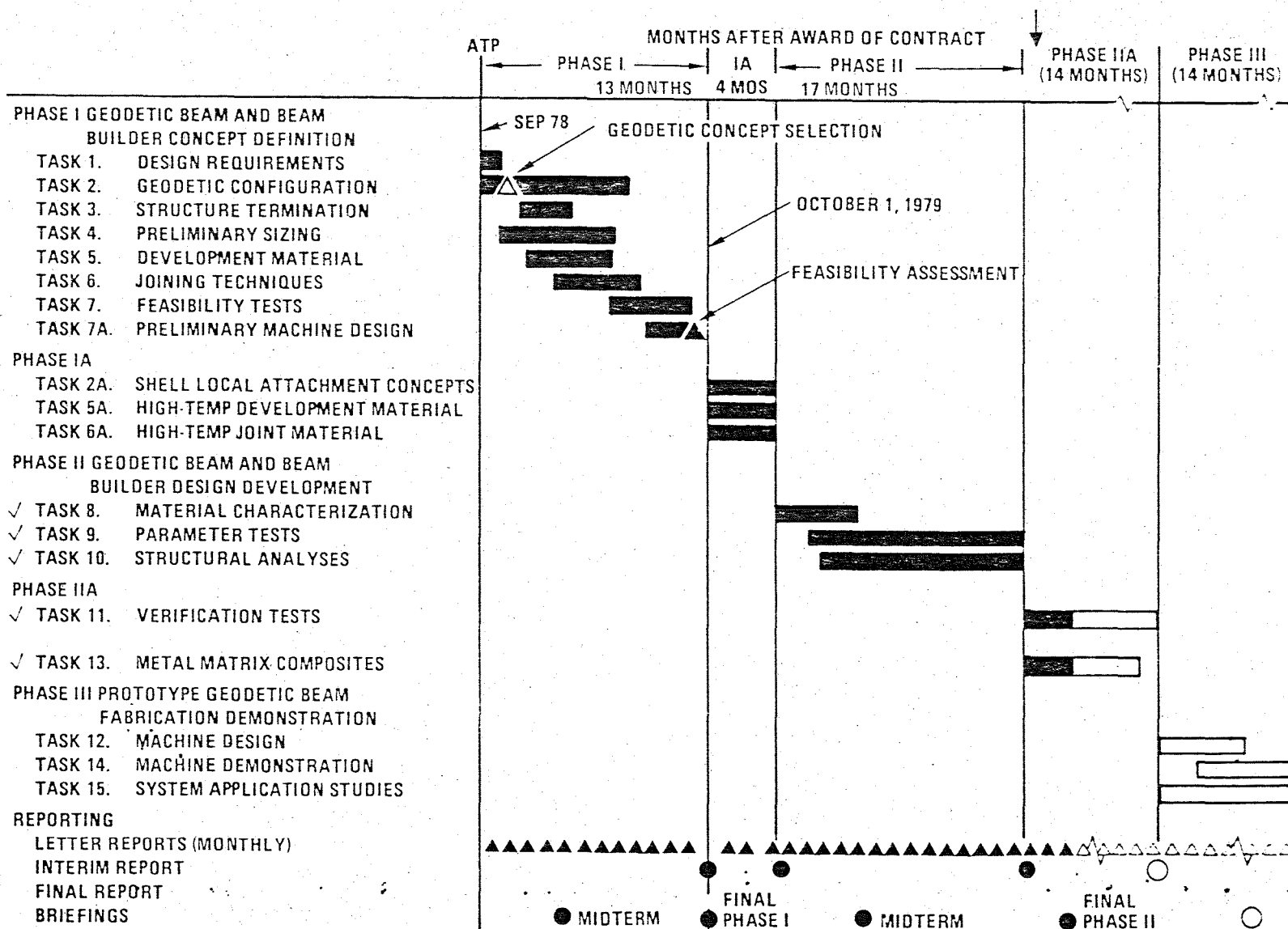


- FINAL REPORT



# OVERALL PROGRAM SCHEDULE

VFM125





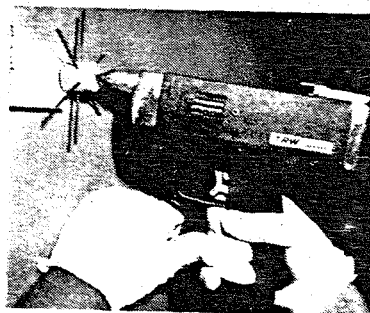
## JOINING TECHNIQUE DEVELOPMENT

56605

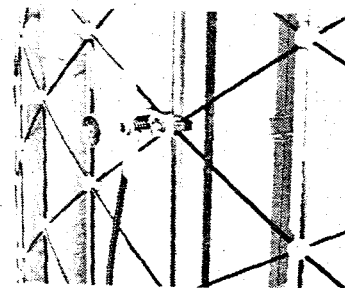
- ULTRASONICALLY WELDED RODS
  - BARE RODS
  - WITH POLYSULFONE FILLED SCRIM
- ULTRASONICALLY WELDED BUTTONS
- JOINT ENCAPSULATION
- TIEING
- TAPING
- SOLVENT BONDING
- ADHESIVE BONDING
- STAPLING
- PINNING
- FUSION BONDING
- RESISTANCE WELDING



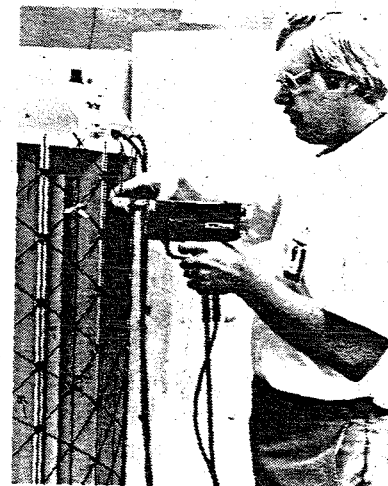
HAND HELD ULTRASONIC  
WELDER



JOINT ENCAPSULATION



RESISTANCE WELDING

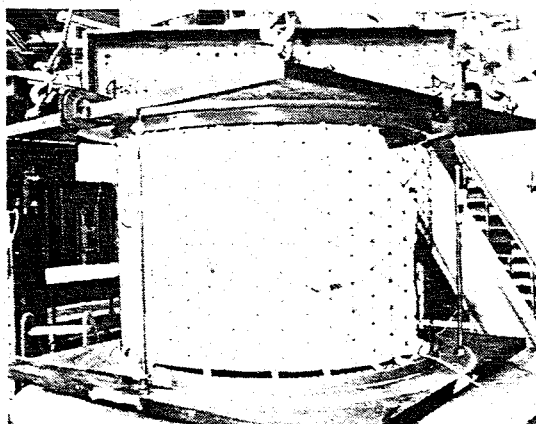
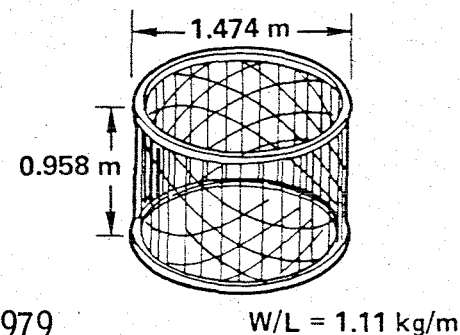


JOINT ENCAPSULATION

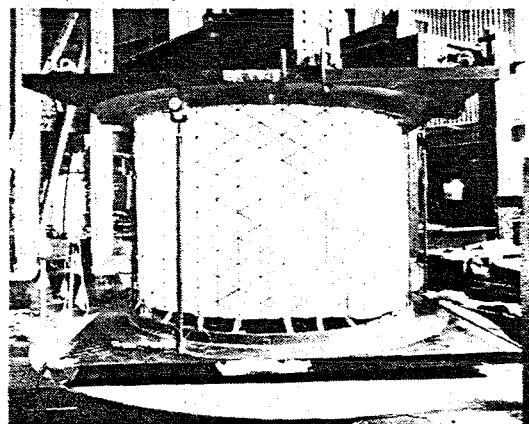
## FEASIBILITY TESTING

- ESTABLISH FEASIBILITY OF GEODETIC BEAM DESIGN CONCEPT THROUGH DESIGN, ANALYSIS, FABRICATION AND TESTING OF GEODETIC CYLINDERS

- DESIGN GEODETIC TEST CYLINDERS WITH GEOMETRY AND WEIGHT/LENGTH SIMILAR TO OPEN CAP TRIANGULAR BEAM
- FAB AND TEST DEMONSTRATION CYLINDER (1) - JANUARY 1979
- FAB AND TEST FEASIBILITY CYLINDERS (2) - JULY 1979



FEASIBILITY TEST CYLINDER NO. 1  
—JOINT ENCAPSULATION  
LOAD = 13,330 N (2990 LB)



FEASIBILITY TEST CYLINDER NO. 2  
—RESISTANCE WELDING  
LOAD = 8,675 N (1950 LB)

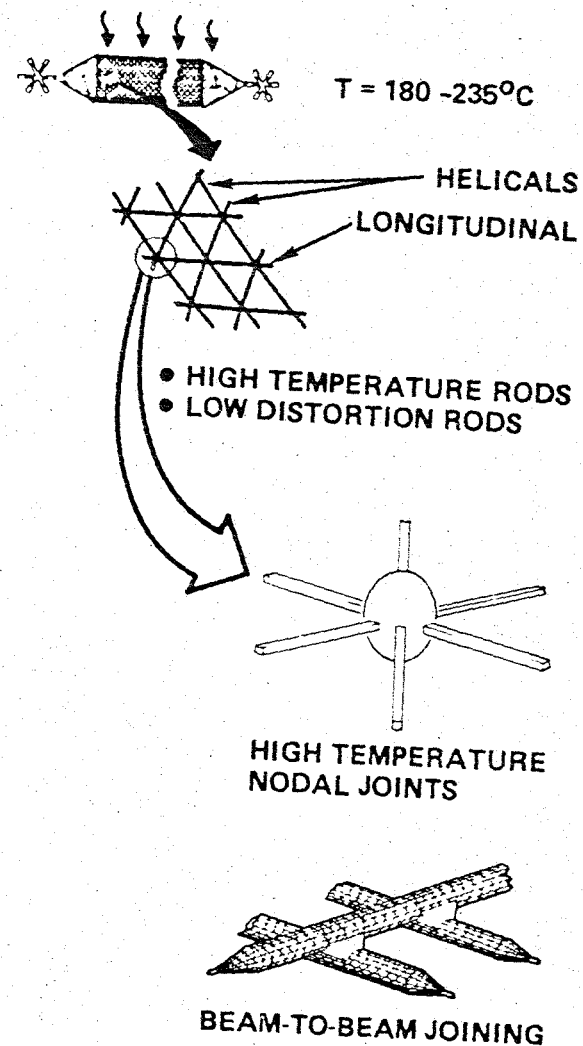
## GEODETIC CYLINDER TEST DATA/ANALYSIS COMPARISON PHASE I

SPECIMEN DESCRIPTION	PREDICTED BUCKLING LOAD, N (LB)	BUCKLING TEST LOAD, N (LB)	FAILURE MODE
DEMONSTRATION CYLINDER ENCAPSULATED JOINTS	11,800 (2,653)	11,780 (2,648)	LOCAL RIB BUCKLING
FEASIBILITY CYLINDER 1 ENCAPSULATED JOINTS	13,350 (3,000)	13,330 (2,990)	LOCAL RIB BUCKLING
FEASIBILITY CYLINDER 2 RESISTANCE WELDED JOINTS	8,850 (1,990)	8,675 (1,950)	EXCESSIVE JOINT FAILURES, LOCAL RIB BUCKLING

## PHASE IA OBJECTIVES

VFE543N

- EVALUATE HIGH TEMPERATURE (180 TO 235°C) ROD STOCK
- ASSESS THERMAL CONTROL COATINGS
- DEVELOP ZERO-CTE RODS
- EVALUATE HIGH TEMPERATURE JOINTS
- DEVELOP DESIGN CONCEPTS FOR JOINING GEODETIC BEAMS



## PHASE I AND IA PROGRAM SUMMARY

### PHASE I

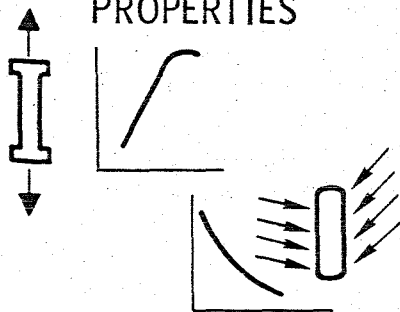
- FEASIBILITY OF THE GEODETIC BEAM CONCEPT HAS BEEN DEMONSTRATED THROUGH STRUCTURAL ANALYSIS, FABRICATION AND TESTING OF DEMONSTRATION AND FEASIBILITY CYLINDERS AND GEODETIC BEAM MACHINE DESIGN
  - HIGH STRUCTURAL EFFICIENCY
  - HIGH PRODUCTION RATE, RELIABLE AUTOMATIC FABRICATION USING LOW POWER

### PHASE IA

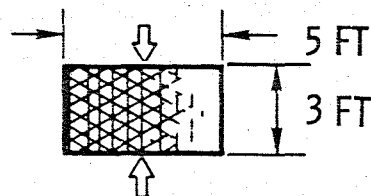
- LOW THERMAL EXPANSION HYBRID PULTRUDED RODS DEVELOPED
- PULTRUDED RODS FOR HIGH TEMPERATURE SERVICE (500°F) DEMONSTRATED
- HIGH TEMPERATURE JOINT ENCAPSULANT MATERIAL DEMONSTRATED
- PRELIMINARY DESIGNS FOR BEAM-TO-BEAM JOINING DEVELOPED

## PHASE II

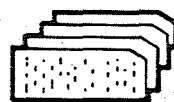
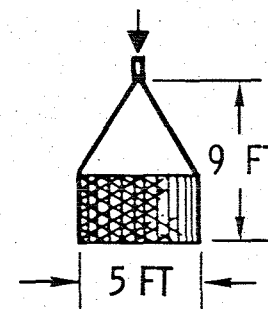
### PHYSICAL AND MECHANICAL PROPERTIES



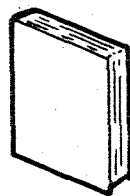
- MATERIAL CHARACTERIZATION TESTS



- TEST STRUCTURES
  - PARAMETER CYLINDER
  - CONE/CYLINDER



- IMPROVED GEODETIC STRUCTURE ANALYSIS CODE



- FINAL REPORT

- 
- VERIFICATION TESTS - PHASE IIA
  - METAL MATRIX COMPOSITE FEASIBILITY - PHASE IIA
  - BEAM MACHINE DESIGN (DEFERRED) - PHASE III

## MATERIAL CHARACTERIZATION OF PULTRUDED ROD (HMS/E-GLASS/P1700)

### PHYSICAL PROPERTIES

- DENSITY AND FIBER/RESIN CONTENT
- THERMAL EXPANSION
- SPECIFIC HEAT
- SOLAR ABSORPTIVITY/INFRARED EMITTANCE
- THERMAL CONDUCTIVITY
- ELECTRICAL CONDUCTIVITY

### MECHANICAL PROPERTIES

- TENSILE STRENGTH AND MODULUS
- COMPRESSIVE STRENGTH AND MODULUS
- TORSION MODULUS
- FLEXURAL STRENGTH AND MODULUS
- SIMULATED SPACE EXPOSURE
- LONG TERM COILED STORAGE

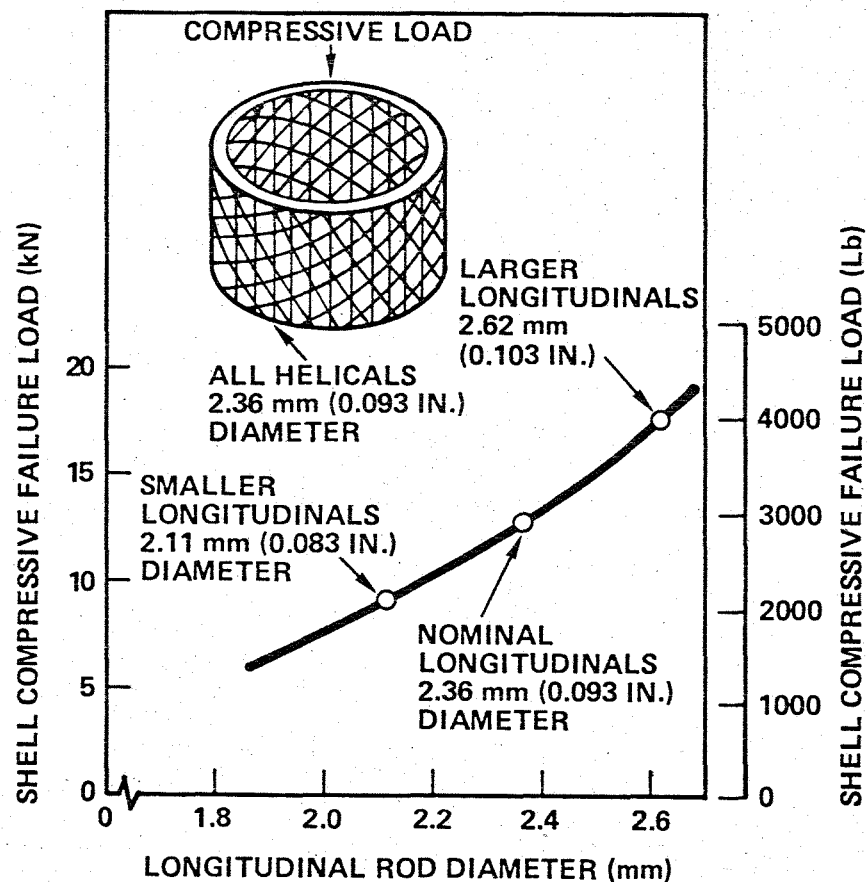


## PARAMETER CYLINDER TESTS

VFM120

### OBJECTIVES:

- DETERMINE STRUCTURAL LOAD CARRYING CAPABILITY FOR VARIOUS RATIOS OF LONGITUDINAL/HELICAL ROD SIZE
- VERIFY GEODETIC STRUCTURE DESIGN/ANALYSIS CAPABILITY



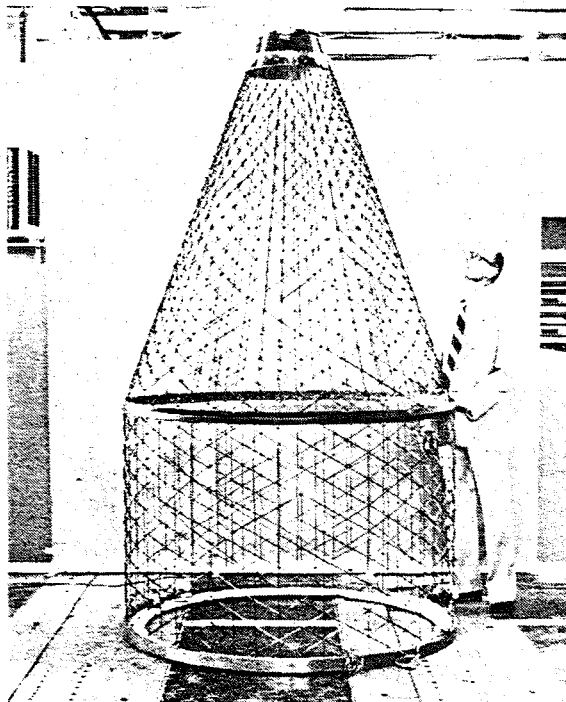
## GEODETIC CONE/CYLINDER TEST

### OBJECTIVE:

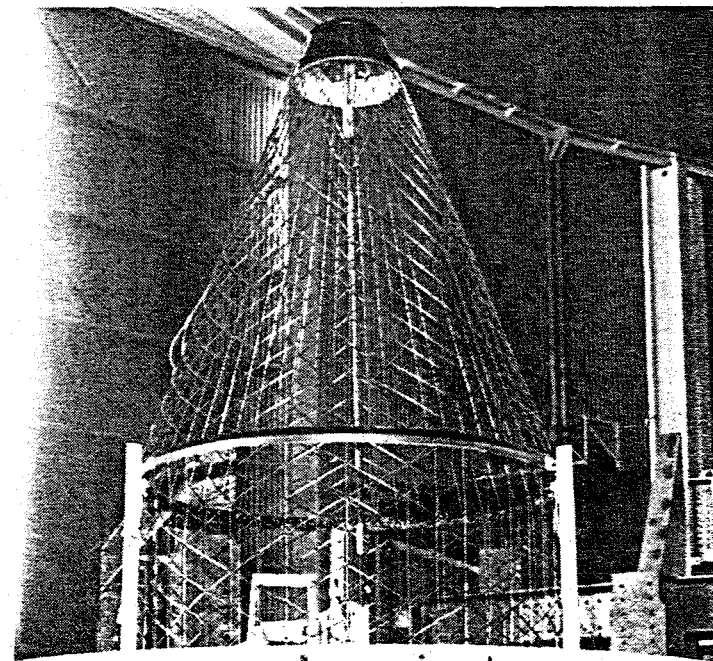
- DEMONSTRATE FEASIBILITY OF GEODETIC BEAM END CLOSURE DESIGN

### TEST RESULTS:

- SUCCESSFUL COMPRESSION TEST; LOCAL RIB BUCKLING AT  $P = 2,000$  LB



COMPLETED TEST STRUCTURE



GEODETIC CONE/CYLINDER TEST SETUP

## TEST DATA/ANALYSIS COMPARISON PHASE II

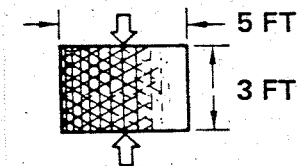
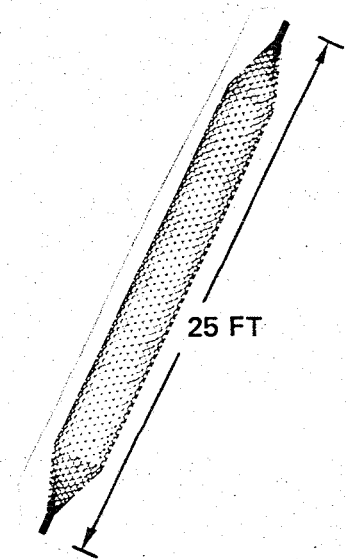
SPECIMEN DESCRIPTION	PREDICTED BUCKLING LOAD, N (LB)	BUCKLING TEST LOAD, N (LB)	FAILURE MODE
PARAMETER CYLINDER:			
<ul style="list-style-type: none"> <li>SECTOR I            HELICALS = 2.36 mm            LONGITUDINALS = 2.36 mm         </li> </ul>	11,685 (2,627)	10,742 (2,415)	LOCAL RIB BUCKLING
<ul style="list-style-type: none"> <li>SECTOR II            HELICALS = 2.36 mm            LONGITUDINALS = 2.11 mm         </li> </ul>	8,576 (1,928)	9,158 (2,059)	LOCAL RIB BUCKLING
<ul style="list-style-type: none"> <li>SECTOR III            HELICALS = 2.36 mm            LONGITUDINALS = 2.62 mm         </li> </ul>	15,679 (3,525)	13,900 (3,125)	GENERAL INSTABILITY
GEODETIC CONE/CYLINDER: CONE RODS = 2.62 mm CYLINDER RODS = 2.36 mm	11,685 (2,627)	8,896 (2,000)	LOCAL RIB BUCKLING IN CYLINDER NEAR CONE/CYLINDER INTERSECTION

## **PHASE II PROGRAM SUMMARY**

- DETAILED PHYSICAL AND MECHANICAL PROPERTY CHARACTERIZATION COMPLETED FOR HMS/E-GLASS/P1700 PULTRUDED ROD
- STRUCTURAL LOAD CARRYING CAPABILITY ESTABLISHED THROUGH PARAMETER CYLINDER TESTS
- IMPROVED STRUCTURAL ANALYSIS TECHNIQUES WERE SHOWN TO CORRELATE WELL WITH TEST RESULTS
- FEASIBILITY OF THE FULL SCALE END CLOSURE DESIGN WAS DEMONSTRATED WITH THE 9-FT LONG CONE/CYLINDER TEST ARTICLE

## PHASE IIA

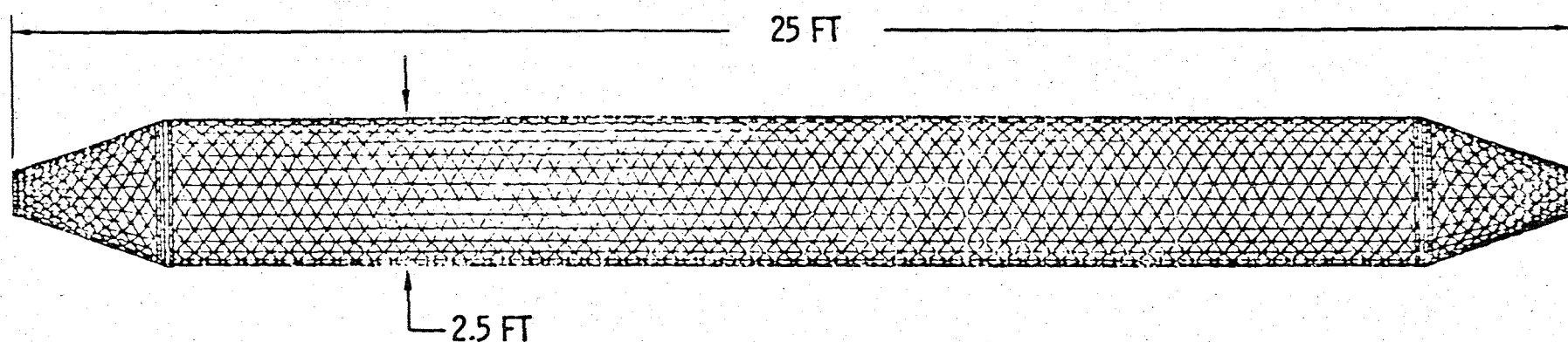
- **Verification Test Beam (Task 11)**
  - 25-Ft Long Graphite/Glass/Polysulfone Beam
  - Design, Fabricate, and Instrument at MDAC
  - Test at NASA/JSC
- **Metal Matrix Geodetic Beam (Task 13)**
  - 3-Ft Long, 5-Ft Diameter MMC Beam
  - Design, Fabricate, and Instrument at MDAC
  - Test at NASA/JSC



# **VERIFICATION TEST BEAM (TASK 11)**

- **Design/Analyze 25-Ft Long HMS/E-Glass/P1700 Geodetic Beam with End Closeouts (Length/Diameter  $\geq 10$ )**
- **Consider Axial, Shear, and Bending Loads**
- **Develop Tooling and Fabricate Beam**
- **Instrument Beam, Recommend Test Methods, Support NASA/JSC Testing, and Conduct Post-Test Analysis**

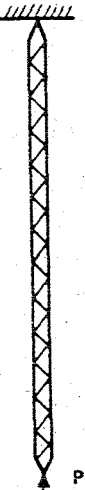
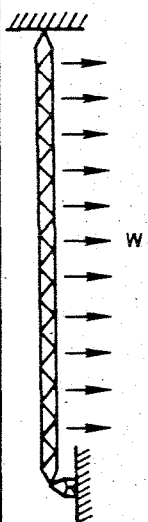
# GEODETIC VERIFICATION TEST BEAM



MATERIAL:	HMS/GLASS/P1700
ROD DIAMETER:	0.103 IN.
NUMBER OF LONGITUDINALS:	30
AXIAL COMPRESSIVE FAILURE LOAD:	3000 LB
CYLINDRICAL SECTION WEIGHT:	0.59 LB/FT
TOTAL WEIGHT:	21.7 LB

# VERIFICATION TESTS


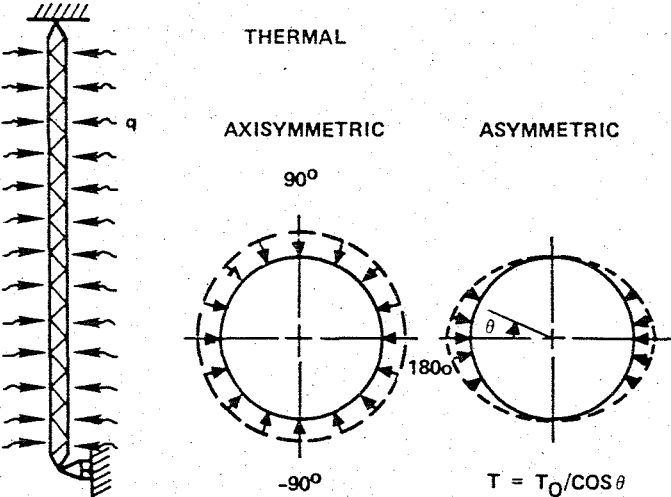
VFE590N

LOADING	INSTRUMENTATION	MEASUREMENTS	CORRELATION OF TEST AND ANALYSIS
 <p><b>AXIAL COMPRESSION</b></p> <ul style="list-style-type: none"> <li>• LOADED IN INCREMENTS UNTIL LOCAL BUCKLING OCCURS</li> </ul>	<ul style="list-style-type: none"> <li>• STRAIN GAGES</li> <li>• DEFLECTION GAGES</li> <li>• LOAD CELL</li> </ul>	<ul style="list-style-type: none"> <li>• STRAIN</li> <li>• LOCAL BUCKLING LOAD</li> <li>• END SHORTENING</li> <li>• LATERAL DEFLECTION</li> </ul>	<ul style="list-style-type: none"> <li>• LOCAL BUCKLING LOAD</li> </ul>
 <p><b>LATERAL LOAD (BENDING AND SHEAR)</b></p> <ul style="list-style-type: none"> <li>• LOADED IN INCREMENTS FROM 0.2g TO 2g</li> </ul>	<ul style="list-style-type: none"> <li>• DEFLECTION GAGES</li> <li>• STRAIN GAGES</li> <li>• LOAD CELLS</li> </ul>	<ul style="list-style-type: none"> <li>• DEFORMATION DUE TO BENDING AND SHEAR.</li> <li>• OVALING OF CROSS SECTION DUE TO BENDING.</li> <li>• STRAIN IN LONGITUDINAL MEMBERS AT <math>0^\circ</math>, <math>\pm 90^\circ</math>, <math>180^\circ</math></li> <li>• STRAIN IN HELICAL MEMBERS AT <math>\pm 90^\circ</math></li> </ul>	<ul style="list-style-type: none"> <li>• TOTAL DEFORMATION</li> <li>• STRAINS IN LONGITUDINAL MEMBERS AT <math>0^\circ</math> AND <math>180^\circ</math> AND STRAINS IN HELICAL MEMBERS AT <math>\pm 90^\circ</math></li> </ul>



# VERIFICATION TESTS (CONTINUED)

VFE591N

LOADING	INSTRUMENTATION	MEASUREMENTS	CORRELATION OF TEST AND ANALYSIS
 <p style="text-align: center;">TORSION</p>	<ul style="list-style-type: none"> <li>• DEFLECTION GAGES</li> <li>• STRAIN GAGES</li> <li>• LOAD CELLS</li> </ul>	<ul style="list-style-type: none"> <li>• ROTATION AT CROSS SECTION</li> <li>• STRAINS IN AXIAL AND HELICAL MEMBERS</li> </ul>	<ul style="list-style-type: none"> <li>• SHEAR STIFFNESS</li> </ul>
 <p style="text-align: center;">THERMAL</p> <p style="text-align: center;">AXISYMMETRIC      ASYMMETRIC</p> <p style="text-align: center;"><math>T = T_0 / \cos \theta</math></p>	<ul style="list-style-type: none"> <li>• DEFLECTION GAGES</li> <li>• STRAIN GAGES</li> <li>• THERMOCOUPLES</li> </ul>	<ul style="list-style-type: none"> <li>• DEFORMATION DUE TO TEMPERATURE AS A FUNCTION OF BEAM LENGTH AND CIRCUMFERENCE</li> <li>• TEMPERATURE DISTRIBUTION</li> <li>• STRAINS IN LONGITUDINAL AND HELICAL MEMBERS AT <math>0^\circ, \pm 90^\circ</math>, AND <math>180^\circ</math></li> </ul>	<ul style="list-style-type: none"> <li>• DEFORMATION</li> <li>• THERMAL STRAIN</li> </ul>

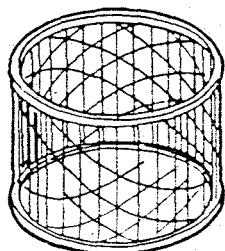
# **METAL MATRIX GEODETIC BEAM FEASIBILITY ASSESSMENT (TASK 13)**

- **Design/Analysis**
- **MMC Joining Technique Development**
- **Fabrication of MMC Beam Segment**
  - **GR/AL or GR/MG Rod Stock by Material Concepts, Inc (MCI) of Columbus, Ohio**
  - **Rod Characterization Tests**
  - **Assembly on Existing Tool**
  - **Joining of MMC Rod Stock**
  - **End Potting (Including Alignment)**
  - **Instrument and Ship to JSC**

# MMC'S OFFER SIGNIFICANT IMPROVEMENT IN GEODETIC BEAM STRUCTURAL PERFORMANCE

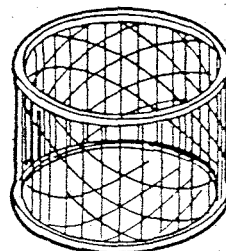
VFE431N

HMS/P1700



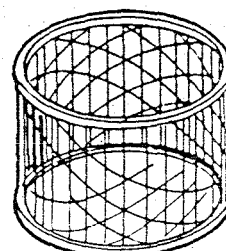
- $\alpha = -0.8 \mu\text{m/m/}^{\circ}\text{C}$  ( $-0.5 \mu \text{ in./in./}^{\circ}\text{F}$ )
- $P_{\text{CR}} = 13,350 \text{ N}$  (3000 lb)

HMS/E-GLASS/P1700



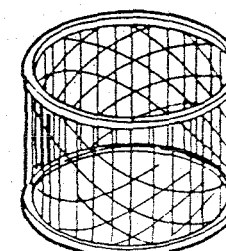
- $\alpha = \pm 0.18 \mu\text{m/m/}^{\circ}\text{C}$  ( $\pm 0.1 \mu \text{ in./in./}^{\circ}\text{F}$ )
- $P_{\text{CR}} = 10,000 \text{ N}$  (2250 lb)

P100/6061 AL



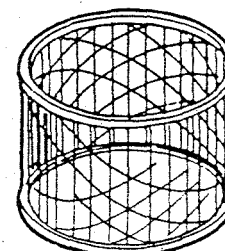
- $\alpha = +0.9 \mu\text{m/m/}^{\circ}\text{C}$   
( $0.5 \mu \text{ in./in./}^{\circ}\text{F}$ )
- $P_{\text{CR}} = 14,000 \text{ N}$  (3150 lb)

P100/AZ91C Mg



- $\alpha = \pm 0.18 \mu\text{m/m/}^{\circ}\text{C}$   
( $\pm 0.1 \mu \text{ in./in./}^{\circ}\text{F}$ )
- $P_{\text{CR}} = 20,000 \text{ N}$  (4500 lb)

P100/LA141A Mg-Li



- $\alpha = \pm 0.18 \mu\text{m/m/}^{\circ}\text{C}$  ( $\pm 0.1 \mu \text{ in./in./}^{\circ}\text{F}$ )
- $P_{\text{CR}} = 26,000 \text{ N}$  (5850 lb)

EQUIVALENT WEIGHT/LENGTH BEAM SEGMENTS

# **METAL MATRIX COMPOSITES (MMC)**

## **Comparison to Resin Matrix Composites**

### **Potential Design Advantage**

- **Higher Thermal and Electrical Conductivity**
- **No "Out-Gassing"**
- **Traditional Metal Familiarity**
- **Metallic Joint Concept**
- **Higher Operating Temperature Capability**
- **No Moisture Absorption**
- **Greater Directed Energy Weapon Resistance**
- **Higher Specific Strength and Stiffness**
- **Improved Fatigue Life**
- **Higher Use Temperature**
- **Improved Dimensional Stability**

## **Comparison to Conventional Metals**

## COMPARISON OF THE SPECIFIC STIFFNESSES OF SOME MMC VERSUS RESIN MATRIX COMPOSITES

	$\alpha$ $\mu\text{m}/\text{m}/^{\circ}\text{C}$ ( $\mu\text{in.}/\text{in.}/^{\circ}\text{F}$ )	$E$ $\text{GN}/\text{m}^2$ ( $\text{msi}$ )	$\rho$ $\text{kg}/\text{m}^3$ ( $\text{LB}/\text{IN}^3$ )	$V_f$ (%)	$E/\rho$ $\text{NMg} \times 10^{-4}$ ( $\text{LBF-IN}/\text{LB}_M$ $\times 10^{-8}$ )
HMS/E-GLASS/P1700	+0.18 ( $\pm 0.10$ )	128.2 (18.6)	1570.0 (0.056)	57.0	8.4 (3.32)
P100/6061 Al*	+0.9 (+0.5)	380.8 (54.2)	2380.0 (0.086)	52.0	16.0 (6.30)
P100/AZ91C Mg	$\pm 0.18$ ( $\pm 0.10$ )	398.0 (57.7)	1922.9 (0.069)	54.8	21.2 (8.36)
P100/LA141A Mg-Li	$\pm 0.18$ ( $\pm 0.10$ )	459.6 (66.7)	1787.5 (0.064)	64.5	26.3 (10.42)

\*MAXIMUM DEMONSTRATED FIBER VOLUME UTILIZED

## METAL MATRIX DEVELOPMENT AT MCI

- Gr/A<sub>2</sub> AND Gr/Mg COMPOSITE WIRE INCORPORATING PITCH 100 FIBERS (AS WELL AS OTHERS) DEMONSTRATED

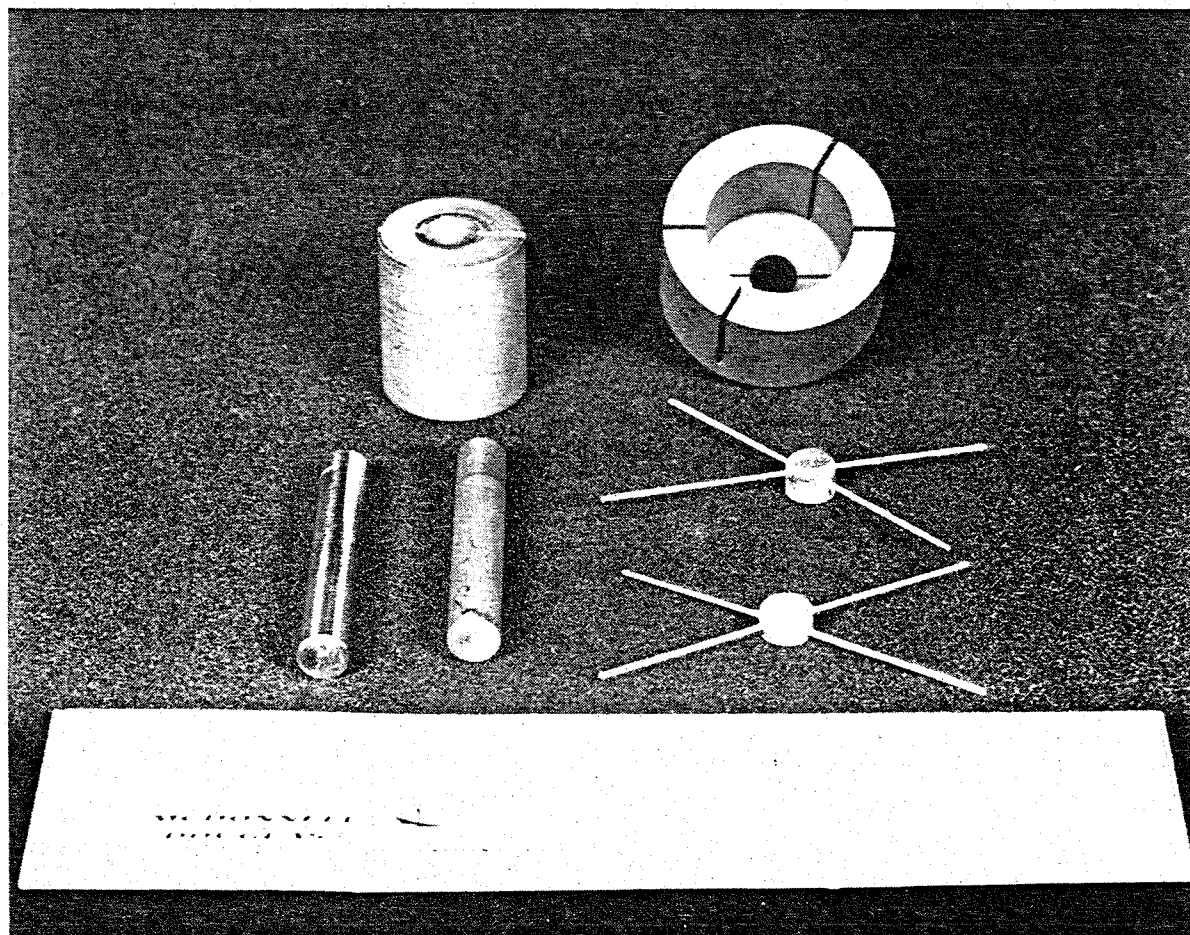
FIBER VOLUME LOADINGS ABOVE 50% (VOL) ARE FEASIBLE

- MAXIMUM Gr/A<sub>2</sub> (VS0054-6061) 52% (VOL)
- MAXIMUM Gr/Mg (VS0054 - AZ91C) 59% (VOL)
- DIAMETERS OVER 0.050 IN. DEMONSTRATED – LARGER DIAMETER FEASIBLE

- COMPOSITE WIRES WITH CONSISTENT PROPERTIES AND STRUCTURAL INTEGRITY ARE BEING MADE BY JUDICIOUS SCREENING OF PITCH 100 FIBERS
- HIGH POTENTIAL FOR FUTURE IMPROVEMENT IN OVERALL QUALITY AND FIBER VOLUME LOADING FOR BOTH Gr/A<sub>2</sub> AND Gr/Mg WITH PITCH 100 FIBERS

## MMC JOINING TECHNIQUE DEVELOPMENT

- Encapsulation  
P100/6061 Al  
P100/AZ91C Mg
- Welding  
P100/6061 Al
- Brazing/Soldering  
TBD



Induction Heating Joint Encapsulation Method



# **ROD CHARACTERIZATION TESTS METAL MATRIX GEODETIC BEAM**

- **Tensile Strength and Modulus**
- **Compressive Strength and Modulus**
- **Torsion Strength and Modulus**
- **Flexural Strength and Modulus**
- **Density**
- **Fiber/Matrix Percentage**
- **Thermal Conductivity**
- **Electrical Conductivity**
- **Specific Heat**
- **Solar Absorptivity**
- **Thermal Expansion**



## **PROGRAM STATUS**

### **Phase I**

- **Geodetic Beam Feasibility Demonstrated**
  - **Pultruded HMS/P1700 Rod Developed**
  - **Rod Joining Process Developed**
  - **Initial Material Characterization Completed**
  - **Three Test Cylinders Fabricated, Instrumented, and Tested**
- **Geodetic Beam Machine Concept Defined**
  - **Preliminary Design Layouts Completed**
  - **Subsystem Studies Completed**
  - **Weight and Power Vs Production Rate Determined**

### **Phase IA**

- **Near-Zero CTE HMS/E-Glass/P1700 Rods Developed**
- **High Temperature (500° F) Pultruded Rods Demonstrated**
- **High Temperature Joint Encapsulant Material Demonstrated**
- **Preliminary Designs for Beam-to-Beam Joining Developed**



## **PROGRAM STATUS (CONT)**

### **Phase II**

- **Physical and Mechanical Properties Obtained**
- **Parameter Cylinder Tests Completed**
- **Geodetic Beam Improved Analysis Verified**
- **Lattice Cone Closeout Demonstrated Through Tests of 9-Ft Long Cone/Cylinder**

### **Phase IIA**

- **25-Ft Long Verification Beam Design Completed**
- **GR/Al and GR/MG Rod Stock Test Material Obtained**
- **Metal Matrix Joining Tests Initiated**



## **PHASE IIA FUTURE ACTIVITIES**

### **Verification Beam:**

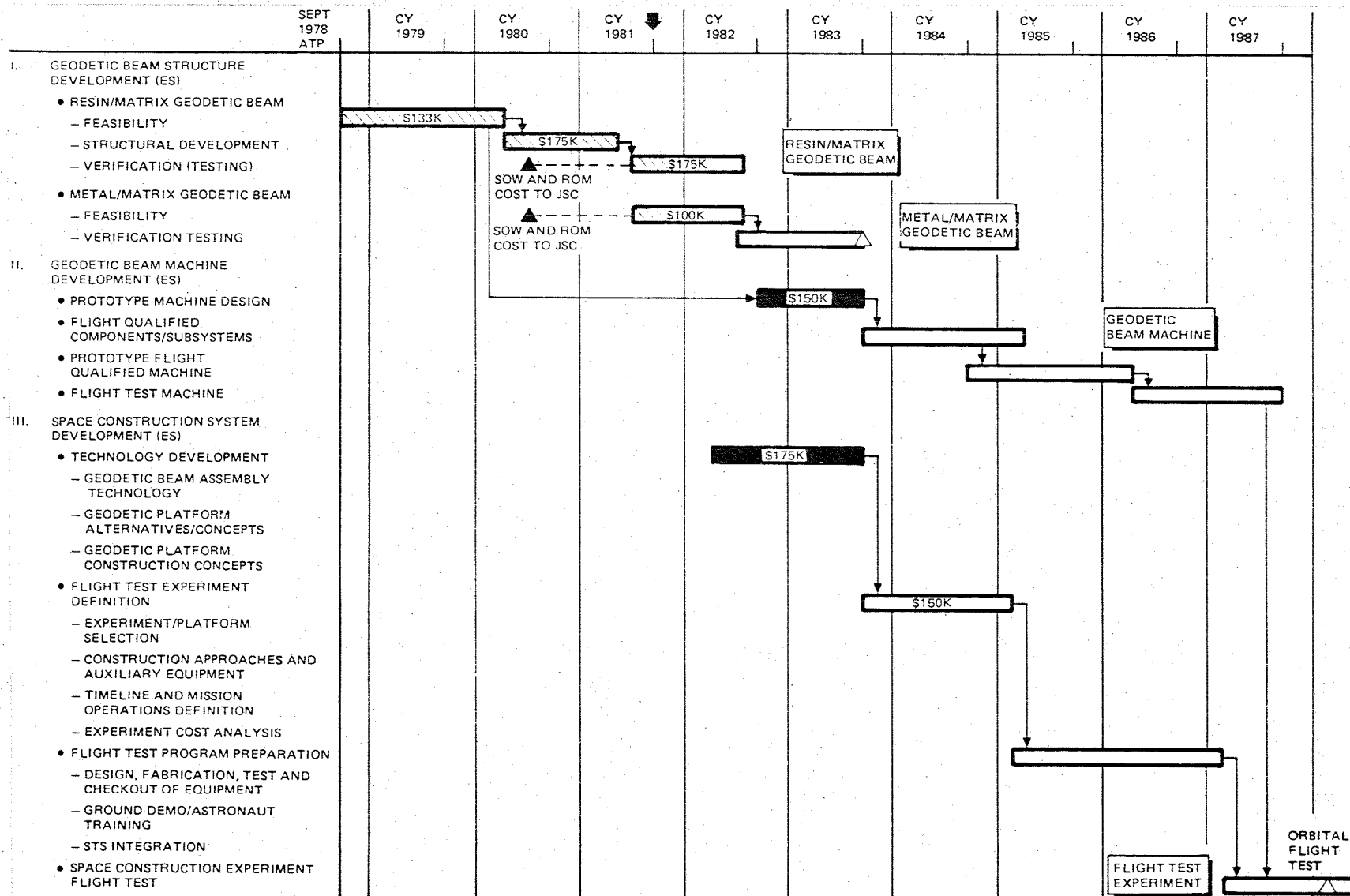
- **Fabricate Tooling and Beam**
- **Instrument and Ship to JSC**
- **Support Tests and Conduct Post-Test Analysis**

### **Metal Matrix Feasibility Cylinder:**

- **Complete Analysis**
- **Characterize MMC Rod Stock**
- **Complete Joining Tests**
- **Fabricate Cylinder**
- **Instrument and Ship to JSC**

# GEODETIC BEAM AND BEAM MACHINE DEVELOPMENT PLAN

VF0739





DEVELOPMENT OF A COMPOSITE GEODETIC  
STRUCTURE FOR SPACE CONSTRUCTION

Technical Letter Progress  
Report No. 29


September 1981

NAS9-15678

Prepared by

*Tony* A. J. Cwiertny, Jr.  
*John* R. Johnson, Jr.  
J. W. Maxted

Approved by:

  
R. F. Zemer, Director  
Advanced Programs  
Design & Technology  
Engineering Division

Prepared under Contract NAS9-15678, DRL No. T-1522, Line Item 1,  
DRD No. MA-003 for

NASA-Johnson Space Center, Houston, Texas 77058

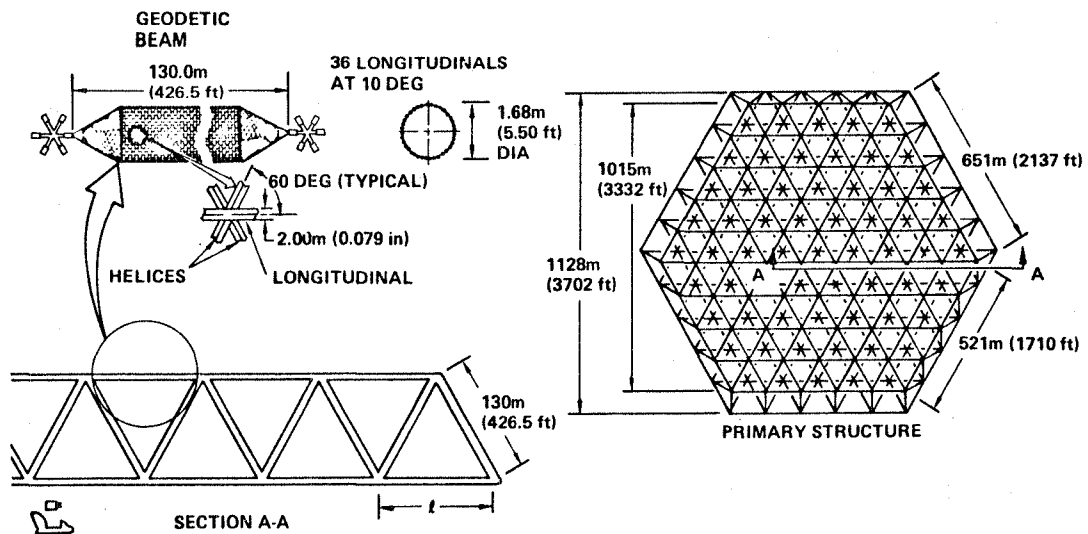
**MCDONNELL DOUGLAS ASTRONAUTICS COMPANY-HUNTINGTON BEACH**

5301 Bolsa Avenue Huntington Beach, California 92647 (714) 896-3311

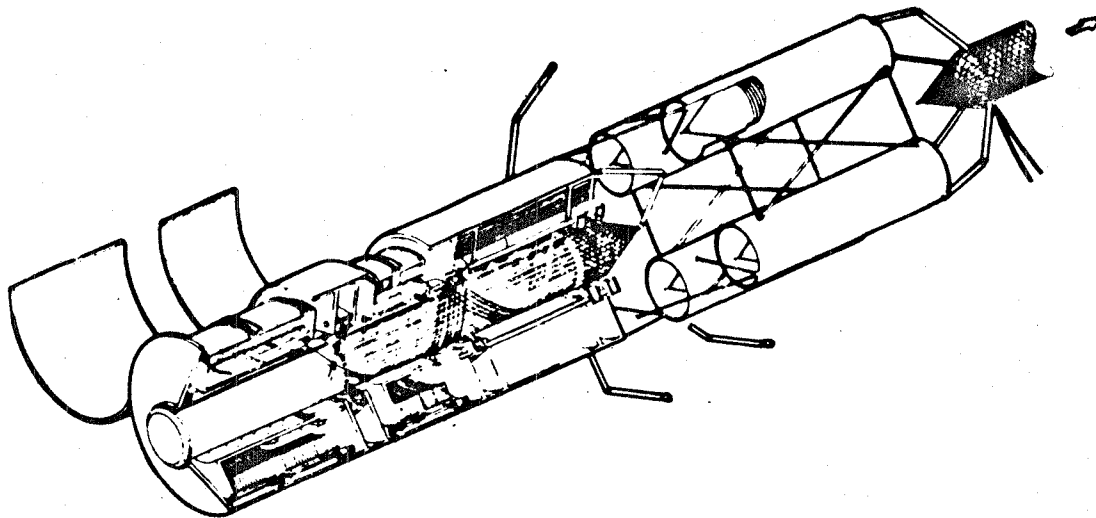
## 1.0 INTRODUCTION

The overall objective of this program is to develop a structurally efficient composite geodetic beam and a beam fabrication machine for on-orbit construction of large space structures (Figure 1). Phase II of the program ended 30 July 1981. Phase IIA was initiated on 1 July 1981 and is proceeding on schedule.

The overall program is divided into three phases to provide an orderly flow of technical accomplishments starting with demonstration of geodetic beam feasibility, continuing with verification of a full size beam, and finally providing a ground demonstration of automatic fabrication of a geodetic beam. Phase I consisted of tasks to (1) develop structural design requirements, (2) develop analytical procedures and select the best configuration for a geodetic beam, (3) develop structural termination concepts for the geodetic beam, (4) accomplish beam preliminary sizing, (5) develop pultruded composite rod stock for use in joining tests and feasibility test articles, (6) select a reliable joining technique, (7) design, fabricate, and test two geodetic test articles to establish concept feasibility, and initiate the preliminary design of a beam fabrication machine. Additional Phase I efforts consisted of preparation of an Orbital Flight Test (OFT) plan and fabrication of a scale model to demonstrate a key subsystem of the geodetic beam machine. Phase II was devoted to detailed material characterization tests of the pultruded composite rods and encapsulated joints (Task 8), parameter tests of a geodetic test cylinder and a cylinder/conical closeout test article (Task 9), and an improved geodetic beam analysis based on the parameter tests (Task 10). Phase IIA, currently being conducted, consists of Tasks 11 and 13. Task 11 involves designing, fabricating, and instrumenting a 25-ft. long verification beam that will be tested at NASA/JSC. Task 13 will establish the feasibility of using metal matrix composite (MMC) materials in fabrication of geodetic beams. Task 12, the detailed design of a geodetic beam machine, was deferred until Phase III. In Phase III, the ground demonstration of automatic fabrication of geodetic beams will be accomplished using pilot-plant equipment capable of automatically fabricating demonstration articles.



a. Geodetic Beam Application to a Microwave Power Transmission Antenna



b. Geodetic Beam Machine Concept

Figure 1. Geodetic Beam and Beam Machine Concept

## 2.0 SUMMARY OF PROGRESS

The final briefing for Phase II was given at NASA-JSC on Wednesday, 26 August 1981. A significant amount of time was spent to prepare and present the briefing. Preliminary sizing of the verification test beam was completed for Task 11. Selection of the preliminary metal matrix composite baseline material was accomplished for Task 13. Phase IIA progress is proceeding on schedule as shown in Figure 2.

### 3.0 VERIFICATION BEAM (Task 11)

Preliminary sizing of the verification test beam was completed.

HMS/E-glass/P1700 pultruded rods will be used because of high stiffness and nominally zero coefficient of thermal expansion characteristics. The beam length to diameter ratio of 25 feet to 2.5 feet was selected to provide long beam internal load distributions under transverse loads. A nominal rod diameter of 0.103 inches was selected to provide good strength and handling ruggedness. There will be thirty longitudinals which will result in a node spacing of 3.63 inches allowing ease of fabrication. This design will result in an axial load capacity in excess of 3000 pounds as shown in Figure 3. Lateral loads anticipated for geodetic beams are expected to be less than 2 g's which amounts to about 12 pounds per longitudinal for the verification beam. Thus, lateral loads will have practically insignificant impact on the axial load carrying capability for this design. The preliminary verification beam design is shown in Figure 4. Design of the cone/cylinder joint has been initiated. The objective is to reduce local bending effects observed in the Phase II cone/cylinder test. In addition to the preliminary sizing activities, a second encapsulating gun has been received. Also, the Versimid 1200 material for the joints has been ordered.

### 4.0 METAL MATRIX COMPOSITE FEASIBILITY (Task 13)

The preliminary assessment of candidate metal matrix composite (MMC) materials and joining techniques has been completed to support the development of a MMC geodetic beam segment for fabrication and test. The primary material candidate selected is P100/6061 aluminum MMC. The aluminum matrix represents



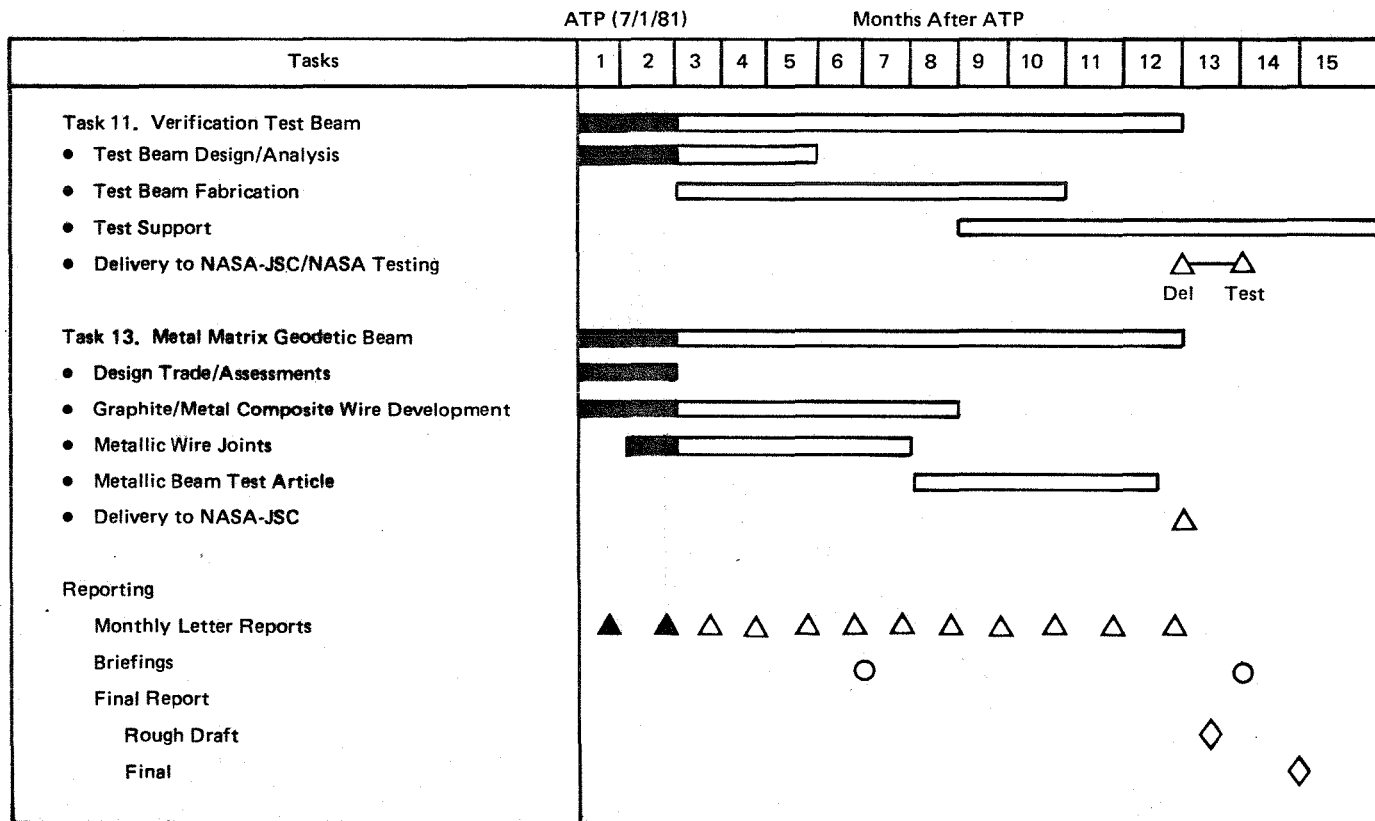


Figure 2. Development of Geodetic Structure for Space Construction – Phase IIA Schedule

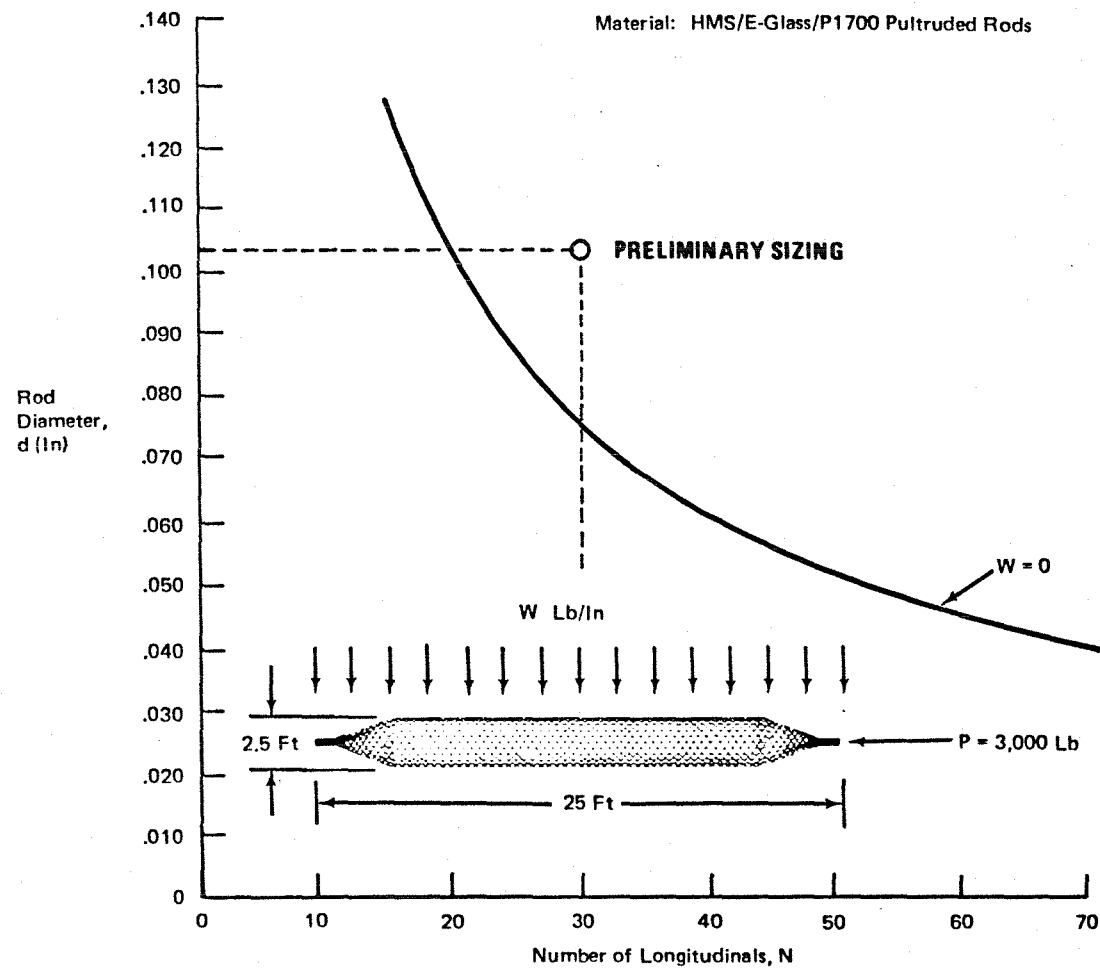
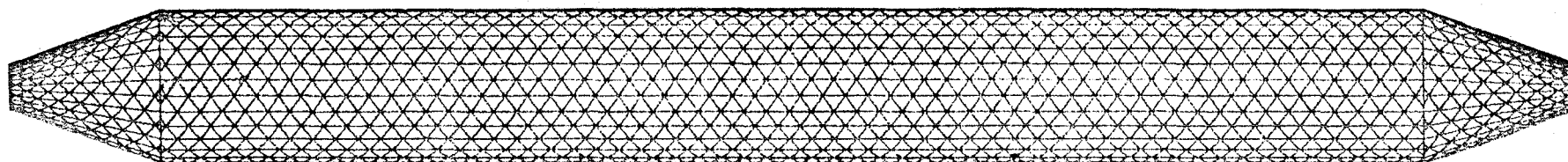


Figure 3. Verification Beam Rod Sizing



- Overall beam length is 300 inches.
- Maximum beam diameter is 30 inches.
- 30 Longitudinals planned.
- Nominal node spacing is 3.63 inches.
- Closeout half-angle is 20 degrees.
- Minimum closeout diameter is 9 inches.
- Helix angle is 60 degrees.
- Nominal rod diameter is .103 inches.

Figure 4. Preliminary Sizing of Verification Test Beam.

adequate stiffness to weight with a minimum risk of oxidation/joining problems. A secondary material candidate is P100/AZ91C magnesium MMC. The magnesium matrix represents superior stiffness to weight, but is difficult to join and is subject to rapid oxidation. The magnesium-lithium matrix represents an untried configuration and has been eliminated from consideration at this time.

An order has been placed with Material Concepts, Inc. (MCI) of Columbus, Ohio. This order is for the following items:

1. On a best effort basis, MCI will develop, produce, and deliver the following precursor wire by standard infiltration techniques.
  - a. 100 feet of VS0054/6061 aluminum 7 ended (.066" diameter) composite wire.
  - b. 100 feet of VS0054/AZ91C magnesium 7 ended (.066" diameter) composite wire.
2. On a best effort basis, MCI will develop, produce, and deliver 200 feed of VS0054/6061 (.066" diameter) die sized precursor wire.

Upon receipt of the material, characterization and joining tests shall be performed to finalize the material and fabrication process.

Preliminary flexure tests have indicated that the MMC rods have a reduced flexural modulus compared to the extensional modulus. Thus, a seven-tow configuration has been selected to maximize the overall flexural modulus.

Preliminary MMC joining tests have been completed. Samples of both aluminum and magnesium matrix rods were used in the joining tests. One successful joining technique has been demonstrated using aluminum matrix rods. This technique employs induction heating to melt an aluminum pellet in a graphite mold that holds the rods. The mold components and test specimens are shown in Figure 5. A photomicrograph of a joint with two wires is presented in Figure 6. The joining technique to be used in the geodetic test beam fabrication must be safe, inexpensive, and feasible for a structure requiring hundreds of joints. The strength of the rods must not be adversely affected by the joining techniques. Additional MMC joining tests will be performed when the multi-tow material arrives from MCI.

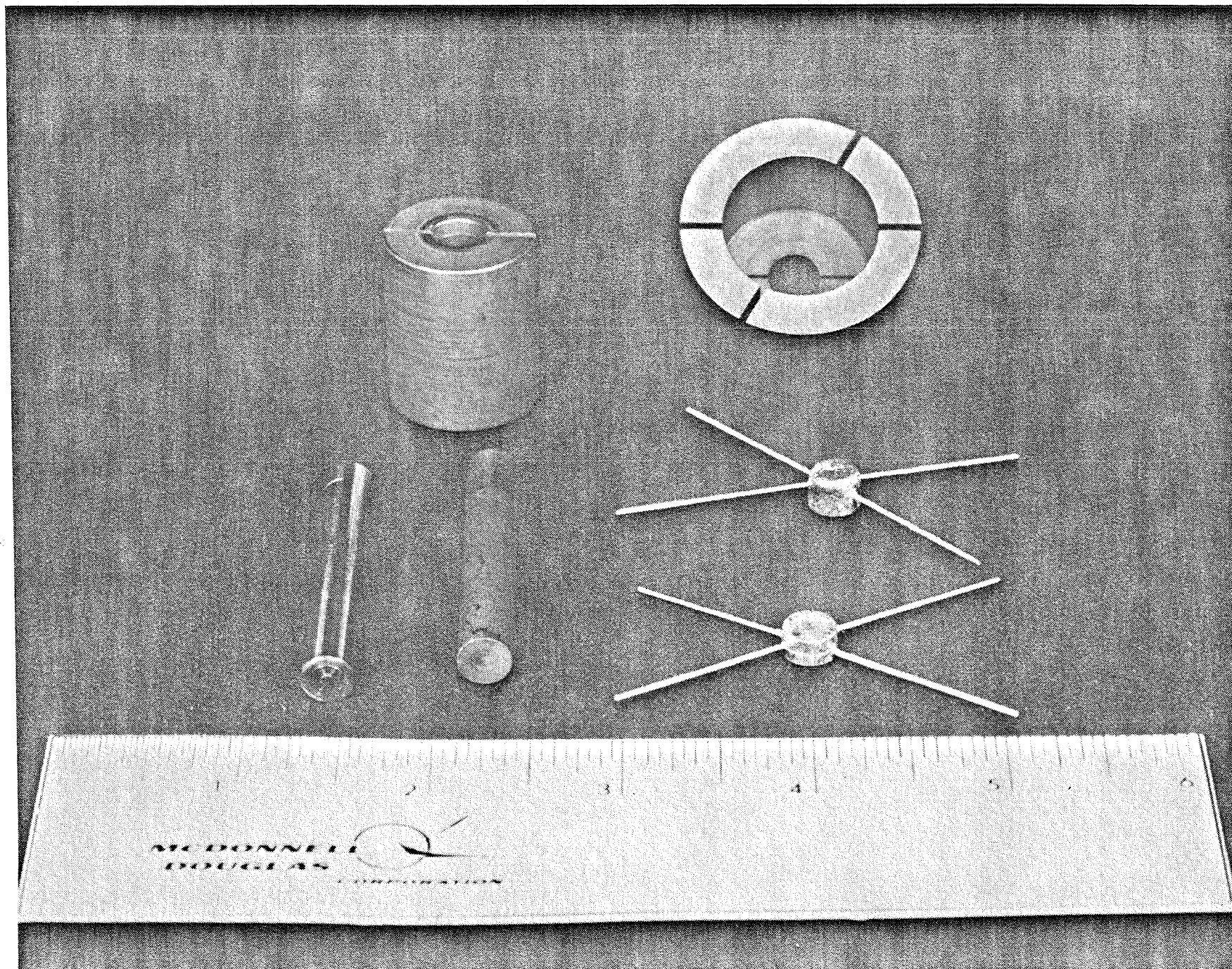


Figure 5. Metal Matrix Composite (Gr/Al) Encapsulated Joints

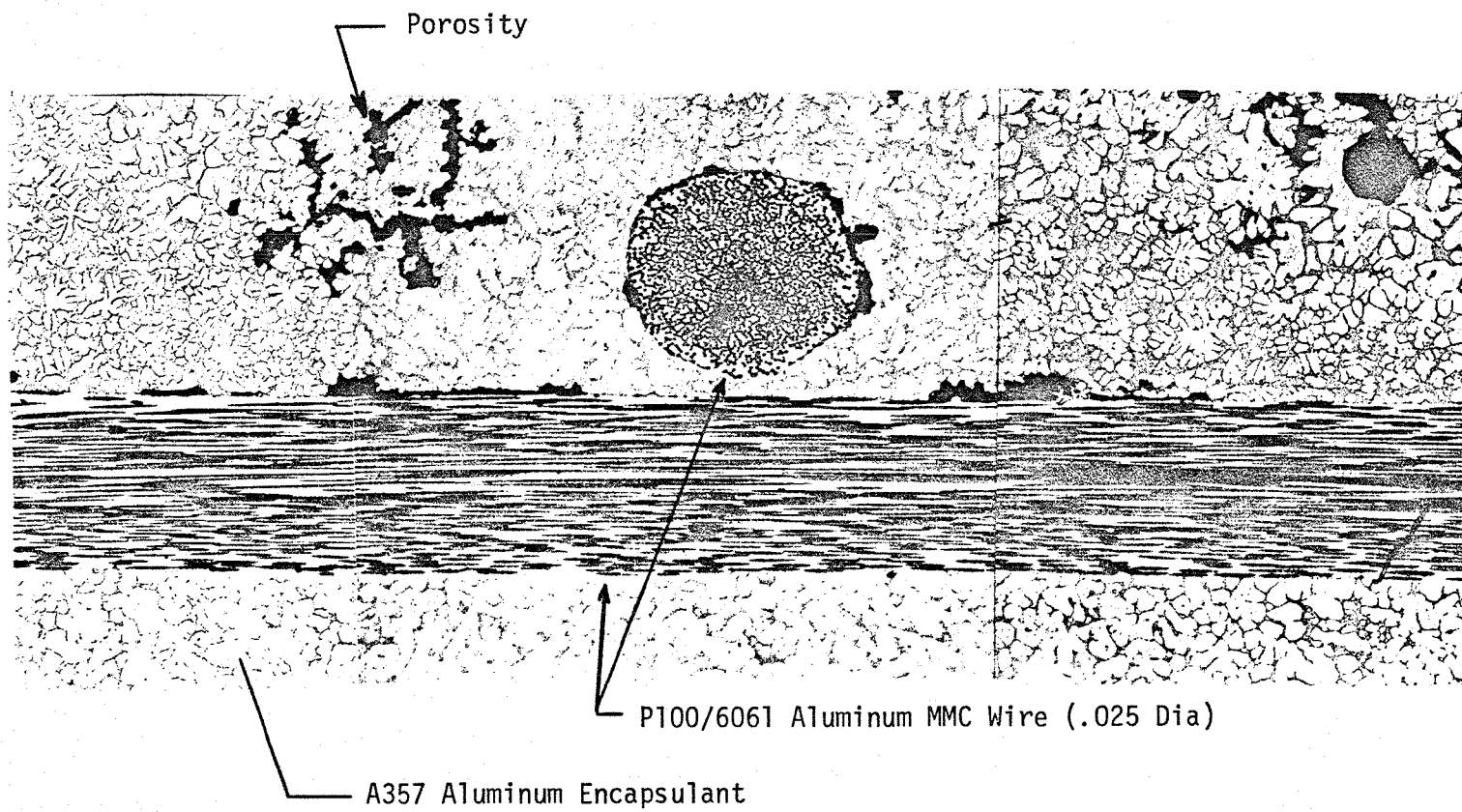


Figure 6. Photomicrograph of Encapsulated MMC Joint (40X)

## 5.0 PROBLEM AREAS

No problems exist at this time.

## 6.0 FUTURE WORK

Work will continue on Tasks 11 and 13 during the next reporting period. Design layouts will be initiated and the prepreg tape for the rods will be ordered. In addition, the details of the cone/cylinder joints will be finalized for the verification test beam.

## 7.0 PROGRAM COST AND SCHEDULE

The program is currently within cost projections and on schedule.

## PREFACE

This report was prepared by the McDonnell Douglas Astronautics Company (MDAC) for the National Aeronautics and Space Administration - Johnson Space Center (NASA-JSC) in accordance with contract NAS9-15678, DRL No. T-1522, DRD No. MA-201 TB, Line Item No. 3. It documents the results of Phase 2 of a three phase program entitled, "Development of a Composite Geodetic Structure for Space Construction", which has as its major objective the development of a geodetic beam and beam fabrication machine, i.e., beam builder, for on-orbit construction of truss-type space structures.

The results of the 17-month Phase 2 program were generated from March 1, 1980 through July 30, 1981, including final report preparation. A mid-term review was held at NASA-JSC in July 1980.

Overall project responsibility for the Development of a Composite Geodetic Structure for Space Construction program was assigned to the MDAC Engineering Division, Research and Development directorate, responsible for all engineering studies and experimental activities. Supervisory authority for the project was given to R. F. Zemer, Director - Design and Technology, Advanced Programs, on all study-related matters. Mr. A. J. Cwiertny was Program Manager and also provided technical support to the program. Mr. R. Johnson was Principal Investigator, responsible for coordinating all technical activities of the program. During the Phase 2 program, subcontract support was provided by the Compositek Engineering Corporation (CEC) of Buena Park, California and Glasforms, Inc., of San Jose, California. Dr. Brian Jones, President of Compositek and Mr. Peter F. Pfaff, President of Glasforms, reported directly to Mr. Cwiertny for coordinating Compositek and Glasforms activities.

The scope of this program was very broad and included many individuals who provided technical support. MDAC, CEC, and Glasforms personnel who significantly contributed to this program include:



Structural Design	- J. F. Dubel
	E. E. Cook
Materials and Processes	- V. L. Freeman
	R. C. Curley
	A. P. Penton
	D. Waldemar (CEC)
	P. F. Pfaff (Glasforms)
	F. J. Schneider
Structural Analysis	- M. H. Schneider
Structural Testing	- G. C. Shanks
Advance Manufacturing Technology	- W. A. Rosene
	L. F. Deane
Structure Fabrication	- A. J. Sutherland
	R. K. Kraft

The NASA-JSC COR for this program was Mr. Tom Dunn of the Structures and Mechanics Division, under D. C. Wade, Chief. Any questions regarding this contract activity should be directed to:

Mr. T. J. Dunn  
Structures and Mechanics Division, ES-/2  
National Aeronautics and Space Administration  
Lyndon B. Johnson Space Center  
Houston, Texas 77058  
Telephone (713) 483-2276

or

Mr. A. J. Cwiertny, Jr.  
Department A3-220, Mail Station 13-3  
Structures and Materials  
Research and Development  
McDonnell Douglas Astronautics Company  
5301 Bolsa Avenue  
Huntington Beach, California 92647  
Telephone (714) 896-3868

## CONTENTS

	<u>Page</u>
Section 1 INTRODUCTION AND SUMMARY	1
1.1 Introduction	
1.2 Summary	
Section 2 GEODETIC BEAM MATERIAL CHARACTERIZATION	5
2.1 Physical Properties	
2.2 Mechanical Properties	
Section 3 PARAMETER TESTS	25
3.1 Geodetic Parameter Cylinder Tests	
3.2 Geodetic Cone/Cylinder Test	
Section 4 STRUCTURAL ANALYSES	58
Section 5 CONCLUSIONS AND RECOMMENDATIONS	68
5.1 Conclusions	
5.2 Recommendations	
Appendix A GEODETIC BEAM MATERIAL PHYSICAL PROPERTY TESTS	A-1

## FIGURES

	<u>Page</u>
1-1 Geodetic Beam and Beam Builder	1
2-1 Absolute Expansion Versus Temperature for HMS/E-Glass/ P1700 Rod Material	8
2-2 Sample DSC Data to Determine Specific Heat of HMS/E-Glass/P1700 Rod Materials.	9
2-3 Specific Heat as a Function of Temperature for HMS/E-Glass/P1700 Rod Material.	10
2-4 Comparison of Specific Heat Versus Temperature for Various Materials.	11
2-5 Thermal Conductivity Test Results for HMS/E-Glass/P1700 Rod Material.	15
2-6 Tensile Test Sample Configuration for HMS/E-Glass/P1700 Pultruded Rods.	19
2-7 Compression Test Sample Configuration for HMS/E-Glass/ P1700 Pultruded Rods.	20
3-1 Compressive Failure Load vs. Longitudinal Rod Diameter	27
3-2 Geodetic Parameter Test Cylinder Detail Design	30
3-3 Test Setup for Parameter Cylinder Tests	31
3-4 Parameter Test Cylinder and Test Fixture	32
3-5 Parameter Cylinder Sector Loading Details	32
3-6 Strain Gage Layout for Three Sector Parameter Test Cylinders.	33
3-7 Compressive Buckling of 2.11 mm (0.083 in.) Diameter Longitudinals.	33
3-8 Strains Measured by Back-to-Back Gages at Center of Sector - 2.11 mm (0.083 in.) Diameter Longitudinals.	34
3-9 Strains Measured at Top Ends and Sides of Sector - 2.11 mm (0.083 in.) Diameter Longitudinals	34
3-10 Strains Measured at Bottom Ends and Sides of Sector - 2.11 mm (0.083 in.) Diameter Longitudinals.	35

	<u>Page</u>
3-11 Load Versus Displacement at Edge of Sector - 2.11 mm (0.083 in.) Diameter Longitudinals.	35
3-12 Compressive Buckling of 2.62 mm (0.103 in.) Diameter Longitudinals.	36
3-13 Strains Measured by Back-to-Back Gages at Center of Sector - 2.62 mm (0.103 in.) Diameter Longitudinals.	37
3-14 Strains Measured at Top Ends and Sides of Sector - 2.62 mm (0.103 in.) Diameter Longitudinals.	38
3-15 Strains Measured at Bottom Ends and Sides of Sector - 2.62 mm (0.103 in.) Diameter Longitudinals.	38
3-16 Load Versus Displacement at Edge of Sector - 2.62 mm (0.103 in.) Diameter Longitudinals.	39
3-17 Compressive Buckling of 2.36 mm (0.093 in.) Diameter Longitudinals	39
3-18 Strains Measured by Back-to-Back Gages at Center of Sector - 2.36 mm (0.093 in.) Diameter Longitudinals.	40
3-19 Strains Measured at Top Ends and Sides of Sector - 2.36 mm (0.093 in.) Diameter Longitudinals	40
3-20 Strains Measured at Bottom Ends and Sides of Sector - 2.36 mm (0.093 in.) Diameter Longitudinals	41
3-21 Load Versus Displacement at Edge of Sector - 2.36 mm (0.093 in.) Diameter Longitudinals.	42
3-22 Comparison of Pretest Analysis and Buckling Test Results for Geodetic Sectors With Various Ratios of Longitudinal-to-Helical Rod Size	43
3-23 Geodetic Cone/Cylinder Test Article	45
3-24 Geodetic Cone/Cylinder Detail Design	47
3-25 Cured Ring and Mandrel	48
3-26 Assembly Fixture for Conical End Closeout	48
3-27 Geodetic Cone/Cylinder Test Article Fabrication and Assembly Process	49
3-28 Geodetic Cone/Cylinder Test Article	50
3-29 Geodetic Cone/Cylinder Test Setup	50
3-30 Geodetic Cone/Cylinder Loading Details	51

3-31	Geodetic Cone/Cylinder Test Article Strain Gage and Displacement Transducer Layout	<u>Page</u> 52
3-32	Buckling of Geodetic Cone/Cylinder Test Article - P = 8,896 N (2,000 lb.)	53
3-33	Axial Load Versus Strain for Geodetic Cone/Cylinder Test Article - Strain Gages 1 and 2.	54
3-34	Axial Load Versus Strain for Geodetic Cone/Cylinder Test Article - Strain Gages 3 and 4.	54
3-35	Axial Load Versus Strain for Geodetic Cone/Cylinder Test Article - Strain Gages 5 and 6	55
3-36	Axial Load Versus Strain for Geodetic Cone/Cylinder Test Article - Strain Gages 7 and 8.	55
3-37	Axial Load Versus Strain for Geodetic Cone/Cylinder Test Article - Strain Gages 9 and 10.	56
3-38	Axial Load Versus Strain for Geodetic Cone/Cylinder Test Article - Strain Gages 11 and 12	56
3-39	Load Versus Displacement for Geodetic Cone/Cylinder Test Article	57
4-1	Geodetic Column Failure Modes	58
4-2	Local Buckling Coefficient for Rib as a Function of Local Stiffness - Out-of-Plane Mode	61
4-3	Buckling Coefficient as a Function of Rotational Spring Constant	62
4-4	Effect of Helical and Axial Member Bending Stiffness on the Local Buckling Coefficient, C	63
A-1	Thermal Plot of DSC Run 1.	A-3
A-2	Thermal Plot of DSC Run 2.	A-3
A-3	Thermal Plot of DSC Run 3.	A-4
A-4	Thermal Plot of DSC Run 4.	A-4
A-5	Thermal Plot of DSC Run 5.	A-5
A-6	Thermal Plot of DSC Run 6.	A-5
A-7	Thermal Conductivity Results.	A-14

		<u>Page</u>
A-8	Coefficient of Thermal Expansion Results for 2.54 cm Samples.	A-17
A-9	Coefficient of Thermal Expansion Results for 2.54 cm Samples	A-18
A-10	Coefficient of Thermal Expansion Results for 2.54 cm Samples	A-19
A-11	Coefficient of Thermal Expansion Results for 15.24 cm Samples	A-20

## TABLES

	<u>Page</u>
2-1 Physical Property Tests - HMS/E-Glass/P1700 Pultruded Rods	6
2-2 Mechanical Property Tests - HMS/E-Glass/P1700 Pultruded Rods	6
2-3 Physical Property Tests	6
2-4 Density, Fiber Content and Resin Content of HMS-E-Glass/P1700 Round Rod	7
2-5 Specific Heat of HMS/E-Glass/P1700 Pultruded Rod	10
2-6 Solar Absorptivity of Uncoated and Coated Samples of HMS/E-Glass/P1700	12
2-7 Infrared Emittance of Graphite/Glass Polysulfone	12
2-8 Thermal Conductivity of HMS/E-Glass/P1700 Using the Kohlrausch Technique	15
2-9 Electrical Resistivity of HMS/E-Glass/P1700 Rods	16
2-10 Comparison of Electrical Conductivity for Various Materials	17
2-11 Summary of Mechanical Properties of HMS/E-Glass/P1700 Pultruded Rod	18
2-12 Tensile Properties of HMS/E-Glass/P1700 Pultruded Rod	20
2-13 Compression Properties of HMS/E-Glass/P1700 Pultruded Rod	21
2-14 Torsional Elastic Modulus of Pultruded HMS/E-Glass/P1700 Rod	21
2-15 Flexural Properties of HMS/E-Glass/P1700 Pultruded Rods	22
2-16 Mechanical Property Tests Results for HMS/E-Glass/P1700 Rod Material Subjected to Simulated Space Exposure	23
3-1 Density, Fiber Content, and Resin Content of Rod Stock for Parameter Cylinder	28
4-1 Correlation of Previous Test Results	64
4-2 Correlation of Phase II Test Results	65

	<u>Page</u>
A-1 Specific Heat of Graphite/Glass Polysulfone	A-6
A-2 Heights of Sapphire Standards	A-6
A-3 Electrical Resistivity of Graphite/Glass Polysulfone	A-8
A-4 Solar Absorptivity of Graphite/Glass Polysulfone	A-9
A-5 IR Emittance of Graphite/Glass Polysulfone	A-10
A-6 Specific Heat Results	A-13
A-7 Thermal Diffusivity Results (23°C)	A-13
A-8 Kohlrausch Results	A-14
A-9 Coefficient of Thermal Expansion Results	A-16
A-10 Linear Regression Data for Coefficient of Thermal Expansion Results	A-17
A-11 Coefficient of Thermal Expansion Results for 15.24 cm Specimens of Graphite/Glass Polysulfone Rod	A-20



## Section 1

### INTRODUCTION AND SUMMARY

#### 1.1 INTRODUCTION

Recent studies of future space systems, such as space platforms, phased arrays, antennas, and solar power satellites, have substantiated the requirement for technology developments which will lead to on-orbit fabrication and assembly of large structural subsystems. In recognition of the need for an on-orbit fabrication capability, the NASA Johnson Space Center initiated a three-phase program in late 1978 with the overall objective of developing a structurally efficient composite geodetic beam and beam fabrication machine, i.e., beam builder, for on-orbit construction of truss type space structures. The geodetic beam, originally proposed by T. J. Dunn of NASA in 1976, is a lightweight, open lattice structure composed of an equilateral gridwork of criss-crossing rods. This beam provides a high degree of stiffness and minimizes structural distortion, due to temperature gradients, through the incorporation of a new graphite and glass reinforced thermoplastic composite material with a low coefficient of thermal expansion. A low power consuming, high production rate, beam builder automatically fabricates the geodetic beams in space using rods preprocessed on earth (Figure 1-1).

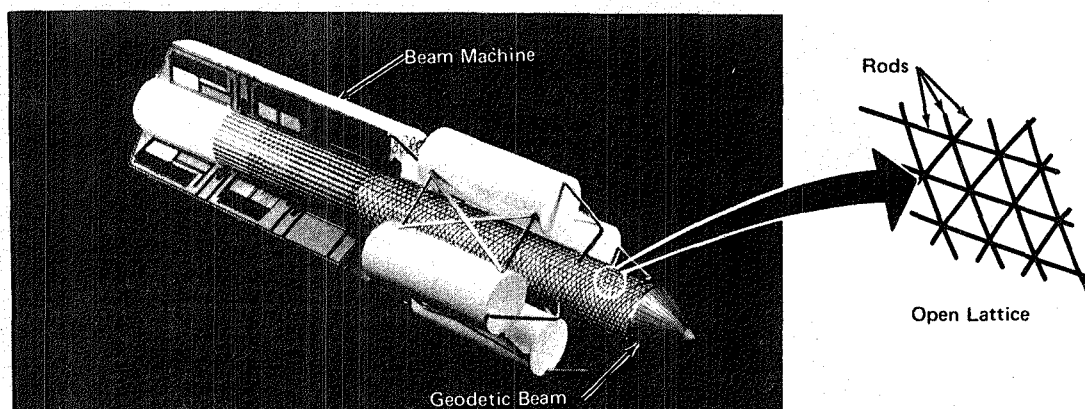


Figure 1-1. Geodetic Beam and Beam Builder

Overall program efforts are divided into three phases. Phase I, initiated on 1 September 1979, consisted of tasks to (1) develop structural design

requirements, (2) develop analytical procedures and select the best configuration for a geodetic beam, (3) develop structural termination concepts for the geodetic beam, (4) accomplish beam preliminary sizing, (5) develop pultruded composite rod stock for use in joining tests and feasibility test articles, (6) select a reliable joining technique, (7) design, fabricate, and test two geodetic test articles to establish concept feasibility, and initiate the preliminary design of a beam fabrication machine. Additional Phase I efforts consisted of preparation of an Orbital Flight Test (OFT) plan for an on-orbit fabrication demonstration and fabrication of a beam machine scale model to demonstrate key subsystems of the geodetic beam machine. Phase I was successfully completed on March 1, 1980.

Phase II was devoted to detailed material characterization tests of the pultruded composite rods, parameter tests of a geodetic test cylinder and a cylinder/conical closeout test article, and an improved geodetic beam analysis based on the parameter test results. A Phase IIA activity, consisting of Phase II tasks which have been deferred because of funding limitations, will consist of verification tests of a 25 foot long graphite/glass composite geodetic test article and feasibility testing of a metal matrix composite geodetic beam segment. In Phase III, geodetic beam machine design will be completed and the ground demonstration of automatic fabrication of geodetic beams will be accomplished using pilot-plant equipment capable of automatically fabricating demonstration articles.

## 1.2 SUMMARY

The Development of a Composite Geodetic Structure for Space Construction program consists of three phases, and this report documents the results of the 17 month Phase II program accomplished under NASA-JSC contract NAS9-15678. The two primary objectives of the Phase II program were to characterize advanced composite materials which best satisfy the requirements of geodetic space structures and to fabricate and test structures to evaluate the structural parameters and characteristics that are required for a full understanding of the structural capabilities of the type of geodetic structure under development. To accomplish these objectives, three tasks were identified and accomplished. These tasks are summarized briefly below.

The primary physical and mechanical properties of the hybrid HMS/E-glass/P1700 rod material used for the fabrication of geodetic beams was established early in the Phase II program (Task 8). This material was selected for detailed characterization based on work conducted in Phase I and IA which indicated that it best satisfied the requirements of geodetic space structures. This material possesses a near zero coefficient of thermal expansion (CTE), high axial and flexure stiffness and strength, low density and can be continuously produced as round rod stock using a pultrusion process by a number of sources. This material can also be joined using a low power consuming joint encapsulation technique to produce reliable, high-stiffness and strength joints as demonstrated during Phase I. The HMS/E-glass/P1700 physical properties determined during this task and discussed in Section 2 were density and fiber/resin content, longitudinal coefficient of thermal expansion, specific heat, solar absorptivity and infrared emittance, thermal conductivity and electrical conductivity. The mechanical properties of HMS/E-glass/P1700 rod material which were determined were tensile, compressive and flexure strength and modulus, torsional modulus, strength degradation due to simulated space exposure and permanent set of elastically strained stored rod stock.

Two geodetic structures were analyzed, designed, fabricated, instrumented and tested to evaluate structural parameters and characteristics that are required for a greater understanding of the capabilities of the composite geodetic beam (Task 9). A geodetic parameter cylinder was designed so that three different sizes of longitudinal rods were used, with each of three circumferential segments of the cylinder containing one of the three rod sizes. Axial load tests of each trisector of this parameter cylinder were used to generate data needed to design minimum weight geodetic structures by varying the sizes of longitudinal and helical rod members.

The second geodetic test article was an end closure structure consisting of a lattice cone closeout joined to a short cylindrical geodetic beam segment. The feasibility of this end closure design was established by axial compression testing of the combined test article. Data was obtained on the distribution of load transferred from the lattice cone closeout to the geodetic cylinder, i.e., load redistribution data were obtained.

In order to have a full understanding of the structural capabilities of the type of geodetic structure under development, refinements of structural analysis techniques were accomplished (Task 10). The analytical procedures developed during the Phase I study were extended and refined to include the effect of different rod stock dimensions for the helical and longitudinal members on local buckling, and the effect of different flexural and extensional moduli on general instability buckling. An analysis and computer code developed by Anderson of NASA was employed to predict general instability.

The following sections present the detailed results of Phase II program activities and the conclusions and recommendations reached based upon these results.

## Section 2

### GEODETIC BEAM MATERIAL CHARACTERIZATION

The objective of this Phase 2 task was to define all of the primary physical and mechanical properties of the pultruded hybrid HMS/E-glass/P1700 rod material used for the fabrication of geodetic beams. Key properties established were used in analysis of the parameter test articles (see Section 3.0). Approximately eighty feet of 2.36 mm (0.093 in.) diameter hybrid rod stock was procured from Composittek Engineering Corporation for use in characterization tests. Physical and mechanical property tests performed are listed in Tables 2-1 and 2-2, respectively and the results of these tests are discussed below.

#### 2.1 PHYSICAL PROPERTIES

The physical property tests conducted are summarized in Table 2-3. The number of specimens utilized to determine each physical property and the range of temperature over which property data were obtained is also presented in Table 2-3. A discussion of physical property testing accomplished is presented briefly below and discussed in detail in Appendix A.

##### 2.1.1 Density and Fiber/Resin Content

Density, fiber content, resin content, and void content were determined for representative samples of rod stock (Table 2-4). Density and fiber/resin content were similar to that obtained for the hybrid material reported in Reference 2-1, e.g., pultruded rod graphite and glass fiber contents differed by less than 1 percent volume. This similarity was expected since the same lot of prepreg material was used in producing both groups of rod stock. Density for the hybrid rod stock material characterized averaged  $1550 \text{ kg/m}^3$ , HMS fiber content averaged 38.26 percent volume, E-glass averaged 14.60 percent volume, resin content averaged 30.04 percent weight, and void content was an average of 9.6 percent volume.

##### 2.1.2 Coefficient of Thermal Expansion

All tests to determine the coefficient of thermal expansion (CTE) of the HMS/E-glass/P1700 rod stock material during the Phase 2 program were conducted by Composite Optics, Inc. of San Diego, California. Two test series were

**Table 2-1**  
**PHYSICAL PROPERTY TESTS –**  
**HMS/E-GLASS/P1700 PULTRUDED RODS**

Type of Test
Density and Fiber/Resin Content
Coefficient of Thermal Expansion
Specific Heat
Solar Absorptivity/Infrared Emittance
Thermal Conductivity
Electrical Conductivity

**Table 2-2**  
**MECHANICAL PROPERTY TESTS –**  
**HMS/E-GLASS/P1700 PULTRUDED RODS**

Type of Test
Tensile Strength and Modulus
Compressive Strength and Modulus
Torsion Modulus
Flexural Strength and Modulus
Strength Degradation
Permanent Deformation Due to Storage

**Table 2-3**  
**PHYSICAL PROPERTY TESTS**

Type of Test	No. of Samples	Comments
Density	6 From Each Pultrusion Run	
Fiber/Resin Content	6 From Each Pultrusion Run	Determine Percentages of Fiber, Resin, and Voids
Coefficient of Thermal Expansion	8	Longitudinal CTE between $-175^{\circ}\text{C}$ and $+150^{\circ}\text{C}$ . Specimen Geometry: 2.36 mm Dia x 2.54 cm Long (6 Samples); 2.36 mm Dia x 15.24 cm Long (2 Samples)
Specific Heat	6	Specific Heat Determined Between $50^{\circ}\text{C}$ ( $122^{\circ}\text{F}$ ) and $500^{\circ}\text{C}$ ( $932^{\circ}\text{F}$ ) Specimen Geometry: Thin Wafers of Round Rod Stock (2.36 mm Dia)
Solar Absorptivity/Infrared Emittance	6	Tests of Both Coated and Uncoated Samples at Room Temperature, Specimen Geometry: 1.27 cm (0.5 in.) Square Specimens, 0.32 cm (0.125 in.) Thick
Thermal Conductivity	2	Tests Conducted between $-175^{\circ}\text{C}$ and $+150^{\circ}\text{C}$
Electrical Conductivity	4	Tests Conducted at Room Temp. Specimen Geometry: 2.36 mm Dia x 10 cm Long Rods

**Table 2-4**  
**DENSITY, FIBER CONTENT AND RESIN CONTENT OF HMS/E-GLASS/P1700 ROUND ROD**

Sample No.	Density kg/m <sup>3</sup> (lb/in. <sup>3</sup> )	Fiber Content – Vol %		Resin Content Wt %	Voids Vol %
		HMS	E-Glass		
1	1527 (0.055)	38.05	14.46	29.52	11.07
2	1567 (0.056)	39.20	15.11	28.86	9.15
3	1573 (0.057)	38.37	14.43	31.09	7.80
4	<u>1533 (0.055)</u>	<u>37.42</u>	<u>14.40</u>	<u>30.68</u>	<u>10.2</u>
Avg	1550 (0.056)	38.26	14.60	30.04	9.6

conducted using the same 2.36 mm (0.093 in.) diameter HMS/E-Glass/P1700 round rod stock. The CTE of six 2.54 cm (1.0 in.) long specimens and two 15.24 cm (6.0 in.) long specimens were measured over the temperature range of -175°C to +150°C. All samples were preconditioned at 150°C for two hours under vacuum prior to testing.

Initial measurements made by Composite Optics on the six 2.54 cm (1.0 in.) long specimens showed slightly higher CTE values than previously reported in Reference 2-1. The testing in Reference 2-1 utilized 15.24 cm (6.0 in.) long CTE specimens. Retesting of the material was ordered after discussions with Composite Optics revealed that the shortness, i.e., 2.54 cm (1.0 in.) length of the specimens was undoubtedly resulting in inaccurate CTE measurements. Because of the greater resolution possible with 15.24 cm (6.0 in.) long specimens, the values obtained more accurately represent the CTE of the round rod material. Absolute expansion data versus temperature data for all eight specimens tested by Composite Optics are presented in Appendix A. The CTE test results for the two 15.24 cm (6.0 in.) long 2.36 mm (0.093 in.) diameter round rod stock specimens are presented in Figure 2-1, along with previous CTE results for similar square rod stock material (Reference 2-1). The round rod data indicate a CTE of near zero over the temperature range of 66°C (150°F) to 150°C (302°F) and a CTE of approximately  $-0.28 \times 10^{-6}$  m/m/K (-0.15 in/in/°F) over the temperature range of -175°C (-283°F) to 40°C (104°F). The difference in CTE results presented in Figure 2-1 for round and square cross-section HMS/E-Glass/P1700 rod stock materials may be due to the sensitivity of rod material CTE to the percentage distribution of graphite, glass and resin in the composite material.

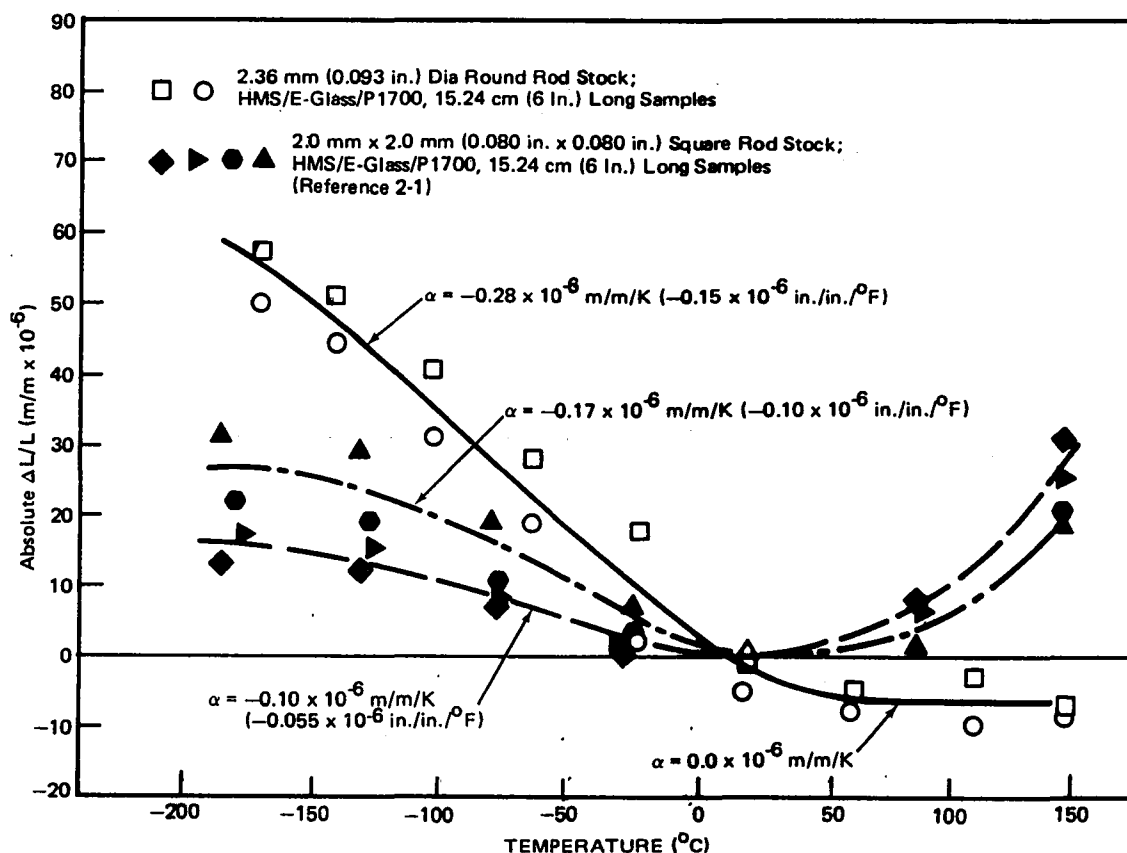


Figure 2-1. Absolute Expansion Versus Temperature for HMS/E-Glass/P1700 Rod Material.

### 2.1.3 Specific Heat

Six samples of HMS/E-Glass/P1700 round rod stock material were analyzed by MDAC by Differential Scanning Calorimetry (DSC) to determine specific heat at temperatures from 50°C (122°F) to 500°C (932°F). A duPont 990 Controller equipped with a duPont DSC cell and cell base was used to perform the analyses. In addition, one Thermogravimetric Analysis (TGA) was performed in order to determine the percentage weight loss as a function of temperature.

Samples were prepared by slicing thin wafers from rod stock with a Unimet saw. Two of these wafers were placed into an aluminum sample pan and an aluminum cover crimped onto the pan. Two empty aluminum pans were then run to establish a baseline and a standard sapphire specimen in an aluminum pan was run versus an empty aluminum pan. Finally, the specimen in an aluminum pan was run versus the empty pan. The following parameters were used:

Atmosphere: Flowing Argon at 20 cc/min.

Heating Rate: 10°C/min



Sensitivity: 0.5 (mcal/sec)/in.

Samples were programmed from ambient to 500°C (932°F).

Calculation of specific heat values at a given temperature was accomplished according to the following formula:

$$Cp_s = (H_s/H_a)(W_a/W_s)(Cp_a) \quad (2-1)$$

where

$Cp_s$  = specific heat of the test samples (cal/g/K)

$H_s$  = height (cm) of the sample curve from the baseline

$H_a$  = height (cm) of the standard curve from the baseline

$W_a$  = weight (g) of the standard curve from the baseline

$W_s$  = weight (g) of the sample corrected for weight loss during heating

$Cp_a$  = specific heat (cal/g/K) of the standard

A sample thermal plot of a DSC run is shown in Figure 2-2. A data summary of the specific heat values for the six specimens is given in Table 2-5. Specific

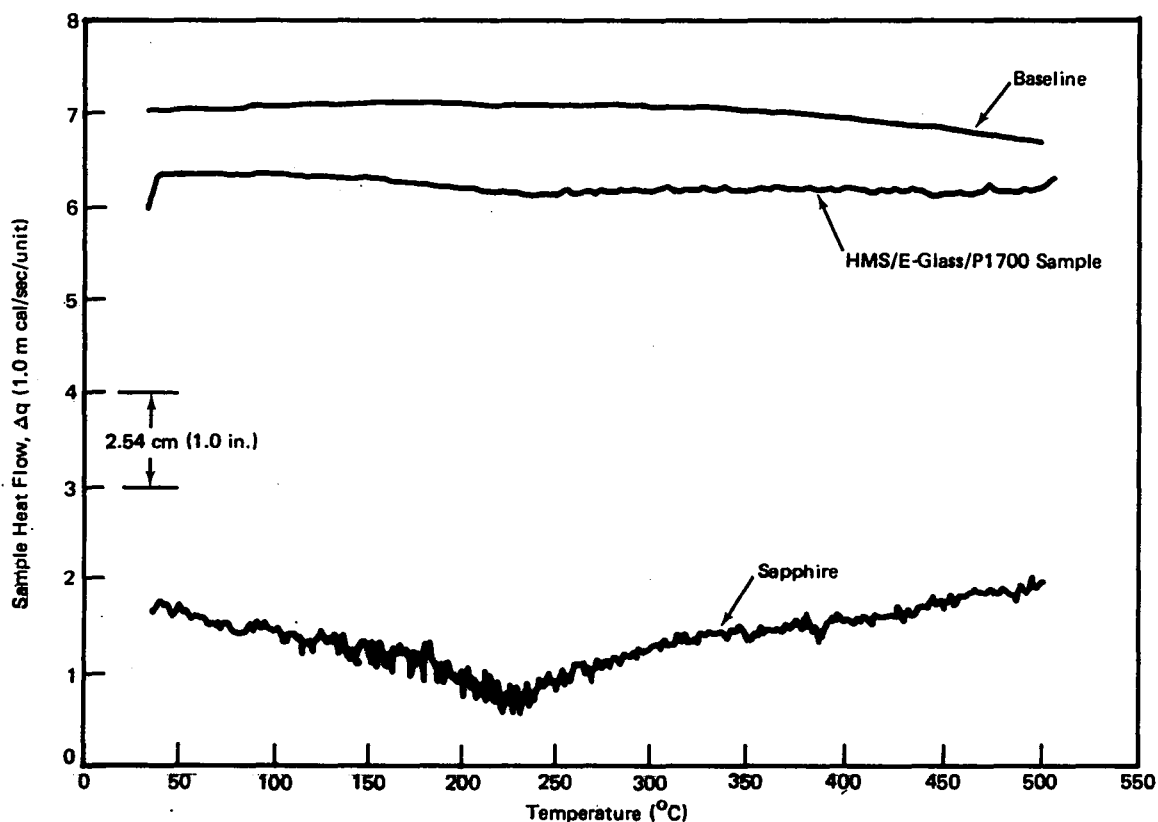


Figure 2-2. Sample DSC Data to Determine Specific Heat of HMS/E-Glass/P1700 Rod Material.

heat values appear to increase from 50°C (122°F) to 400°C (752°F), then decrease at 500°C (932°F). The standard deviation for the specific heat values is approximately 15%. Figure 2-3 shows the variation of specific heat for the HMS/E-Glass/P1700 rods as a function of temperature. Figure 2-4 presents comparison of specific heat versus temperature for graphite/epoxy, aluminum, S-Glass/epoxy and the HMS/E-glass/P1700 materials.

Table 2-5  
SPECIFIC HEAT OF HMS/E-GLASS/P1700 PULTRUDED ROD

Sample No.	Specific Heat, cal/g-K					
	Temperature, °C					
	50	100	200	300	400	500
1	0.150	0.169	0.213	0.238	0.233	0.171
2	0.202	0.225	0.276	0.307	0.292	0.229
3	0.192	0.217	0.265	0.312	0.299	0.269
4	0.152	0.180	0.219	0.246	0.277	0.253
5	0.202	0.233	0.291	0.320	0.334	0.307
6	<u>0.229</u>	<u>0.254</u>	<u>0.315</u>	<u>0.338</u>	<u>0.361</u>	<u>0.324</u>
Avg	0.188	0.213	0.263	0.294	0.299	0.259

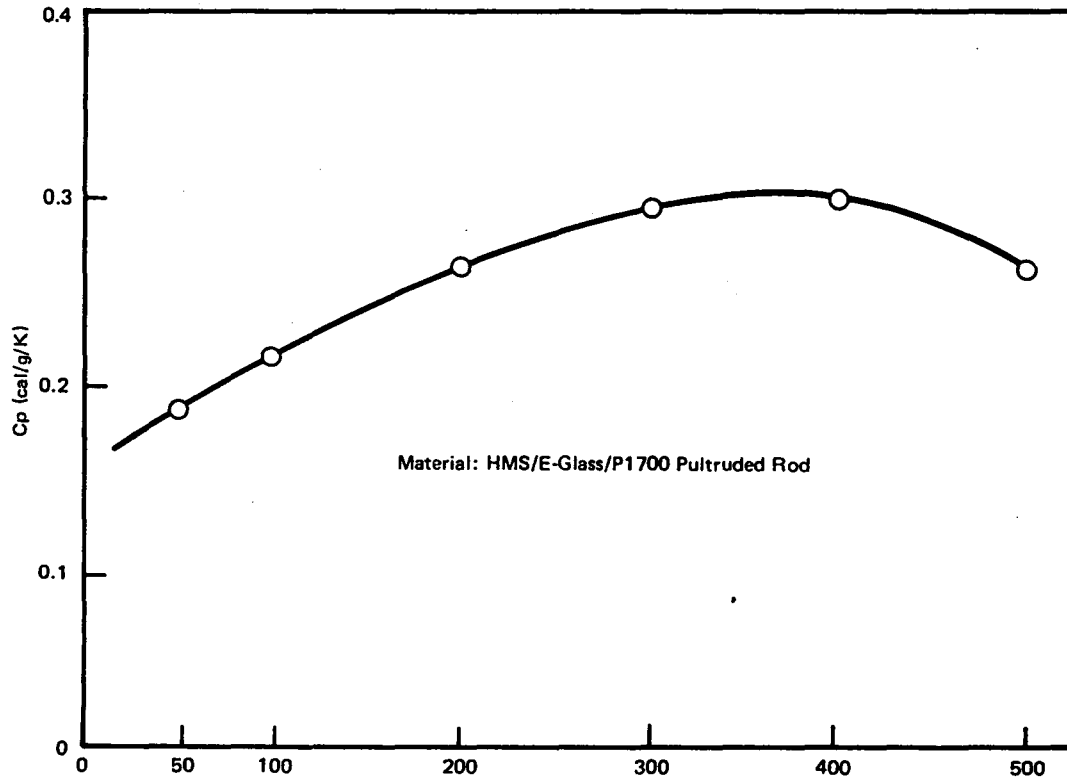


Figure 2-3. Specific Heat as a Function of Temperature for HMS/E-Glass/P1700 Rod Material.

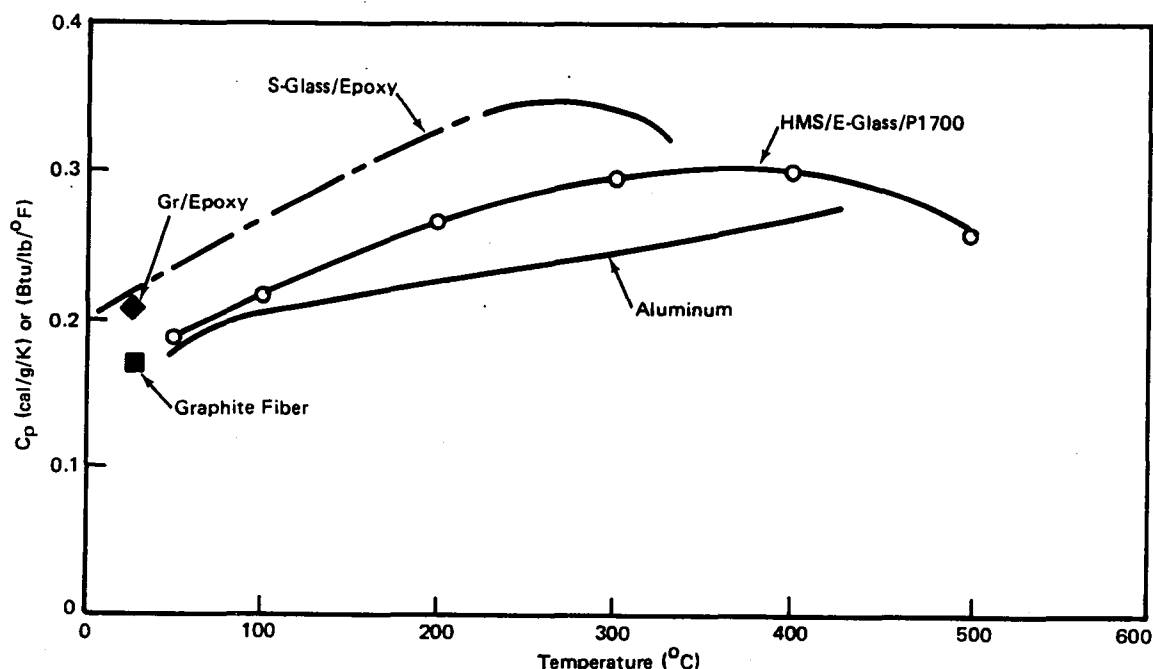


Figure 2-4. Comparison of Specific Heat Versus Temperature for Various Materials.

#### 2.1.4 Solar Absorptivity/Infrared Emittance

Solar absorptivity was measured on six samples using a Gier Dunkle model MS 251 Solar Reflectometer. The 1.27 cm (0.5 in.) square specimens were formed from the HMS/E-Glass/P1700 material. Three samples were coated with a system composed of SS4044 primer and S13G/L0 thermal control coating. Three others were left uncoated. One measurement of solar absorptivity was made per sample. A stray light measurement was made and stray light was found to be approximately 2%. This correction was applied to values obtained in sample measurement.

Table 2-6 gives values of solar absorptivity for coated and uncoated graphite/glass polysulfone samples. The white coated samples absorb much less light in the solar wavelength region than the black uncoated samples. The average absorptivity for uncoated samples is 0.913 and for coated samples, 0.146.

Infrared (IR) emittance was measured using a Gier Dunkle Model DB100 Infrared Reflectometer. The specimens of graphite/glass polysulfone used in solar absorptivity measurements were also used to measure IR emittance. The specimens were slightly smaller than the sample port of the infrared reflectometer. In order to prevent the leakage of infrared radiation around the edges of the sample, the sample port was masked with gold foil. The reflectometer was

**Table 2-6**  
**SOLAR ABSORPTIVITY OF UNCOATED AND COATED SAMPLES**  
**OF HMS/E-GLASS/P1700**

Samples	Solar Absorptivity $\alpha_s$
<b>Uncoated Samples</b>	
1	0.910
2	0.915
3	0.915
	<hr/>
	Avg = 0.913
<b>Coated Samples</b>	
1	0.150
2	0.139
3	0.148
	<hr/>
	Avg = 0.146

calibrated against two standards, one a high reflectance gold standard and the other a low reflectance black standard. Calibration was repeated before every specimen measurement.

Table 2-7 gives values of infrared emittance for coated and uncoated graphite/glass polysulfone samples. The white coated samples show a greater emittance in the infrared than the black uncoated samples. The average emittance for the uncoated samples is 0.771 and for coated samples is 0.895. The ratio of

**Table 2-7**  
**INFRARED EMITTANCE OF GRAPHITE/GLASS POLYSULFONE**

Samples	Infrared Emittance $\epsilon$	Solar Absorptivity/ Infrared Emittance $\alpha/\epsilon$
<b>Uncoated</b>		
1	0.764	1.19
2	0.777	1.18
3	0.771	1.19
	<hr/>	<hr/>
	Avg = 0.771	Avg = 1.19
<b>Coated</b>		
1	0.894	0.168
2	0.891	0.156
3	0.901	0.164
	<hr/>	<hr/>
	Avg = 0.895	Avg = 0.163

$\alpha/\epsilon$  was calculated to be 0.163 and 1.19 for coated and uncoated samples, respectively. The uncoated samples have an approximately seven-fold greater  $\alpha/\epsilon$  ratio than the coated samples. In view of the desirability of low  $\alpha/\epsilon$  for space structure materials, in order to reduce material UV degradation and temperature excursions, coatings should be used to protect HMS/E-glass/PI700 material for geodetic space structures.

#### 2.1.5 Thermal Conductivity

Thermal conductivity tests were conducted on two samples of the hybrid HMS/E-Glass/PI700 pultruded rod by the Thermophysical Properties Research Laboratory of the Center for Information and Numerical Data Analysis and Synthesis (CINDAS), West Lafayette, Indiana. The longitudinal thermal conductivity of samples of graphite/glass polysulfone rod was measured using two techniques. The first involved the measurement of thermal diffusivity using the flash diffusivity technique on several specimens cut from the rod at different locations on the same sample. The apparatus consists of a Korad K2 laser, a high vacuum system including a bell jar with viewing windows, a tube heater/chiller surrounding the sample, a spring loaded thermocouple, appropriate biasing circuits, amplifiers, A-D converters, crystal clocks and a minicomputer-based digital acquisition system. This first method was used as a check at room temperature to compare with the results from the Kohlrausch technique, the second method was used for determining the thermal conductivity.

Specific heat values were measured with a Perkin-Elmer Model 2 DSC over a small temperature interval to convert the thermal diffusivity results to thermal conductivity values using the relation

$$K = \alpha C_p d \quad (2-2)$$

$K$  = thermal conductivity (W/cm-K)

$\alpha$  = thermal diffusivity ( $\text{cm}^2/\text{sec}$ )

$C_p$  = heat capacity (W-sec/g-K)

$d$  = bulk density ( $\text{g}/\text{cm}^3$ )

The second method, the Kohlrausch technique, was used to determine thermal conductivity over the desired temperature range. The temperature rise data did not follow the theoretical model because of the large differences in the

ability of the graphite fibers and the matrix to conduct heat. A conductivity method was used in order to obtain the temperature dependency. Two specimens were chosen whose room temperature conductivity values approximated those obtained from diffusivity measurements.

The Kohlrausch method involves the measurement of the product of thermal conductivity and electrical resistivity. This is achieved by passing constant direct current through the sample and heating it while the ends are maintained at a constant temperature. An external heater minimizes radial heat loss. Thermocouples are positioned at the center of the sample and one centimeter on each side of the center. The thermocouples are also used to measure voltage. With the center thermocouple at position 2 and the others at positions 1 and 3, the product of thermal conductivity and electrical resistivity can be measured as

$$K\rho = (V_3 - V_1)^2 / 4[2T_2 - (T_1 + T_3)] \quad (2-3)$$

where:

- k = thermal conductivity ( $\text{W cm}^{-1} \text{K}^{-1}$ )
- $\rho$  = electricity resistivity (ohm-cm)
- $V_3 - V_1$  = voltage drop between outside thermocouples (volts)
- $T_1 + T_3$  = sum of temperatures at the outside thermocouples ( $^{\circ}\text{K}$ )
- $T_2$  = temperature of the center thermocouple ( $^{\circ}\text{K}$ )

Electrical resistivity is measured as

$$\rho = (V_3 - V_1)A/IL \quad (2-4)$$

where:

- A = cross-sectional area ( $\text{cm}^2$ )
- I = current (amperes)
- L = distance between outside thermocouples (cm)

Using these measured values, K can be calculated. Data collection and calculations were computerized and the measurements were made while the sample was under vacuum and the external heater temperature was set to  $T_2$ . When one set of measurements was completed, more current was applied and after equilibrium established, a new set of measurements was made. This method has been used previously on a number of fiber-reinforced materials.

Kohlrausch results for two samples are given in Table 2-8. In Figure 2-5, these results are plotted along with the longitudinal thermal conductivity

**Table 2-8**  
**THERMAL CONDUCTIVITY OF HMS/E-GLASS/P1700 USING THE KOHLRAUSCH TECHNIQUE**

Sample No.	Temp (°C)	K (w-cm <sup>-1</sup> ·K <sup>-1</sup> )	Temp (°F)	K (Btu-in.-hr <sup>-1</sup> ·ft <sup>-2</sup> ·F <sup>-1</sup> )
1	-196	0.043	-322	30
	-175	0.060	-283	42
	-148	0.079	-235	55
	-114	0.120	-173	83
	-87	0.145	-124	101
	-55	0.180	-67	125
	-39	0.193	-38	134
	-22	0.210	-8	146
	-5	0.227	23	157
	58	0.277	136	192
	80	0.290	176	201
	108	0.307	226	213
	132	0.327	269	227
	146	0.336	295	233
2	-142	0.155	-224	107
	-84	0.220	-119	153
	-35	0.258	-31	179
	-6	0.283	21	196
	52	0.326	126	226
	85	0.350	185	243
	138	0.381	280	264

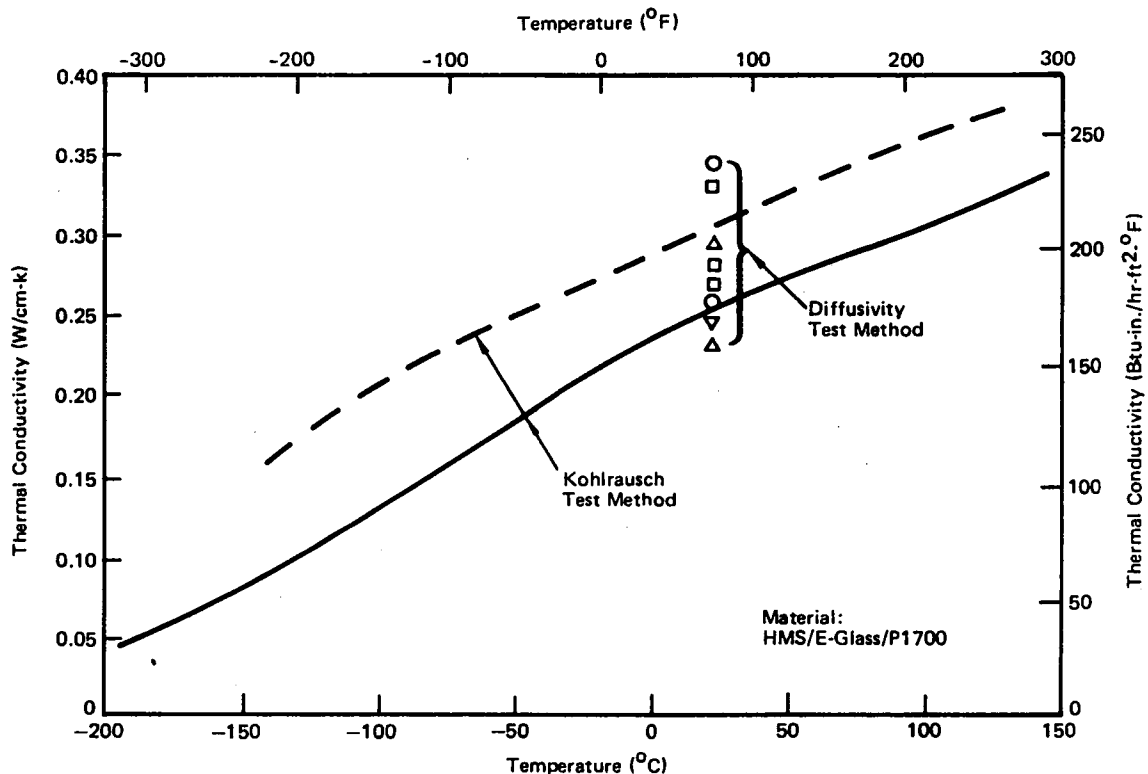


Figure 2-5. Thermal Conductivity Test Results for HMS/E-Glass/P1700 Rod Material.

values obtained by the thermal diffusivity method. The results obtained from the Kohlrausch method fall within the range of values determined from thermal diffusivity. The rather wide range of diffusivity values may be due to the non-uniform distribution of fibers in the material. Although the heterogeneity of the material may lead to differences in thermal conductivity, an average of the two Kohlrausch results represents the thermal conductivity of the material. The Kohlrausch results also show that thermal conductivity increases with increasing temperature.

The room temperature thermal conductivity of aluminum is 1.71 W/cm-K (1,188 BTU-in./Hr/Ft<sup>2</sup>/°F). The data presented in Figure 2-5 indicates that rod stock longitudinal thermal conductivity is approximately one-sixth that of aluminum.

#### 2.1.6 Electrical Conductivity

Electrical conductivity of graphite/glass polysulfone rod material was determined through measurement of its electrical resistance. The apparatus used to determine electrical conductivity consisted of a constant current power supply, a Keithley model 179 Multimeter and two gold plated contacts. To make an electrical resistance measurement, the constant current power supply was adjusted so that a 100 mA current was measured by the Keithly Model 179 Multimeter when the leads were attached with clips to the extreme ends of the graphite/glass polysulfone rod. The gold-plated contacts were adjusted to be 10.0 cm apart and the rod was pressed against them until a steady voltage was read on the multimeter. The measurement was repeated along the length of the rod at 10 cm intervals.

Table 2-9 gives a summary of electrical conductivity values for two rods of graphite/glass polysulfone. The measured voltage drop showed a variation of

Table 2-9  
ELECTRICAL RESISTIVITY OF HMS/E-GLASS/P1700 RODS

Sample No.	Resistivity, $\mu\Omega$ -cm		
	Minimum Value	Maximum Value	Average
1	2,278	2,936	2,607
2	2,060	2,980	2,520



of roughly  $\pm 25\%$  as the rod was rotated so that different areas touched the gold contacts. This is apparently due to non-uniform distribution of graphite and glass fibers in the matrix. The highest and lowest resistance values for each 10 cm length of rod as well as the average resistance for each rod are given in Table 2-9.

The voltage drop across each 10 cm length of rod was approximately 0.05V, so the total power dissipated over a 10 cm length was:

$$W = iE$$

$$= (0.100A)(0.05V) = 5 \times 10^{-3}W \quad (2-5)$$

where:

W = power (watts)  
i = current (amperes)  
E = voltage (volts)

Under the conditions used, heating of the rod was negligible.

Table 2-10 presents a comparison of the graphite/glass polysulfone electrical conductivity results with those of many other metallic and nonmetallic materials. These data indicate that the resistivity of HMS/E-glass/P1700 rod material is very similar to that of graphite/epoxy.

Table 2-10  
COMPARISON OF ELECTRICAL CONDUCTIVITY FOR VARIOUS MATERIALS

<u>Material</u>	<u>Resistivity (microhm-cm)</u>
HMS/E-Glass/P1700	2,564
Graphite/Epoxy	3,000
S-Glass/Epoxy	10 <sup>20</sup>
Steel	12.7
Aluminum	3.8
Titanium	171

## 2.2 MECHANICAL PROPERTIES

The results of tests accomplished to determine the mechanical properties of HMS/E-Glass/P1700 rod material at room and elevated temperatures are summarized in Table 2-11 and discussed briefly below.

**Table 2-11**  
**SUMMARY OF MECHANICAL PROPERTIES OF HMS/E-GLASS/P1700 PULTRUDED ROD**

Temperature	Tensile Strength MN/m <sup>2</sup> (psi)	Tensile Modulus GN/m <sup>2</sup> (msi)	Compression Strength MN/m <sup>2</sup> (psi)	Compression Modulus GN/m <sup>2</sup> (msi)	Torsional Modulus GN/m <sup>2</sup> (msi)	Flexural Strength MN/m <sup>2</sup> (psi)	Flexural Modulus GN/m <sup>2</sup> (msi)
Room Temperature	852.9 (123,720)	152.2 (22.08)	343.2 (49,780)	151.7 (22.0)	3.58 (0.52)	709.8 (102,960)	162.2 (18.3)
121°C (250°F)	887.5 (128,732)	152.5 (22.12)	—	150.8 (21.9)	—	622.7 (90,330)	109.6 (15.9)

### 2.2.1 Tensile Strength and Extensional Modulus

Tests to evaluate tensile strength and elastic modulus of HMS/E-Glass/P1700 2.36 mm (0.093 in.) diameter round rod material at room temperature and at 121°C (250°F) were accomplished. Sample configuration is shown in Figure 2-6, and the test results are presented in Table 2-12. Tensile strength and modulus data show essentially no change in short-time tensile properties between room temperature conditions and 121°C (250°F) for the hybrid HMS/E-glass/P1700 rod material. The slightly higher average values at 121°C (4 percent for ultimate tensile strength and 0.2 percent for modulus) are attributed to normal scatter in the test data.

### 2.2.2 Compression Strength and Extensional Modulus

The compression strength sample configurations for ultimate strength and modulus tests are shown in Figure 2-7. The longer configuration for the modulus samples was required to allow attachment of an extensometer. As expected, the compression strength of the rods was significantly less than the tensile strength because of the dominant influence of the lower strength resin matrix in compression. However, the ultimate compression strength shown in Table 2-13 (average of 343.2 MN/m<sup>2</sup> or 49,780 psi) is not critical since an efficiently designed geodetic beam experiences elastic buckling at approximately one-fifth of the compression ultimate stress. For example, the Phase I program feasibility test cylinder with encapsulated joints experienced elastic buckling at a stress level of approximately 61.5 MN/m<sup>2</sup> (8,920 psi). Compression strength and modulus data obtained are summarized in Table 2-13.

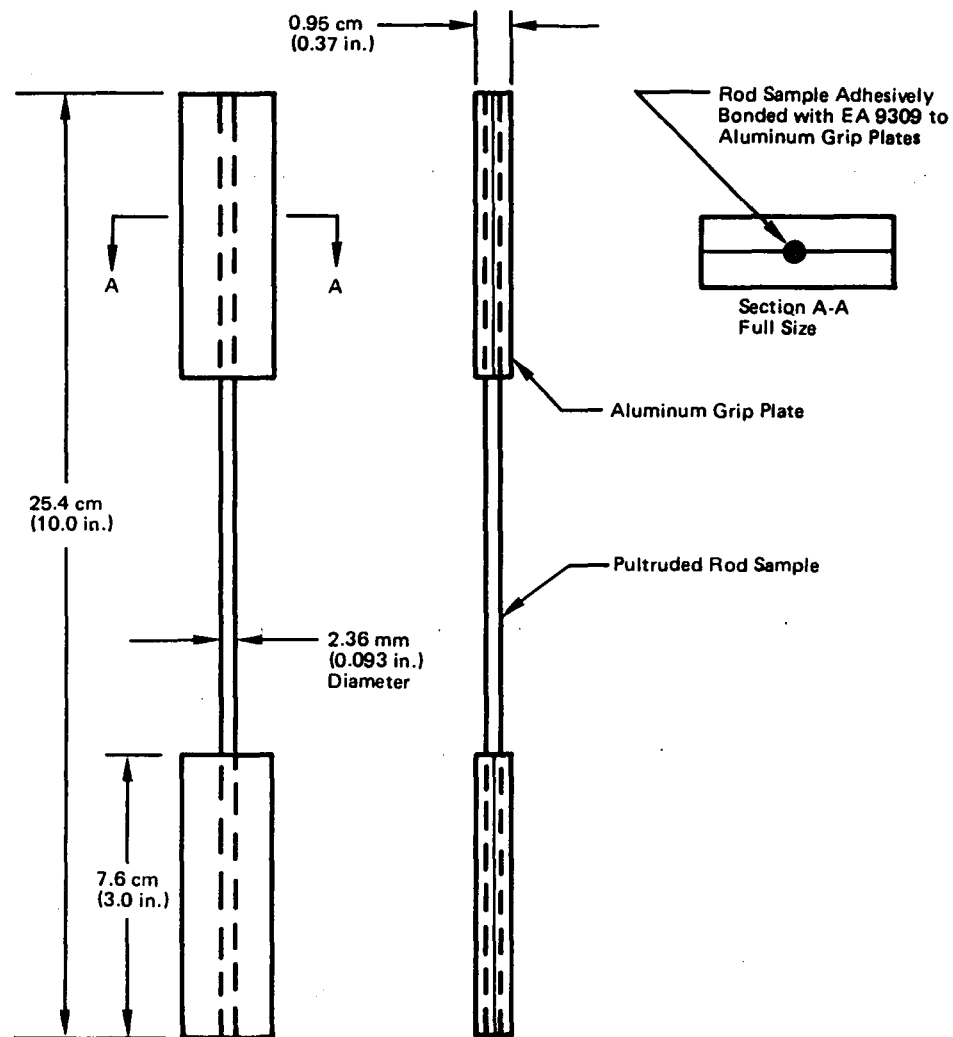


Figure 2-6. Tensile Test Sample Configuration for HMS/E-Glass/  
P1700 Pultruded Rods.

**Table 2-12**  
**TENSILE PROPERTIES OF HMS/E-GLASS/P1700 PULTRUDED ROD**

	Sample No.	Ultimate Tensile Strength, FTJ, MN/m <sup>2</sup> (psi)		Extensional Modulus, GN/m <sup>2</sup> (psi x 10 <sup>-6</sup> )	
Room Temp	1	824.4	(119,585)	148.2	(21.49)
	2	964.4	(139,890)	142.1	(20.61)
	3 <sup>(1)</sup>	—	—	143.3	(20.78)
	4	855.5	(124,095)	159.5	(23.14)
	5	881.5	(127,860)	185.2	(26.86)
	6	902.2	(130,865)	152.5	(22.12)
	7	689.6	(100,030)	134.7	(19.54)
	Avg	852.9	(123,720)	152.2	(22.08)
121°C (250°F)	8	829.6	(120,335)	152.5	(22.12)
	9	849.4	(123,215)	151.9	(22.04)
	10	989.6	(143,550)	167.5	(24.30)
	11 <sup>(1)</sup>	—	—	148.7	(21.57)
	12	881.3	(127,830)	141.9	(20.59)
	Avg	887.5	(128,732)	152.5	(22.12)

(1) Specimen Pulled Out From End Fitting; No Valid Ultimate Strength Achieved

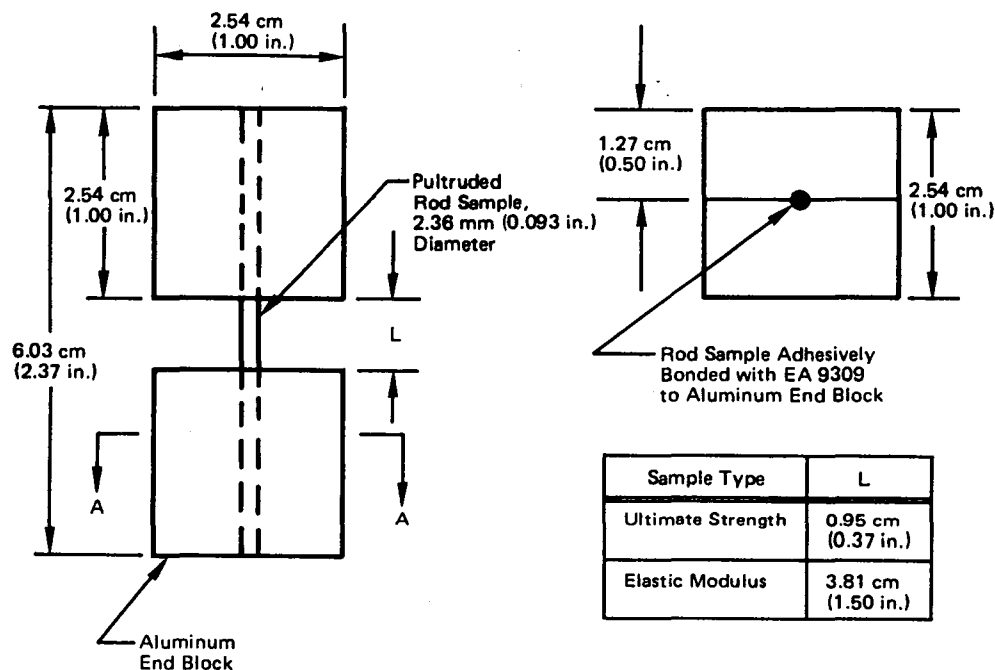


Figure 2-7. Compression Test Sample Configuration for HMS/E-Glass/P1700 Pultruded Rods.

**Table 2-13**  
**COMPRESSION PROPERTIES OF HMS/E-GLASS/P1700 PULTRUDED ROD**

	Sample No.	Ultimate Compression Strength, $F_{CU}$ , $MN/m^2$ (psi)		Extensional Modulus, $GN/m^2$ (psi $\times 10^6$ )	
Room Temperature	1	396.0	(57,440)	—	
	2	290.4	(42,120)	—	
	3	—		159.9	(23.2)
	4	—		131.0	(19.0)
	5	—		150.3	(21.8)
	6	—		162.0	(23.5)
				155.1	(22.5)
	Avg	343.2	(49,780)	151.7	(22.0)
121°C (250°F)	7	—		143.4	(20.8)
	8	—		155.8	(22.6)
	9	—		159.3	(23.1)
	10	—		144.8	(21.0)
	Avg			150.8	(21.9)

### 2.2.3 Torsional Modulus Characteristics

Torsional deflection tests were conducted at room temperature with sample rods to determine the elastic shear modulus,  $G_T$ , under torsional loads. Rod samples approximately 35.6 cm (14 in.) long were used in combination with a special torsion loading head in an Instron test machine. A 25.4 cm (10 in.) free length between heads was used. Modulus values derived from these tests are presented in Table 2-14. No failures were recorded in the tests due to the highly flexible characteristics of the small diameter rods. Maximum rotational deflections were approximately 265 degrees, at which point the test rod exhibited a torsional buckling behavior near its center. Since this degree of torsional deflection is substantially larger than would be experienced in the geodetic beam prior to elastic buckling of the wall, failure of the rods was not pursued.

**Table 2-14**  
**TORSIONAL ELASTIC MODULUS OF PULTRUDED HMS/E-GLASS/P1700 ROD**

Sample No.	Torsional Shear Modulus $GN/m^2$ (psi $\times 10^{-5}$ )
1	3.13 (4.54)
2	4.28 (6.21)
3	3.61 (5.24)
4	3.30 (4.79)
Avg	3.58 (5.20)

NOTE: All samples run at room temperature.

## 2.2.4 Flexure Strength and Modulus

Flexure tests of HMS/E-glass/P1700 rod stock were conducted at both room temperature and 121°C (250°F). Data from flexural tests are shown in Table 2-15. These data indicate approximately a 13% reduction in flexure strength and flexure modulus at 121°C (230°F).

Table 2-15  
FLEXURAL PROPERTIES OF HMS/E-GLASS/P1700 PULTRUDED RODS

	Sample No.	Flexural Ultimate Strength MN/m <sup>2</sup> (psi)		Flexural Modulus GN/m <sup>2</sup> (psi x 10 <sup>6</sup> )	
Room Temp	1	649.3	( 94,180)	117.2	(17.0)
	2	500.5	( 72,600)	118.0	(17.4)
	3	730.5	(105,960)	119.3	(17.3)
	4	701.7	(101,790)	128.2	(18.6)
	5	791.3	(114,780)	133.7	(19.4)
	6	663.4	( 96,230)	135.1	(19.6)
	7	838.1	(121,570)	130.3	(18.9)
	8	785.7	(113,970)	115.8	(16.8)
	9	777.8	(112,820)	127.5	(18.5)
	10	659.5	( 95,660)	136.5	(19.8)
	Avg	709.8	(102,956)	126.2	(18.3)
121°C (250°F)	11	519.4	( 75,345)	106.2	(15.4)
	12	604.5	( 87,685)	108.2	(15.7)
	13	651.0	( 94,430)	120.0	(17.4)
	14	621.4	( 90,135)	111.0	(16.1)
	15	587.6	( 85,230)	117.9	(17.1)
	16	752.4	(109,145)	93.8	(13.6)
	Avg	622.7	( 90,328)	109.6	(15.9)

## 2.2.5 Strength Degradation

Mechanical property testing of HMS/E-glass/P1700 rod material which had been subjected to simulated short-duration space exposure was accomplished to assess the effects on rod material strength and stiffness. Both bare and coated (S13G/L0) rod specimens, six each, of 2.36 mm (0.093 inch) diameter HMS/E-glass/P1700 rods were subjected to simulated space vacuum exposure at 150°F for 30 days and then tested at room temperature to assess degradation of tensile and flexure strength and modulus. Mechanical property test results are presented in Table 2-16.

Table 2-16 also summarizes room temperature mechanical property data previously presented in Tables 2-12 and 2-15 for similar rod material which had not been subjected to simulated space exposure prior to mechanical property testing.

Table 2.16  
MECHANICAL PROPERTY TESTS RESULTS FOR HMS/E-GLASS/P1700 ROD  
MATERIAL SUBJECTED TO SIMULATED SPACE EXPOSURE

Mechanical Property	Simulated Space Environment Exposure		Bare (Uncoated) Material (Ref)
	Bare (Uncoated) Material	Coated (S13G/LO) Material	
Tensile Strength — MN/m <sup>2</sup> (PSI x 10 <sup>-3</sup> )	894.2 (129.7)	922.4 (133.8)	852.8 (123.7)
Tensile Modulus — GN/m <sup>2</sup> (PSI x 10 <sup>-3</sup> )	156.5 (22.7)	142.7 (20.7)	152.4 (22.1)
Flexure Strength — MN/m <sup>2</sup> (PSI x 10 <sup>-6</sup> )	694.2 (100.7)	707.3 (102.6)	709.4 (102.9)
Flexure Modulus — GN/m <sup>2</sup> (PSI x 10 <sup>-6</sup> )	139.9 (20.3)	127.5 (18.5)	126.2 (18.3)

These results indicate, considering the scatter in the test data, that tensile and flexure modulus of bare-material specimens is not significantly affected by short-time elevated temperature, simulated space exposure. Comparison of results for coated and bare-material specimens indicate no significant difference in flexure or tensile properties. These results generally indicate that short-duration space exposure at elevated temperature has no significant effects on HMS/E-glass/P1700 flexure or tensile material properties.

#### 2.2.6 Storage Induced Permanent Set of Rod Stock

Geodetic beam rod stock material will be stored in cylindrical canisters prior to being used for the fabrication of geodetic structures. Because of the effect of rib curvature imperfections on the load carrying capability of lattice geodetic structures, permanent set (bowing) of rod stock produced by canister storage is very detrimental.

Simulated storage testing of 2.36 mm (0.093 in.) diameter rod stock was conducted over a period of nine months. Rod stock material was elastically coiled to a radius of 38.1 cm (15.0 in), producing a rod longitudinal strain of approximately 0.25%, simulating a relatively severe storage condition, i.e., storage of rod stock at a strain level equal to one-half of the rod stock failure strain. After nine months, the rod stock was removed from the test fixture and measured on a flat surface to establish the magnitude of permanent deformation. No permanent deformation, or set, of the tested rod stock was observed.

### 2.3 REFERENCES FOR SECTION 2

- 2-1. Development of a Composite Geodetic Structure for Space Construction,  
Phase 1A Final Report, MDC G8456, 31 January 1980.



### Section 3

#### PARAMETER TESTS

The objective of this Phase II task was to fabricate and test structures to evaluate the structural parameters and characteristics that are required for a full understanding of the structural capabilities of the type of geodetic structure under development. Two geodetic structures were analyzed, designed, fabricated, instrumented and tested to evaluate structural parameters and characteristics in order to gain a greater understanding of the capabilities of composite geodetic structures. A geodetic parameter cylinder was designed so that three different sizes of longitudinal rods were used, with each of these circumferential segments of the cylinder containing one of the three rod sizes. Axial load tests of each trisector of this parameter cylinder were used to generate data needed to design minimum weight geodetic structures by varying the sizes of longitudinal and helical rod members. The second geodetic test article was an end closure structure consisting of a lattice cone closeout joined to a short cylindrical geodetic beam segment. The feasibility of this end closure design was established by axial compression testing of the combined test article. The results of design/analysis, fabrication and testing activities associated with the parameter tests are described in the sections that follow.

#### 3.1 GEODETIC PARAMETER CYLINDER TESTS

As part of the parameter tests, a geodetic test cylinder having three ratios of longitudinal-to-helical rod stock size was designed, fabricated and tested. All helicals were the same size while three different sizes of longitudinals were used. Each of three circumferential sectors, i.e., trisectors of the cylinder, had a different size of longitudinal rod. In this manner, the global stiffness effect of the helical mesh was different in each trisector and the effects on the local failure of the longitudinals and the load carrying capability of geodetic structures could be evaluated. Axial compression loading tests (3) with the loading isolated on one trisector at a time were accomplished. Results of parameter cylinder design, fabrication and testing activities are presented below.

### 3.1.1 Preliminary Sizing and Design of the Geodetic Parameter Cylinder

Initial analysis to establish parameter test cylinder longitudinal rod sizes were made early in the Phase II program. Factors considered in evaluating the different longitudinal sizes included (1) correlation of cylinder test data from Phase I tests, (2) dimensional tolerances of the pultruded rods, and (3) load spillover effects from one sector to another. To enhance correlation with test data from the feasibility cylinder tests conducted in Phase I (Reference 3-1), a rod size for the helicals and one set of longitudinals was chosen to have the same moment of inertia (I) as those used in Phase I feasibility test cylinders. Also, cylinder diameter (1.44 m) and number of longitudinals (50) were maintained the same as used in the feasibility cylinders. Thus, local buckling capability in one sector of the cylinder was approximately equivalent, assuming comparable rod material flexure modulus, to that of the feasibility cylinders and provided a basis for comparison with Phase I test results. The rod diameter for the helicals and one set of longitudinals were chosen as 2.36 mm (0.093 in.) to provide the same moment of inertia as the 2.08 x 2.08 mm (0.082 x 0.082 in.) square rods previously used. A smaller longitudinal rod was considered for one of the other sectors and a larger longitudinal rod size was considered for the third sector.

The diametral tolerance on pultruded rods was a second consideration since wide variations in pultruded rod sizes would necessitate a wider spread in nominal rod size. This would be required to prevent rods in adjacent sectors from having nearly equal stiffness and thus causing local buckling at very nearly equal load intensities. A review of past measurements made on round pultruded rods with a nominal diameter of 2.36 mm (0.093 in.) showed a tolerance range of approximately -0.0254 mm (-0.001 in.) to +0.0508 mm (+0.002 in.). Based on a total tolerance range of approximately 0.076 mm (0.003 in.), a minimum difference in rod diameters for adjacent sectors of 0.152 mm (0.006 in.) was established.

Load spillover effects for the adjacent sectors having the maximum and minimum size rods were studied to determine if premature buckling in the sector with smaller longitudinals would require sector isolation. Study results indicated that a larger spread in rod diameter between the three different sizes

of longitudinals, than the 0.152 mm (0.006 in.) minimum identified above, was required. A diameter difference of 0.25 mm (0.010 in.) was selected to guarantee that pultruded rod tolerance build-up would not cause nearly equal failure loads to occur on adjoining sectors. Thus, the final diameter of longitudinal rod stock in each of the three segments of the geodetic parameter cylinder was established as 2.11 mm (0.083 in.), 2.36 mm (0.093 in.) and 2.62 mm (0.103 in.), while all helical rod stock had a diameter of 2.36 mm (0.093 in.).

Preliminary structural analysis of geodetic cylinders with various ratios of longitudinal-to-helical rod stock diameter was accomplished to establish the relationship between geodetic cylinder buckling load carrying capability and structure weight using the analysis code developed by M. S. Anderson (Reference 3-2) and discussed in Section 4.0. Buckling failure load analysis results for cylinders with three different sizes of longitudinals are presented in Figure 3-1. Analysis results established that a nominal rod diameter difference

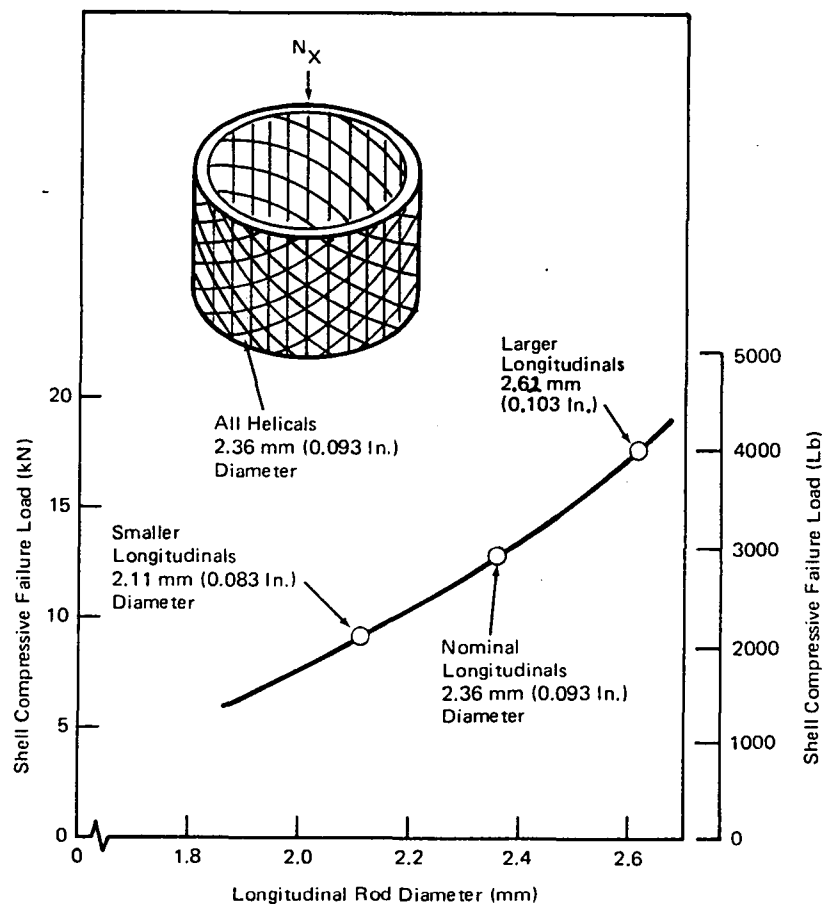


Figure 3-1. Compressive Failure Load vs Longitudinal Rod Diameter.

of 0.25 mm (0.010 in.) provides a predicted buckling load of 12,960 N (2,914 lb.) for a cylinder with 2.36 mm (0.093 in.) diameter longitudinals, a buckling load of 17,390 N (3,909 lb.) for a cylinder with 2.62 mm (0.103 in.) diameter longitudinals and a load of 9,510 N (2,138 lb.) for a cylinder with 2.11 mm (0.083 in.) diameter longitudinal rods. Failure loads corresponded to those expected from a local rib buckling failure mode. These results indicate that significant increases in load carrying capability (approximately 35%) can be achieved with small increases (approximately 7%) in weight for cylindrical geodetic structures and that the rib buckling mode still dominates as the shell buckling failure mode.

Final structural analysis of the geodetic parameter cylinder, including pretest prediction of buckling failure loads for each of the three sectors of the cylinder, was accomplished using Anderson's code and the results of rod material physical property testing and mechanical property tests which were used to fabricate the parameter cylinder. Physical property characterization tests to determine density, fiber content and resin content were accomplished for the rod material as received from CEC. Test results, shown in Table 3-1, indicate that the material had a 7% higher resin content than that exhibited by the rod material characterized in Section 2.0 (see Table 2-4). The average

Table 3-1  
DENSITY, FIBER CONTENT, AND RESIN CONTENT OF ROD STOCK FOR PARAMETER CYLINDER

Sample No.	Rod Diameter mm (in.)	Density (kg/m <sup>3</sup> )	Fiber Content (Volume %)		Resin Content (Weight %)	Voids (Volume %)
			HMS	E-Glass		
1	2.36 (0.093)	1500	35.37	9.50	39.82	6.96
2	2.36 (0.093)	1510	31.90	13.66	37.51	8.75
3	2.36 (0.093)	1470	34.86	10.33	38.07	9.68
4	2.36 (0.093)	1470	35.25	10.10	37.71	9.95
5	2.11 (0.083)	1490	32.78	14.43	34.26	11.62
6	2.11 (0.083)	1500	31.24	13.75	37.76	9.33
7	2.62 (0.103)	1580	35.83	14.47	34.33	5.96
AVG		1503	33.89	12.32	37.07	8.89

density of the rod material was therefore lower by approximately 5% as was the HMS and E-glass fiber contents. Because of the lower fiber content

compared to the material characterized in Section 2, the flexure modulus as determined from four-point bending tests, was approximately  $113.5 \text{ GN/M}^2$  ( $16.5 \times 10^6 \text{ psi}$ ), i.e., approximately 10% lower than the flexure modulus of the material characterized in Section 2. Based on analysis results for complete geodetic cylinders from Anderson's code, using this slightly lower flexure modulus, the predicted rib buckling failure loads for each sector of the parameter cylinder were 2916 N (655 lb.), 3974 N (894 lb.) and 5013 N (1,127 lb.), respectively. These loads are approximately one-third of the cylinder buckling load levels presented above, since only approximately one-third of the parameter cylinder was loaded during any of the three axial load tests. A discussion of parameter cylinder fabrication and testing activities follows.

### 3.1.2 Fabrication

Assembly of the geodetic parameter cylinder was accomplished on the same tooling used for the Phase I program feasibility test cylinder fabrication (Reference 3-1). This tooling and the geodetic parameter cylinder are described in Figure 3-2. The HMS/E-glass/PI700 rod stock for the cylinder was fabricated by the CEC and all nodal joints were encapsulated using Versimid 1200. After assembly, each end of the parameter test cylinder was potted on a high accuracy surface table using a Hysol two-part epoxy.

### 3.1.3 Testing

The test setup of the parameter cylinder tests (3) is presented in Figure 3-3. MDAC designed and fabricated the test fixture presented in Figure 3-3 for the testing of the Phase I feasibility test cylinders. A detailed description of how this fixture was used for accomplishing axial compressive buckling tests of the parameter cylinder is presented below.

The parameter cylinder was bonded to the lower platen, shown in Figure 3-4, with a full perimeter bond. The upper platen was positioned and balanced on the center support post with a substantial gap between the upper platen and upper edge of the specimen. After recording the balanced platen force, the gap was reduced to a nominal 2.03 mm (0.080 in.) by raising the lower platen/parameter cylinder assembly. Three rods, equally spaced around the cylinder

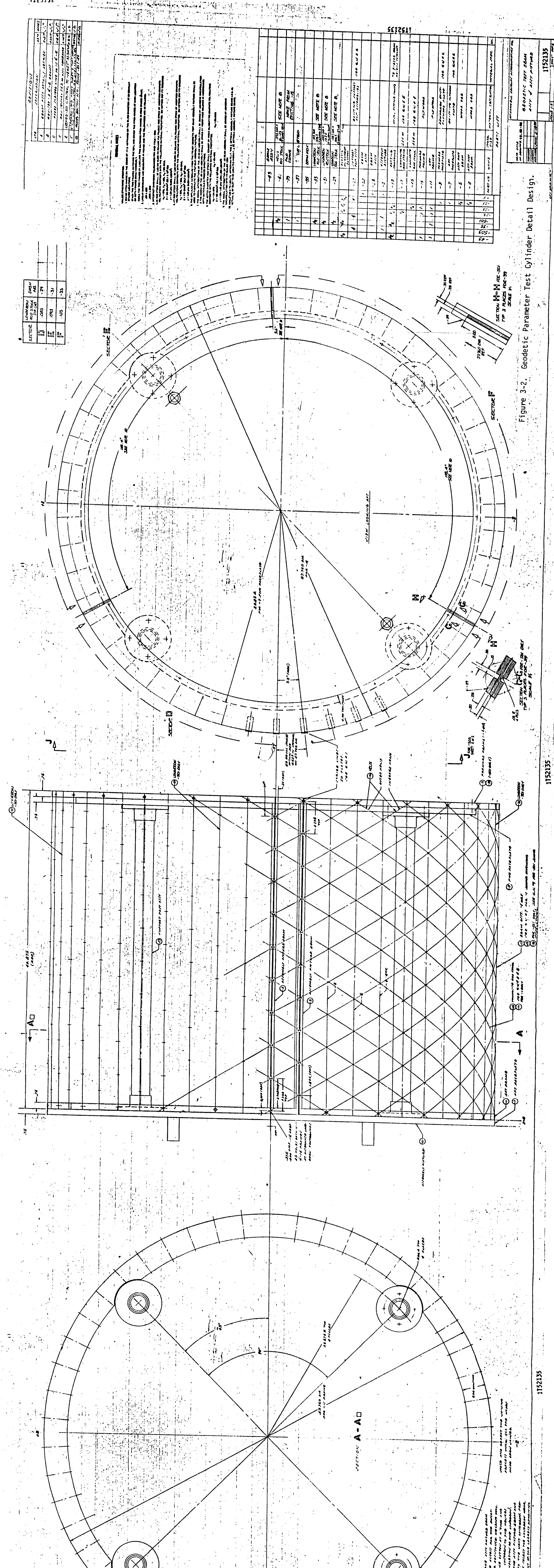
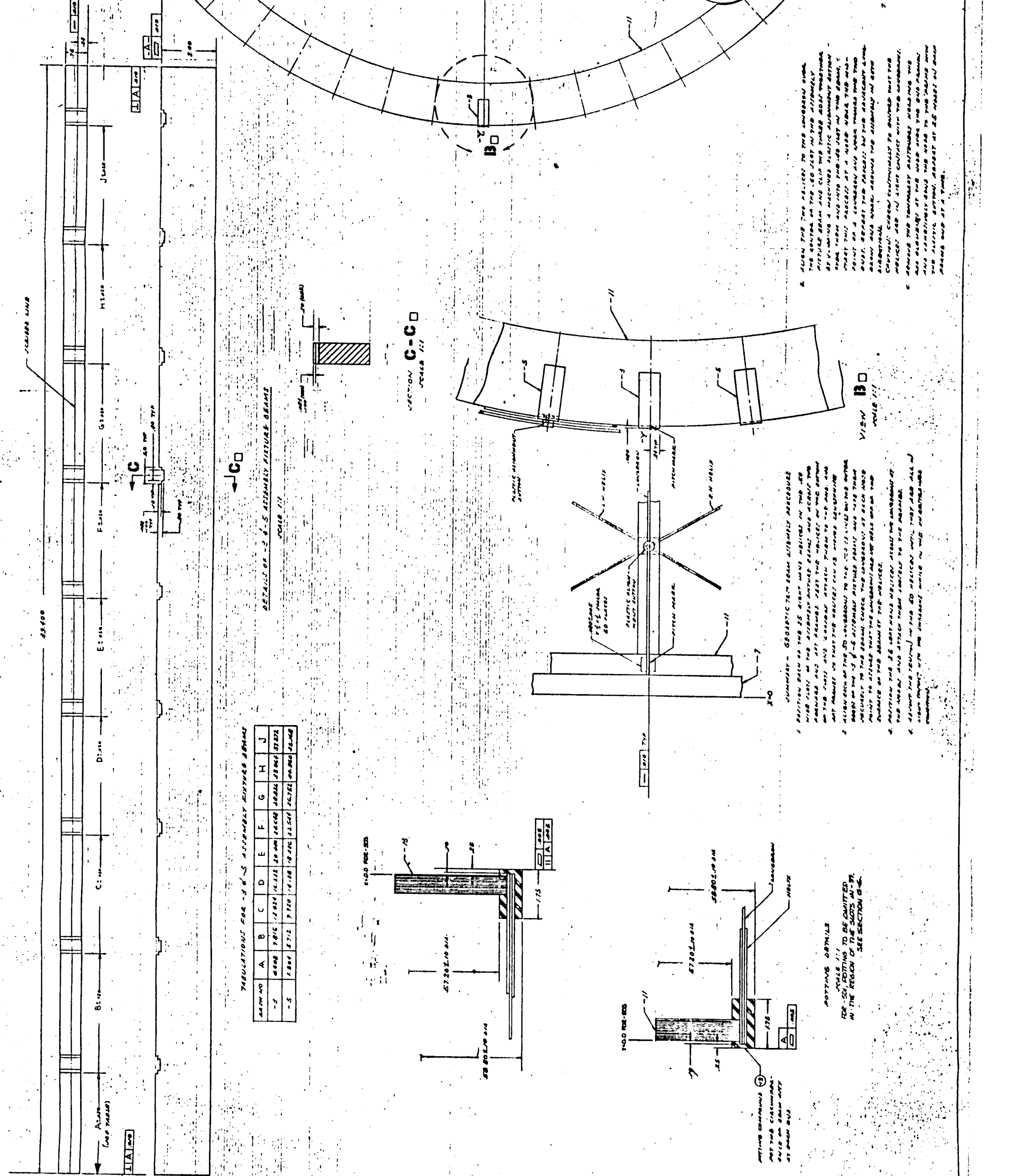


Figure 3-2. Geodetic Parameter Test Cylinder Detail Design.

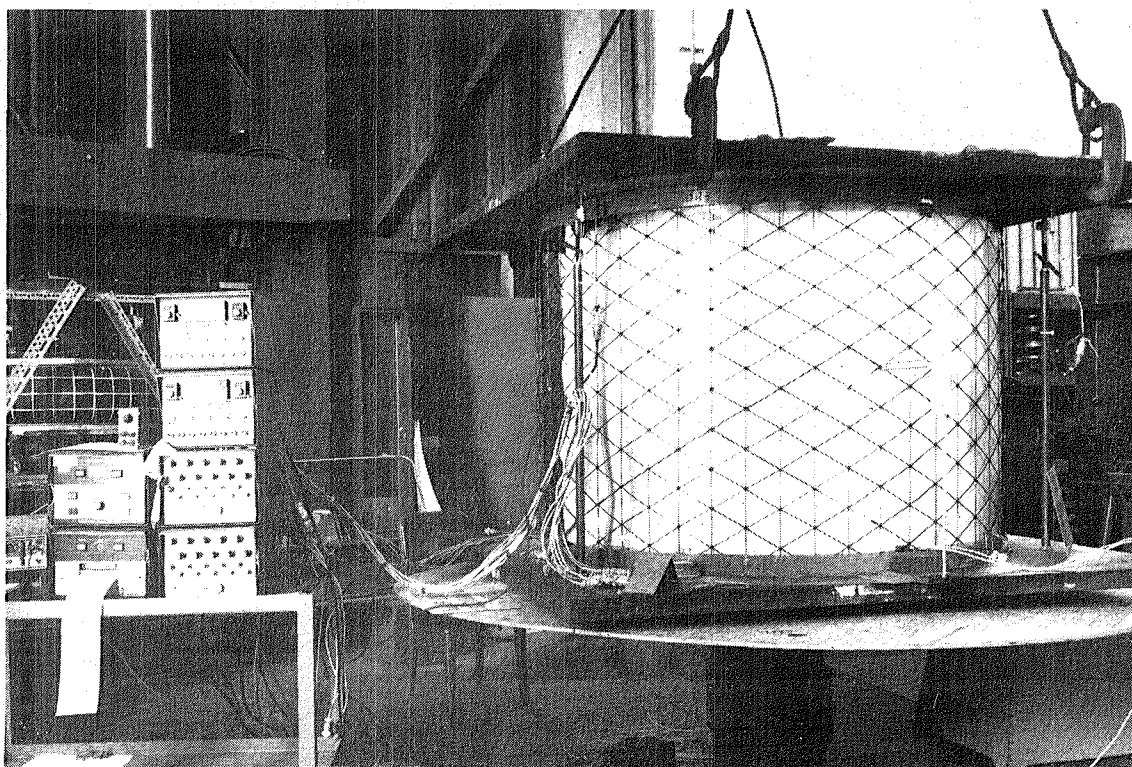


Figure 3-3. Test Setup for Parameter Cylinder Tests

perimeter, were adjusted to just contact the upper platen. These rods acted as stabilizers for maintaining a constant gap. The upper platen was removed; a bead of bonding material was placed on the upper edge of one trisector; the platen was reinstalled; the bond line, as shown in Figure 3-5, was allowed to cure, undisturbed. After cure, the two rods at the bonded sector edges were backed away from the platen 0.76 mm (0.030 in.). The rod diametrically opposite the sector was adjusted so that its integral load cell indicated zero load, but still maintained in contact with the upper platen. Deflection transducers were attached to the two gapped rods, as shown in Figure 3-4, to measure relative movement between upper and lower platen. Loading the sector was accomplished by raising the lower platen. This action gradually transferred the upper platen weight from the center support to the rod/load cell and the sector, as shown in Figure 3-5. Load distribution in the specimen was monitored by strain gages. If the distribution was unsatisfactory, then a symmetrical bias was introduced by adjusting the rod/load cell to transfer load between the sector center and edges.



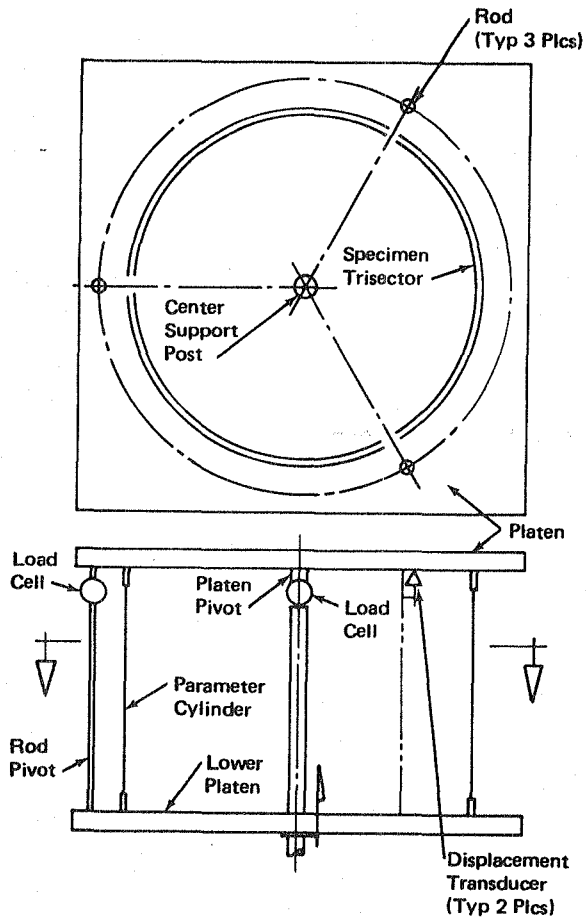


Figure 3-4. Parameter Test Cylinder and Test Fixture.

Compression tests of the parameter cylinder were conducted by loading one sector at a time in each of three tests. The cylinder end rings were notched to provide flexibility in a longitudinal direction while maintaining radial stiffness. Despite the reduced axial stiffness in the rings, some residual stiffness still remained, and therefore strain gages were located at both ends of the cylinder in each sector area to determine the extent of load spillover to adjoining areas from the loaded sector.

The parameter test cylinder was instrumented with sets of back-to-back strain gages at the center of each sector and eighteen single strain gages at the ends of the sectors to establish the magnitude of load spillover. Two displacement transducers were located at the edges of each sector for each test to measure axial displacement. The instrumentation layout for the parameter cylinder is shown in Figure 3-6.

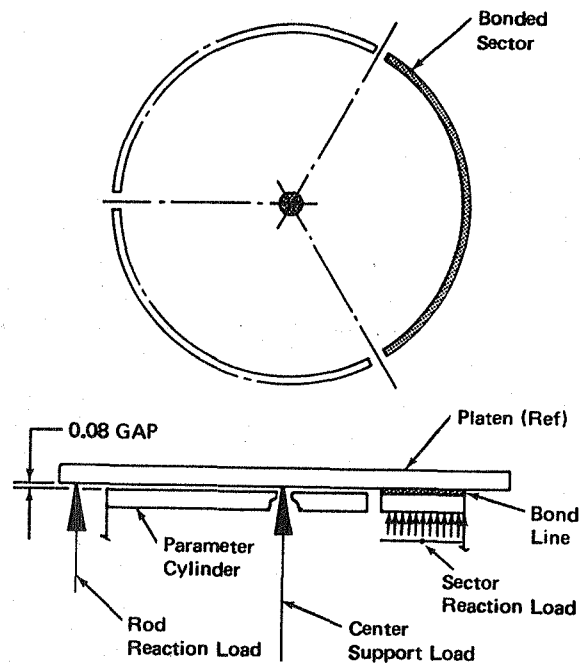
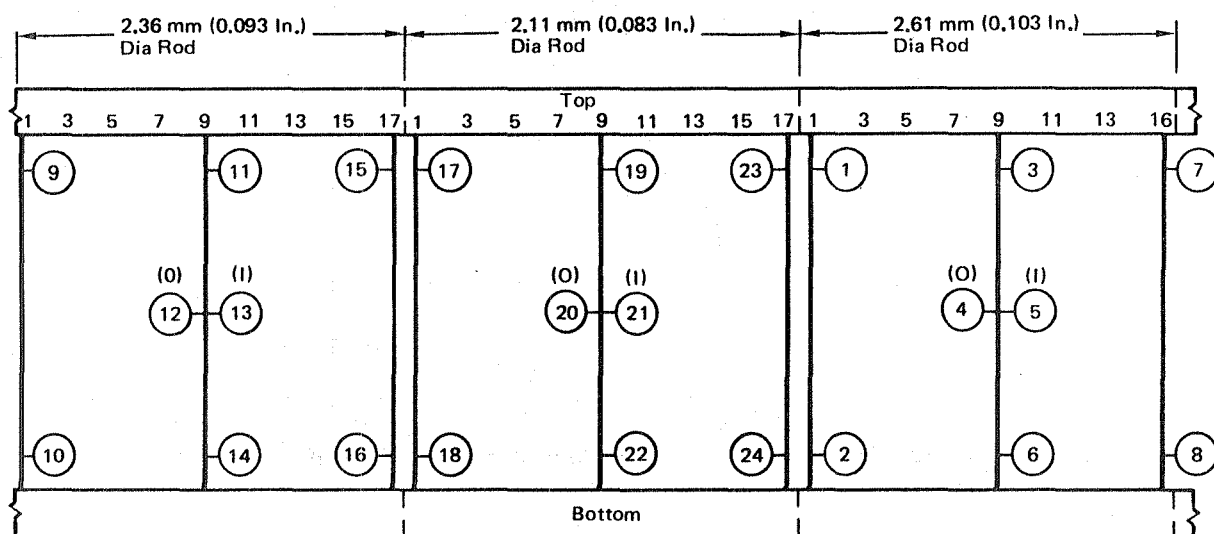


Figure 3-5. Parameter Cylinder Sector Loading Details





○ Strain Gage Location Number

Figure 3-6. Strain Gage Layout for Three Sector Parameter Test Cylinder.

The first sector tested was the one containing the 2.11 mm (0.083 in.) diameter longitudinals. The maximum load attained was 3,114 N (700 lb.), a compressive load that exceeded the predicted buckling load for this sector of 2,916 N (655 lb.) by approximately seven percent. A photograph of the buckled 2.11 mm (0.083 in.) diameter longitudinals is presented in Figure 3-7. Strain gage data for this sector are presented in Figures 3-8 through 3-10 and displacement transducer data are presented in Figure 3-11. The strain gage data presented in Figure 3-8 and the displacement

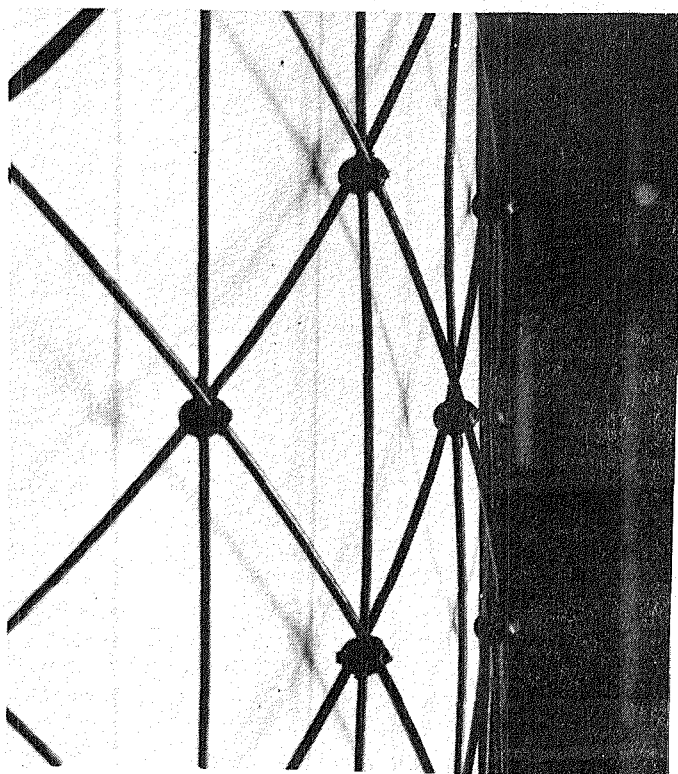


Figure 3-7. Compressive Buckling of 2.11 mm (0.083 in.) Diameter Longitudinals.

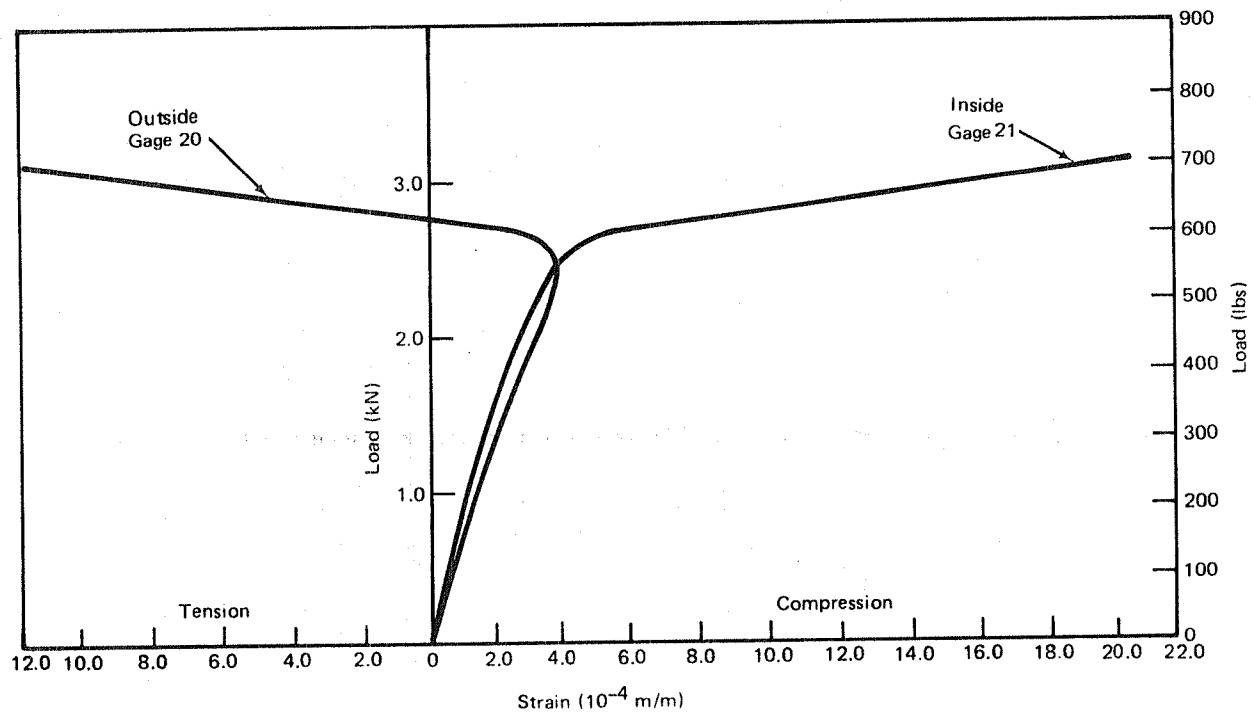


Figure 3-8. Strains Measured by Back-to-Back Gages at Center of Sector - 2.11 mm (0.083 in.) Diameter Longitudinals.

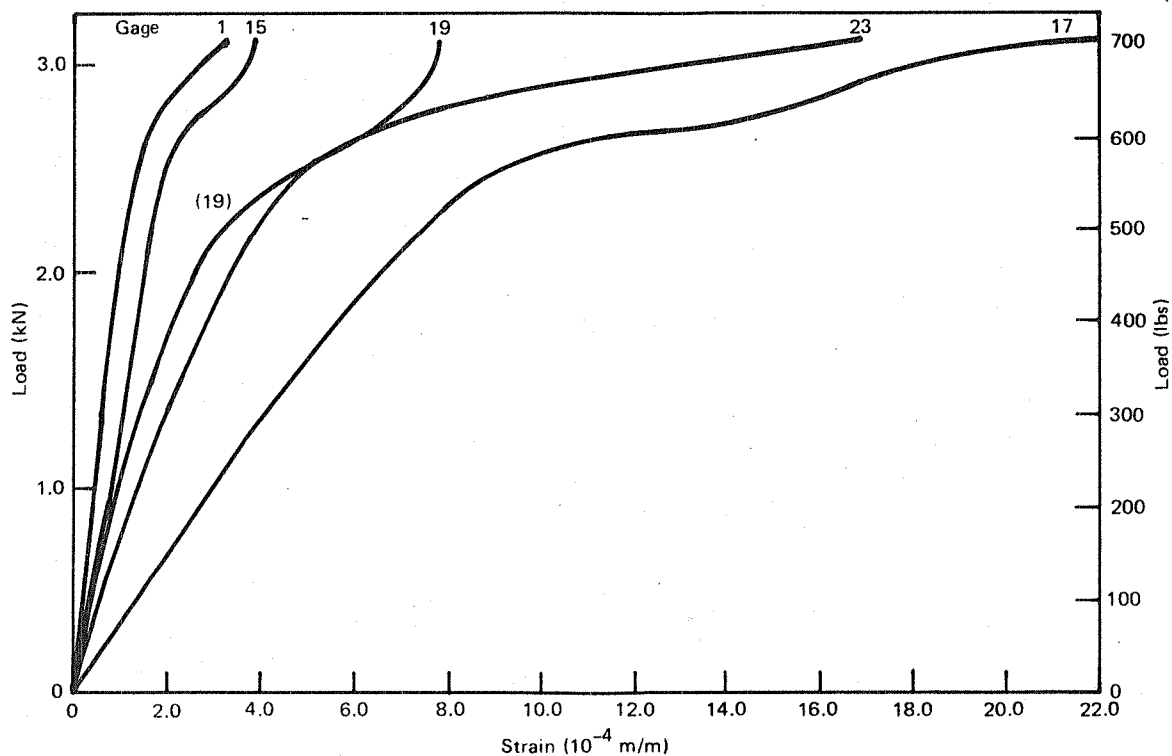


Figure 3-9. Strains Measured at Top Ends and Sides of Sector - 2.11 mm (0.083 in.) Diameter Longitudinals.

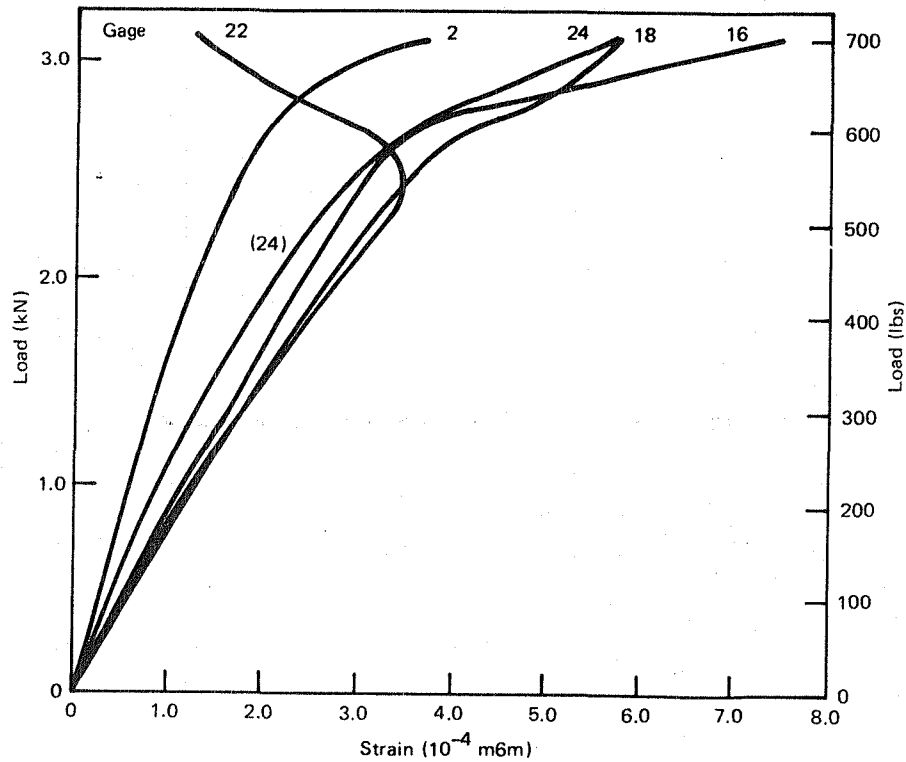


Figure 3-10. Strains Measured at Bottom Ends and Sides of Sector - 2.11 mm (0.083 in.) Diameter Longitudinals.

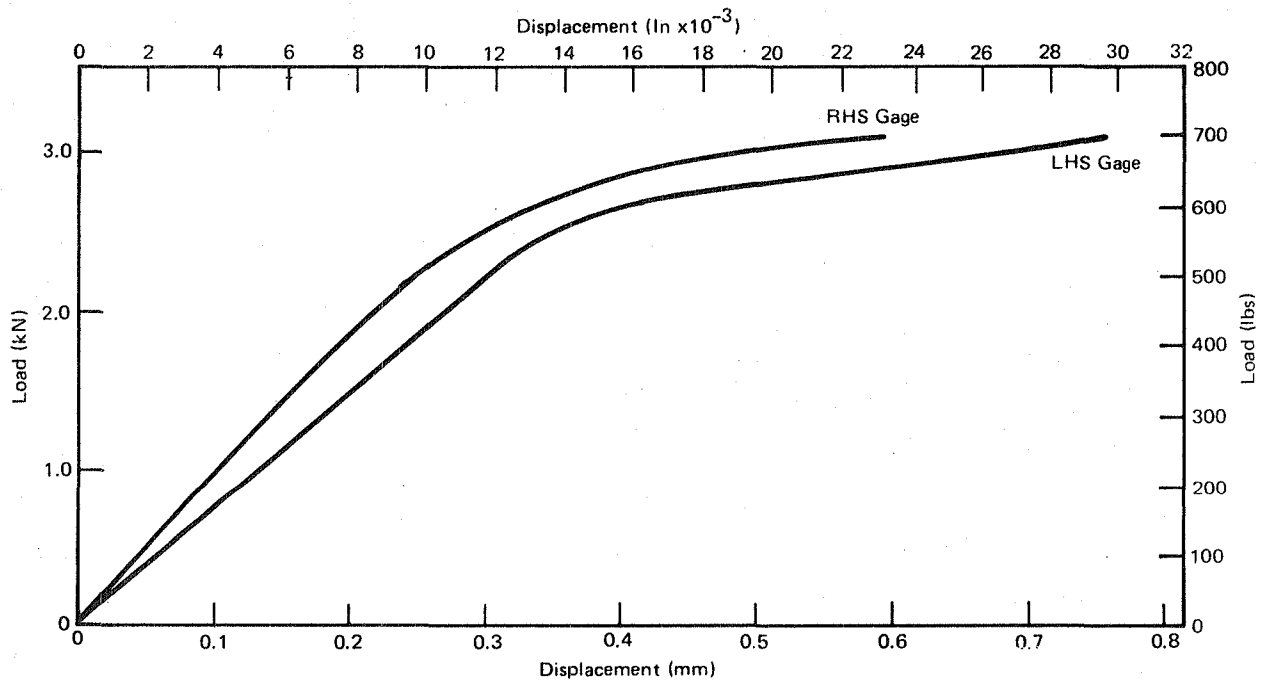


Figure 3-11. Load Versus Displacement at Edge of Sector - 2.11 mm (0.083 in.) Diameter Longitudinals.

transducer data presented in Figure 3-11 indicate the onset of buckling and the inability of the sector to carry additional axial load at approximately 3,114 N (700 lb.). The strain gage data presented in Figure 3-9 and 3-10 indicate that significant load spillover to the other sectors did not occur, i.e., the tested sector was fairly well isolated.

The second sector tested was the one containing the 2.62 mm (0.103 in.) diameter longitudinals. Figure 3-12 shows the buckle pattern for this sector, and a large buckled area is evident. Strain gage and displacement transducer data for this sector is presented in Figures 3-13 through 3-16. Strains from the back-to-back gages in the center of the sector are shown in Figure 3-13. The buckling characteristics of this sector appeared to differ from that of the sector with smaller diameter 2.11 mm (0.083 in.) longitudinals. This sector did not buckle at the center of the sector, appearing instead to deform into larger dished areas covering several nodes rather than the previously observed sinusoidal pattern in each longitudinal with points of inflection at each node. The center longitudinal in this sector was located at the edge of a large buckle pattern and thus did not show the sharp increase in strain associated with buckling as observed in previous tests (see Figure 3-8). Figures 3-14 and 3-15 show strains recorded by the gages located at the ends and sides of this sector. Isolation of this sector was not quite as good as that achieved during testing of the first sector. The maximum load attained for this sector was 4,448 N (1,000 lb.), which was 11 percent less than the predicted buckling load of 5,013 N (1,125 lb.).

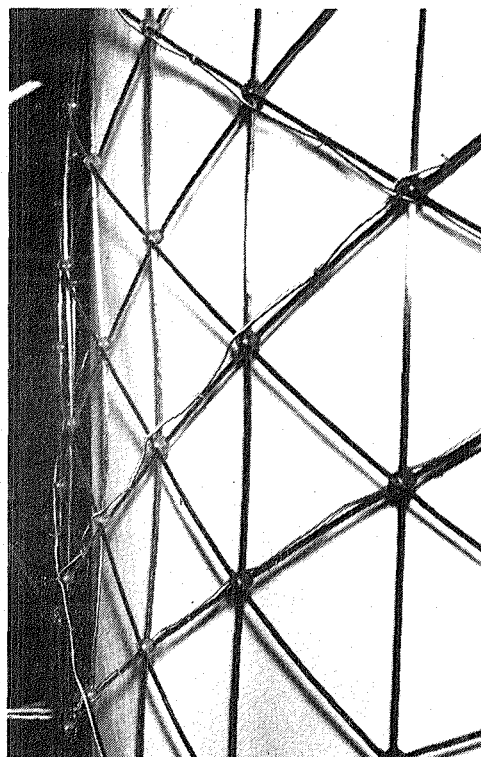


Figure 3-12. Compressive Buckling of 2.62 mm (0.103 in.) Diameter Longitudinals.

The lower than predicted load carrying capability for this sector is probably due to the fact that the buckling mode observed was a general instability mode rather than a rib buckling mode as predicted by pretest analysis.

The final sector to be tested was the one containing the 2.36 mm (0.093 in.) diameter longitudinals, i.e., the sector with longitudinals of the same moment of inertia as the Phase I feasibility test cylinders. The maximum load attained for this sector was approximately 3,652 N (821 lb.) or approximately 92 percent of the pretest predicted buckling load. Rib buckling occurred at the center of this sector (Figure 3-17). Strain gage data for this sector is presented in Figures 3-18 through 3-20 and displacement transducer data are presented in Figure 3-21. The strain gage data presented in Figures 3-19 and 3-20 indicate that this sector was fairly well isolated during testing.

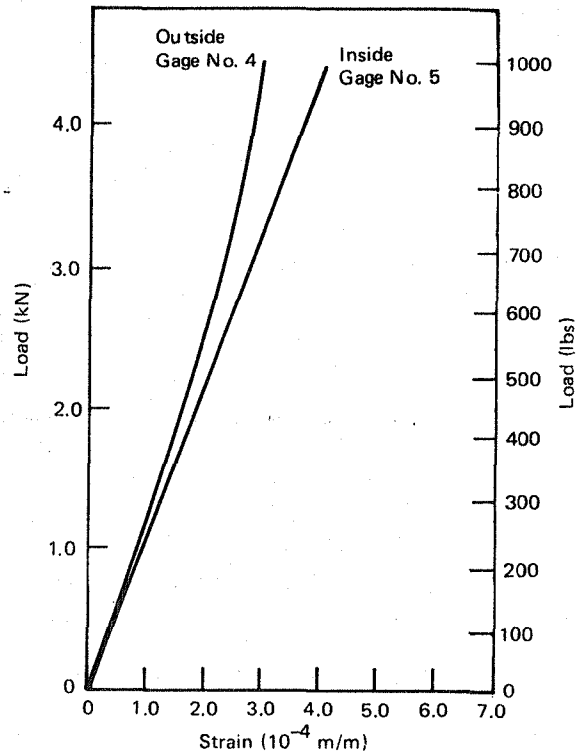


Figure 3-13. Strains Measured by Back-to-Back Gages at Center of Sector - 2.62 mm (0.103 in.) Diameter Longitudinals.

Correlation of the test data for the test sector with 2.36 mm (0.093 in.) diameter round longitudinals with test data obtained during Phase I feasibility testing of a geodetic cylinder with 2.03 x 2.03 mm (0.082 x 0.082 in.) square longitudinals, i.e., longitudinals with approximately the same moment of inertia, indicates that local rib buckling occurred at load levels of 214.8 N/rod (48.3 lb/rod) and 266.0 N/rod (59.8 lb/rod) for the test sector and Phase I feasibility test cylinder, respectively. The difference in buckling load carrying capability appears to be due primarily to the approximately 10% lower flexure modulus of the sector rod stock material. The sector rod stock material (HMS/E-glass/P1700) had a flexure modulus of  $113.75 \text{ GN/m}^2$ .

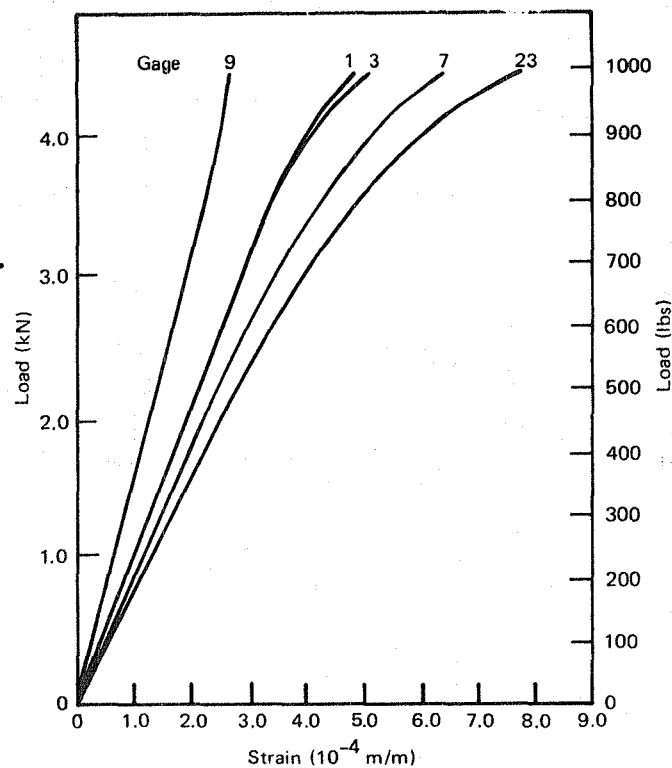


Figure 3-14. Strains Measured at Top Ends and Sides of Sector - 2.62 mm (0.103 in.) Diameter Longitudinals.

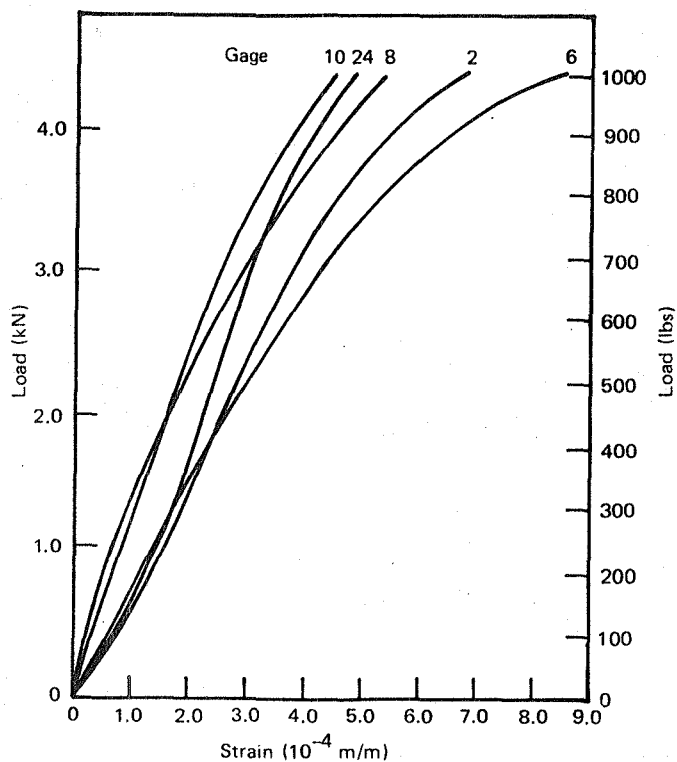


Figure 3-15. Strains Measured at Bottom Ends and Sides of Sector - 2.62 mm (0.103 in.) Diameter Longitudinals.

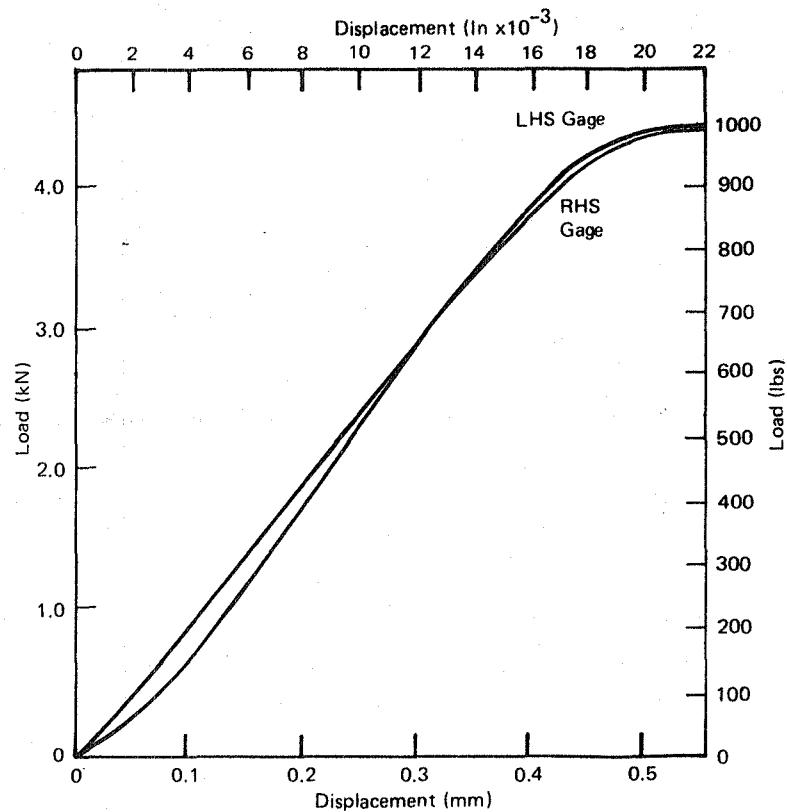


Figure 3-16. Load Versus Displacement at Edge of Sector - 2.62 mm (0.103 in.) Diameter Longitudinals.

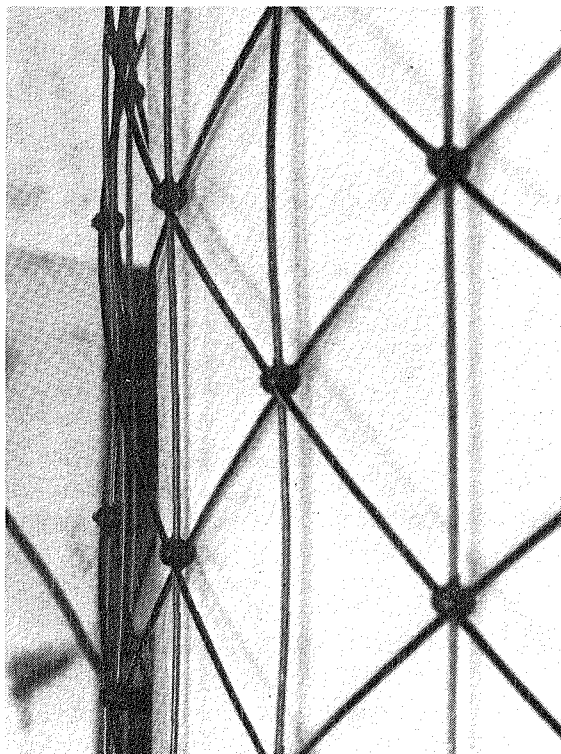


Figure 3-17. Compressive Buckling of 2.36 mm (0.093 in.) Diameter Longitudinals.

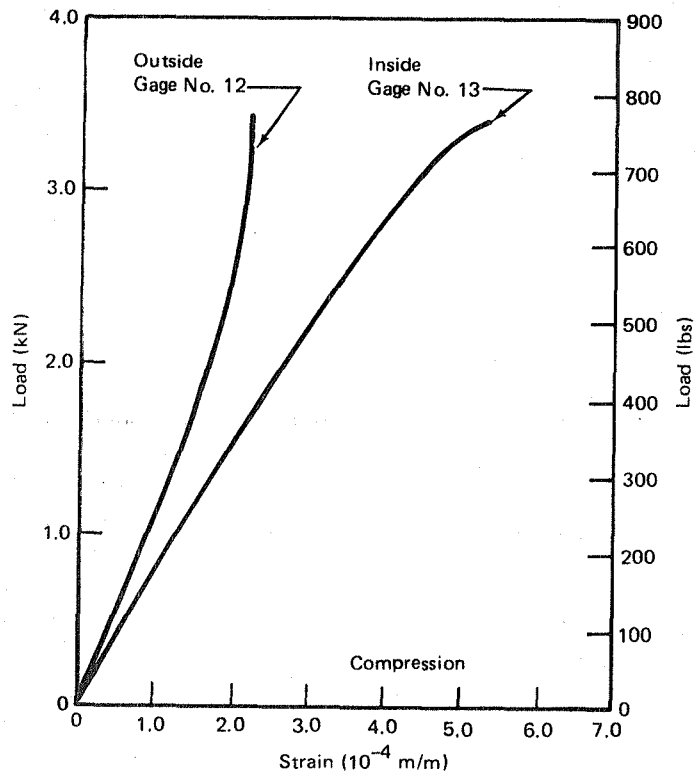


Figure 3-18. Strains Measured by Back-to-Back Gages at Center of Sector - 2.36 mm (0.093 in.) Diameter Longitudinals.

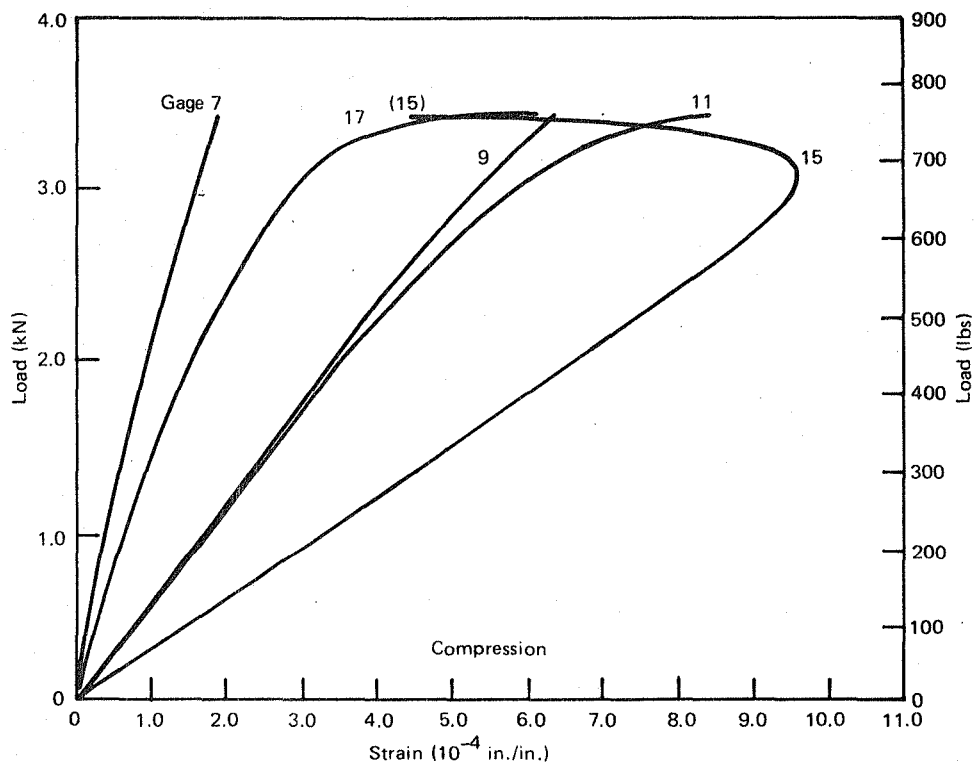


Figure 3-19. Strains Measured at Top Ends and Sides of Sector - 2.36 mm (0.093 in.) Diameter Longitudinals.



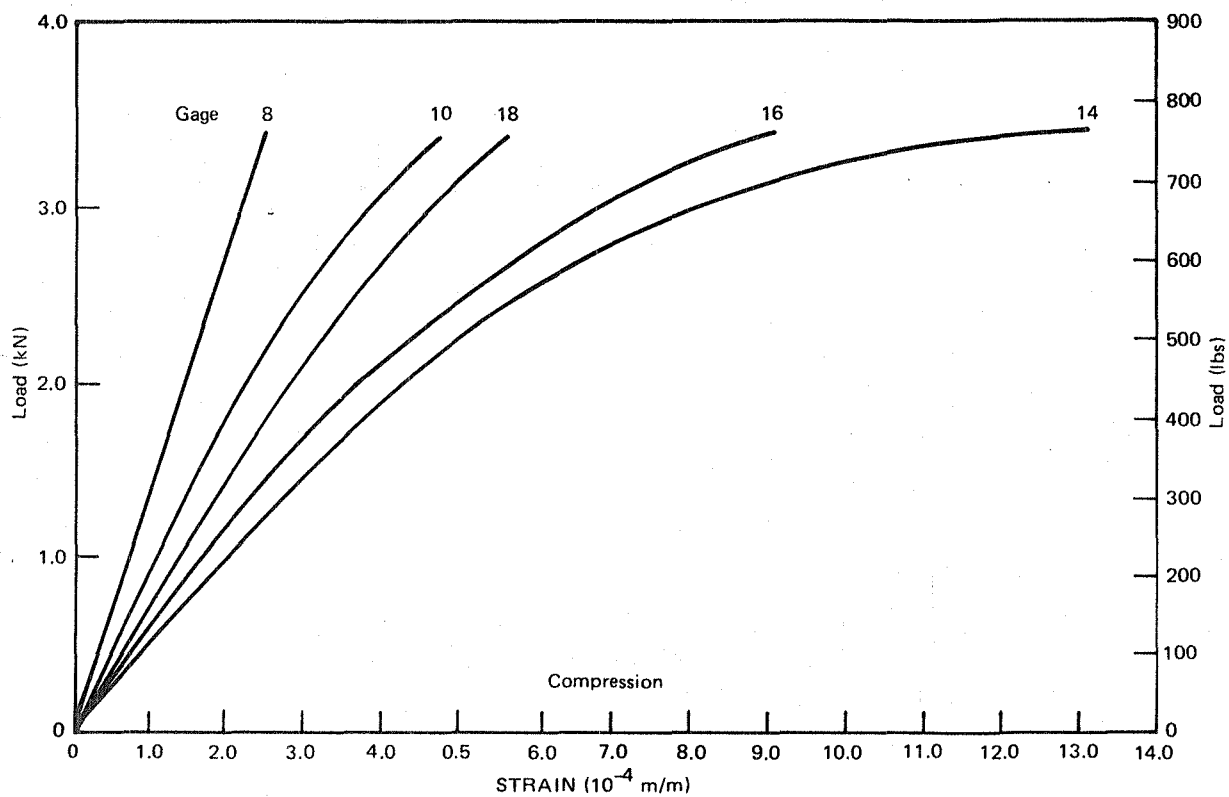


Figure 3-20. Strains Measured at Bottom Ends and Sides of Sector - 2.36 mm (0.093 in.) Diameter Longitudinals.

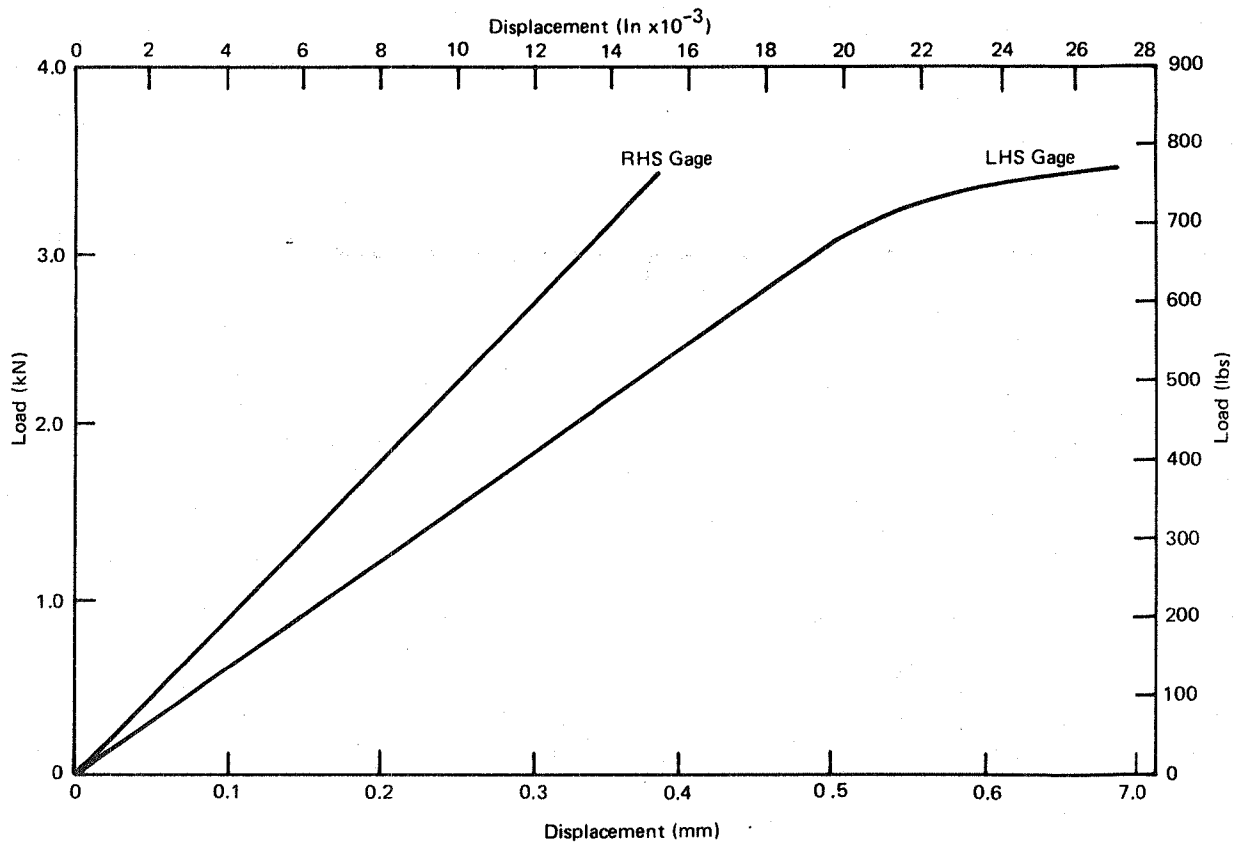


Figure 3-21. Load Versus Displacement at Edge of Sector - 2.36 mm (0.093 in.) Diameter Longitudinals.

( $16.5 \times 10^6$  psi) while the Phase I feasibility cylinder longitudinal material (HMS/P1700) had a flexure modulus of  $125.5 \text{ GN/m}^2$  ( $18.2 \times 10^6$  psi). Considering this difference in material property and its effect upon local rib buckling, the correlation of test results is good.

A comparison of pretest buckling load prediction for each of the parameter cylinder sectors is presented in Figure 3-22 along with actual buckling load levels achieved during testing. These data generally indicate good correlation

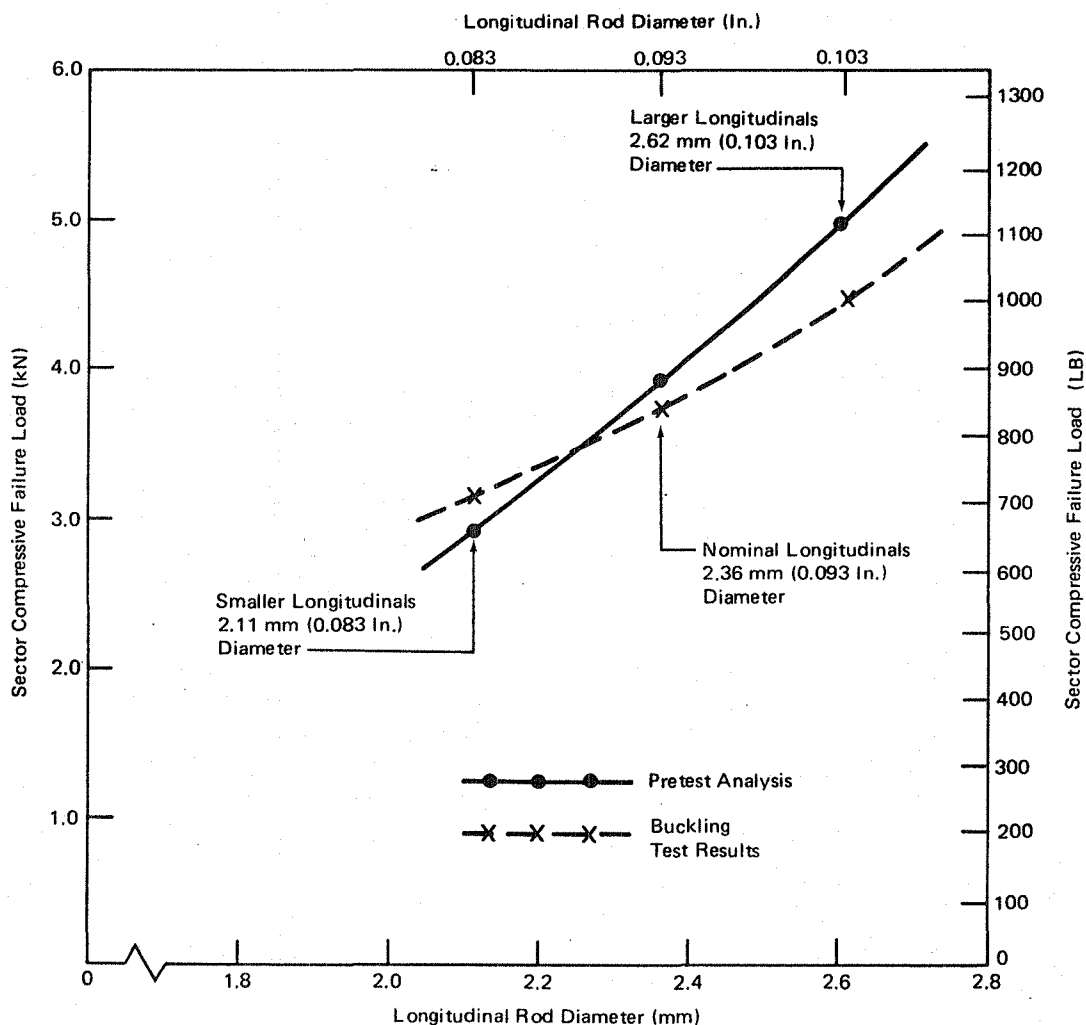


Figure 3-22. Comparison of Pretest Analysis and Buckling Test Results for Geodetic Sectors With Various Ratios of Longitudinal-to-Helical Rod Size.

between test and analysis and that the rib buckling analysis results as predicted by Anderson's code for geodetic structures with various ratios of longitudinal-to-helical rod sizes agrees well with the trends observed during testing. However, based upon the test results obtained for the sector with 2.62 mm (0.103 in.) diameter longitudinals, it should be noted that although a significant increase in load carrying capability over that of the 2.36 mm (0.093 in.) diameter longitudinal sector was achieved (approximately 22%) with only a small increase in structure weight (approximately 7%) the failure mode observed was that of shell general instability rather than rib buckling, i.e., a failure mode more difficult to predict and design for than rib buckling. These results indicate the significant role that the helical members of a geodetic structure play in the overall buckling characteristics of this structure. Future minimum weight geodetic structures optimized for maximum load carrying capability through the reduction of helical rod diameter, will have to be analyzed in sufficient detail so as to either avoid the general instability buckling mode or be designed with confidence and ability to predict the onset of this failure mode.

### 3.2 GEODETIC CONE/CYLINDER TEST

In order to demonstrate the feasibility of the geodetic beam end closure design concept selected during Phase I, a full scale end closure structure, consisting of a geodetic lattice cone closeout, a geodetic cylinder segment and an attach ring for joining the cylinder and cone, was fabricated and tested. This activity, as was the work presented in Section 3.1, was oriented toward evaluating more fully the structural parameters and characteristics of the type of geodetic beam being developed under this program. Results of geodetic cone/cylinder test article design, fabrication and testing activities are presented below.

#### 3.2.1 Geodetic Cone/Cylinder Test Article Design

The geodetic cone/cylinder assembly consisted of three separate advanced composite structures, a geodetic lattice cone closeout, a geodetic cylinder and a cone/cylinder attach ring. The overall geometry of the cone/cylinder assembly is presented in Figure 3-23.

The geodetic cone/cylinder test article was designed to have the same buckling load carrying capability as the sector with 2.36 mm (0.093 in.) diameter longitudinals described in Section 3.1. Based on parameter cylinder test results, the design load carrying capability was established as 214.8 N/rod (48.3 lb/rod), or 10,742 N (2,415 lb.) for a geodetic cylinder with 50, 2.36 mm (0.93 in.) diameter longitudinals.

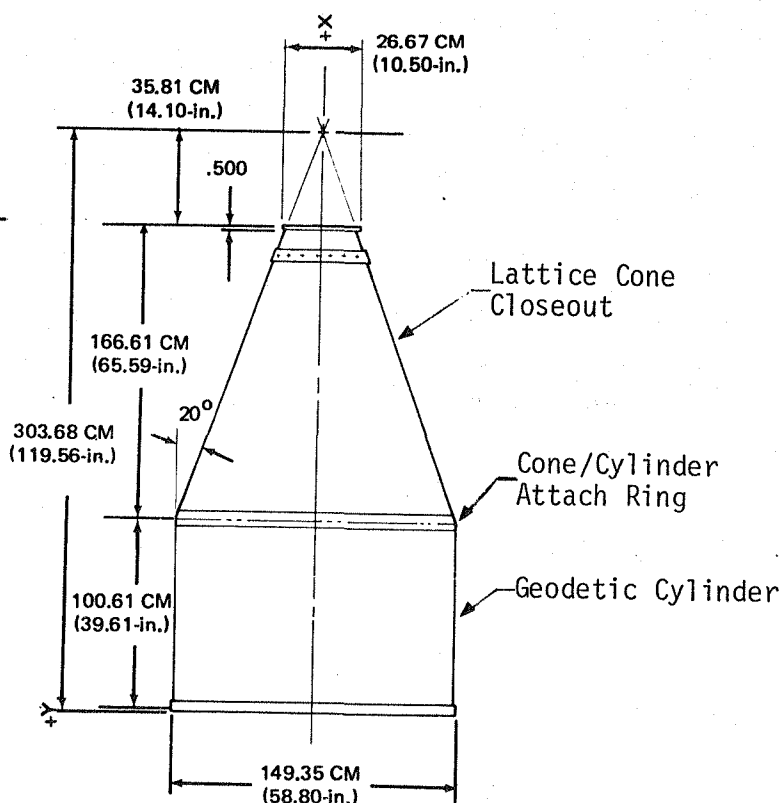


Figure 3-23. Geodetic Cone/Cylinder Test Article.

The geometry of the geodetic cylinder of the cone/cylinder assembly was identical to that of the Phase I feasibility cylinders and allowed the use of existing tooling for structure fabrication. The geodetic cone was designed to have a half-cone angle of  $20^\circ$  and also had 50 load carrying longitudinals. The rib length between two longitudinal nodes of the cone was constant along cone longitudinals and was identical to that of the geodetic cylinder. The diameter of the rod stock used for the conical closeout was selected such that the buckling load carrying capability of the cone was greater than that of the cylinder. Thus, buckling would occur in the geodetic cylinder, providing a comparison with previous Phase I feasibility cylinder test results while allowing an assessment of the uniformity of load transfer from the geodetic lattice cone into the cylinder. At the predicted buckling load for the cylinder, i.e., 214.8N/rod (48.3 lb/rod), the load in the cone longitudinal rods was predicted to be approximately 228.6N/rod (51.4 lb/rod), thus requiring rods larger than 2.36 mm (0.093 in.) diameter in order to prevent cone buckling prior to cylinder buckling. A rod stock diameter of 2.62 mm

(0.103 in.) was finally selected for the cone longitudinals because of the availability of a die set fabricated earlier for pultrusion of the parameter cylinder 2.61 mm (0.103 in.) diameter rod material. Figure 3-24 presents the design details for the geodetic cone/cylinder assembly.

### 3.2.2 Fabrication

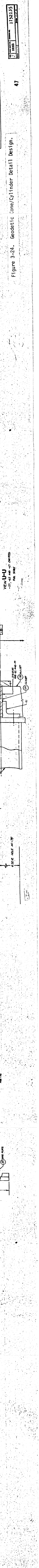
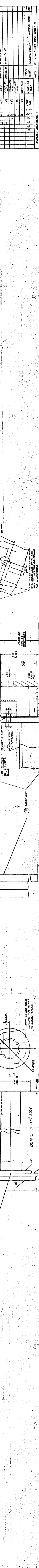
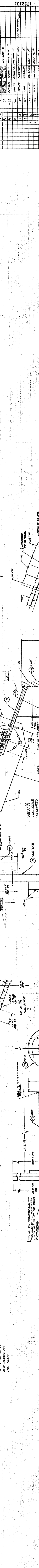
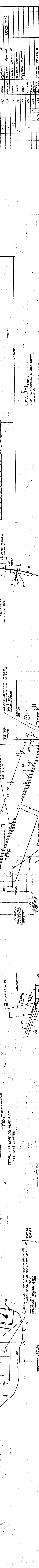
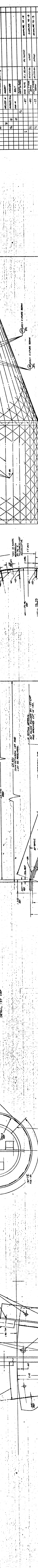
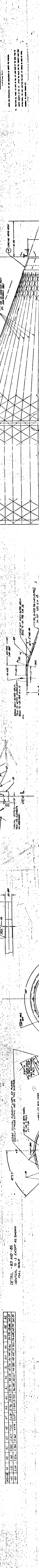
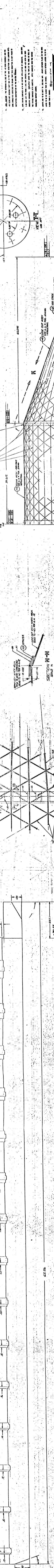
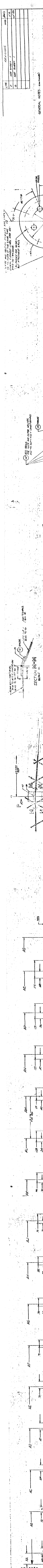
The rod stock used for the fabrication of all components of the cone/cylinder assembly was pultruded by Glasforms, Inc., of San Jose, California. Because of higher priority pultrusion commitments, CEC was not able to fabricate the approximately 365 m (1,200 ft.) of HMS/E-glass/PI700 round rod stock required for the cone/cylinder assembly. The physical and mechanical properties of the rod material received from Glasforms were determined to be almost identical to those of the material from CEC used in the fabrication of the parameter cylinder.

The geodetic cylinder was made on an existing fixture which had been designed and fabricated during the Phase I program. After completion of joint encapsulation, the lower end of the cylinder was potted on a surface table.

The cone/cylinder attach ring was a continuous 1.98 mm (0.078 in.) thick ring made of T300/934 bidirectional cloth prepreg laid-up and cured on an aluminum mandrel. Figure 3-25 shows the completed ring and the aluminum mandrel. The cured ring was trimmed to final width prior to use in assembling the cylinder and conical closeout.

The conical end closeout was fabricated on the assembly fixture shown in Figure 3-26 and described in detail in Figure 3-24 using the 2.62 mm (0.103 in.) diameter rod stock procured from Glasforms, Inc. After completing encapsulation of approximately 750 joints, the cone/cylinder attach ring was bonded to the conical closeout structure. This subassembly was then bonded to the upper end of the geodetic cylinder using room temperature curing adhesive, i.e., each longitudinal and helical rod was bonded to the inner surface of the cone/cylinder attach ring (see Figure 3-24). The sequence of fabrication/assembly operations used to construct the cone/cylinder assembly are presented in detail in Figure 3-27. The completed geodetic cone/cylinder test article is shown in Figure 3-28.





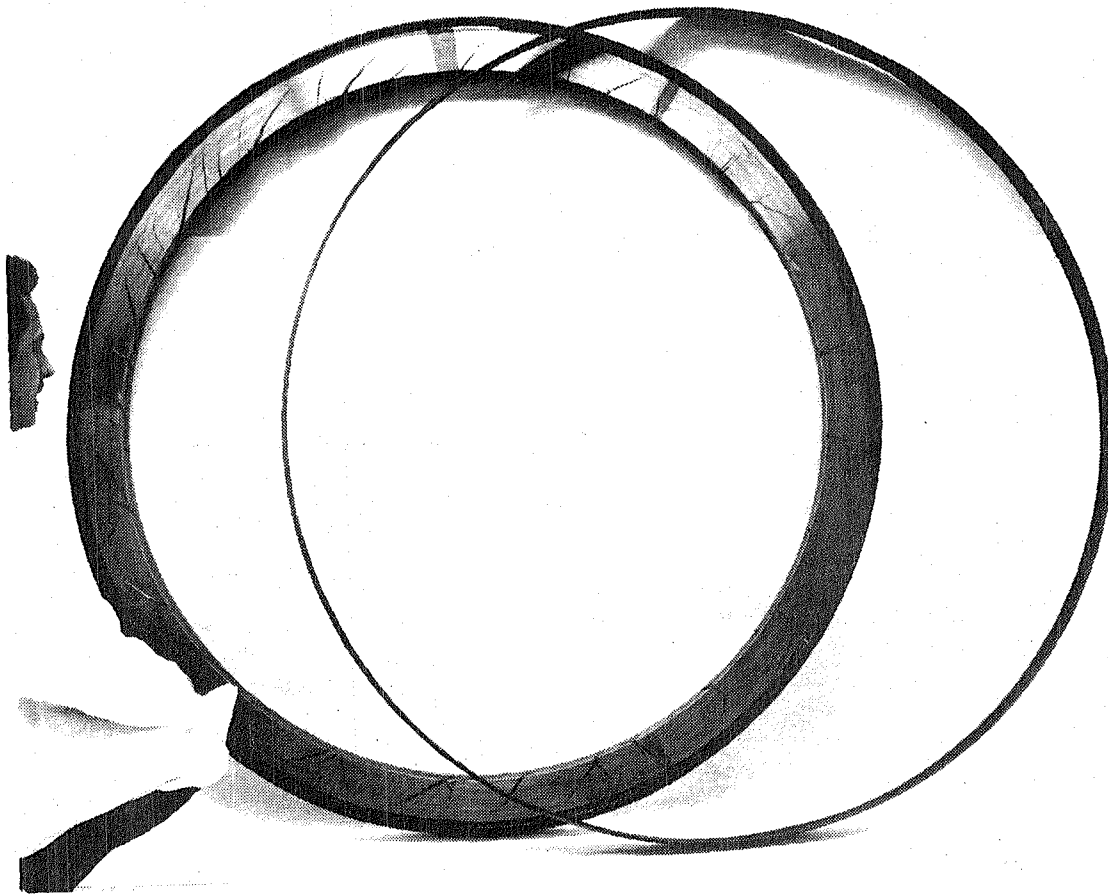


Figure 3-25. Cured Ring and Mandrel.

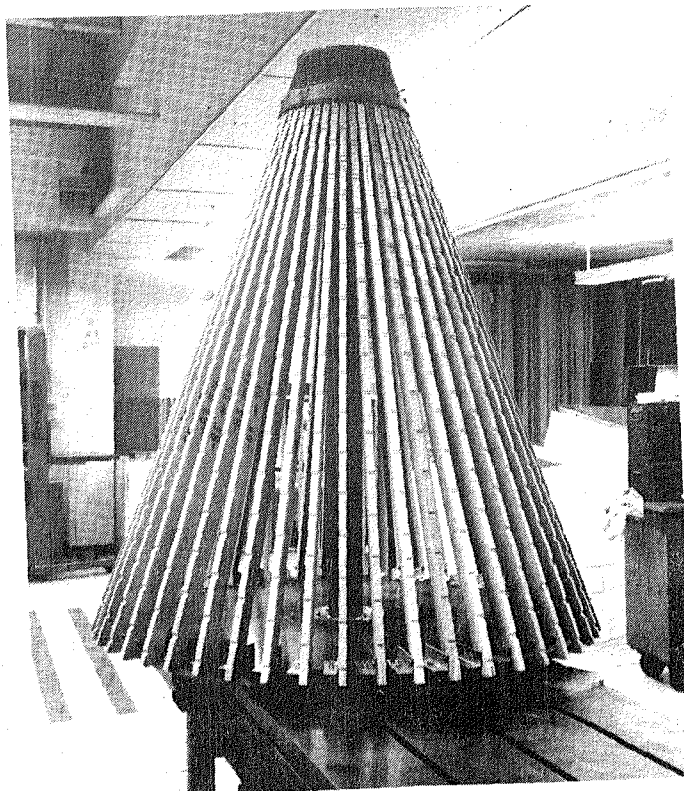


Figure 3-26. Assembly Fixture for Conical End Closeout.



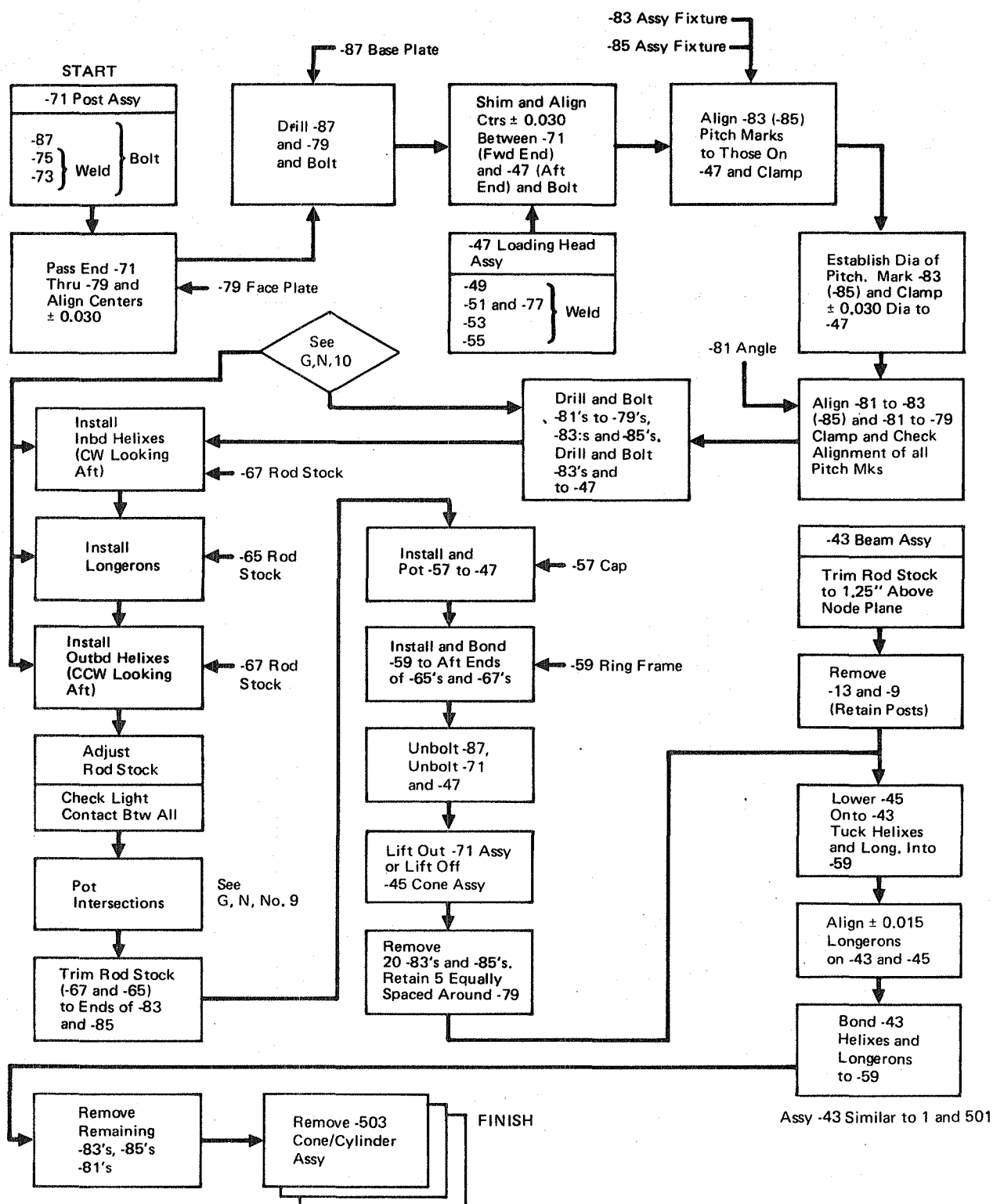


Figure 3-27. Geodetic Cone/Cylinder Test Article Fabrication and Assembly Process.

### 3.2.3 Testing

The test setup for the geodetic cone/cylinder test article is presented in Figure 3-29. This test setup was designed and fabricated by MDAC specifically for testing of the cone/cylinder assembly. The cone/cylinder assembly, as fabricated above, was bonded to an elevated platen (Figure 3-30). A tension rod was connected to a pivot link located near the specimen cone apex and terminated at the floor line through a load transducer and turnbuckle. The turnbuckle was used to apply compressive load.

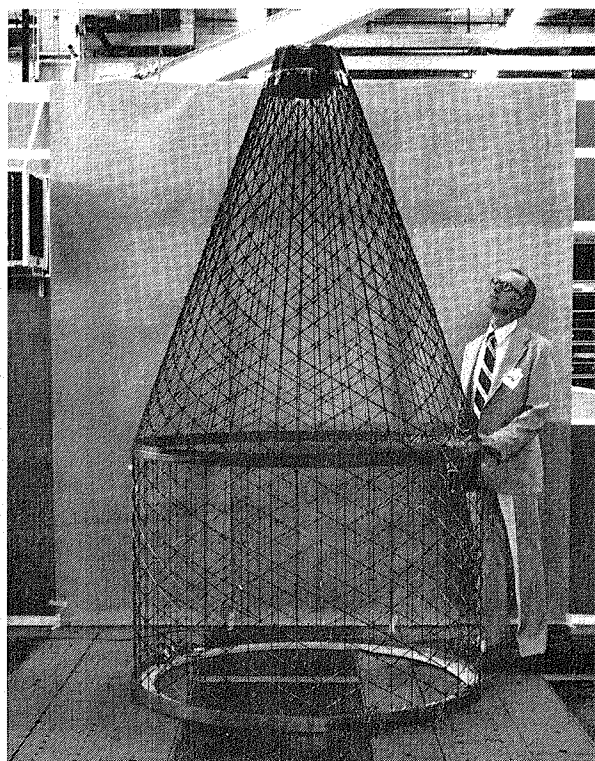


Figure 3-28. Geodetic Cone/Cylinder Test Article.

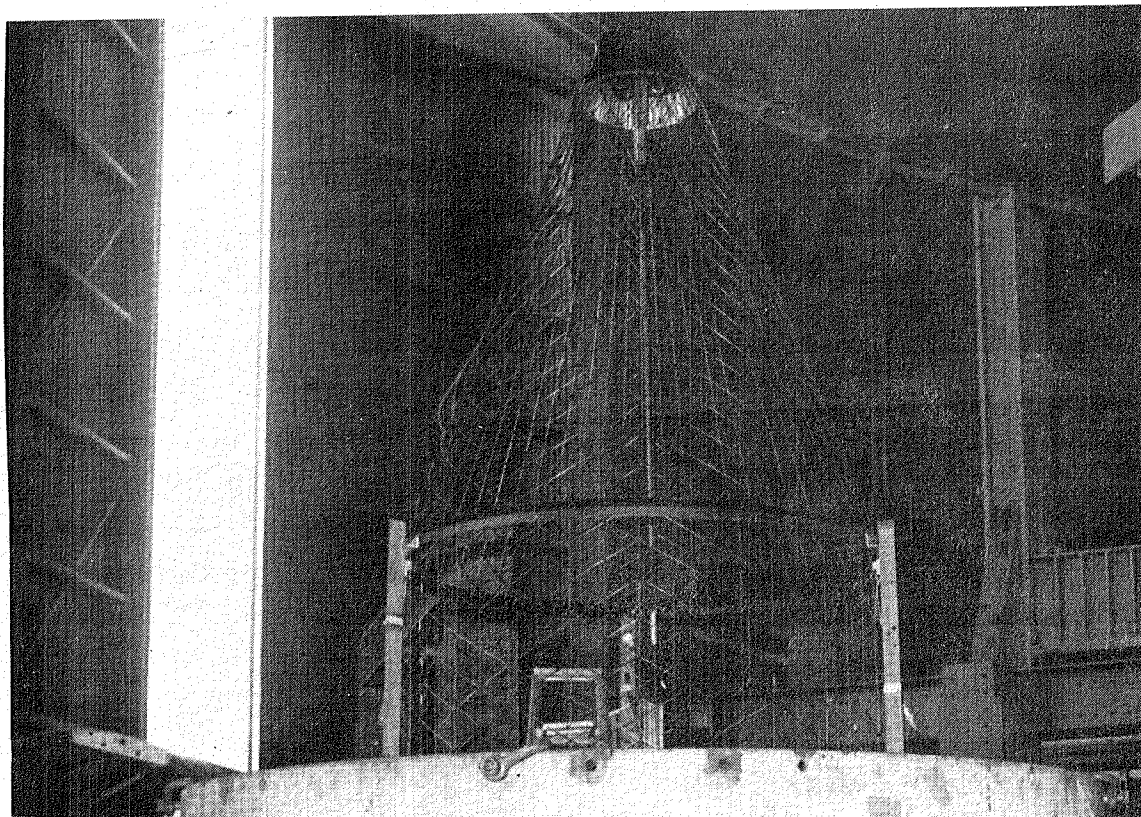


Figure 3-29. Geodetic Cone/Cylinder Test Setup.

The cone/cylinder test article was instrumented with six sets of back-to-back strain gages and three displacement transducers which were located 120° apart around the assembly circumference and which were referenced to the cone/cylinder attach ring and the elevated platen. As shown in Figure 3-31, four sets of back-to-back strain gages were located on one longitudinal at the center of the first four bays just below the cone/cylinder attach ring.

These gages were used to monitor bending response down the length of the cylinder induced by the bending (kick) load introduced at the cone/cylinder interface. The other two sets of back-to-back gages were located at cylinder mid-length on longitudinals approximately 90° and 180° away from the instrumented longitudinal discussed above.

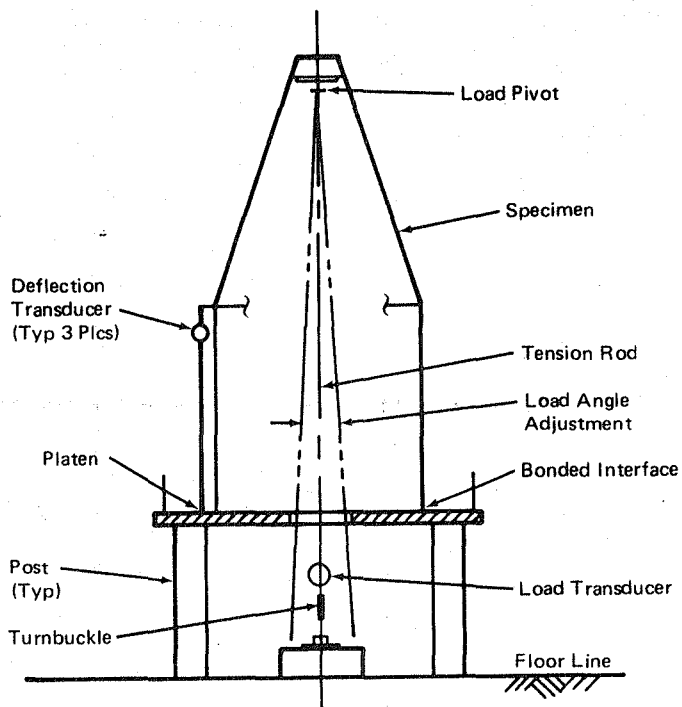


Figure 3-30. Geodetic Cone/Cylinder Loading Details.

The cone/cylinder assembly was successfully tested in axial compression. Local rib buckling occurred in the upper half of the geodetic cylinder at a load of approximately 8,896 N (2,000 lb.), i.e., approximately 85% of the predicted buckling load of 10,742 N (2,415 lb.) based on the test results obtained for the parameter cylinder sector with 2.36 mm (0.093 in.) diameter longitudinals. Photographs of the buckled geodetic cone/cylinder test articles are presented in Figure 3-32.

Strain gage data for the four back-to-back gages located on the 0° longitudinal (see Figure 3-31) are presented in Figures 3-33 through 3-36. These data indicate that significantly more bending occurred prior to cylinder buckling

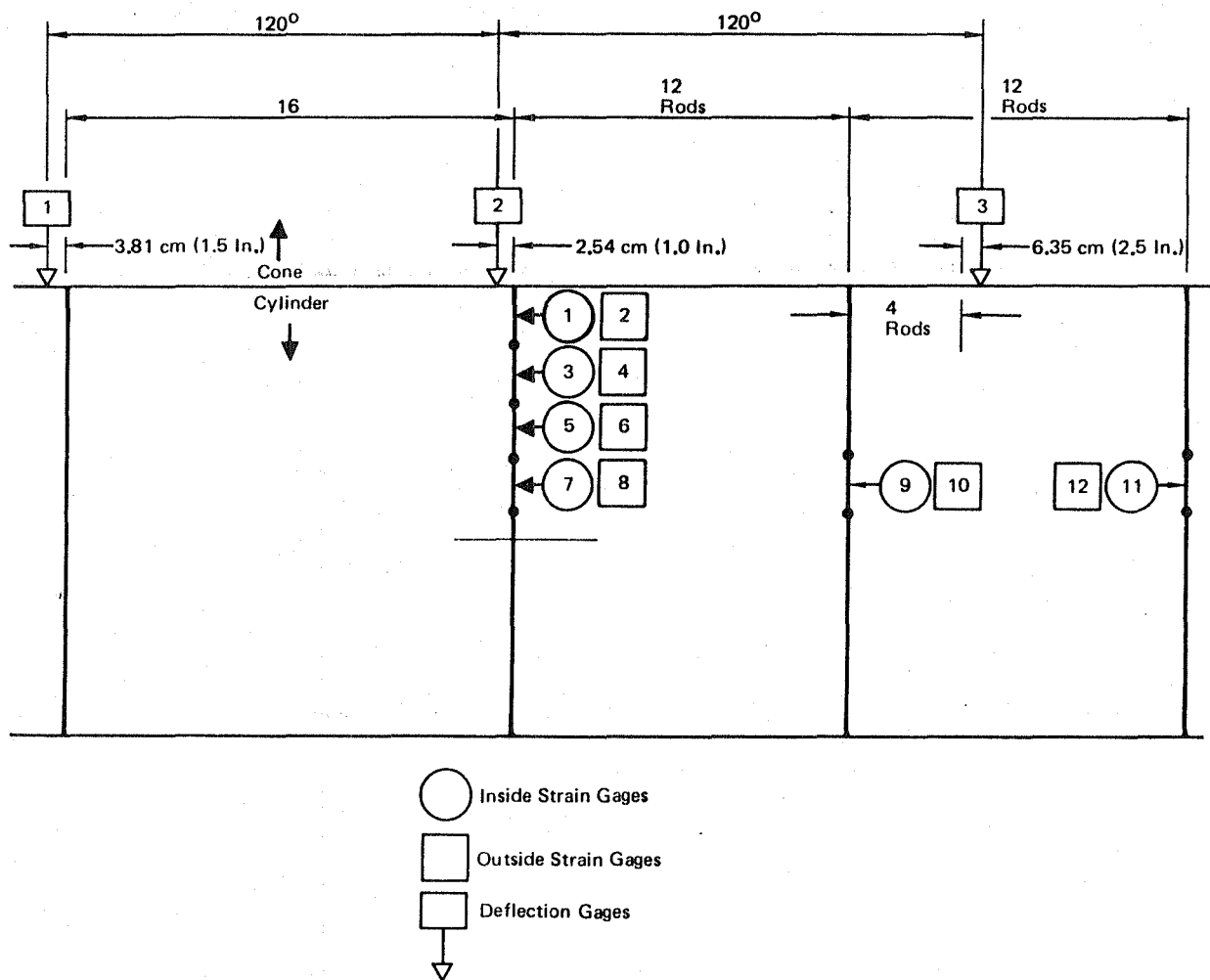


Figure 3-31. Geodetic Cone/Cylinder Test Article Strain Gage and Displacement Transducer Layout.

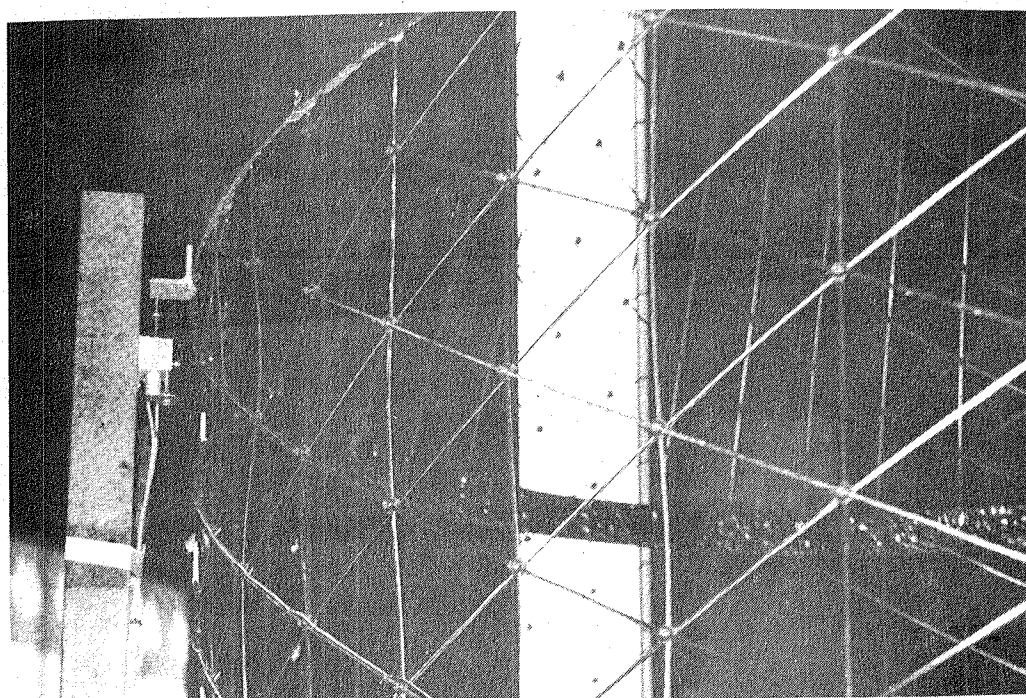
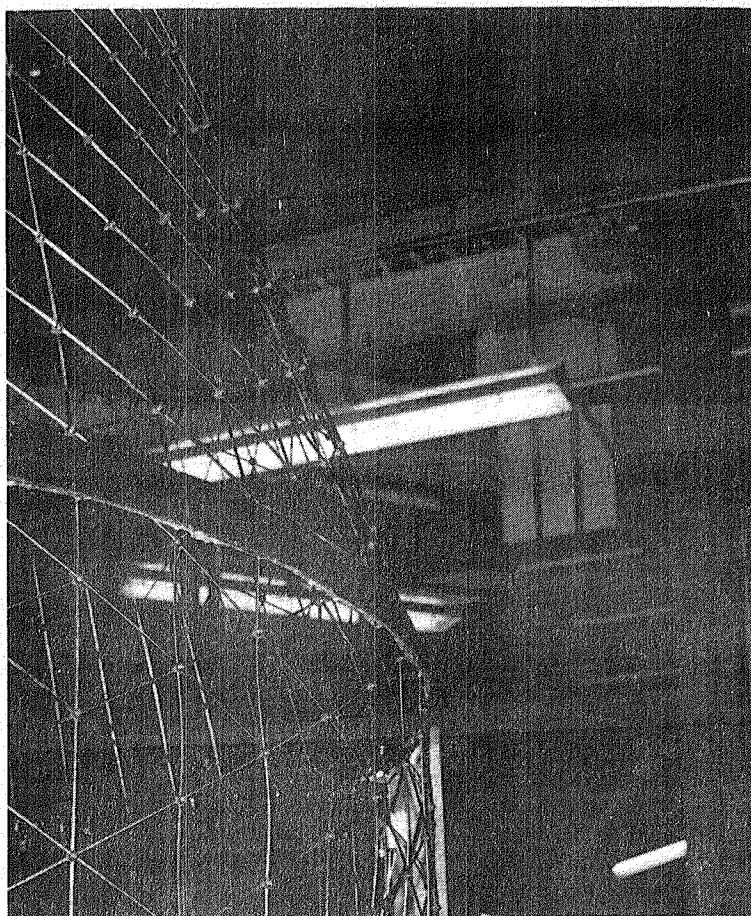


Figure 3-32. Buckling of Geodetic Cone/Cylinder Test Article -  
 $P = 8,896 \text{ N (2,000 lb.)}$

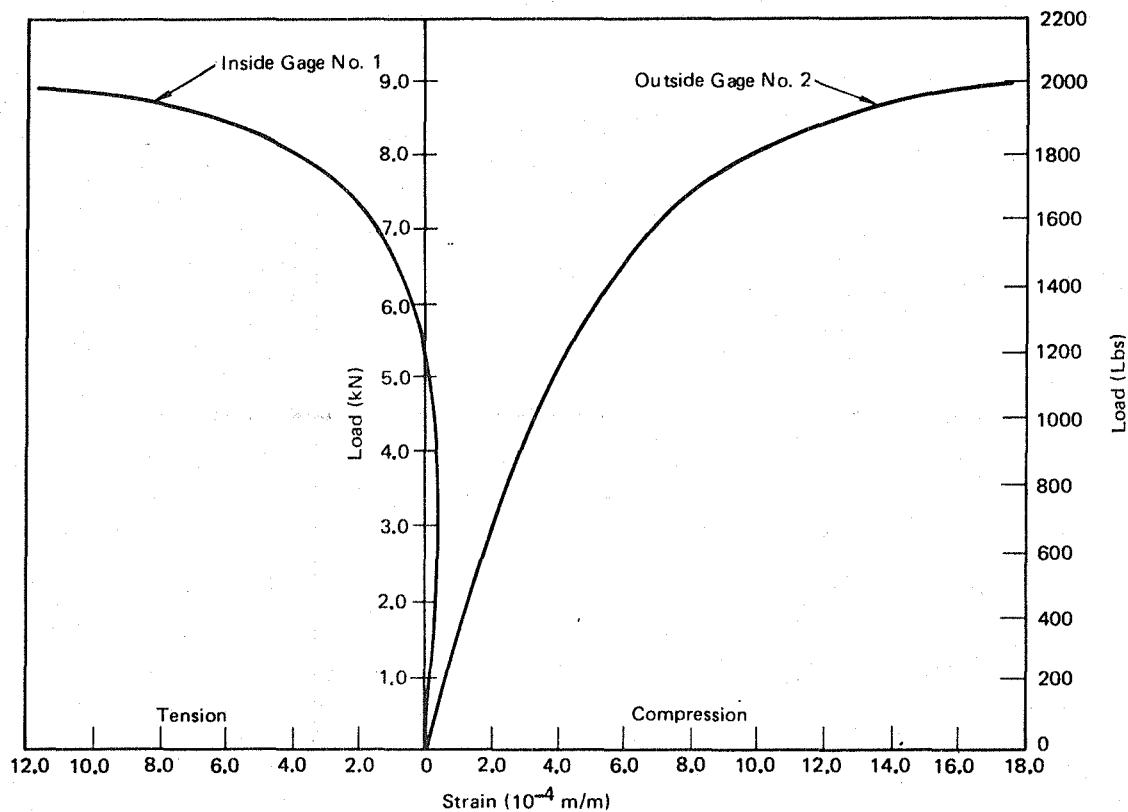


Figure 3-33. Axial Load Versus Strain for Geodetic Cone/Cylinder Test Article - Strain Gages 1 and 2.

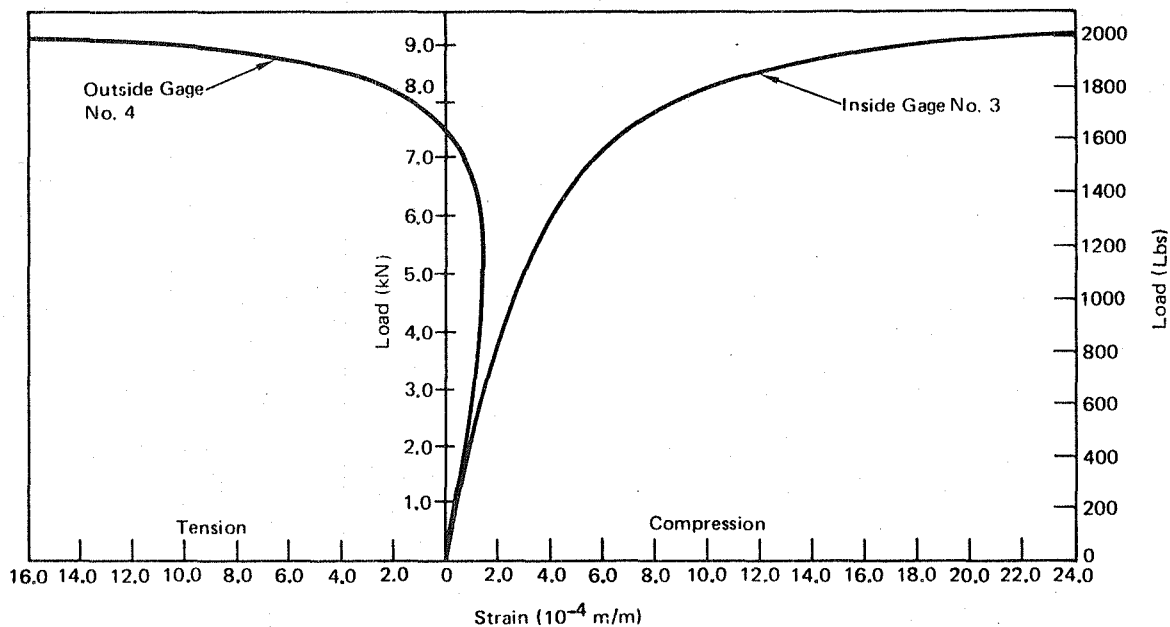


Figure 3-34. Axial Load Versus Strain for Geodetic Cone/Cylinder Test Article - Strain Gages 3 and 4.

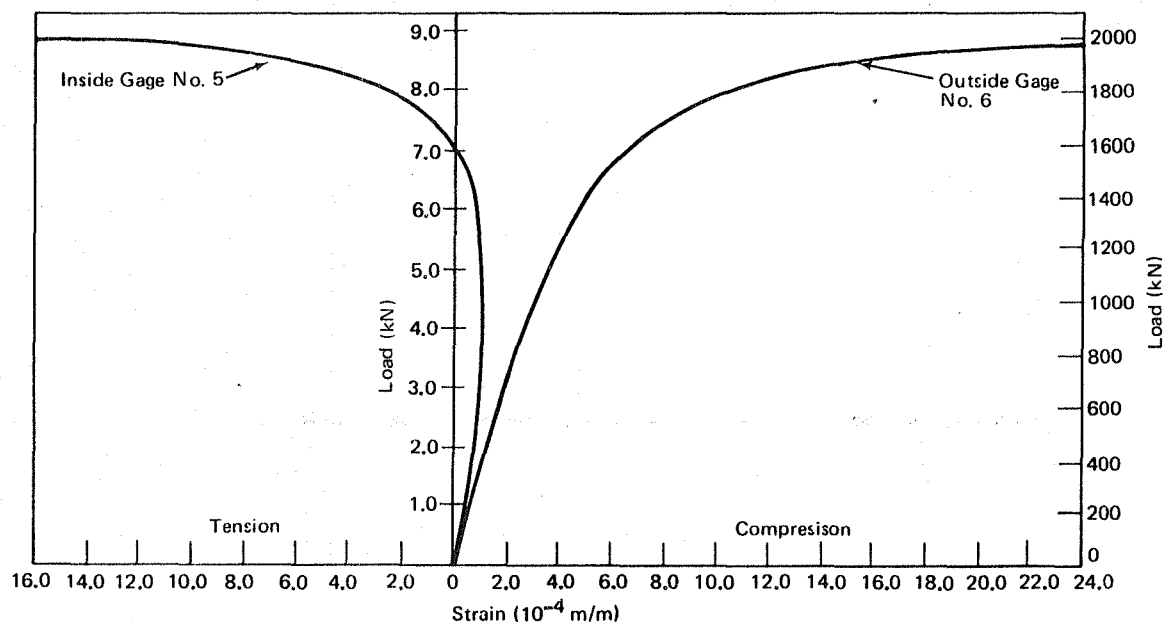


Figure 3-35. Axial Load Versus Strain for Geodetic Cone/Cylinder Test Article - Strain Gages 5 and 6.

in the bays nearest the cone/cylinder attach ring than in the bay at middle of the cylinder. The strain gage data obtained at 90° and 180° locations prior to buckling (Figures 3-37 and 3-38) are very similar to the strain gage data obtained at the middle of the cylinder at 0° (Figure 3-36), indicating the uniformity of loading achieved during the test. Displacement transducer data are presented in Figure 3-39 and these data indicate the onset of buckling and the inability of the cone/cylinder assembly to carry

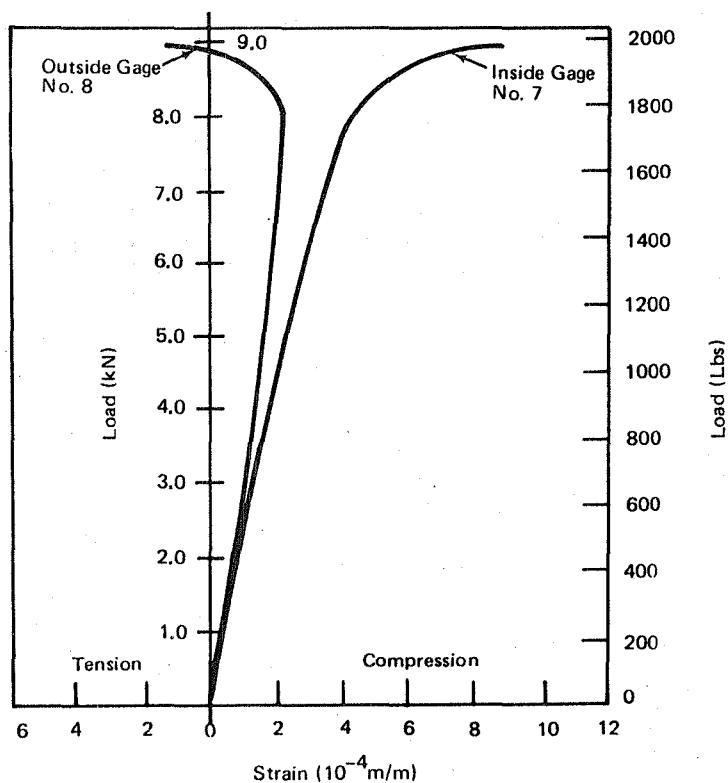


Figure 3-36. Axial Load Versus Strain for Geodetic Cone/Cylinder Test Article - Strain Gages 7 and 8.

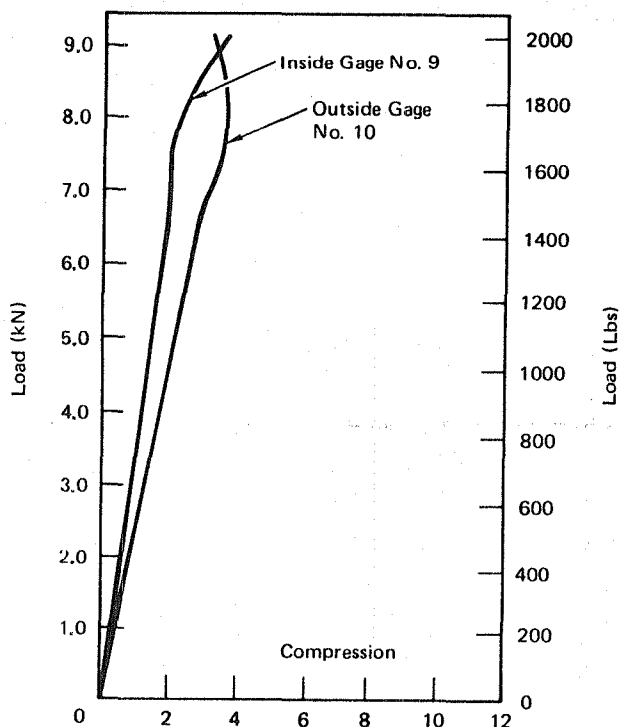


Figure 3-37. Axial Load Versus Strain for Geodetic Cone/Cylinder Test Article - Strain Gages 9 and 10.

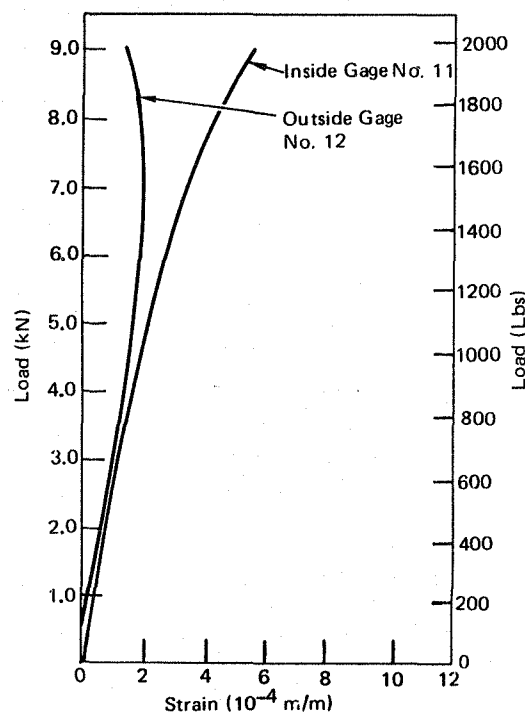


Figure 3-38. Axial Load Versus Strain for Geodetic Cone/Cylinder Test Article - Strain Gages 11 and 12

additional load at approximately 8,896 N (2,000 lb.). The uniformity of geodetic displacement versus load around its circumference indicates the uniformity of load transfer from the lattice cone closeout to the geodetic cylinder through the attach ring.

The reduced compressive buckling load carrying capability of the cone/cylinder assembly, compared to that predicted based on the results of the parameter cylinder test for the sector with 2.36 mm (0.093 in.) diameter longitudinals, was due to the large amount of bending produced in the bays nearest the cone/cylinder attach ring. This bending, predominately a result of the kick-load at the attach ring, produced rib buckling at a load level approximately 85% of that associated with buckling due to a pure compressive load. The increased bending in the bays near the cone/cylinder attach ring could also have been promoted by longitudinal rib imperfection produced during structure assembly,



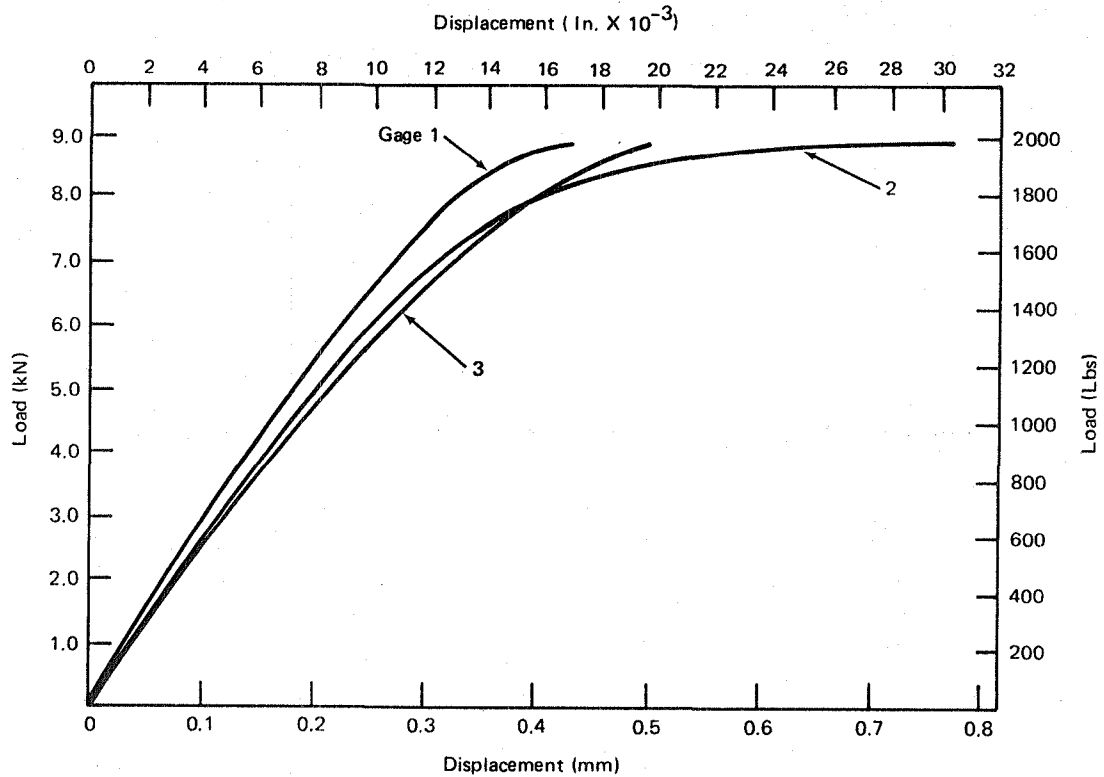


Figure 3-39. Load Versus Displacement for Geodetic Cone/Cylinder Test Article.

i.e., mating of the cone/attach ring assembly to the cylinder. Future geodetic beam designs will either have to minimize bending effects at the cone/cylinder attach frame through the use of a modified ring design, minimize assembly induced rib imperfections, or reduce overall beam design load capability to account for the increased bending.

### 3.3 REFERENCES FOR SECTION 3

- 3-1 Development of a Composite Geodetic Structure for Space Construction, Phase 1 Final Report, MDC G8079, 1 October 1979.
- 3-2 Anderson, M. S., Buckling of Periodic Lattice Structures. AIAA Paper No. 80-0681. Presented at the AIAA/ASME 21st Structure, Structural Dynamics, and Materials Conference, Seattle, Washington, May 12-14, 1980.

## Section 4

### STRUCTURAL ANALYSIS

The analytical procedures developed during the Phase I study were extended and refined to include the effect of different rod stock dimensions for the helical and longitudinal members on local buckling, and the effect of different flexural and extensional moduli on general instability buckling. An analysis and computer code developed by Anderson of NASA (Reference 4-1) was employed to predict general instability. When compared to the Phase I test data, the correlation achieved with the Anderson code showed significant improvement over the prior general instability analysis (Reference 4-2).

Failure modes for the geodetic structure include buckling (local, general instability and column) and strength (local joint failure) (See Figure 4-1). Under the Phase I program effort, analytical methods were developed to predict local rib buckling, general instability, and joint strength requirements.

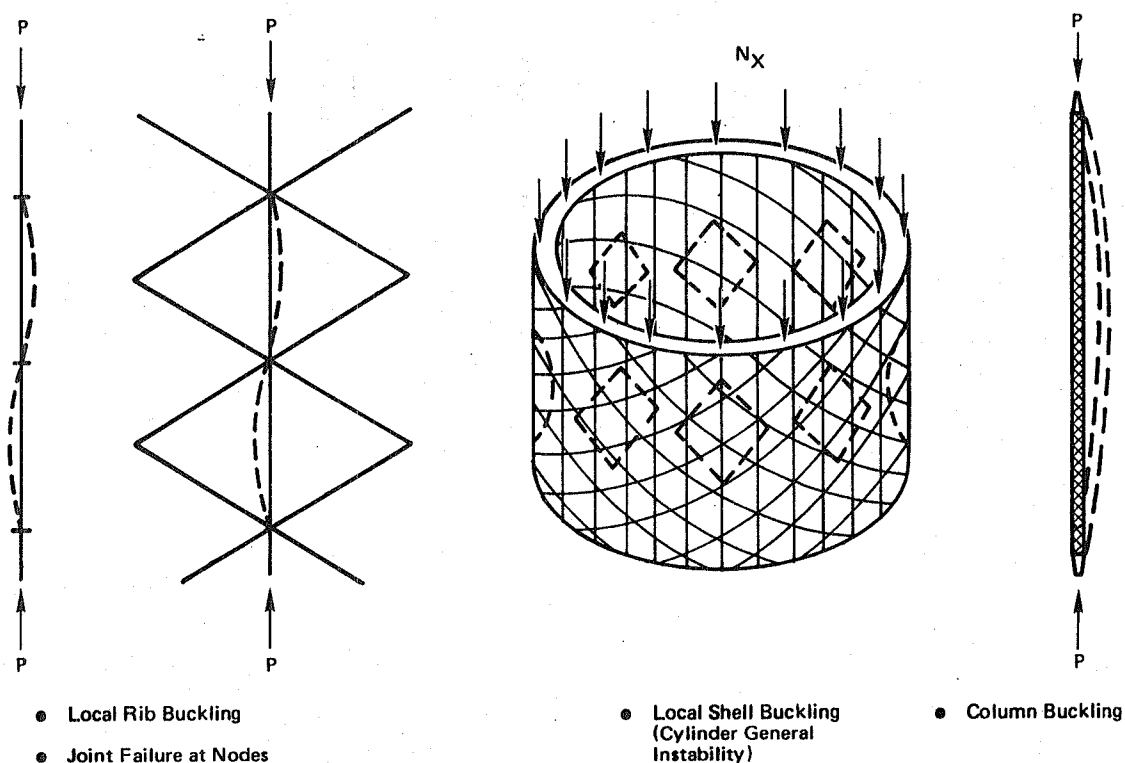


Figure 4-1. Geodetic Column Failure Modes

#### 4.1 Local Buckling

Local buckling of the rib was predicted by considering both the global stiffness and local stiffness of the joints (cross over points for axial and helical members). The global stiffness is provided primarily by the geometry of the isogrid pattern and the bending stiffness of the helical members and to a lesser degree by the torsional and extensional rigidity of the helical. In these analyses it was assumed that an adequate foundation stiffness (a function of extensional stiffness of the helicals and radius of curvature) was provided by the helical members so as to prevent buckling through a joint.

Local stiffness of the joint is related to how the helical and axial members are joined. If the joint is infinitely rigid, then only the global stiffness affects the local buckling coefficient,

$$C = \frac{P_{cr_{rib}}}{\pi^2} \frac{L^2}{EI} \quad (4-1)$$

where

$C$  = local buckling coefficient

$P_{cr_{rib}}$  = local buckling load for axial rib

$L$  = distance between joints

$EI$  = bending stiffness of longitudinal rib

The buckling coefficient for a column varies from 1.0 for simply supported ends to 4.0 for fixed ends. For local buckling of the axial member, the upper bound on the buckling coefficient is established by the stiffness provided by the helical members. For the case of a joint with infinite local stiffness and equal stiffness axial and helical members, the buckling coefficient was determined in Reference 4-3 to be  $C = 1.67$ .

The effect of local joint stiffness was incorporated into the determination of  $C$  by adding the local and global stiffnesses as springs in series and then establishing  $C$  from a plot of  $C$  vs. total stiffness. The total stiffness at a joint is given by:

$$\hat{K} \equiv \hat{K}_{total} = \frac{1}{\frac{1}{\hat{K}_{GL}} + \frac{1}{\hat{K}_L}} \quad (4-2)$$

where

$\hat{K}_{total}$  = total joint nondimensional spring constant

$\hat{K}_{GL}$  = global joint nondimensional spring constant

$\hat{K}_L$  = local joint nondimensional spring constant

Since the axial and  $\pm 60^\circ$  helical members are attached at different elevations within the joint,  $K_L$  can be expressed as the sum of the rotational stiffness provided at each attach plane

$$K_L = K_{+60^\circ} + K_{-60^\circ} + K_{rib} \quad (4-3)$$

The quantity  $K_L$  must be experimentally determined by conducting a bending test on the joint. From the measured rotation,  $\theta$ , is the local spring constant  $K_L = M/\theta$  is determined. The nondimensional spring constant  $\hat{K}_L$  is then determined from

$$\hat{K}_L = K_L \frac{L}{EI} = \frac{M}{\theta} \frac{L}{EI} \quad (4-4)$$

Figure 4-2 shows the total nondimensional spring constant and buckling coefficient,  $C$ , as a function of the local nondimensional spring constant,  $\hat{K}_L$ , for buckling in the out-of-plane mode.

Test on joints have shown that the  $\hat{K}_L$  varies from a low of 2 ( $C = 1.04$ ) for resistance welded joint to a high of 47.5 ( $C = 1.60$ ) for encapsulated joints. For the encapsulated joint currently used a value of  $\hat{K} \approx 30$  and  $C = 1.57$  is used.

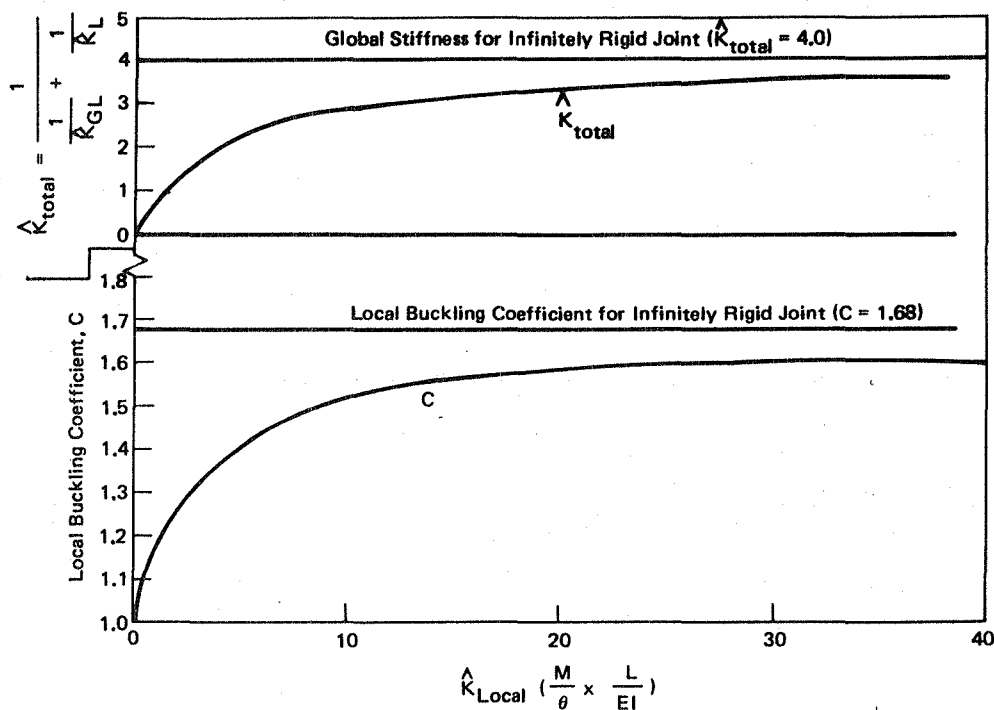


Figure 4-2. Local Buckling Coefficient for Rib as a Function of Local Stiffness - Out-of-Plane Mode

Local rib buckling is a major factor in the design of geodetic columns. Studies have shown that weight efficiency of the structure can be improved by switching from a cylinder with equal helical and axial member sizes to structures where the axial members are of larger dimensions (higher EI) than the helical members. Figure 3-1 illustrates the increased load carrying ability that can be achieved by varying the proportions of helical and axial members. There is an upper limit for the efficiency that can be achieved. This corresponds to the case where the foundation modulus becomes so weak that buckling occurs through a joint. The parameter cylinder tests (discussed in Section 3.1) were conducted to correlate the predicted buckling loads for three ratios of helical to axial member bending stiffnesses.

The analysis for local buckling of axial members when they have the same bending stiffness as the helical members can be extended to members of unequal

stiffness. The nondimension spring constant for the global stiffness can be modified to give

$$\hat{K}_{GL} = \hat{K}_{GL_{EQ}} \frac{(EI)_{\text{Helicals}}}{(EI)_{\text{Longitudinal}}} \quad (4-5)$$

from which the buckling coefficient can be determined from Figure 4-3. The quantity  $\hat{K}_{GL_{EQ}}$  is the stiffness for axial and helical members with equal bending stiffness, and is equal to 4.0 for the out-of-plane buckle mode.

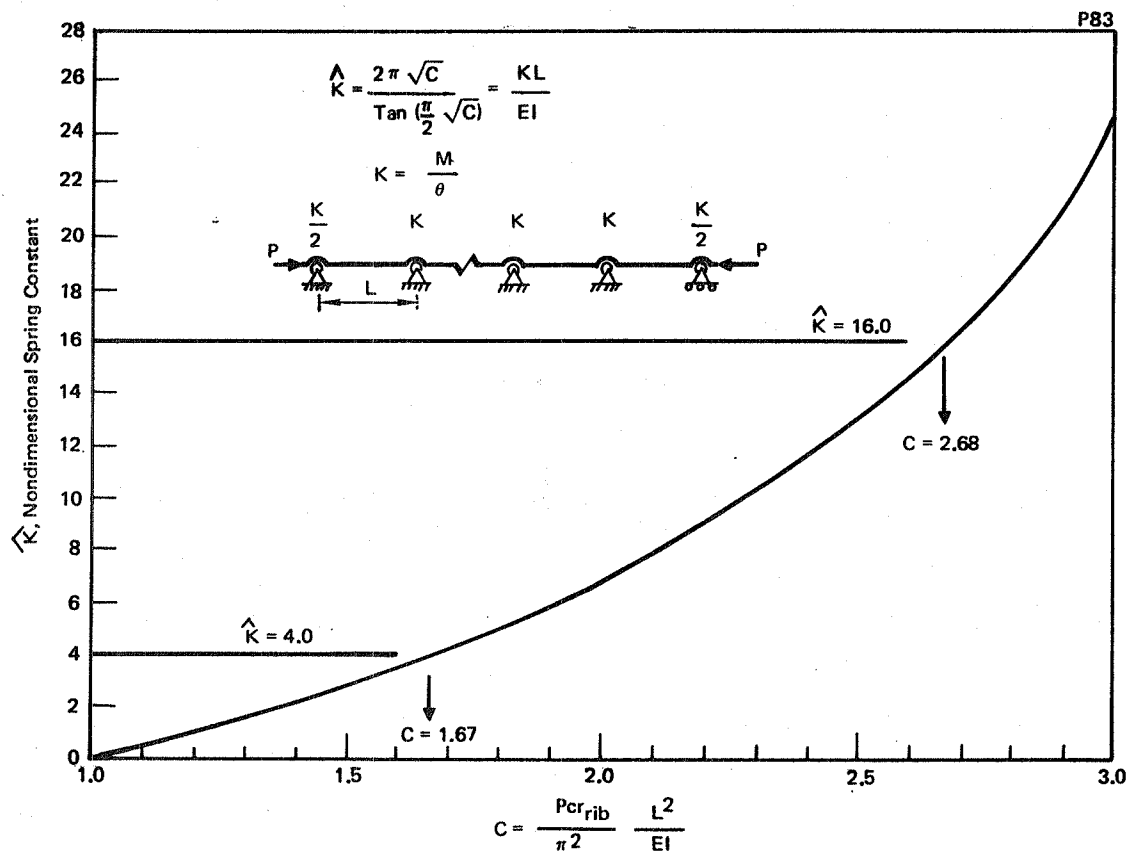


Figure 4-3. Buckling Coefficient as a Function of Rotational Spring Constant

Figure 4-4 shows the buckling coefficient,  $C$ , as a function of the helical and axial member bending stiffness. The result of this analyses will be correlated with experimental data at the end of this section.

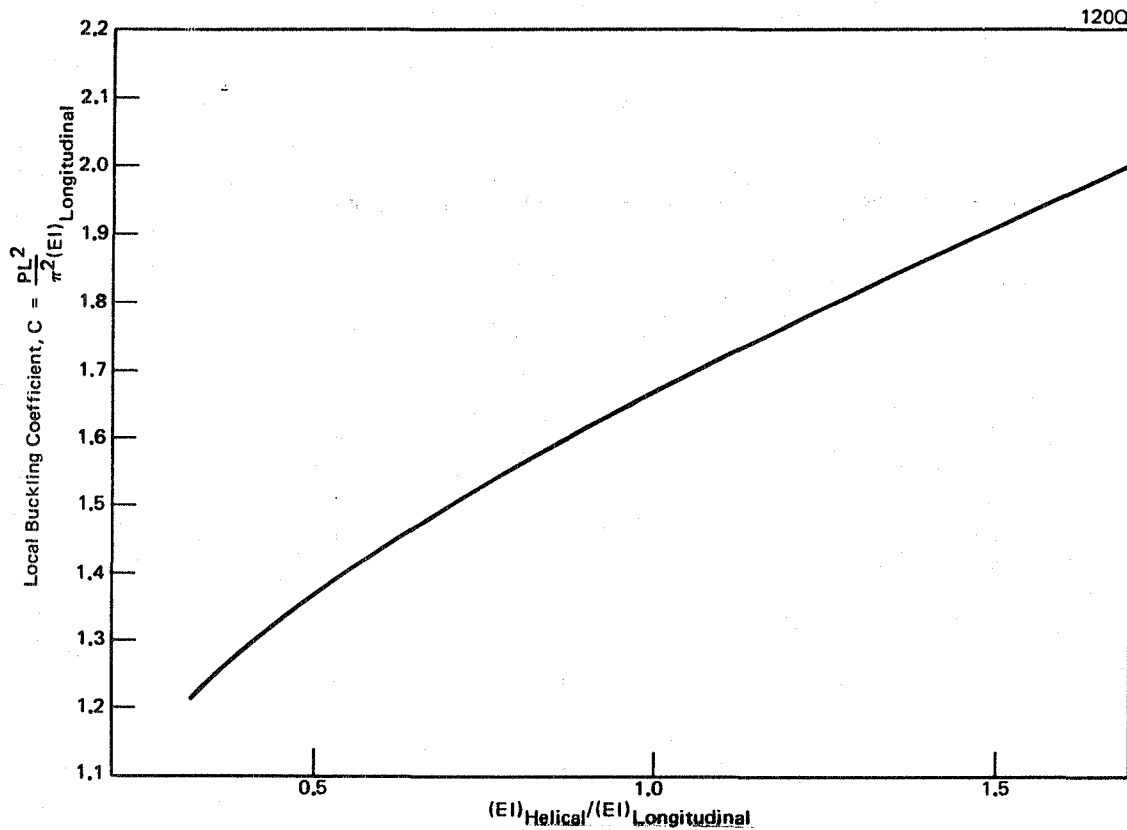


Figure 4-4. Effect of Helical and Axial Member Bending Stiffness on the Local Buckling Coefficient,  $C$

#### 4.2 General Instability

As pointed out in Reference 4-3, the use of a buckling analysis that treats the discreteness of the structure is necessary to accurately predict buckling for cylinders composed of members with large slenderness ratios ( $L/r_g \approx 200$ , where  $L$  is the local member length and  $r_g$  is the radius of gyration). The common method of analyzing stiffened shell structures for buckling is by treating the stiffening as an equivalent orthotropic shell. This produces valid results over a very narrow range of slenderness ratios that are not of interest in the current designs. The general instability analysis presented

in Reference 3-1 has been extended to incorporate the buckling analysis by Anderson (Reference 4-1).

In Reference 3-1, equations are developed for the buckling of a general lattice structure that has repetitive geometry. Equilibrium at a typical node is expressed using finite element techniques, and the only assumption is that the response is periodic. By basing the stiffness matrix on the exact solution of the beam column equation, accurate results are obtained for complex buckling behavior that would require a very large system of equations using conventional techniques. Anderson's method requires the Eigen values of only a 6 x 6 determinant. The analysis considers the joints as locally rigid, therefore the local rotation resulting from finite stiffness at the joints is not presently accounted for.

The test data from Phase I program experiments and those published in the literature that were correlated with the local buckling analysis presented in Reference 4-3, and the general instability analysis of Reference 4-2 are shown in Table 4-1 with the predictions based on the analysis of Anderson (Reference 4-1). The Anderson code predictions show excellent correlation of analysis and test data. Data obtained under Phase II are correlated in the following section.

Table 4-1. Correlation of Previous Test Results

Test Cylinder Description	Predicted Buckling Loads N (Lb)				Experimental Data N (Lb)
	Local Buckling (Ref 4-3) N (Lb)	General Instability			
		Shell Theory (Ref 4-3) N (Lb)	Forman/Hutchinson (Ref 4-2, 4-3) N (Lb)	Anderson (Ref 4-1) N (Lb)	
Feasibility Test Cylinder Encapsulated Joints (Reference 4-3)	13,345 (3,000)	53,376 (12,000)	11,164 (2,510)	13,172 (2,961)	13,300 (2,990)
Aluminum Rod Cylinder Bonded Joints (Reference 4-4)	---	50,974 (11,460)	12,597 (2,832)	14,011 (3,150)	14,011 (3,150)

\*For Infinitely Rigid Joints



### 4.3 Correlation of Phase II Test Data

The above analyses are correlated with the test data reported in Sections 3.1 and 3.2. Table 4-2 summarizes the predicted buckling loads based on local buckling and general instability and compares these results to test data. In the case of the parameter cylinder test, the data for each section has been reported as if an entire cylinder was tested. (Actual loads are 17/50 and 16/50 of those shown in Table 4-2.)

Table 4-2. Correlation of Phase II Test Results

Parameter Cylinder Test

P83

Number of Longitudinals In Sector	Helical Member Diameter mm (In.)	Longitudinal Member Diameter mm (In.)	Predicted Buckling Load			Experiment Based on Equivalent Cylinder N (Lb)
			Local Buckling		General Instability (Anderson, Ref 4-1) N (Lb)	
			Infinitely Rigid Joints $\hat{K}_{LOCAL} = \infty$ N (Lb)	Finite Rigidity Joint $\hat{K}_{LOCAL} = 30.0$ N(Lb)		
17	2.36 (0.093)	2.11 (0.083)	C = 1.94 9,194 (2,067)	C = 1.86 8,816 (1,982)	8,576 (1,928)	9,158 (2,059)
17	2.36 (0.093)	2.36 (0.093)	C = 1.67 9,194 (2,763)	C = 1.57 8,816 (2,597)	11,685 (2,627)	10,742 (2,415)
16	2.36 (0.093)	2.62 (0.103)	C = 1.47 16,613 (3,735)	C = 1.44 16,271 (3,658)	15,679 (3,525)	13,900 (3,125)

E<sub>EXTENSION</sub> = 21 X 10<sup>6</sup> Psi, E<sub>flex</sub> = 16.5 X 10<sup>6</sup> Psi

Cylinder/Cone Test						
50 Longitudinals Total	2.36 0.093	2.36 0.093	C = 1.67 12,290 (2,763)	C = 1.57 11,551 (2,597)	11,685 (2,627)	8,896 (2,000)

The buckling loads predicted in Table 4-2 are for local buckling for both infinitely rigid joints and for finite joint rigidity (corresponding to  $\hat{K}_{local}$  of 30.), and for general instability using the analysis of Anderson (Reference 4-1) which corresponds to infinitely rigid joints. The data for the parametric cylinder shows that fairly good correlation ( $\approx 4-9\%$ ) is achieved for the 2.11 mm (0.083 in.) and 2.36 mm (0.093 in.) diameter longitudinals, but the test data are considerably below ( $\approx 13-17\%$ ) predictions for the

2.62 mm (0.103 in.) diameter longitudinal members. The predicted buckle mode shape was a local buckle between joints, whereas the observed buckle mode was a mode shape encompassing at least one joint. Reason for the discrepancy in buckling load and mode shape is not presently known.

The cylinder/cone test buckling load is shown compared to local buckling and general instability calculations at the bottom of Table 4-2. The test results are lower than predicted and also lower than the results for the parametric cylinder with 2.36 mm (0.093 in.) diameter longitudinals. Apparently, local curvature induced by a local moment at the cylinder/cone junction reduced the buckling load to approximately 85% of that measured for the parametric cylinder and to approximately 76% of the predicted value. Stiffening of the frame at the cylinder/cone juncture should improve future correlations.

#### 4.4 References for Section 4

- 4-1. Anderson, Melvin S.: Buckling of Periodic Lattice Structures. AIAA Paper No. 80-0681, presented at the AIAA/ASME 21st Structures and Structural Dynamics and Materials Conference, Seattle, Washington, May 12-14, 1980.
- 4-2. Forman, S. E. and Hutchinson, J. W.: Buckling of Reticulated Shell Structures.
- 4-3. Development of a Composite Geodetic Structure for Space Construction, Phase I Final Report. McDonnell Douglas Astronautics Company Report MDC G8079, September 1979.
- 4-4. Dunn, T. J.: A Cylindrical Structure Made with Continuous Rods. NASA-Lyndon B. Johnson Space Center, Unpublished report.

## Section 5

### CONCLUSIONS AND RECOMMENDATIONS

This section presents the conclusions reached based on the results presented in the preceding sections and provides recommendations for subsequent program efforts.

#### 5.1 CONCLUSIONS

Detailed conclusions are presented in the following paragraphs in the same sequence as the preceding sections.

##### 5.1.1 Geodetic Beam Material Characterization

During this program, HMS/E-glass/PI700 was thoroughly characterized as to mechanical and physical properties. Conclusions, based on the results of material characterization work are presented below:

- (a) A near-zero CTE composite rod material suitable for the fabrication of geodetic structures is achievable by a proper mixture of HMS graphite and E-glass fibers in a PI700 thermoplastic matrix.
- (b) Pultruded HMS/E-glass/PI700 round rod stock with constant high axial and flexure stiffness and strength, low density and near zero CTE can be continuously produced as round rod stock using a pultrusion process by different suppliers. This material can be reliably joined using a low-power consuming encapsulation technique to produce high stiffness/strength joints for geodetic structures.
- (c) Limited exposure to simulated space exposure revealed no significant degradation in the strength and stiffness characteristics of geodetic beam rod stock.
- (d) Laboratory testing indicates no tendency of elastically coiled (strained) rod stock to develop a permanent set.
- (e) Geodetic beam HMS/E-glass/PI700 rod stock material with low  $\alpha/\epsilon$  (absorptivity/emittance) of 0.163 can be obtained by the use of selected coatings, e.g., a S13G/L0 thermal control coating. Bare rod stock has a relatively high  $\alpha/\epsilon$  of 1.19.

- (f) Results of physical property characterization testing of HMS/E-glass/PI700 pultruded rod indicate that:
- The specific heat of rod stock is similar to that of aluminum.
  - The electrical resistivity of rod stock is approximately 1000 times greater than that of aluminum.
  - The longitudinal thermal conductivity of rod stock is approximately one-sixth that of aluminum.

#### 5.1.2 Parameter Tests

Two geodetic structures, a parameter cylinder and a cone/cylinder test article, were successfully analyzed, designed, fabricated, instrumented and tested to evaluate structural parameters and characteristics in order to gain a greater understanding of the capabilities of composite geodetic structures. Conclusions based on the results of testing accomplished are presented below:

- (a) The analytically predicted change in load carrying capability of geodetic structures with the ratio of longitudinal-to-helical rod size was demonstrated in parameter cylinder tests.
- (b) Significant increases in geodetic beam load carrying capability (approximately 22%) were achieved with only a small increase (approximately 7%) in structure weight by increasing the diameter ratio of longitudinal-to-helical rod stock from 1.00 to 1.10 (e.g., only 10%). However, this small change also resulted in shell failure in a general instability rather than rib buckling mode. Therefore, future minimum weight geodetic structures optimized for maximum load carrying capability through the reduction of helical rod diameter, will have to be analyzed in sufficient detail so as to either avoid the general instability mode or be designed with confidence in an ability to predict the onset of this failure mode.
- (c) The full-scale geodetic beam end closure design concept selected during Phase I, consisting of a geodetic lattice cone closeout, a geodetic cylinder segment and an attach ring for joining the cylinder and cone, is a highly feasible geodetic structure based on results of design/analysis, fabrication and testing work. The cone/cylinder test article failed in the cylindrical segment in rib

buckling as predicted at a load level approximately 85% of that associated with buckling due to a pure compressive load.

- (d) Induced bending in the geodetic cylinder segment near the cone/cylinder intersection was a contributing factor to the reduced buckling load carrying capability of the cone/cylinder test article. Future geodetic beam designs will either have to minimize bending effects at the cone/cylinder attach ring through the use of a modified ring design, minimize assembly induced rib imperfections, or reduce overall beam design load capability to account for increased bending.
- (e) Based on cone/cylinder test results, the distribution of load transferred from the lattice cone closeout to the geodetic cylinder segment is extremely uniform around the circumference of the cylinder.

### 5.1.3 Structural Analyses

Based on the structural analysis results, the following conclusions were reached:

- (a) Analytical techniques for predicting local rib buckling and general instability of geodetic structures correlate very well (4-9%) with test data when the longitudinal member is equal to, or less than the stiffness of the helical member.
- (b) Analytical techniques over predict geodetic structure local rib buckling and general instability loads by approximately 17% when longitudinal members have a higher bending stiffness than helical members.
- (c) The cylinder/cone test failure level was influenced by edge moment that occurred at cylinder/cone juncture. The discreteness of the structural configuration influences the axial distance over which the local moment damps out. In the test, local buckling occurred near the juncture and produced a 17% lower buckling load than observed in the parameter cylinder test.

## 5.2 RECOMMENDATIONS

Recommendations based upon the results presented in Sections 2 through 4 are presented in the following paragraphs.

### 5.2.1 Development Testing

- (a) Based on the successful feasibility testing of the geodetic cone/cylinder test article, future program efforts should include the verification testing of a complete geodetic beam, including lattice cone closeouts. This testing will be the final verification of the structural integrity of the geodetic beam concept prior to the start of geodetic beam machine final design. Mechanical loading tests, including axial compression, bending, shear and torsion loads, and thermal loading tests should be conducted.
- (b) The geodetic beam concept can be fabricated using many structural materials, e.g., resin matrix composites, traditional metallic alloys and metal matrix composites. Because of recent fabrication breakthroughs which allow the production of continuing lengths of round graphite reinforced metal matrix rod stock using low cost pitch fibers, an assessment of the applicability of metal matrix composites for geodetic structures should be conducted. This assessment should include metal matrix composite with fabrication and joining technique development tasks as well as feasibility testing of a geodetic cylinder segment fabricated using metal matrix composites. Metal matrix composites offer long life, no-outgassing and high specific stiffness and the potential of geodetic structures which are more structurally efficient than those fabricated using resin matrix composites.

### 5.2.2 Geodetic Beam Machine Development

- (a) Geodetic beam machine design should be accomplished with particular emphasis on the joint encapsulation and shear cutting subsystems. Demonstration tests of these critical subsystem should be accomplished as soon as possible in order to prove feasibility of the geodetic beam machine concept.

### 5.2.3 Geodetic Structure Design and Analysis

The following recommendations are made for improving and extending design/analysis techniques for geodetic structures:

- (a) Include local joint stiffness effects in the general instability calculations.
- (b) Investigate the design of joints in structures with discrete stiffness.



## APPENDIX A

### GEODETIC BEAM MATERIAL PHYSICAL PROPERTY CHARACTERIZATION TESTS

This appendix presents a detailed discussion of physical property characterization testing of HMS/E-glass/P1700 pultruded rod stock. The HMS/E-glass/P1700 material was obtained from U.S. Polymeric, Inc., in prepreg tape form and subsequently pultruded to final rod form by the Composithek Engineering Corporation (CEC).

Samples of HMS/E-glass/P1700 graphite polysulfone rods were analyzed by several techniques. Six samples were analyzed by differential scanning calorimetry (DSC) to determine specific heat at ambient, 100°C and 200°C temperatures. Electrical conductivity of two specimens was measured by determination of the electrical resistivity at 10 cm intervals along a rod. Solar absorptivity was measured on six 1.27 cm x 1.27 cm x 0.32 cm specimens using a Gier Dunkle Model MS 251 Solar Reflectometer. Of the six samples, three were uncoated graphite polysulfone squares and three were coated with SS4044 primer and S13G/L0 coating. Thermal conductivity of two specimens over the temperature range -196°C to 146°C was obtained through thermal diffusivity measurements and through the Kohlrausch method. These tests were done by the Thermophysical Properties Research Laboratory (TPRL) of the Center for Information and Numerical Data Analysis and Synthesis (CINDAS). The coefficient of thermal expansion of six samples of pultruded rod stock was determined using thermomechanical analysis (TMA) over the temperature range -175°C to 150°C. These tests were done by Compoite Optics Inc., San Diego, CA. A detailed discussion of all testing accomplished is presented below.

#### A.1 Specific Heat

A DuPont 990 Controller, equipped with a DuPont DSC cell and cell base, was used to perform the analyses. In addition, one thermogravimetric analysis (TGA) was performed in order to determine the percentage weight loss as a function of temperature.

Samples were prepared by slicing 0.16-cm-thick wafers from rod stock with a Unimat saw. Two of these wafers were placed into an aluminum sample pan, and an aluminum cover crimped onto the pan. Two empty aluminum pans were then run to establish a baseline and a standard sapphire specimen in an aluminum pan was run versus an empty aluminum pan. Finally, the specimen in an aluminum pan was run versus the empty pan. The following parameters were used:

Atmosphere: Argon at 20 cc/min

Heating Rate: 10°C/min

Sensitivity: 0.197 (mcal/sec) cm

Samples were programmed from ambient to 500°C.

Calculation of specific heat values at a given temperature was accomplished according to the following formula:

$$CP_s = (H_s/H_a)(W_a/W_s)Cp_a \quad (A-1)$$

where

$Cp_s$  = specific heat of the sample (cal/g/K)

$H_s$  = height of the sample curve from the baseline (cm)

$H_a$  = height of the standard curve from the baseline (cm)

$W_a$  = weight of the standard (g)

$W_s$  = weight of the sample corrected for weight loss during heating (g)

$Cp_a$  = specific heat of the standard (cal/g/K)

Thermal plots of DSC runs are shown in Figures A-1 through A-6. A data summary of the specific heat values and heights of the sapphire standard from the baseline for six specimens is given in Tables A-1 and A-2. Specific heat values appear to increase from 50°C to 400°C, then decrease at 500°C. The standard deviation for the specific heat values is approximately 16%, while the standard deviation of the sapphire standard is approximately 3%. This difference occurs because the distribution of fibers in the graphite/glass polysulfone rod is not uniform, causing a larger deviation from sample to sample than the sapphire values would indicate.

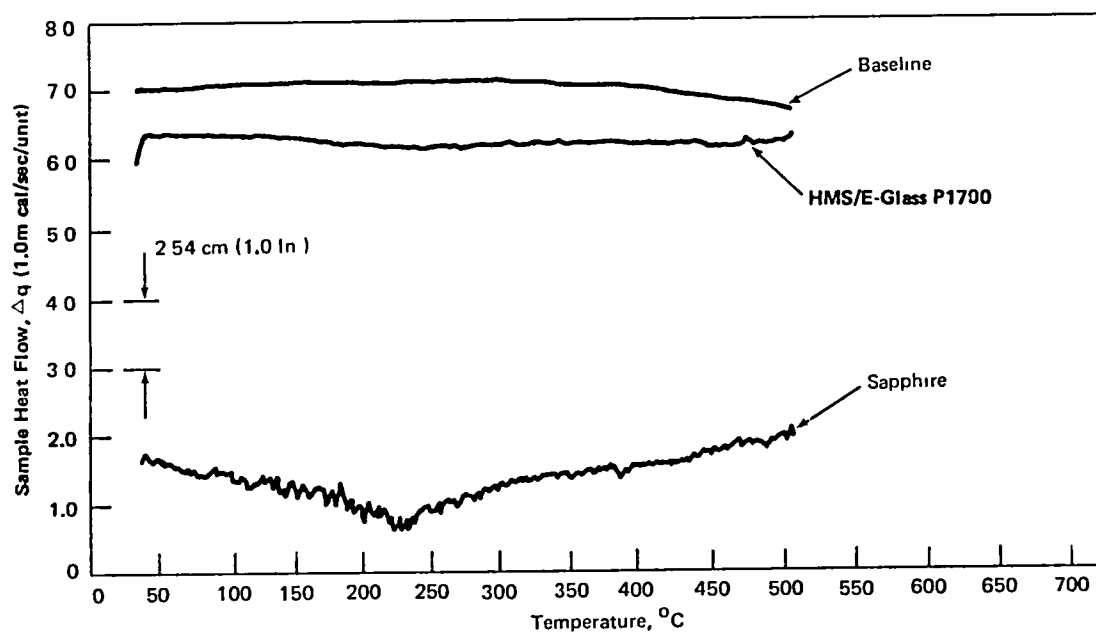


Figure A-1. Thermal Plot of DSC Run 1.

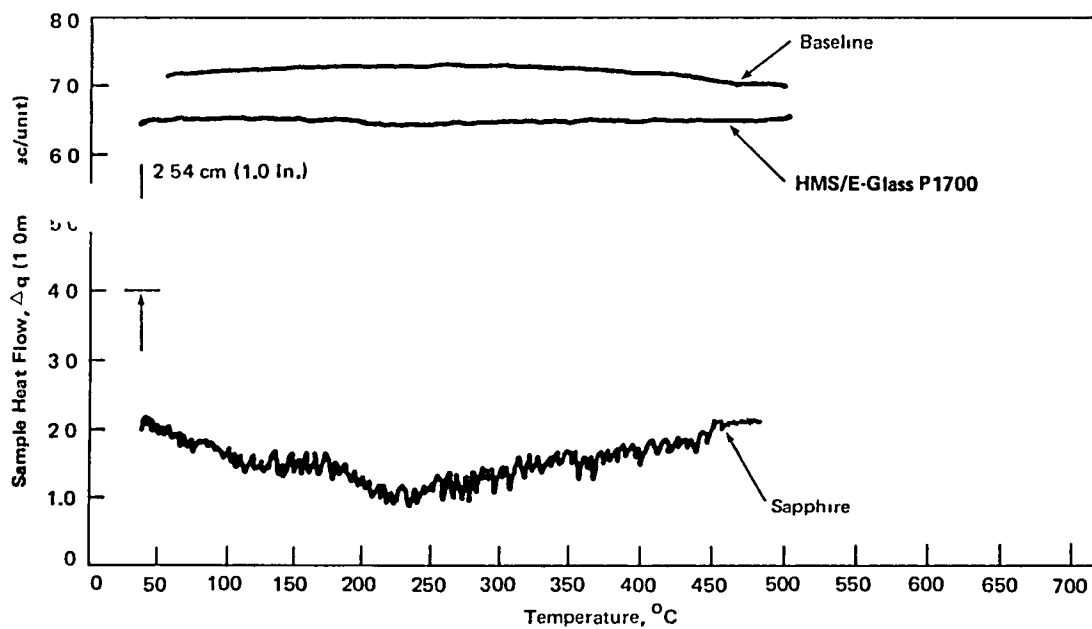


Figure A-2. Thermal Plot of DSC Run 2.

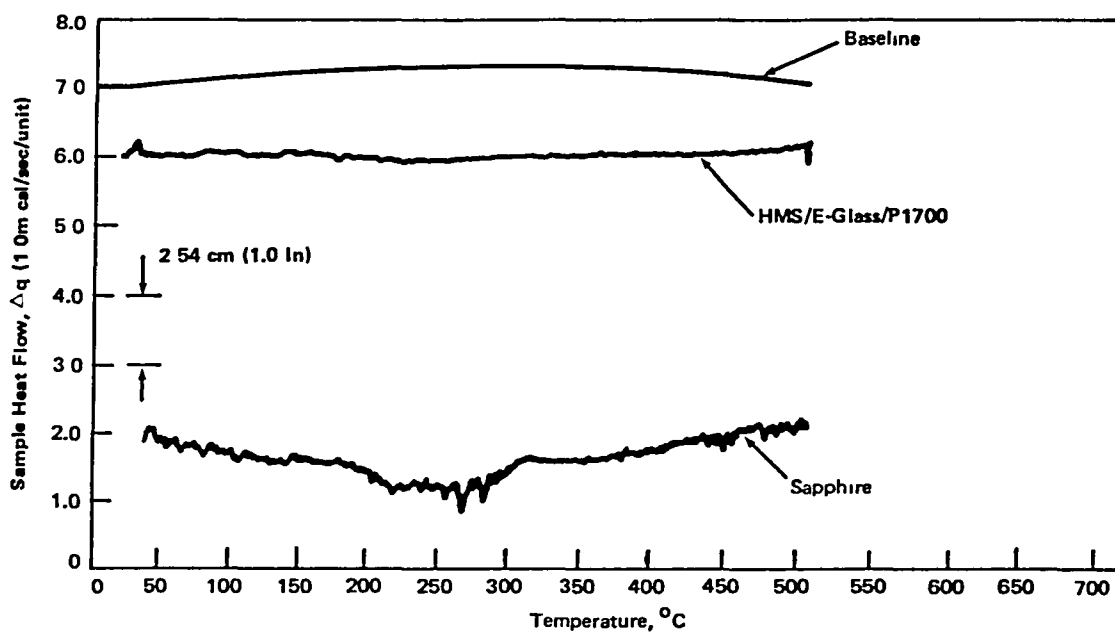


Figure A-3. Thermal Plot of DSC Run 3.

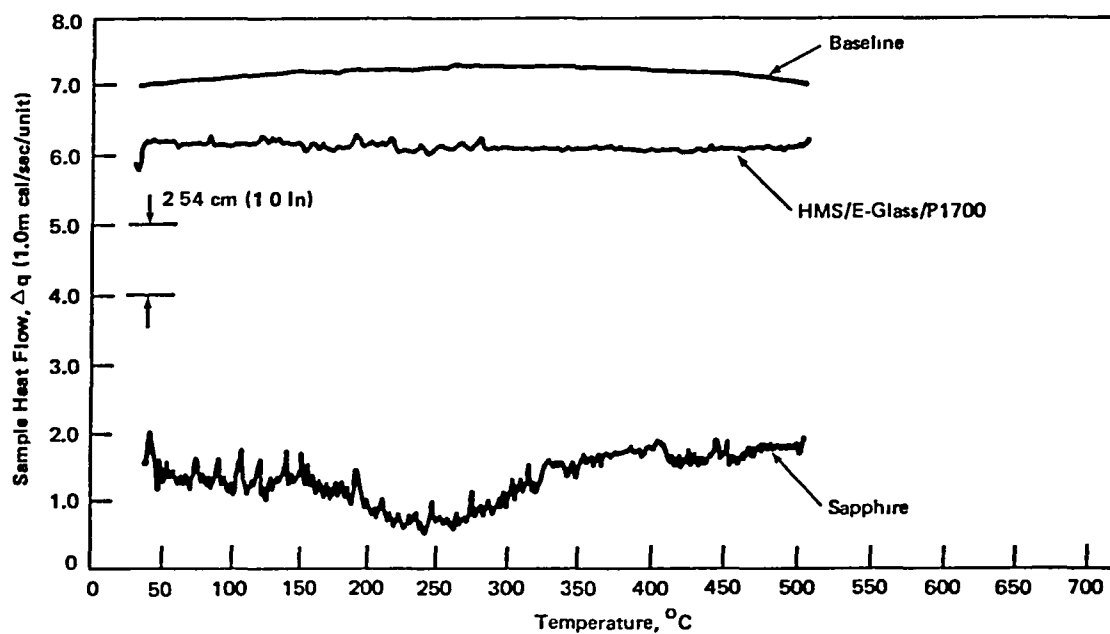


Figure A-4. Thermal Plot of DSC Run 4.

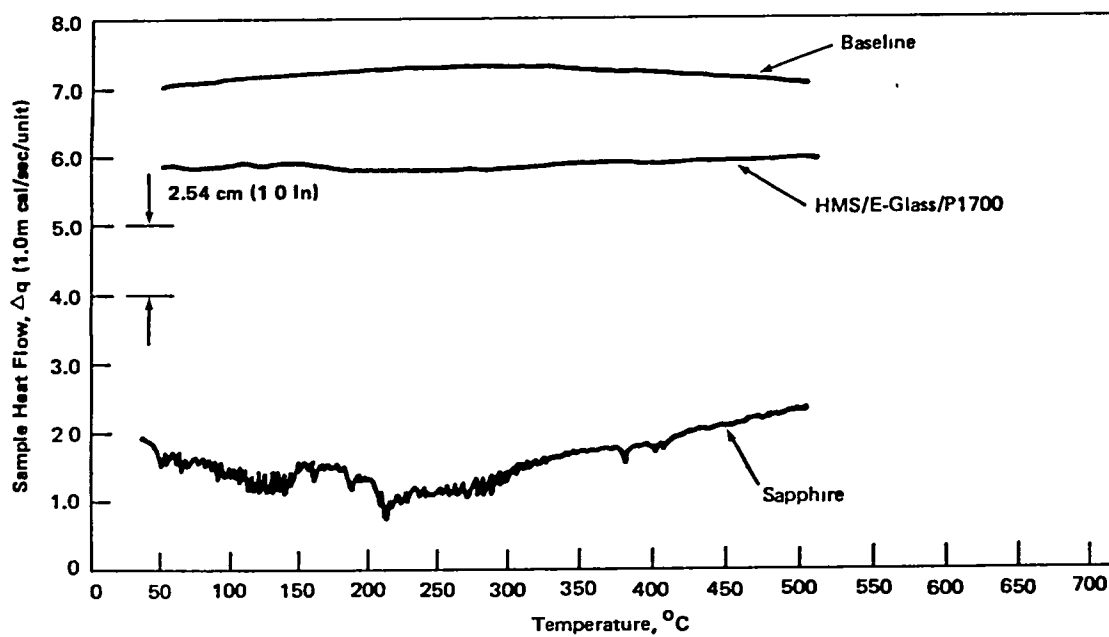


Figure A-5. Thermal Plot of DSC Run 5.

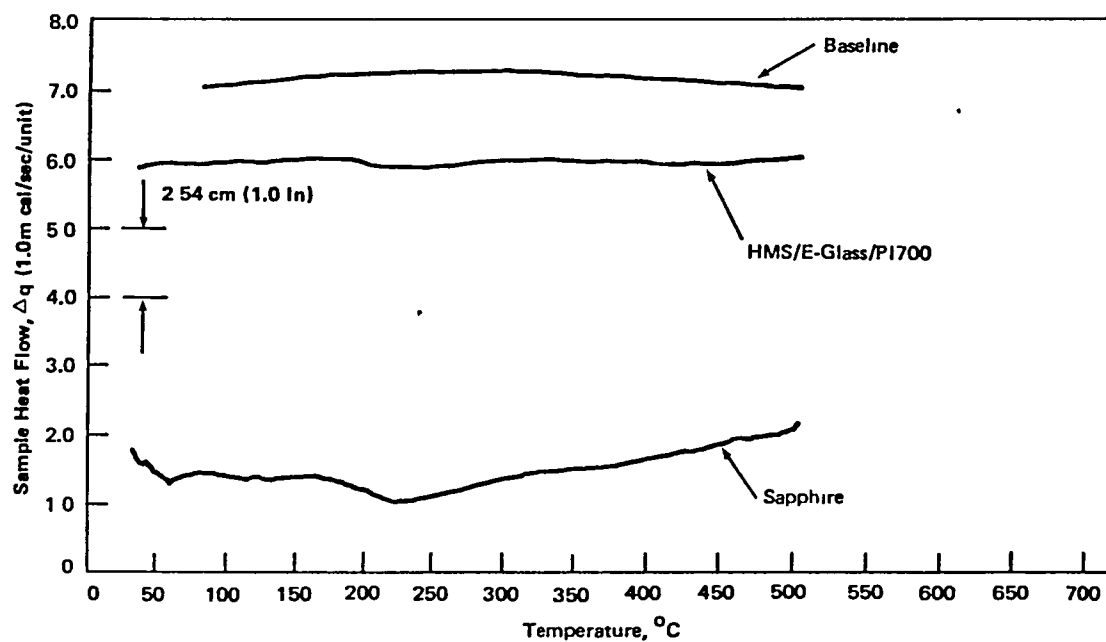


Figure A-6. Thermal Plot of DSC Run 6.

TABLE A-1  
SPECIFIC HEAT OF GRAPHITE/GLASS POLYSULFONE

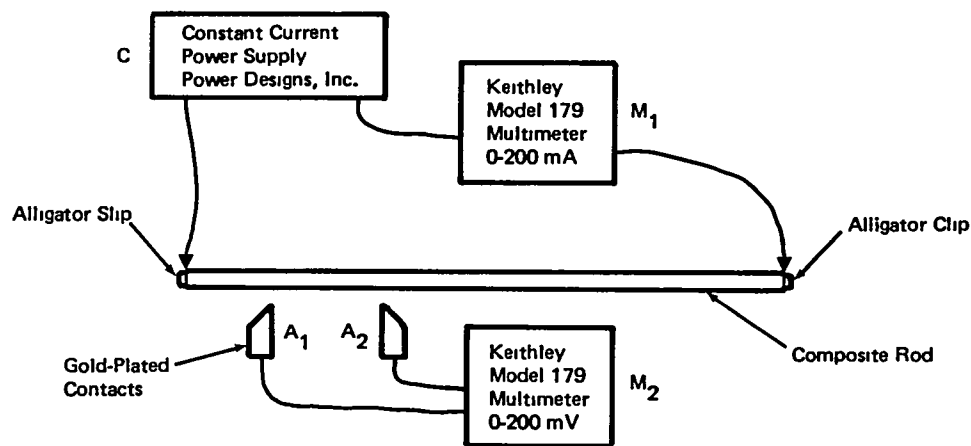
	Temperature (°C)	50	100	200	300	400	500
Sample Wt (mg)	Cp in cal/g <sup>o</sup> K (Btu/lb <sup>o</sup> F)						
10.144	Cp <sub>1</sub>	0.1496 (0.1496)	0.1691 (0.1691)	0.2133 (0.2133)	0.2384 (0.2384)	0.2331 (0.2331)	0.1713 (0.1713)
7.197	Cp <sub>2</sub>	0.2021 (0.2021)	0.2250 (0.2250)	0.2760 (0.2760)	0.3072 (0.3072)	0.2917 (0.2917)	0.2294 (0.2294)
12.119	Cp <sub>3</sub>	0.1924 (0.1924)	0.2169 (0.2169)	0.2650 (0.2650)	0.3117 (0.3117)	0.2993 (0.2993)	0.2688 (0.2688)
12.017	Cp <sub>4</sub>	0.1516 (0.1516)	0.1798 (0.1798)	0.2192 (0.2192)	0.2461 (0.2461)	0.2770 (0.2770)	0.2532 (0.2532)
12.164	Cp <sub>5</sub>	0.2015 (0.2015)	0.2334 (0.2334)	0.2906 (0.2906)	0.3195 (0.3195)	0.3338 (0.3338)	0.3071 (0.3071)
10.194	Cp <sub>6</sub>	0.2292 (0.2292)	0.2542 (0.2542)	0.3148 (0.3148)	0.3383 (0.3383)	0.3609 (0.3609)	0.3238 (0.3238)
	$\overline{C_p}$	0.1877	0.2131	0.2632	0.2935	0.2993	0.2589
	$\delta C_p$	0.0315	0.0323	0.0396	0.0415	0.0446	0.0554

TABLE A-2  
HEIGHTS OF SAPPHIRE STANDARDS

Temperature (°C)	50	100	200	300	400	500
h sap1	5.37	5.69	6.17	5.85	5.42	4.90
h sap2	5.11	5.62	6.05	6.04	5.55	4.84
h sap3	5.14	5.42	5.82	5.85	5.46	4.96
h sap4	5.66	5.80	6.25	6.29	5.55	5.31
h sap5	5.33	5.62	5.96	5.89	5.37	4.79
h sap6	5.49	5.70	6.01	5.90	5.52	5.00
$\overline{h}$ sap	5.35	5.64	6.04	5.97	5.48	4.97
$\delta h$ sap	0.21	0.20	0.27	0.17	0.07	0.18

## A.2 Electrical Conductivity

Electrical conductivity of graphite/glass polysulfone rod stock was determined through measurement of the electrical resistance. The apparatus consists of a constant current power supply, a Keithley model 179 Multimeter, and two gold-plated contacts. The following setup was used:



To make a measurement, a Power Designs Inc., constant-current power supply (C) was adjusted so that a 100 mA current was measured by the Keithly Model 179 Multimeter (M<sub>1</sub>) when the leads were attached with alligator clips to the extreme ends of the graphite/glass polysulfone rod. The gold-plated contacts (A<sub>1</sub> and A<sub>2</sub>) were adjusted to be 10.0 cm apart and the rod was pressed against them until a steady voltage was read on the multimeter (M<sub>2</sub>). The measurement was repeated along the length of the rod at 10 cm intervals.

Table A-3 gives a summary of electrical conductivity values for two rods of graphite/glass polysulfone. The measured voltage drop showed a variation of roughly  $\pm 25\%$  as the rod was rotated so that different areas touched the gold contacts. This is apparently due to non-uniform distribution of graphite and glass fibers in the matrix. The highest and lowest resistance for each 10 cm length of rod as well as the average maximum and minimum resistance for each rod are given in Table A-3.

TABLE A-3  
ELECTRICAL RESISTIVITY OF GRAPHITE/GLASS POLYSULFONE

Min. Resistance per 10 cm Length (Note Values Given in $\Omega/\text{cm}$ )	Max. Resistance per 10 cm Length (Note Values Given in $\Omega/\text{cm}$ )
Rod No. 1	
0.047 $\Omega/\text{cm}$ 0.051 $\Omega/\text{cm}$ 0.054 $\Omega/\text{cm}$ 0.053 $\Omega/\text{cm}$ 0.054 $\Omega/\text{cm}$ 0.052 $\Omega/\text{cm}$  Average = 0.052 $\Omega/\text{cm}$	0.070 $\Omega/\text{cm}$ 0.058 $\Omega/\text{cm}$ 0.064 $\Omega/\text{cm}$ 0.060 $\Omega/\text{cm}$ 0.064 $\Omega/\text{cm}$ 0.087 $\Omega/\text{cm}$  Average = 0.067 $\Omega/\text{cm}$
Rod No. 2	
0.053 $\Omega/\text{cm}$ 0.060 $\Omega/\text{cm}$ 0.047 $\Omega/\text{cm}$ 0.053 $\Omega/\text{cm}$ 0.051 $\Omega/\text{cm}$ 0.048 $\Omega/\text{cm}$ 0.051 $\Omega/\text{cm}$ 0.029 $\Omega/\text{cm}$ 0.034 $\Omega/\text{cm}$ 0.044 $\Omega/\text{cm}$  Average = 0.047 $\Omega/\text{cm}$	0.080 $\Omega/\text{cm}$ 0.080 $\Omega/\text{cm}$ 0.061 $\Omega/\text{cm}$ 0.060 $\Omega/\text{cm}$ 0.061 $\Omega/\text{cm}$ 0.055 $\Omega/\text{cm}$ 0.060 $\Omega/\text{cm}$ 0.068 $\Omega/\text{cm}$ 0.077 $\Omega/\text{cm}$ 0.081 $\Omega/\text{cm}$  Average = 0.068 $\Omega/\text{cm}$

The voltage drop across each 10 cm length of rod was approximately 0.05 V, so the total power dissipated over a 10 cm length was:

$$\begin{aligned}
 W &= iE \\
 &= 0.100 \text{ A} \times 0.05 \text{ V} = 5 \times 10^{-3} \text{ W}
 \end{aligned}
 \tag{A-2}$$

where

$W$  = power (watts)  
 $i$  = current (amperes)  
 $E$  = voltage (volts)

Under the conditions used, heating of the rod was negligible.

### A.3 Solar Absorptivity

Solar absorptivity was measured using a Gier Dunkle Model MS251 Solar Reflector. Six square specimens, 1.27 cm x 1.27 cm x 0.32 cm, were formed from the graphite/glass polysulfone (HMS/E-glass/P1700) material. Of these six, three were coated with a system composed of SS4044 primer and S13G/L0 coating; the other three were left uncoated. One measurement of solar absorptivity was



made per sample. The coated side was measured on the coated samples, and on the uncoated samples the shinier, smoother side was measured. A stray light measurement was made and stray light was found to be approximately 2%. This value was used to correct values obtained in sample measurement.

Table A-4 gives values of solar absorptivity for coated and uncoated graphite/glass polysulfone samples. The white-coated samples absorb much less light in the solar wavelength region than the black uncoated samples. The average absorptivity for uncoated samples is 0.913, and for coated samples, 0.146.

TABLE A-4  
SOLAR ABSORPTIVITY OF GRAPHITE/GLASS POLYSULFONE

	Solar Absorptivity $\alpha_s$
Uncoated Samples	
1	0.910
2	0.915
3	0.915
	<u>0.915</u>
	Avg = 0.913
Coated Samples	
1	0.150
2	0.139
3	0.148
	<u>0.148</u>
	Avg = 0.146

#### A.4 Infrared Emittance

Infrared emittance was measured using a Gier Dunkle Model DB100 Infrared Reflectometer. The specimens of graphite/glass polysulfone used in solar absorptivity measurements were also used to measure IR emittance. The specimens were slightly smaller than the sample port of the infrared reflectometer. In order to prevent the leakage of infrared radiation around the edges of the sample, the sample port was masked with gold foil. The reflectometer was calibrated against two standards - one a high reflectance gold standard, and the other a low reflectance black standard. Calibration is repeated before every specimen measurement.

Table A-5 gives values of infrared emittance for coated and uncoated graphite polysulfone samples. The white-coated samples show a greater emittance in the infrared than the black uncoated samples. The average emittance for the uncoated samples is 0.771, and for coated samples is 0.895. The ratio of  $\alpha/\epsilon$  was calculated for both coated and uncoated samples. The uncoated samples have an approximately seven-fold greater  $\alpha/\epsilon$  ratio than the coated samples.

TABLE A-5  
IR EMITTANCE OF GRAPHITE/GLASS POLYSULFONE

	$\epsilon$	$\alpha/\epsilon$
Uncoated		
1	0.764	1.19
2	0.777	1.18
3	<u>0.771</u>	<u>1.19</u>
	Avg = 0.771	Avg = 1.19
Coated		
1	0.894	0.168
2	0.891	0.156
3	<u>0.901</u>	<u>0.164</u>
	= 0.895 Avg	Avg = 0.163

#### A.5 Thermal Conductivity

The thermal conductivity of samples of graphite/glass polysulfone rod was measured using two techniques. The first involved the measurement of thermal diffusivity using the flash diffusivity technique on several specimens cut from the rod and at different locations on the same sample. The apparatus consists of a Korad K2 laser, a high vacuum system including a bell jar with viewing windows, a tube heater/chiller surrounding the sample, a spring-loaded thermocouple, appropriate biasing circuits, amplifiers, A-D converters, crystal clocks, and a minicomputer-based digital acquisition system.

Specific heat values were measured with a Perkin-Elmer Model 2 DSC over a small temperature interval to convert the thermal diffusivity results to thermal conductivity values, using the relation:

$$K = \alpha C_p \delta \quad (A-3)$$

where

$\alpha$  = thermal diffusivity ( $\text{cm}^2/\text{sec}$ )

$C_p$  = heat capacity ( $\text{Ws/g-K}$ )

$\delta$  = bulk density ( $\text{g/cm}^3$ )

The Kohlrausch techniques were used to determine thermal conductivity over the desired temperature range. The temperature rise data did not follow the theoretical model because of the large differences in the ability of the graphite fibers and the matrix to conduct heat. A conductivity method was used in order to obtain the temperature dependency. Two specimens were chosen whose room temperature conductivity values approximated those obtained from diffusivity measurements.

The Kohlrausch method involves the measurement of the product of thermal conductivity and electrical resistivity. This is achieved by passing constant direct current through the sample, heating it while the ends are maintained at a constant temperature. An external heater minimizes radial heat loss. Thermocouples are positioned at the center of the sample and 1 centimeter on each side of the center. The thermocouples are also used to measure voltage. With the center thermocouple at position 2 and the others at positions 1 and 3, the product of thermal conductivity and electrical resistivity can be measured as:

$$K\rho = \frac{(V_3 - V_1)^2}{4[2T_2 - (T_1 + T_3)]} \quad (A-4)$$

where

$K$  = thermal conductivity ( $\text{W cm}^{-1}\text{K}^{-1}$ )

$\rho$  = electrical resistivity ( $\text{ohm/cm}$ )

$V_3 - V_1$  = voltage drop between outside thermocouples (volts)

$T_1 + T_3$  = sum of temperatures at outside thermocouples (K)

$T_2$  = temperature of center thermocouple (K)

Electrical resistivity is measured as

$$\rho = \frac{(V_3 - V_1) A}{IL} \quad (A-5)$$

where

A = cross-sectional area ( $\text{cm}^2$ )

I = current (amperes)

L = distance between outside thermocouples (cm)

Using these measured values, K can be calculated. Data collection and calculations are computerized and the measurements are made while the sample is under vacuum and the external heater temperature is set to  $T_2$ . When one set of measurements is completed, more current is applied; after equilibrium is established, a new set of measurements is made. This method has been used previously on a number of fiber-reinforced materials.

Tables A-6 through A-8 show a data summary for the thermal conductivity determination. Table A-6 gives specific heat values over a narrow temperature range. The units are  $\text{Ws-gm}^{-1}\text{-K}^{-1}$  in the first column, and  $\text{BTU-lb}^{-1}\text{-F}^{-1}$  or  $\text{cal-g}^{-1}\text{-K}^{-1}$  in the second column. These values extrapolated to  $23^\circ\text{C}$  give a value for specific heat of  $0.800 \text{ Ws-gm}^{-1}\text{-K}^{-1}$ . Comparison of the specific heat results given in Table A-1 indicates that the specific heat values obtained by CINDAS are generally higher than those obtained by MDAC-HB. The range of CINDAS values is narrow, so comparison is possible only around  $100^\circ\text{C}$ . At this temperature, the CINDAS specific heat value is comparable to the highest value for specific heat obtained in Table A-1 ( $C_{p6} = 0.2542 \text{ cal-g}^{-1}\text{-K}^{-1}$ ).

Thermal diffusivity values for four samples, with three locations measured on each sample, are given in Table A-7. Bulk density values for two 7.62 cm sections of rod were found to be 1.5275 and  $1.5248 \text{ g/cm}^3$ . From these results, thermal diffusivity values have been converted to thermal conductivity values and the results shown in Table A-7. The average longitudinal thermal conductivity value is  $0.275 \text{ W-cm}^{-1}\text{-K}^{-1}$  at  $23^\circ\text{C}$ .

Kohlrausch results for two samples are given in Table A-8. In Figure A-7, these results are plotted along with the conductivity values obtained by the thermal diffusivity method. The results obtained from the Kohlrausch method fall within the range of values determined from thermal diffusivity. The rather wide range of diffusivity values may be due to the non-uniform

TABLE A-6  
SPECIFIC HEAT RESULTS

Sample Weight 0 02550  
Standard Weight 0 026400

(C)	Temperature (K)	Specific Heat (Ws gm <sup>-1</sup> K <sup>-1</sup> )	Specific Heat (BTU lb <sup>-1</sup> °F <sup>-1</sup> )*
66.9	339.9	0.96179	0.22987
72.0	345.0	0.97550	0.23315
77.0	50.0	0.98813	0.23617
82.0	355.0	1.00227	0.23955
87.0	360.0	1.01556	0.24273
91.9	364.9	1.02926	0.24600
97.0	370.0	1.04914	0.25075
101.9	374.9	1.06745	0.25513
106.9	379.9	1.06084	0.25355
111.9	384.9	1.04833	0.25056
117.0	390.0	1.08136	0.25845
122.0	395.0	1.09414	0.26150
127.0	400.0	1.10597	0.26433
131.9	404.9	1.11790	0.26718
137.0	410.0	1.13101	0.27032
142.0	415.0	1.14441	0.27352
146.9	419.9	1.16131	0.27756
152.0	425.0	1.18011	0.28205
157.0	430.0	1.19976	0.28675
161.0	434.9	1.22326	0.29237
167.0	440.0	1.24783	0.29824
172.0	445.1	1.25467	0.29987
177.0	450.0	1.27588	0.30494
181.9	454.9	1.30248	0.31130

\*Or cal g<sup>-1</sup> K<sup>-1</sup>

TABLE A-7  
THERMAL DIFFUSIVITY RESULTS (23°C)

Sample (No.)	Diffusivity (cm <sup>2</sup> sec <sup>-1</sup> )	Conductivity † (w cm <sup>-1</sup> K <sup>-1</sup> )
1	0.230	0.281
2	0.240	0.293
3	0.220	0.268
4	0.200	0.244
1	0.270	0.329
2	0.200	0.268
3	0.280	0.342
4	0.200	0.268
1	0.200	0.268
2	0.190	0.232
3	0.210	0.256
4	0.205	0.250

† Based on  $k = \alpha C_p d$  Where  $d$  is 1.525 gm cm<sup>-3</sup> and  $C_p$  is 0.800 ws gm<sup>-1</sup> K<sup>-1</sup>.

TABLE A-8  
KOHLEAUSCH RESULTS

Sample No.	Temp. (°C)	K (w cm <sup>-1</sup> K <sup>-1</sup> )	Temp. (°F)	K (BTU in hr <sup>-1</sup> ft <sup>-2</sup> F <sup>-1</sup> )
1	-196	0.043	-322	30
	-175	0.060	-283	42
	-148	0.079	-235	55
	-114	0.120	-173	83
	- 87	0.145	-124	101
	- 55	0.180	- 67	125
	- 39	0.193	- 38	134
	- 22	0.210	-  8	146
	-  5	0.227	23	157
	- 58	0.277	136	192
	80	0.290	176	201
	108	0.307	226	213
	132	0.327	269	227
	146	0.336	295	233
2	-142	0.155	-224	107
	- 84	0.220	-119	153
	- 35	0.258	- 31	179
	-  6	0.283	21	196
	52	0.326	126	226
	85	0.350	185	243
	138	0.381	280	264

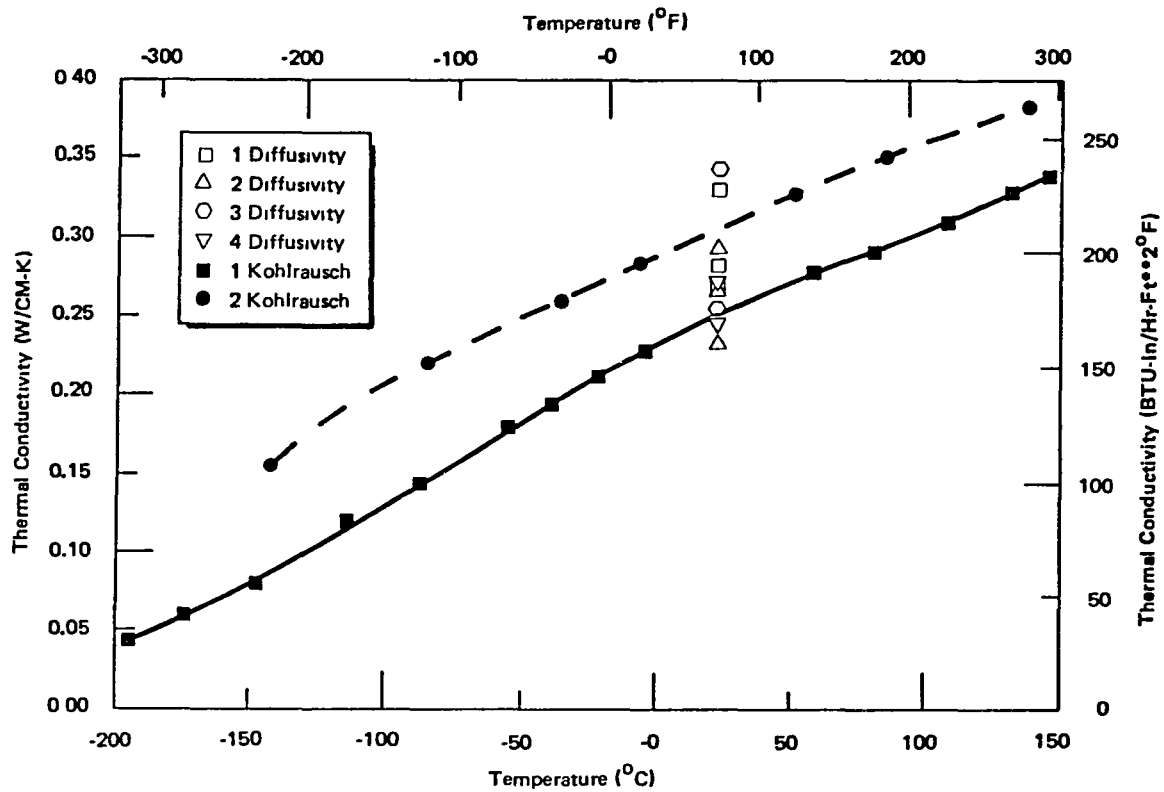


Figure A-7. Thermal Conductivity Results.

distribution of fibers in the material. Although the heterogeneity of the material may lead to differences in thermal conductivity, an average of the two Kohlrausch results represents the thermal conductivity of the material. The Kohlrausch results also show that thermal conductivity is dependent on temperature in a positive direction.

#### A.6 Coefficient of Thermal Expansion

The coefficient of thermal expansion of six 2.54 cm specimens of graphite/glass polysulfone was measured from -184°C to 149°C. The samples were preconditioned at 142°C for 2 hours under vacuum.

The measurements were made by comparing the sample with a calibrated length of fused silica. As the sample and standard are heated, an optical system composed of mirrors and a laser is used to measure length. Samples were kept under vacuum or under a dry nitrogen purge. The temperature of the samples was stabilized under vacuum; the temperature was raised under dry nitrogen. With a 2.54 cm sample, resolution is 0.1 ppm and repeatability is 1 ppm.

Two 15.24 cm samples were measured using the same instrument and under the same conditions as the 2.54 cm specimens. However, a small leg of graphite/glass polysulfone rod was fastened to the center of each 15.24 cm sample with Hysol EA934 adhesive. The leg minimized sagging of the 15.24 cm specimens during heating.

Coefficient of thermal expansion results for the 2.54 cm samples are shown in Tables A-9 and A-10. In Figures A-8 through A-10, absolute expansion in ppm is plotted against temperature for all six 2.54 cm specimens. The coefficient of thermal expansion is consistently negative. The plots in Figures A-8 through A-10 are fairly linear; slopes and y-intercepts for these plots were obtained by linear regression. These values are given in Table A-10. The standard deviation for the slope values is approximately 9.74%, and the standard deviation of the intercept values is about 1164%. Values of  $r^2$  for each plot indicate a good fit of the linear regression line with the data points.

TABLE A-9  
COEFFICIENT OF THERMAL EXPANSION RESULTS

Point No	Sample AA-1		Sample AB-1	
	Temp (°F)	ΔL/L (ppm)	Temp. (°F)	ΔL/L (ppm)
1	75.3	0.0	75.3	0.0
2	150.3	-23.02	150.3	-26.36
3	229.8	-37.21	229.8	-49.33
4	307.8	-73.99	307.8	-86.11
5	-4.0	26.01	-4.0	16.13
6	-73.8	62.21	-73.8	48.79
7	-144.8	97.44	-144.8	85.40
8	-220.3	143.69	-220.3	118.64
9	-301.3	187.19	-301.3	153.31
10	76.0	-11.48	76.0	-6.78
Point No	Sample AA-2		Sample AB-2	
	Temp (°F)	ΔL/L (ppm)	Temp. (°F)	ΔL/L (ppm)
1	78.0	0.0	78.0	0.0
2	147.8	-23.91	147.8	-28.05
3	226.3	-45.18	226.3	-47.25
4	305.8	-95.03	305.8	-82.10
5	5.3	44.66	5.3	50.14
6	-69.8	86.23	-69.8	87.23
7	-147.3	122.90	-0147.3	126.49
8	-218.3	154.01	-218.3	159.21
9	-267.5	164.79	-267.5	170.32
10	70.0	0.69	70.0	6.34
Point No.	Sample BA-1		Sample BB-1	
	Temp (°F)	ΔL/L (ppm)	Temp (°F)	ΔL/L (ppm)
1	75.3	0.0	78.3	0.0
2	150.3	-15.63	147.3	-33.09
3	229.8	-36.13	226.3	-63.52
4	307.8	-57.46	305.8	-80.16
5	-4.0	27.05	-4.0	44.86
6	-73.8	43.39	-073.8	85.30
7	-144.8	67.44	-144.8	128.22
8	-220.3	79.03	-220.8	177.12
9	-301.3	84.78	-301.3	224.03
10	76.0	31.37	76.0	1.43

Note: These Results Superseded by Tests of 15.24 cm Length Samples. See Table A-11.



TABLE A-10  
LINEAR REGRESSION DATA FOR COEFFICIENT OF THERMAL EXPANSION RESULTS

Sample ID	Slope	Y-Intercept	$r^2$
AA-1	-0.4216	41.09	0.9696
AB-1	-0.3842	29.02	0.9896
AA-2	-0.4654	46.98	0.9907
AB-2	-0.4664	50.31	0.9896
BA-1	-0.2428	24.69	0.9534
BB-1	-0.5229	53.07	0.9844
Standard Deviation	9.47 Percent Deviation in Slope	1164 Percent Deviation in Y-Intercept	$r^2$ Avg = 0.9796 or 2.04 Percent Deviation From An Analytically Linear Plot

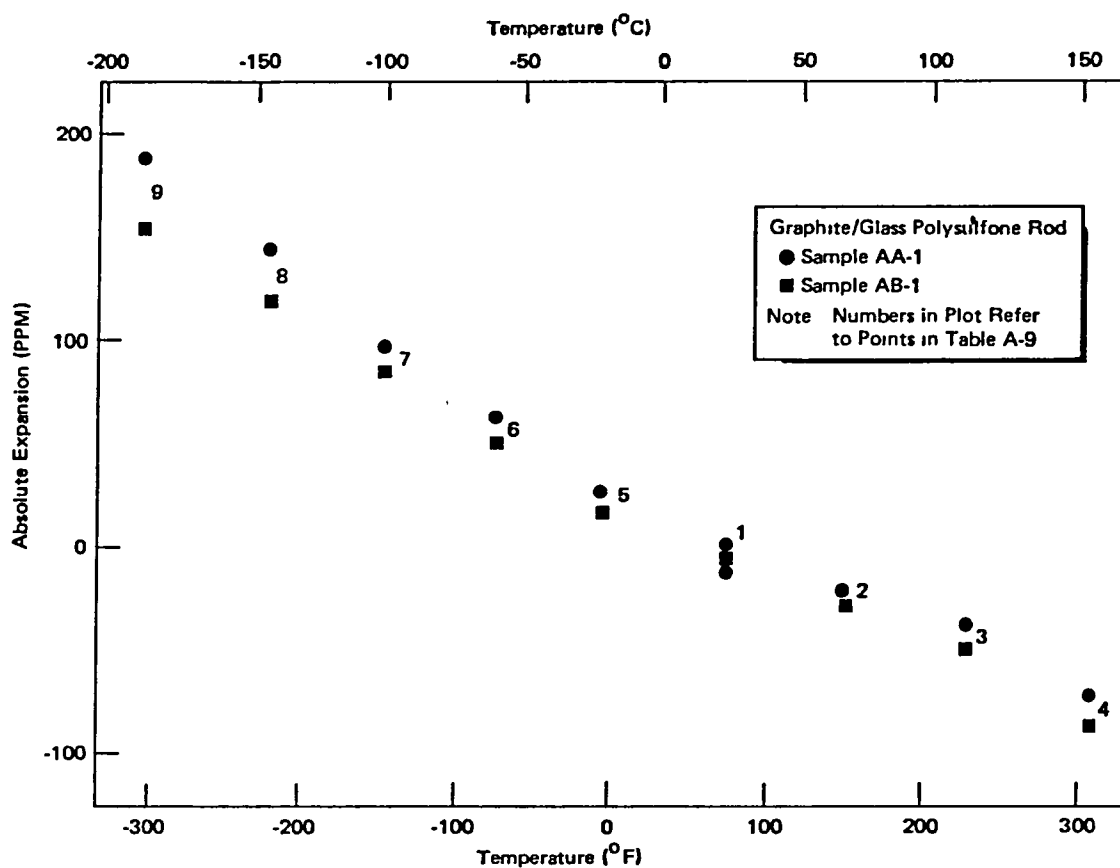


Figure A-8. Coefficient of Thermal Expansion Results for 2.54 cm Samples

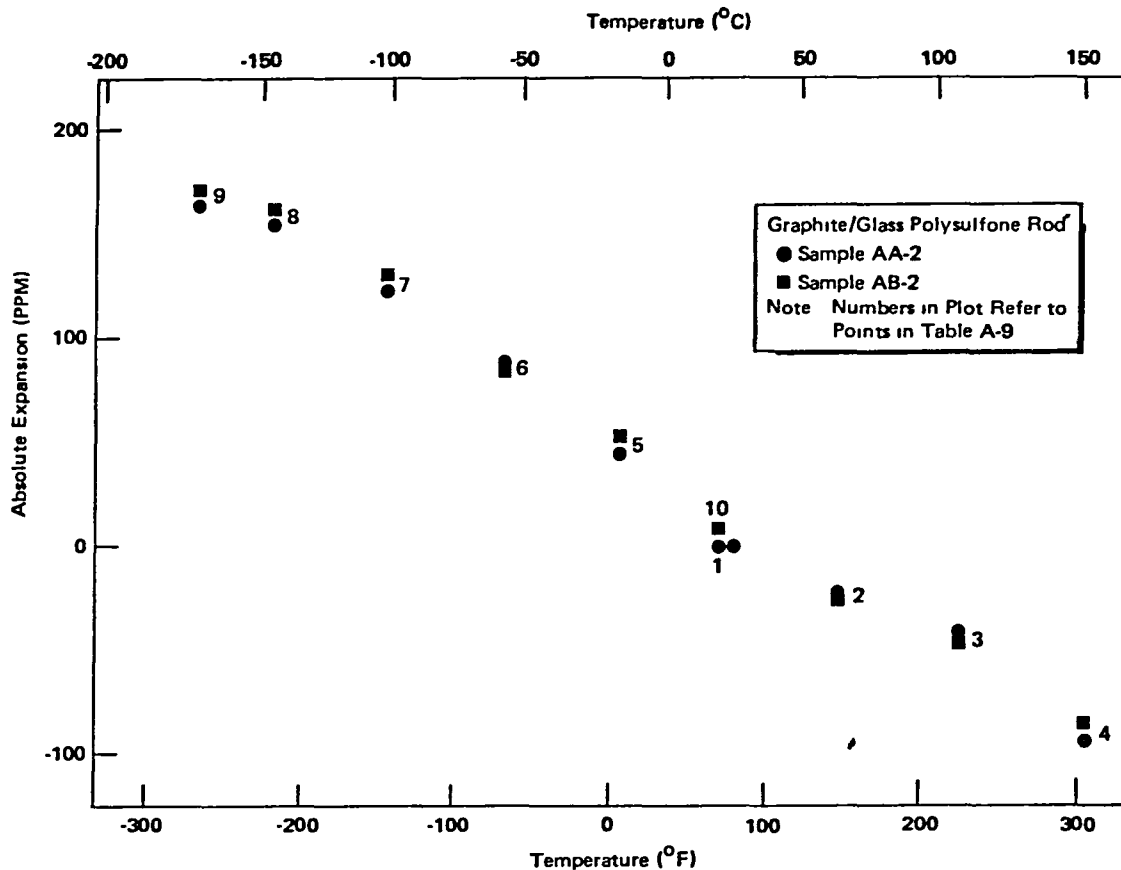


Figure A-9. Coefficient of Thermal Expansion Results for 2.54 cm Samples

Coefficient of thermal expansion results for 15.24 cm samples are shown in Table A-11. In Figure A-11, absolute expansion in parts-per-million is plotted against temperature in degrees Fahrenheit for both 15.24 cm samples. The plots in Figure A-11 are fairly linear; slopes and Y-intercepts for these plots were obtained by linear regression. The coefficient of thermal expansion is consistently negative for the 15.24 cm specimens; however, the values are approximately three times smaller than those from the 2.54 cm samples. Because of the greater resolution possible with longer samples, the values obtained using 15.24 cm samples more accurately represent the coefficient of thermal expansion of the material. In Figures A-8 through A-11, the plots were generated by Composite Optics Corporation. These thermal plots are submitted as received and no attempt has been made to curve fit the points, as familiarity with specific instruments would be required.

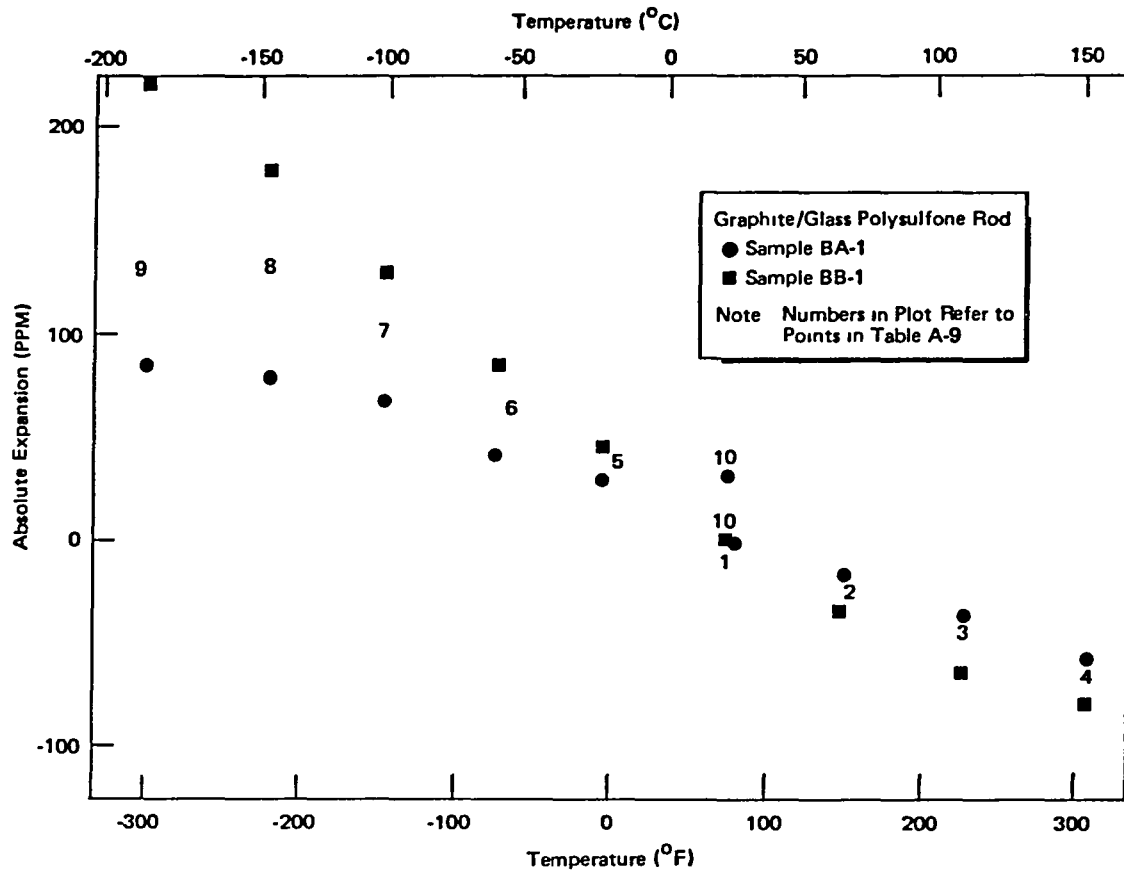


Figure A-10. Coefficient of Thermal Expansion Results for 2.54 cm Samples

TABLE A-11  
COEFFICIENT OF THERMAL EXPANSION RESULTS FOR 15.24 CM  
SPECIMENS OF GRAPHITE/GLASS POLYSULFONE ROD

Point No.	Sample A		Sample B	
	Temp. (°F)	$\Delta L/L^*$ (ppm)	Temp. (°F)	$\Delta L/L$ (ppm)
1	71.0	-0.10	71.0	-0.10
2	148.0	-7.83	148.0	-5.18
3	236.0	-9.63	236.0	-2.55
4	300.0	-8.28	300.0	-7.62
5	-2.5	2.32	-2.5	17.38
6	-83.0	18.25	-83.0	28.03
7	-149.5	31.58	-149.5	41.11
8	-219.5	44.34	-219.5	52.59
9	-275.0	50.17	-275.0	57.82
10	69.0	-5.41	69.0	-4.37
Linear Regression Results for 15.24 cm Specimens				
	Sample A		Sample B	
Slope	-0.133		-0.126	
Y-Intercept	12.61		18.90	
$r^2$	0.884		0.896	

\*Change in Length of Sample Divided by Total Length

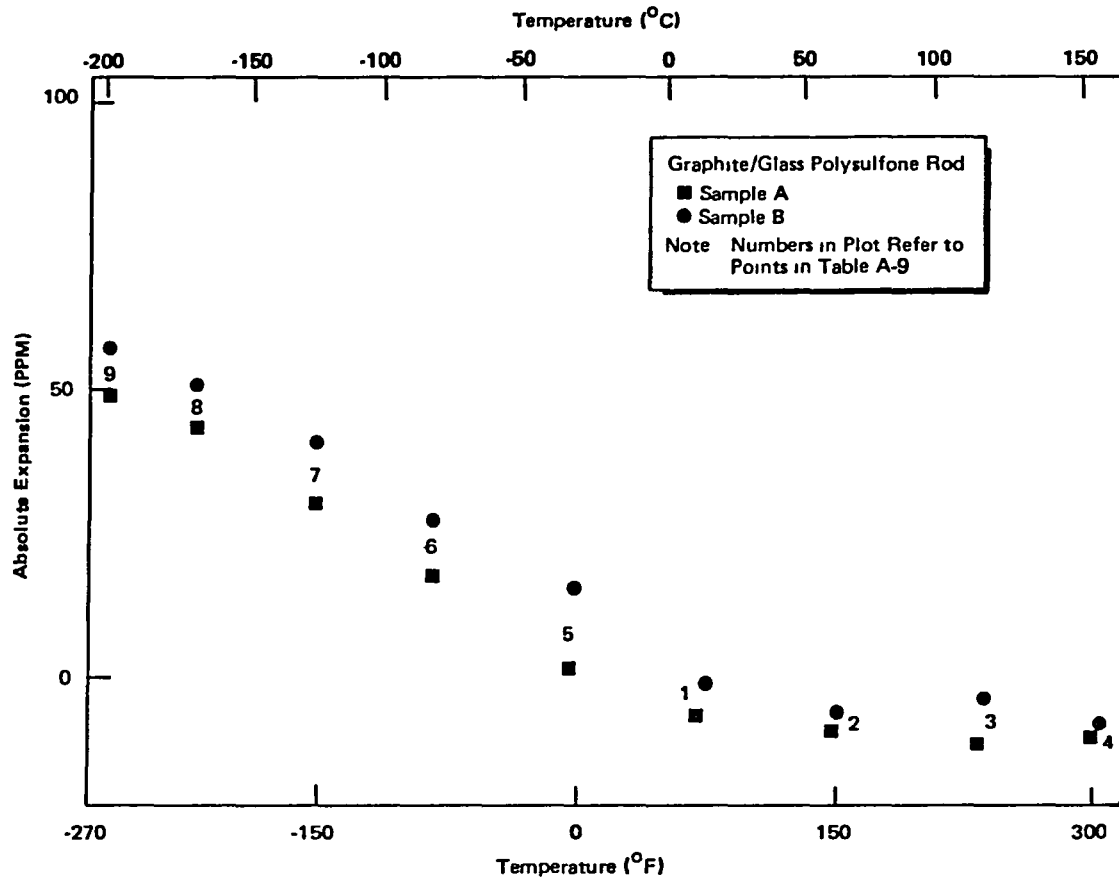


Figure A-11. Coefficient of Thermal Expansion Results for 15.24 cm Samples.

**End of Document**